On the Core Flow and Turbulent Boundary Layer in a Curved Duct

Phillip Lawrence Wilson
University College London
University of London

A thesis submitted for the degree of
Doctor of Philosophy.
Supervisor: Prof. F.T. Smith F.R.S.
September 2003

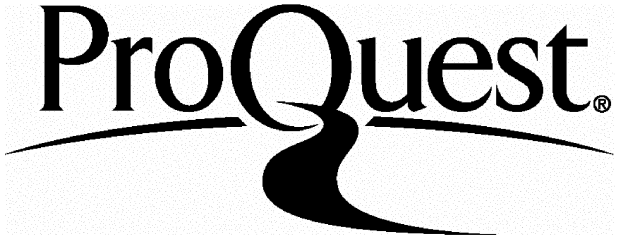

Abstract

Curved ducts for transporting fluids are commonplace in industry and nature and, whilst many previous studies have concentrated on viscous responses to curvature, there are configurations and/or occasions when the fluid flow is sufficiently rapid that an inviscid approximation is more appropriate. One such occasion is the rapid flow of compressed air through an ejector in a food-sorting machine, which occurs over a typical timescale of 3 milliseconds. The particulars of the current project are connected with the interests of a manufacturer of food-sorting machines, and consequently variations around a specific geometry are studied in this thesis. Using asymptotic analysis and computational techniques, the thesis first studies the steady inviscid response of the flow to the curvature of the duct. Part I concentrates on the core-flow response to the curvature, extending a recent study to include compressibility. Bulk properties of the flow are derived analytically, along with far-downstream predictions of the flow behaviour and the response close to sharp corners of the cross-section. These results are supported by weakly and fully non-linear computational solutions of the steady three-dimensional Euler equations. Part II then studies the growth and development of the turbulent boundary layer in a curved duct. It is observed that there is an apparent lack of experimental data for the level of curvature specified by the industrial application. Entry region analysis suggests the turbulent boundary layer velocities split into a component matching the core flow and a turbulent component. Solutions are found for the turbulent components in the entry region. Three downstream regimes of the major parameters are also identified and described. One, the quasi-straight regime, is studied in detail numerically and comparisons with experiments are made. Increasing curvature effects are discussed by means of the other two regimes.

Acknowledgements

My first and most heartfelt thanks go to my supervisor, Prof FT Smith, FRS, for his perpetual encouragement, insight and support. His expertise and infectious enthusiasm have made the past three years the most challenging and enjoyable of my life. In so many areas and by so many means he has given me skills and memories which I shall always treasure. I also wish to sincerely thank Dr S Bee and Dr M Honeywood of Sortex, Ltd, for their openness, encouragement and feedback on the physical implications of this thesis. I gratefully acknowledge the financial support of EPSRC and of Sortex, Ltd.

On a more personal note, the academic staff, support staff, and postgraduate students of the mathematics department at UCL deserve my thanks for some wonderful memories, and for innumerable acts of assistance over the years. I wish also to warmly acknowledge the love and support of my friends and family over the past three years. In the former category I wish to mention Mr K Gautama who has been a source of inspiration since first opening my mind to mathematics some 14 years ago. Amongst my family members I deeply thank Peter, Janet, and Harrison Dalby whose love and support have helped in more ways than they can possibly imagine. Most importantly, my love and thanks go to my parents, Chris and Ken. Their abiding love and belief in me have rendered many difficult times more bearable, many daunting tasks surmountable, and have given me the liberty to pursue my dreams, for which I am eternally indebted to them.

Finally, the dedication overleaf is to my wife, Yuri, whose love sustains me always.

For Yuri,

who said yes.

Contents

List of Figures

Chapter 1

Introduction

An understanding of the flow of fluids through ducts has been sought since times of antiquity. Perhaps over millenia, many now nameless hydraulic engineers contributed to a body of expertise which must have been known to Hero of Alexandria when he wrote his *Dioptra* in the 2nd century BCE. The description of a principle of continuity contained within is the earliest we know of, and predates Leonardo da Vinci's clearer exposition by some 17 centuries. Between these two men stand lessons learnt, forgotten, and re-learnt by the great Roman engineers and the inhabitants of pre-Rennaissance Europe. The fresh- and waste-water piping systems in continents across the ancient world are also testament to the early practical understanding of duct flows and their importance to managing ever larger human settlements.

In the modern world, predicting and controlling flows through ducts seemingly grow in importance as our technological sophistication and knowledge of biological systems increase. In particular, it is fair to say that ducts with bends are commonplace in nature and in human constructs, where they arise either by design or by necessity. The positive and negative effects, depending

on application, of convoluted piping systems are of interest to industry, for example in enhancing heat transfer or necessitating the installation of pumps to overcome pressure head losses. The flows through mass exchangers, turbomachinery, rocket engines, animal and artificial hearts, microfluidic machines and many other industrial applications besides involve fluids of different kinds moving at a range of velocities over a range of length and time scales and through a variety of levels of duct curvature.

Consequently an important parameter of duct flow is the *Reynolds number*, denoted Re, and defined as

$$Re = \frac{U_\infty L_\infty}{\nu_\infty} , \tag{1.1}$$

where L_∞ is a representative length scale of the flow, and U_∞, ν_∞ are representative values of the fluid velocity and kinematic viscosity, respectively. The definition of Re was of course originally formulated in a study of the factors influencing the transition to turbulence of fluids flowing through straight ducts, and has since found general application. Flows in which Re is relatively low involve a balance of inertia and viscosity and tend to remain laminar. Relatively high Reynolds number flows, on the other hand, can approximate an ideal inviscid fluid for which Re is infinite and are more likely to exhibit turbulence.

Many — though by no means all — examples of flows through curved ducts are in the low Reynolds number regime. Perhaps due to the significance of several such flows (the blood flow through the arteries of the brain, for example), the effects of streamwise duct curvature in low Reynolds number flows have received much attention. Work in this area began with studies of fully developed flows in curved channels and ducts. Uniform streaming of the surface flow to the outer wall of a curved open channel was first recorded in

[87]. The next step, according to [7], was the discovery that the location of the maximum axial velocity of a Poiseuille flow shifted to the outer wall of curved ducts, whilst [34] discovered that a larger pressure gradient was required to produce a given flow rate in curved ducts than in straight ones. Eustice, in [31] and references therein, measured secondary, swirling flows in such ducts. These experimental results were confirmed analytically for circular cross-sections by Dean in [25] and references therein, in which the problem was formulated mathematically for the first time. The formulation in [25] effectively lays the foundations of future work in viscous laminar flow through curved ducts and furnished us with the dimensionless *Dean number*, K — effectively, the ratio of the product of inertial and centrifugal forces to the viscous forces, though its exact definition depends on the paper in which it appears. Such flows are characterised by the ratio $h : a$, the ratio of the typical cross-sectional width to radius of curvature of the bend, and by K.

As well as finding analytical solutions which matched the known experimental results, [25] demonstrated the existence of twin counter-rotating helical vortices in the upper and lower halves of the duct. These counter-rotating vortices are the subject of continuing research. For example, the question of the exact mechanism of viscous return across the centre of the duct is still open, but for large values of K boundary layers are known to develop, carrying mass around the circumference of the duct away from a "source" point at the outer bend, with the layers gradually thickening towards the inside of the bend. Here, after a finite distance, collision and separation occur and a re-entrant jet is formed across the horizontal symmetry plane of the duct, returning the fluid to the source point. Similar mechanisms are known to operate in ducts of non-circular cross-section; for a fuller discussion, see [7, pp.476ff] and refer-

ences therein. Under certain conditions, such as those in [85, 96] and references therein, the twin-vortex solution can bifurcate into a four-vortex solution.

Developing entry flows in viscous regimes have also been the subject of analytical, numerical, and experimental work as described in the introductions to [77, 96]. For example, [71] showed that the boundary layer adjusts upstream of the onset of the bend in the entry region. The introduction to [77] also contains several references to related experimental, analytical, and numerical work on unsteady flows through two-dimensional bends.

Despite the interest in essentially viscous responses to curvature there are many physical situations involving high Reynolds number flow through three-dimensional curved ducts. Many of the ducts are slender and turn the flow through a significant angle, and any inviscid responses to curvature may be compounded by the flow in such bends becoming turbulent and/or unsteady. Often, three-dimensional ducts in practice have simple, uniform cross-sections such as rectangles or circles in order to lower the cost and raise the precision of manufacture. A good example, which we will now describe, of a high Reynolds number flow through such a duct will serve as the motivating physical system for the work in this thesis. The system is connected with the flow of air through ejector guns in food sorting machines. These machines contain arrays of ejectors supplied by air which is pressurised to between three and six atmospheres, depending on the application. The flow through each ejector is instigated by the operation of a piezo-electric diaphragm which opens and closes over 3 milliseconds at up to 150 Hertz. The flow rates involved are substantial and typically equivalent to 20 litres of air per minute through each duct. Design of the machine as a whole forces certain constraints on the design of the ejectors which often entail a departure from the ideal straight duct. At

present, the air in each ejector must pass down a straight rectangular duct section before being twice turned sharply through a significant angle and then ejecting from the duct into the atmosphere. Such complex factors are likely to render a linear one-dimensional analysis (see just below) inadequate and call for a full non-linear three-dimensional treatment. The multi-component nature of the array and the multiple firing of each ejector increases the complexity of the problem.

A standard one-dimensional linearised shock tube analysis of the flow in a typical example of the above motivating industrial system — such as that in [53, pp.70ff] — suggests an atmosphere-ejection speed in the region of 290 ms^{-1}, whereas the experimental value is close to 30 ms^{-1}. This serves to emphasise the importance of understanding the effects of the bend in attenuating the flow (through loss of pressure head), and to demonstrate some restrictions of the one-dimensional analysis.

The large Reynolds number and short duration of the flow described above, together with the likelihood of turbulent effects due to unavoidable manufacturing defects for example, here point to a non-linear inviscid treatment. This approach is to be seen as complementary to the Dean-type studies summarised earlier. In contrast to the large number of low Reynolds number studies, attempts to shed light on three-dimensional inviscid flows through curved ducts seem to date to consist mainly of hydraulic estimates of pressure head losses and empirical suggestions of the existence of secondary flows, with relatively little hydrodynamic treatment. Typical examples of such engineering-based empirical results are given in [6, §10.3], which builds on the "essentially definitive" work of [46, 47]. Studies relating to the transition to turbulence of flows entering and traversing curved ducts have also been carried out, for example

by [84, 32] and references therein.

An important feature of such studies is the ratio $h : a$ defined above. Many experimental studies of the three-dimensional turbulent core or turbulent boundary layer flow through curved ducts are either in the strongly curved regime when $h : a$ is of order unity, or the very weakly curved regime when $h : a$ is two orders of magnitude smaller. Examples are [68] in the former regime and [42] in the latter. The motivating industrial system described above, on the other hand, has $h : a$ approximately 0.1, lying between these two regimes. Although experiments, such as [30], have been reported for this level of curvature they seem restricted to measuring correlation functions and energy spectra near the wall in order to inform turbulence models, but they tend to give little insight into the bulk flow development. Previous studies relevant to turbulent duct flows are discussed in more detail in §6.1 of this thesis.

In the context of the lack of theoretical insight into high Reynolds number flows through curved three-dimensional ducts, [77] presented an analytical and numerical investigation of the three-dimensional flow of an incompressible inviscid fluid through a curved duct of simple cross-section corresponding to the industrial system described earlier. The non-linear approach studied a slightly disturbed uni-directional incident flow entering a sizable bend; typical turning angles were 90°. Unsteady effects were assumed to be confined to thin negligible wall layers. Aside from the duct curvature, the dominant factors were found to be the input swirl in the plane of the cross-section and the shear of the input streamwise velocity profile. Swirl and shear are produced by (for example) the complex upstream conditions which include the opening of the diaphragm, a possible precursor bend, and possible wall roughness. For both

weak and strong input swirl the integrated vorticity was found to grow linearly with bend length. The smallness of the pressure losses as described in [77, §6.2] was also contrasted with that in viscous flows.

Amongst the successes of the work in [77] was the demonstration of doubly-peaked axial velocity profiles and embedded helical vortices which have been witnessed in experiments as summarised in [7]. The authors of [77] also proposed extensions to their approach which it was hoped would give the results greater physical relevance. Such extensions involve the inclusion of real gas effects as well as a more strongly non-linear study and a consideration of turbulent flow effects. We re-iterate that viscous effects are often negligible over the short time scales considered herein.

This thesis aims at extending the work of [77] to include real-gas effects and turbulent behaviours in the motivating industrial system via a mutually supportive combination of analytical and numerical work. The basis of the work, which will in general be three-dimensional and non-linear, is the Navier-Stokes equations which are given in Chapter 2 with real-gas effects being considered in Chapters 3, 4, and 5. The effects of turbulent fluctuations in the flow are studied in Chapters 7 and 8 and will be modelled by a two-tier mixing-length model given in Chapter 6. The flow is considered to be attached throughout, based on the discussion for finite scaled time in [77, p.318]; essentially, the laminar cases would remain attached over the short time scales of relevance here, while turbulent (plug) flow is not likely to separate anyway. Exceptions to this assumption — which do not affect the analysis herein — are discussed in [77, p.340].

Part I of this thesis consists of Chapters 2 to 5 and is concerned with extending the inviscid model to include real gas effects. Laminar or turbulent

viscous layers attatched to the duct walls are assumed to be negligibly thin. Chapter 2 begins this work by introducing the initial formal mathematical model of the motivating industrial problem, based on that in [77]. The high Reynolds number flow in the duct is considered steady, the fluid incompressible, and the level of curvature is given. As an extension to [77] the entry flow problem is considered first, and we show that the flow adjusts smoothly to the sudden onset of the bend via a small upstream influence. For the longer scale which enables a study of the full length of the bend, the principal results and arguments of [77] are summarised, before new solutions to the governing equations are presented which emphasise the influence of the input streamwise velocity shear and cross-plane swirl on the downstream flow.

Real-gas effects are considered for the first time in Chapter 3. This chapter contains an account of the relevant thermodynamical results which are required for the inclusion of real-gas effects in the model. A concise summary of the equations to be carried forward into forthcoming chapters is given at the end of Chapter 3. This work is required for Chapter 4 in which the coupled governing equations are derived for when compressibility and viscosity are present, although in fact the viscous cases are not analysed in this thesis for reasons given above. Next, we perform an analytical study of the weakly non-linear compressible inviscid case which reveals behaviour bearing similarities to the incompressible case of Chapter 2. For example, the pressure drop is relatively small and the vorticity grows linearly with bend length. However, variations in the fluid density in general appear. Far-downstream behaviours are considered both for bends which terminate at a finite distance and others which are maintained indefinitely. Streamwise-invariant states of all variables are attained if the bend terminates, while the vorticity continues to increase

with bend length for large distances if the bend is maintained, leading to more strongly non-linear interactions downstream. The influence of sharp corners in the duct cross-section is also considered, and although singularities develop in the vorticity close to the corners the density is found to be well-behaved there. In certain limits of the governing equations connections with the more strongly non-linear studies of Chapter 5 are discussed.

Chapter 5 is divided into four main sections. The first two are concerned with numerical solutions of the weakly non-linear compressible case, while the second two parts deal with solutions of the fully non-linear compressible case. The numerical approach is explained in detail in §5.1, and is based on an implicit/iterative scheme to solve the relevant coupled set of tridiagonal equations, with compact differencing and mid-point averaging. Numerical solutions are given in §5.2 for a range of input swirls, input streamwise velocity shear and curvature strengths to show the dependence of the downstream flow on these variables. The analytical predictions of Chapter 4 are confirmed within the computational limits of the numerical scheme. The chapter continues with §5.3 in which the governing equations of a fully non-linear compressible inviscid study are derived. The strongly non-linear and coupled nature of the equations render this case a largely numerical one, of course, and the numerical approach is also explained here. Solutions are then given in §5.4 for a range of input values and also for the fully non-linear incompressible inviscid case; mutually supportive analytical and numerical work is carried out in a range of asymptotic limits to assess the reliability of the numerical scheme. An interesting conclusion to emerge is that due to the smallness of the pressure drop the fully non-linear compressible case corresponds to the fully non-linear incompressible case. Real gas effects are thus less influential in the fully non-linear studies

than they are in the weakly non-linear ones.

Part II of this thesis, comprising Chapters 6 to 8, is concerned with the effects of turbulence in the duct flow, from a boundary layer perspective initially. As such, Chapter 6 contains a fairly full background to the description and modelling of turbulence with particular emphasis on two-tier mixing length models. It also gives the details of the *Cebeci-Smith* model which will serve as the standard model in this thesis. The governing equations for the turbulent boundary layer flow in a duct with streamwise curvature are derived. We consider next two specific cases. The development of the turbulent boundary layer in inlet flow in a straight duct is shown to be similar to that for the turbulent boundary layer over a flat plate at zero incidence, as given in [60]. The governing equations in the entry region of a duct with the same level of curvature as that in Part I are given. We then consider the far-downstream behaviour in the entry region wherein as the scaled boundary layer wall normal coordinate tends to infinity the flow in the turbulent boundary layer matches with the far-downstream entry region core flow of Part I. This leads to the introduction of an important parameter: the ratio of the magnitude of the core flow swirl to the magnitude of the turbulent fluctuations in the boundary layer.

The influence of the magnitude of the important ratio just described, *i.e.* the swirl-turbulence ratio, is explored further in Chapter 7. We show that, although there are apparently three identifiable magnitudes, in the entry region each case can be analysed as one by a suitable separation of the influences in the streamwise and cross-stream directions. The core flow influences are felt through terms which are constant across the height of the boundary layer on an outer tier length scale, while the fully turbulent parts of the streamwise and cross-stream boundary layer velocities become the objects of study in the

far-downstream region of the entry region. Here, we derive solutions for the streamwise velocity, which develops similarly to that in the turbulent boundary layer over a flat plate, and for the cross-stream velocity which is non-zero in general and depends on the cross-sectional profile of the duct. Furthermore, a novel kind of cross-stream behaviour is shown to hold here in which the local maximum of the cross-stream flow in the turbulent boundary layer lies very close to the duct wall.

A discussion of longer scale behaviours and their dependence on the swirl-turbulence ratio is also given in Chapter 7 and one of these cases is examined in Chapter 8. This case occurs when the turbulent fluctuations are much stronger than the curvature-induced swirl in the core. As such it is denoted the "quasi-straight" regime. We study this regime over a new length scale where the turbulent boundary layers grow to merge and fill the duct. Firstly, a two-dimensional study is performed in which we show that the duct centre-line velocity is an important parameter which influences both the flow development and the far-downstream behaviour. The junction between the two layers of the two-tier mixing-length model, and leading order variations in centre-line velocity and pressure, are shown to develop linearly with streamwise distance before the junction position and the centre-line velocity suddenly bend to constant values which hold thereafter. An analysis of the governing equations based on a small parameter is performed and the sudden bending described above is shown to be smoothed over a shorter length scale. Generalising, the quasi-straight regime in a three-dimensional axisymmetric duct is considered next; once again, the centre-line velocity is an important parameter and the pressure is predicted to develop linearly with streamwise distance. An analysis based on a small parameter predicts linear growth in the variation in centre-

line velocity and in the junction position with a sudden bending to an invariant state, in keeping with the marching calculations. Unlike in laminar flow, the turbulent fully developed flow solution far downstream is found to depend on the flow behaviour globally, *i.e.* on the complete flow development beforehand.

A summary of the main results of the current thesis and suggestions for future work are contained in Part III (Chapter 9).

Part I

The inviscid model

Chapter 2

The Incompressible Inviscid case

The following configuration, shown graphically in Figure 2.1, constitutes the basic model of the physical situation described in Chapter 1. We take the fluid in the duct to be both incompressible and inviscid. The duct, which is of simple cross-section, is straight fore and aft of the bend, and turns through a total angle denoted by θ_1. In the straight sections, the coordinate x_D is in the direction of the duct axis, and y_D and z_D are the mutually orthogonal coordinates in the cross-sectional plane perpendicular to x_D. We non-dimensionalise the coordinate system with respect to a typical upstream cross-sectional distance h_D, and the corresponding velocity components u_D, v_D, w_D are measured relative to the typical upstream axial flow speed U_D at the onset of the bend. As a result, a natural scaling of the pressure variation p_D is based on twice the dynamic pressure head, namely $\rho_D U_D^2$, where ρ_D is the density of the fluid. We take the radius of curvature of the inside bend of the duct, a_D, to be constant and also non-dimensionalised with respect to h_D giving a large ratio $a_D/h_D \equiv a$. For the flow in the bend, we use cylindrical polar coordinates $r_D, \tilde{\theta}, y_D$ where $\tilde{\theta}$ is zero at the onset of the bend and θ_1 at the termination of

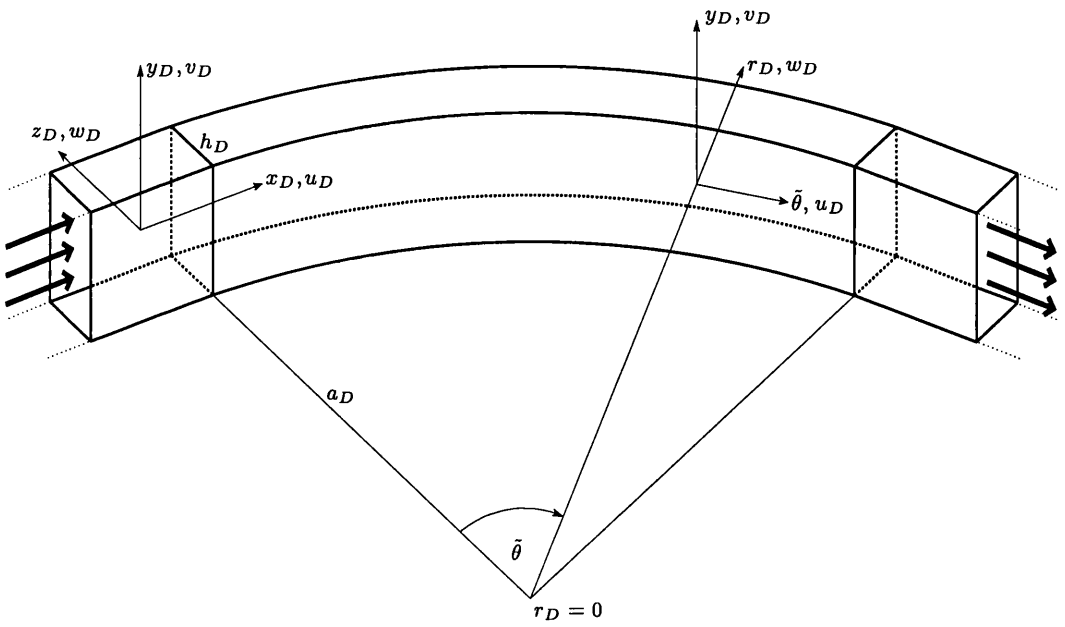

Figure 2.1: Coordinate configuration. The fore and aft straight sections are much longer than drawn here. A duct of rectangular cross-section has been drawn for clarity, although the work herein holds in general for other ducts of simple cross-section.

the bend. It is supposed that the bend is turning through a significant angle of a circular arc, so that θ_1 is for example $\frac{\pi}{2}$. At the focus of the bend, $r_D = 0$ and in the duct $r_D = a_D + z_D$ where $z = z_D/h_D$ is typically of order unity. The coordinate $\tilde{\theta}$ is equivalent to x/a and is here assumed to be also of order unity. Note that the coordinate system $(r_D, \tilde{\theta}, y_D)$ has corresponding velocity components (w_D, u_D, v_D) again.

The equations governing this flow are the dimensional continuity and steady Euler equations:

$$\boldsymbol{\nabla}_D \cdot \boldsymbol{u}_D = 0 \tag{2.1a}$$

$$\text{and } (\boldsymbol{u}_D \cdot \boldsymbol{\nabla}_D)\boldsymbol{u}_D = -\frac{1}{\rho_D}\boldsymbol{\nabla}_D p_D \ . \tag{2.1b}$$

We take the incident flow to be nearly uniform and nearly unidirectional, in the sense that u is unity to within a small order ϵ, and v and w are small.

2.1 Entry flow

In this section we show that as the fluid enters the bend the pressure adjusts smoothly to the sudden onset of the bend via a small upstream influence. By extension, the velocities in the duct also respond smoothly.

We consider the entry region indicated in Figure 2.2 described by order unity values of the non-dimensional Cartesian coordinates x,y, and z. In the reference frame of the entry region the duct walls deviate from the upstream straight section ($x < 0$) by a distance of order $\epsilon \ll 1$ in the downstream section $x > 0$. This deviation will be seen to create a small pressure perturbation which drives the cross-flow locally.

We want to discover how a uniform unidirectional straight-duct flow responds to the onset of the bend, and so we substitute the perturbations

$$(u, v, w) = (1, 0, 0) + \epsilon(\tilde{u}, \tilde{v}, \tilde{w}) + \dots \ , \tag{2.2a}$$

$$p = 1 + \epsilon\tilde{p} + \dots \tag{2.2b}$$

into the non-dimensional continuity and Euler equations. This yields the following system:

$$\tilde{u}_x + \tilde{v}_y + \tilde{w}_z = 0 \ ; \tag{2.3a}$$

$$\tilde{u}_x = -\tilde{p}_x \ ; \tag{2.3b}$$

$$\tilde{v}_x = -\tilde{p}_y \ ; \tag{2.3c}$$

$$\tilde{w}_x = -\tilde{p}_z \ . \tag{2.3d}$$

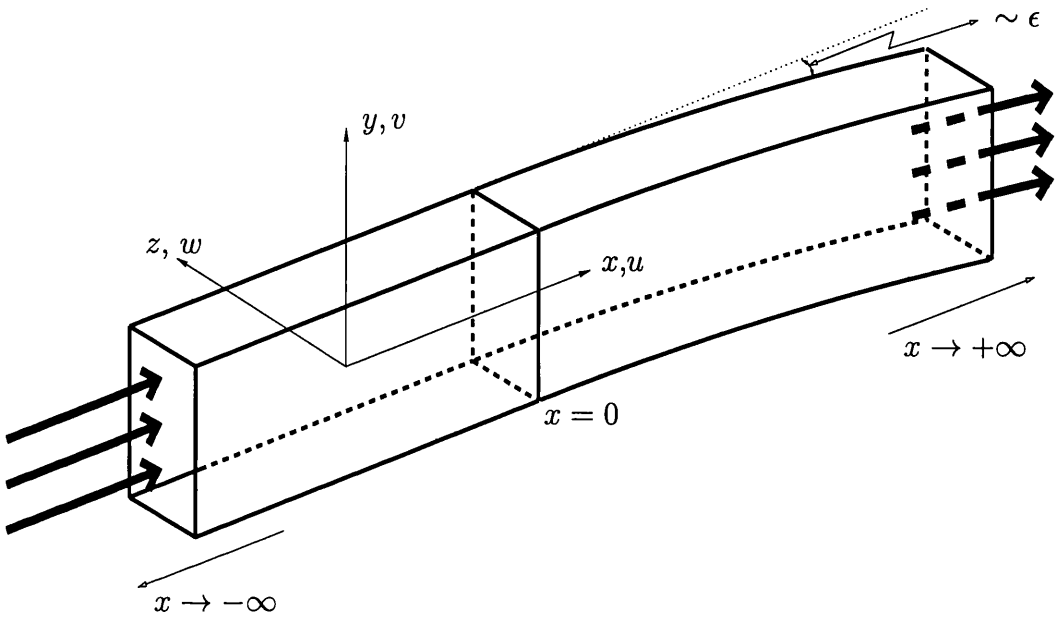

Figure 2.2: Coordinates in the entry region. The straight and curved sections continue upstream and downstream, respectively. A rectangular cross-section is drawn for clarity.

The equations (2.3a–d) yield a three-dimensional Laplace problem for the pressure perturbation $\tilde{p}$:

$$\nabla_{3D}^2 \tilde{p} = 0 \ . \tag{2.4}$$

The boundary conditions are considered next.

We suppose now that the shape of the duct for $x > 0$ is given by

$$z = f = \hat{a} + \epsilon \tilde{f}(x, y) \ , \tag{2.5}$$

whereas for $x < 0$ $\tilde{f}$ is identically zero. The apparent spatial movement of the walls in the Cartesian frame of reference causes a pressure gradient at the walls. Newton's second law requires the force at the wall to equal the acceleration per unit mass it produces. The force produced on the fluid by the moving wall is the negative pressure gradient at the wall, while the acceleration of the wall

is $\frac{\partial^2 f}{\partial x^2} = \epsilon \frac{\partial^2 \tilde{f}}{\partial x^2}$. Thus in general we require

$$\frac{\partial \tilde{p}}{\partial n} = -\frac{\partial^2 \tilde{f}}{\partial x^2} \tag{2.6}$$

at the wall, where n is the local wall-normal coordinate. More specifically, on the wall $z = f(x, y)$ we must have $\boldsymbol{u} \cdot \boldsymbol{\nabla}(z) = \boldsymbol{u} \cdot \boldsymbol{\nabla}(f)$, which gives

$$w = u f_x + v f_y \ . \tag{2.7}$$

With the perturbations (2.2a,b) and with (2.3d) we therefore obtain

$$-\tilde{p}_z = \tilde{f}_{xx} \tag{2.8}$$

when the shape of the duct is given by (2.5). This is the pressure condition on $z = \hat{a}$ for $x > 0$, in line with (2.6). The condition for $x < 0$ is $\tilde{p}_z = 0$ on the walls.

There are at least two possible methods to solve (2.4). One method would be to take Fourier transforms in the z direction, in which case we need to solve the following Poisson equation for the Fourier transform $\tilde{p}^*$ of $\tilde{p}$:

$$\nabla_{2D}^2 \tilde{p}^* = \omega^2 \tilde{p}^* \ . \tag{2.9}$$

We observe that the solution to the Poisson equation in a duct of circular cross-section would involve circular or Bessel functions, while that in a duct of rectangular cross-section would involve trigonometric functions. Use of the convolution theorem would then return the solution for $\tilde{p}$.

An alternative, and ultimately equivalent method of solution of the Laplace problem is to set

$$\tilde{p} = \begin{cases} \sum_{\lambda>0} A_\lambda e^{\lambda x} q_\lambda(y, z) & \text{for } x < 0 \ , \\ \sum_{\lambda<0} B_\lambda e^{\lambda x} Q_\lambda(y, z) + p_\infty(y, z) & \text{for } x > 0 \ , \end{cases} \tag{2.10}$$

and solve for the eigen-functions q_λ, Q_λ and the eigen-values λ. Equation (2.10) requires some discussion. Firstly we note that in the upstream and downstream sections we have chosen the sign of λ and the form of the exponential term such that $\tilde{p}$ is bounded as $x \to -\infty$ and $x \to +\infty$. We have also included the non-zero term $p_\infty(y,z)$ since we aim to show that a non-zero pressure perturbation persists far downstream which will connect with that in the longer scale flow studied in §2.2 and the remainder of Part I of this thesis. The coefficients A_λ, B_λ are to be determined to ensure that the solution is smooth across $x = 0$. We note that this approach ties in with the work of [76, §§3,6].

Let us now consider a rectangular duct with a given deviation $\tilde{f} \sim kx^2$ for $x > 0$. Then for all x in the downstream section $x > 0$ we must have

$$\tilde{p}_z\Big|_{z=\hat{a}} \sim -2k \tag{2.11}$$

by (2.8). Therefore we set

$$p_\infty = -2kz \quad \text{for all } y, z\ . \tag{2.12}$$

We observe that this form of p_∞ satisfies (2.4) far downstream, and that it furthermore satisfies the other wall condition, namely $p_{\infty y}\Big|_{y=\text{const.}} = 0$. This far-downstream pressure variation yields the following velocity variation from (2.3d):

$$\tilde{w} \sim 2kx\ , \tag{2.13}$$

as $x \to \infty$. We also observe that then $|\tilde{v}| \ll |\tilde{w}|$ as $x \to \infty$, a point discussed on page 39 below.

It is clear that for the rectangular cross-section the solution can have $\tilde{v}$ identically zero for all x, in fact. Thus the problem is a quasi-two dimensional

one, requiring us to find the coefficients $A_\lambda, \bar{A}_\lambda, B_\mu, \bar{B}_\mu$ in

$$\tilde{p} = \begin{cases} \sum_{\lambda>0} e^{\lambda x}\left(A_\lambda cos(\lambda z) + \bar{A}_\lambda sin(\lambda z)\right) & \text{for } x < 0\ , \\ \sum_{\mu>0} e^{-\mu x}\left(B_\mu cos(\mu z) + \bar{B}_\mu sin(\mu z)\right) - 2kz & \text{for } x > 0 \end{cases} \tag{2.14}$$

such that the pressure adjusts smoothly across $x = 0$.

Since in the upstream section there is a zero normal pressure gradient at the inner and outer walls we must have

$$\sum_{\lambda>0} e^{\lambda x}\lambda\left(-A_\lambda sin(\lambda\hat{a}) + \bar{A}_\lambda cos(\lambda\hat{a})\right) = 0 = \sum_{\lambda>0} e^{\lambda x}\lambda\left(-A_\lambda sin(0) + \bar{A}_\lambda cos(0)\right)\ . \tag{2.15}$$

Thus $\bar{A}_\lambda = 0$ for all λ and $\lambda = \frac{n\pi}{\hat{a}}$. Hence

$$\tilde{p}_< = \sum_{n=1}^{\infty} A_n e^{\frac{n\pi x}{\hat{a}}} cos\left(\frac{n\pi z}{\hat{a}}\right)\ , \tag{2.16}$$

where $\tilde{p}_<$ is the pressure in the region $x < 0$.

Next we consider the pressure $\tilde{p}_>$ in the region $x > 0$. By applying (2.11) we obtain

$$\sum_{\mu>0} e^{-\mu x}\mu\left(-B_\mu sin(\mu\hat{a}) + \bar{B}_\mu cos(\mu\hat{a})\right) - 2k = -2k$$
$$= \sum_{\mu>0} e^{-\mu x}\mu\left(-B_\mu sin(0) + \bar{B}_\mu cos(0)\right) - 2k\ , \tag{2.17}$$

which leads to the solution:

$$\tilde{p}_> = \sum_{n=1}^{\infty} B_n e^{-\frac{n\pi x}{\hat{a}}} cos\left(\frac{n\pi z}{\hat{a}}\right) - 2kz\ . \tag{2.18}$$

It now remains to find A_n, B_n such that the adjustment across $x = 0$ is smooth, which requires at $x = 0$ that we have equality of $\tilde{p}_<$ and $\tilde{p}_>$ and also of the derivatives $\tilde{p}_{<x}$ and $\tilde{p}_{>x}$. The latter condition requires that

$$\sum_{n=1}^{\infty}\left(\frac{n\pi}{\hat{a}}\right)(A_n + B_n)\, cos\left(\frac{n\pi z}{\hat{a}}\right) = 0 \tag{2.19}$$

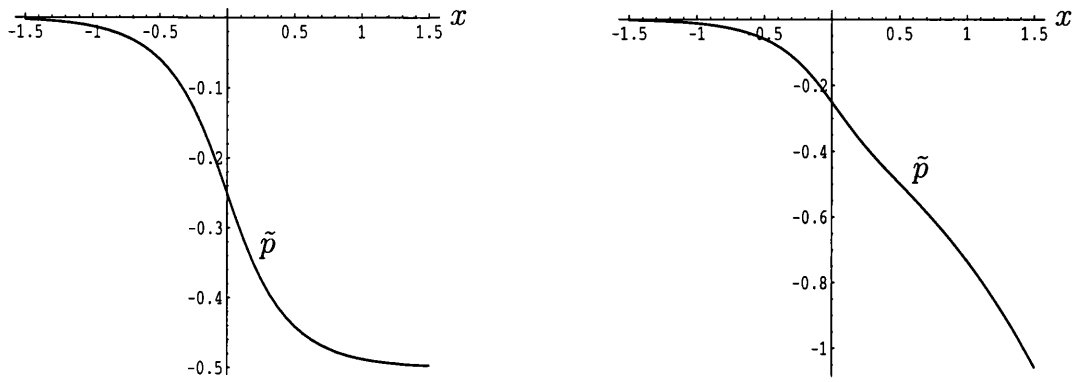

Figure 2.3: Left: plot of (2.23) at fixed $z = 0.5$. Right: plot of (2.23) following the corresponding interior point.

for all z, and thus $A_n = -B_n$. Substituting this into the condition of equality of $\tilde{p}_<$ and $\tilde{p}_>$ across $x = 0$ yields:

$$\sum_{n=1}^{\infty} B_n cos\left(\frac{n\pi z}{\hat{a}}\right) = kz \ . \tag{2.20}$$

Equation (2.20) involves a Fourier cosine series of period $\hat{a}$, and thus inverting (and taking care due to the omission of the $n = 0$ term) we have the formula

$$B_n = \frac{2}{\hat{a}} \int_0^{\hat{a}} (kz + B_0) cos\left(\frac{n\pi z}{\hat{a}}\right) \ dz \ . \tag{2.21}$$

Applying the formula for $n = 0$ gives $B_0 = -k\hat{a}$. Integration by parts then yields the even coefficients B_{2n} (and hence the coefficients A_{2n}) as zero and the odd coefficients as

$$B_{2n-1} = -\frac{4k\hat{a}}{(2n-1)^2\pi^2} \quad \text{and thus} \quad A_{2n-1} = \frac{4k\hat{a}}{(2n-1)^2\pi^2} \ . \tag{2.22}$$

Therefore we have found that

$$\tilde{p} = \begin{cases} \sum_{n=1}^{\infty} \frac{4k\hat{a}}{(2n-1)^2\pi^2} e^{\frac{(2n-1)\pi x}{\hat{a}}} cos\left(\frac{(2n-1)\pi z}{\hat{a}}\right) & \text{for } x < 0 \ , \\ \sum_{n=1}^{\infty} -\frac{4k\hat{a}}{(2n-1)^2\pi^2} e^{-\frac{(2n-1)\pi x}{\hat{a}}} cos\left(\frac{(2n-1)\pi z}{\hat{a}}\right) + k(\hat{a} - 2z) & \text{for } x > 0 \ . \end{cases} \tag{2.23}$$

We note that away from the duct centre line there is a small upstream influence which smooths the transition. Let us now briefly consider a specific duct with $-k = \hat{a} = 1$ and $\epsilon = 0.125$ and the sample point $z_0 = \frac{\hat{a}}{4} = 0.25$ here, recalling that the solution is independent of y. We will show the streamwise pressure development at this position first from the point of view of fixed z and second at a point fixed relative to the duct walls in order to see how the local pressure of the fluid responds within the duct itself. To do so, we note that a given point z_0 in the upstream cross-section of the duct corresponds to the point $z = z_0 + \epsilon k x^2$ in the downstream cross-section of the duct. *Mathematica* was used to plot (2.23) for $-1.5 < x < 1.5$ with 100 terms of each sum taken. The two perspectives are shown in Figure 2.3. We observe that the adjustment across $x = 0$ is smooth and that the far downstream state can be seen emerging.

2.1.1 Discussion of the entry flow

On page 36 we observed that $|\tilde{v}| \ll |\tilde{w}|$ in the entry region of a curved rectangular duct. Thus while w is of $\mathcal{O}(\epsilon)$, v is expected to be of $\mathcal{O}(\epsilon^2)$. We recall that the above study of the entry region is in a frame of reference in which the walls of the duct deviate from a straight path by an $\mathcal{O}(\epsilon)$ amount. Thus the different orders of magnitude of v and w are explained by the fact that the latter is required simply to move the fluid through a distance of order ϵ as the walls themselves move. In other words, $\tilde{w}$ is required to be non-zero since the fluid must move with the walls, but any cross-flow generated within the duct is of an order of magnitude lower still. This is an observation which aids the understanding of the work in Chapter 7 in which the core entry flow is examined from a frame of reference which moves with the walls of the duct. The sketch in Figure 2.4 also helps to elucidate matters.

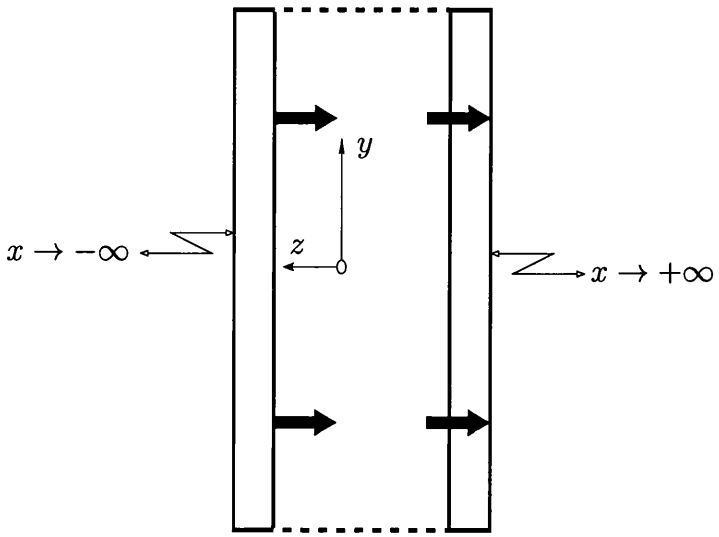

Figure 2.4: Sketch of the far-upstream and far-downstream regions from a point of view aligned with the centre of the duct at $x = 0$. The large arrows indicate the movement of the duct in a fixed frame of reference and the velocity component $\tilde{w}$ moves the fluid along uniformly with the walls.

2.2 Longer scale flow

Our concern hereinafter is with the flow when the total angle turned through is of order unity. In this section we summarise the approach and selected results of [77], with a view to setting the scene for the novel developments to come. In addition, we will present original numerical solutions of the governing equations which verify the results of [77] and describe the methodology to be employed herein. Only sufficient detail to provide a readable presentation of the relevant results and techniques will be given here, and the reader is referred to [77] for further elaboration.

For the flow in the bend the governing equations are:

$$\frac{w}{r} + w_r + \frac{u_\theta}{r} + v_y = 0 \ , \tag{2.24a}$$

$$wu_r + \frac{u}{r}u_\theta + vu_y + \frac{uw}{r} = -\frac{p_\theta}{r} \ , \tag{2.24b}$$

$$wv_r + \frac{u}{r}v_\theta + vv_y = -p_y \ , \tag{2.24c}$$

$$ww_r + \frac{u}{r}w_\theta + vw_y - \frac{u^2}{r} = -p_r \ . \tag{2.24d}$$

In a long, straight duct the two centrifuging terms $\frac{uw}{r}$ on the left hand side of (2.24b) and $-\frac{u^2}{r}$ on the left hand side of (2.24d) disappear, and then a solution to equations (2.24a–d) is

$$(u, v, w) = (1, 0, 0) \ , \ p = p_0 \tag{2.25}$$

for some constant p_0. However, the practical flow which motivated our study features a valve opening upstream, a precursor bend, and the sudden bending of the straight section into the bend being investigated (see the discussion of the motivating industrial problem in Chapter 1). These factors are taken to impose perturbations onto a uniform flow, although under strict conditions to be discussed some simple analytical solutions exist.

A balance of magnitudes of the terms in the continuity equation suggests that v and w are of $\mathcal{O}(a^{-1})$ at most, which implies a radial inertial force (which is proportional to $v\frac{\partial w}{\partial y}$ and $w\frac{\partial w}{\partial r}$) proportional to a^{-2}. This is to be contrasted with the centrifugal force $\propto -\frac{u^2}{r}$ in equation (2.24d) which represents the main effect of the bend as it is proportional to a^{-1}. Thus we expand as follows:

$$\begin{aligned} u &= 1 + \epsilon\tilde{U} + \dots \ ; \\ v &= \epsilon\tilde{V} + \dots \ ; \\ w &= \epsilon\tilde{W} + \dots \ , \end{aligned} \tag{2.26}$$

where as above ϵ is small, while $\tilde{U}, \tilde{V}, \tilde{W}$ are typically of order unity and depend on $\tilde{\theta}, y, z$. We find that it is natural to take a pressure variation in the bend of

$$\epsilon\tilde{p}_1(\tilde{\theta}) + \Lambda\left(\frac{z}{a} - \frac{z^2}{2a^2}\right) + \epsilon^2\tilde{p}_2(\tilde{\theta}, y, z) + \dots \ . \tag{2.27}$$

In this expansion, we have introduced the curvature parameter Λ which is identically 0 in the straight sections of the duct and is identically 1 when in the bend . This idea of a curvature or centrifuging parameter was used in [77], where the letter employed was Γ. We will also use the parameter

$$\alpha \equiv \epsilon a \tag{2.28}$$

which is taken to be of order unity. This form of the pressure variation arises by first considering a standard expansion

$$p = [p_0 + \epsilon p_1 + \epsilon^2 p_2 + \dots](\tilde{\theta}, y, z) \ . \tag{2.29}$$

Due to the form of the other variations, it can easily be shown from the governing equations that p_0 is a constant (which does not appear in the equations) and p_1 is a function only of $\tilde{\theta}$. We note here the appearance of a pressure perturbation of $\mathcal{O}(\epsilon)$ which connects with the work of §2.1. After the non-dimensionalising and change of coordinates, the equations are examined to the lowest order of ϵ. Finally, we normalise the resulting equations as follows:

$$\tilde{\theta} = \theta_1\theta \ , \tag{2.30a}$$

$$[\tilde{U} + \frac{\Lambda z}{\alpha}, \tilde{V}, \tilde{W}] = \frac{1}{\alpha\theta_1^2}[U, \theta_1 V, \theta_1 W] \ , \tag{2.30b}$$

$$\tilde{p}_1 = \frac{1}{\alpha\theta_1^2}p_1 \ , \tag{2.30c}$$

$$\tilde{p}_2 = \frac{1}{\alpha^2\theta_1^2}p_2 - \frac{\Lambda z^2}{\alpha^2} \ . \tag{2.30d}$$

The governing equations are then

$$V_y + W_z = 0 \,, \tag{2.31a}$$

$$U_\theta + VU_y + WU_z = -p_1'(\theta) \,, \tag{2.31b}$$

$$V_\theta + VV_y + WV_z = -p_{2y} \,, \tag{2.31c}$$

$$W_\theta + VW_y + WW_z - 2\Lambda U = -p_{2z} \,. \tag{2.31d}$$

The velocity components U, V, and W, and the pressure components p_1 and p_2 are to be found.

These equations are the governing equations of the inviscid, incompressible model, studied in [77], and are parabolic in θ subject to given starting conditions at $\theta = 0$.

2.3 Numerical methods

We decided that a computational solution of the inviscid, incompressible equations (2.31a–d) should first be attempted in order to verify the results presented in [77]. Since the detailed quantitative form of the solutions depends very strongly on the initial conditions, a re-creation of some numerical results with the same initial conditions and others with a novel set-up was attempted. The assumption was that a close correspondence between both sets of numerical results — derived independently, and with perhaps subtle differences in style — would both imply the veracity of the results and provide a strong basis of belief in the numerical approach for the new work in Chapter 5, which starts with the technique to be described here and then renders it fourth-order accurate via compact differencing. It should be noted that only a summary of the techniques and results is given in this section. A more detailed description of the numerical techniques will be provided in Chapter 5.

The variable θ acts as a time-like variable in that the governing equations exhibit a parabolic dependency on it, suggesting a forward-marching approach, solving the equations in successive planes θ = constant. As an initial attempt, the first order θ-derivatives are made first-order accurate with a backward-difference. The first- and second-order derivatives in the plane are made second-order accurate by using central-differencing in the planes θ = constant. The solution of the difference equations thus obtained requires either a fully implicit solution of the resultant block-tridiagonal system, or an implicit line-by-line approach combined with iteration for convergence. The inversion of a block-tridiagonal matrix is somewhat involved, and the implicit/iterative method is widely used with success, as discussed in [65, p.87]. With the superscript n denoting the θ-step, we assume that all variables are known at the n-level, and proceed to solve at the $(n+1)$-level. The subscript j denotes the gridline perpendicular to the y-axis, and k that for the z-axis, so that $j = 1$ corresponds to $y = 0$ and $k = 1$ to $z = 0$. In this way, for example, the backward differencing in θ for the derivative $\frac{\partial U}{\partial \theta}$ at the point (j,k) is

$$\frac{U_{j,k}^{(n+1)} - U_{j,k}^{(n)}}{\Delta\theta}\,, \tag{2.32}$$

and $\frac{\partial U}{\partial y}$ would be replaced by the central-space difference

$$\frac{U_{j+1,k}^{(n+1)} - U_{j-1,k}^{(n+1)}}{2\Delta y}\,, \tag{2.33}$$

for example, and so on in the usual fashion; see for example [65].

The approach now is to assume total knowledge of the variables ahead of and behind the line j, but total ignorance of them on that line. We solve for the variables on the line j and sweep in the direction of increasing j. At any given iteration level we use values from the previous iterative level for the variables on line $j+1$. On the first iteration, the converged value from the

previous θ-plane is used ahead of the line. Thus all first-order y-derivatives of a variable X on the line j can be replaced in terms of the known values from line $j-1$ and the assumed values from the line $j+1$. We are left then with a tridiagonal system in k on the line j, resulting from the discretisation of the z-derivatives, with a known right hand side. This and other resulting tridiagonal systems are solved by a standard inversion algorithm, closely resembling that in [21, pp. 77 ff].

Once jj, corresponding to the wall $y = y_1$, is reached, the newly-derived values at each point in the plane of the cross-section are compared with the results from the previous iteration. If the maximum absolute difference is within a prescribed level of accuracy, then the results are said to have converged and we advance to the next θ-level. If convergence has not been obtained, by which we mean there persists a large absolute difference in values of at least one of the variables at at least one point between successive iterations , then we continue to iterate at the present plane.

The coupled system of equations we wish to solve can be written

$$U_\theta + VU_y + WU_z = -p_1'(\theta) \ , \tag{2.34a}$$

$$R_\theta + VR_y + WR_z = 2\Lambda U_y \ , \tag{2.34b}$$

$$R = \nabla_{2D}^2 \psi \ , \tag{2.34c}$$

$$V = -\psi_z \ , \ W = \psi_y \ . \tag{2.34d}$$

In these equations, R denotes the scaled streamwise vorticity $(W_y - V_z)$, and equation (2.34b) is derived by cross-differentiating equations (2.31c) and (2.31d). Also ∇_{2D}^2 represents the two-dimensional (2D) Laplacian operator $\partial^2/\partial y^2 + \partial^2/\partial z^2$, and equation (2.34c) arises from the definition of the vorticity. The variable ψ represents the scaled stream-function defined by (2.34d), introduced in light of the mass conservation for the cross-plane flow implied

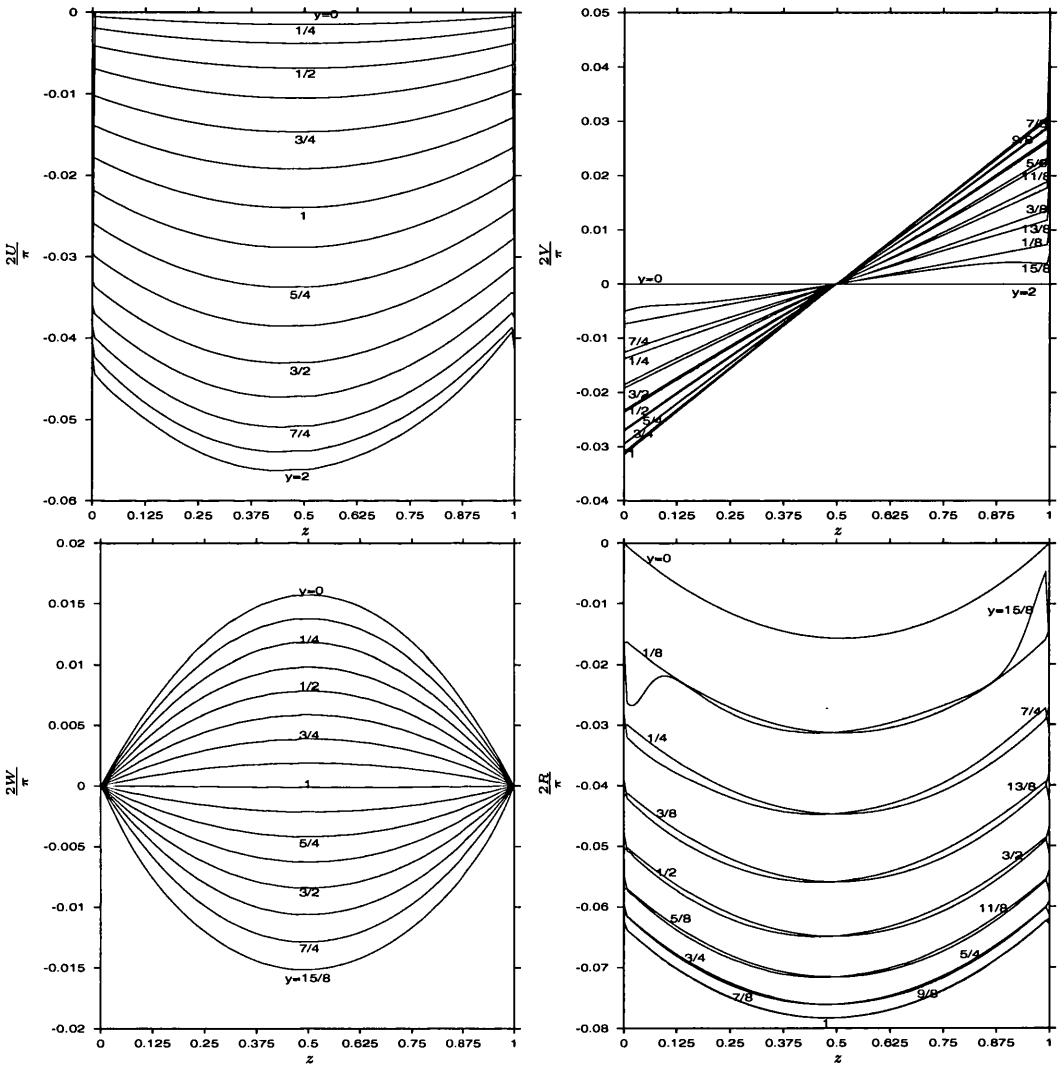

Figure 2.5: Plots of $2U/\pi$, $2V/\pi$, $2W/\pi$, $2R/\pi$ profiles at $\theta = 1$ for a 161×161 grid, and a step size of 0.00002. The starting condition is given by (2.39). Plots are on lines of constant y at intervals of $1/8$, from $y = 0$, but note that for W and R the results for $y = 2$ are not shown here, as in this second-order accurate scheme, they diverged significantly from the solution.

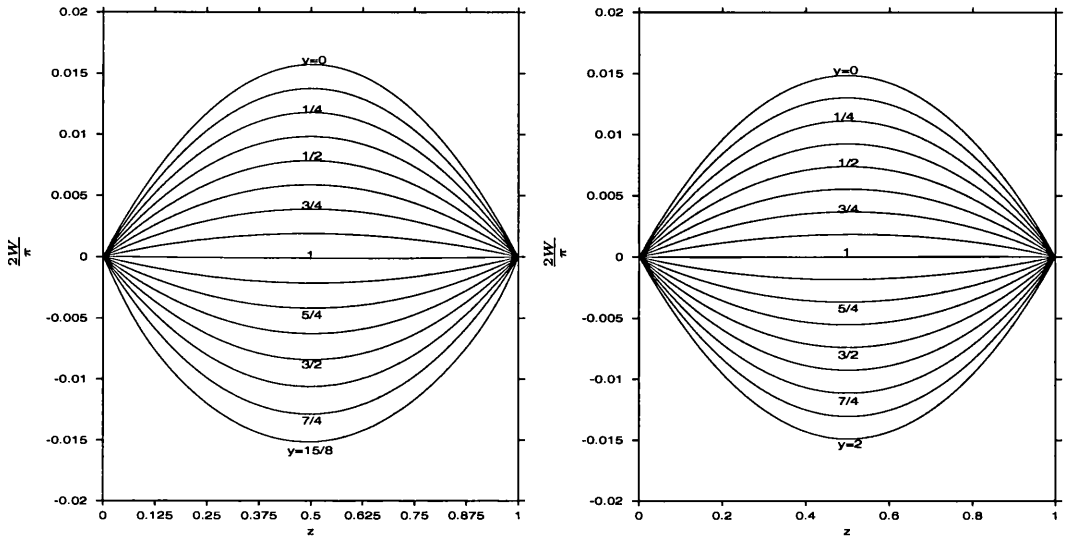

Figure 2.6: Plot of $2W/\pi$ profile at $\theta = 1$ from Figure 2.5. Also shown on the right hand side for comparison is the corresponding profile from [77], with kind permission of the authors.

by equation (2.31a). The boundary conditions at each θ-station are

$$\psi = 0 \text{ at the duct boundary} , \tag{2.35a}$$

$$\iint U dy dz = \text{constant (for all } \theta). \tag{2.35b}$$

The second of these conditions is the result of integrating the continuity balance at higher order.

In fact, equation (2.34a) can be further simplified. For a uniform duct cross-section, a double integration of equation (2.34a) and an application of Green's theroem yields

$$p_1 \equiv 0 , \tag{2.36}$$

since the boundary conditions (2.35a,b) hold. Thus (2.34a) becomes

$$U_\theta + VU_y + WU_z = 0 . \tag{2.37}$$

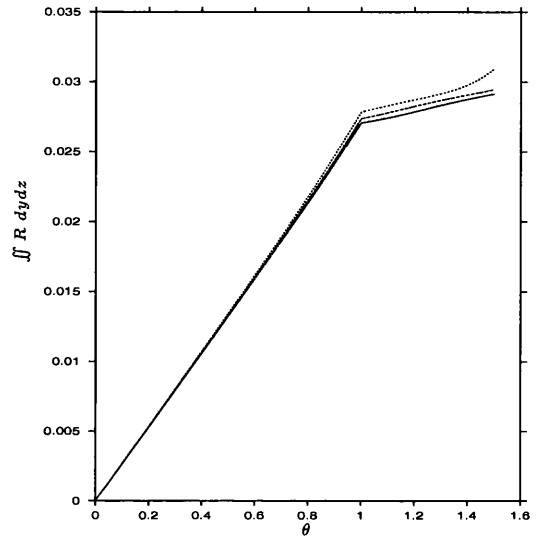

Figure 2.7: Comparison of the double integral of R over three grids. Bottom to top: $(\Delta\theta, \Delta y, \Delta z) = (\frac{1}{10000}, \frac{1}{50}, \frac{1}{100})$; $(\Delta\theta, \Delta y, \Delta z) = (\frac{1}{20000}, \frac{1}{60}, \frac{1}{120})$; $(\Delta\theta, \Delta y, \Delta z) = (\frac{1}{50000}, \frac{1}{80}, \frac{1}{160})$.

The coupled equations are solved as described above in the following order. Assuming that values of V and W are guessed at the level $n+1$, we proceed to solve (2.37) to obtain $U^{(n+1)}$. It is then possible to solve (2.34b) for $R^{(n+1)}$, and subsequently we solve (2.34c) for $\psi^{(n+1)}$. It is then straightforward to solve the explicit, algebraic equations (2.34d) to update the values of $V^{(n+1)}$ and $W^{(n+1)}$. The solution of the Poisson equation could be made more accurate and its convergence more rapid if successive over relaxation as described in [21, pp158–161] and [65, pp107ff] were used, but as a first attempt we solve it as a semi-implicit tridiagonal system as outlined above. The derivatives at the boundaries are treated by forward- or backward-differencing, initially with only two points near the boundary. Since there is no perpendicular flow at the walls, the equations to be solved there are different. They become simple, algebraic expressions which provide the top and bottom rows in the tridiagonal

matrices.

In general, the coordinate y runs from $y = 0$ (the "bottom" of the duct) to $y = y_1$ (the "top"), and z runs from $z = 0$ (the wall at the inside of the bend) to $z = z_1$ (the wall at the outside of the bend). For the numerics, we consider a 2×1 duct, taller than it is wide, and take the entrance values

$$[U, V, W] = [U_I, V_I, W_I](y, z) \text{ at } \theta = 0 \ , \tag{2.38}$$

to be

$$[U_I, V_I, W_I] = 2c[y^3/3 - y^2 + z^2 y - zy, 0, 0] \ , \tag{2.39}$$

where $c = 10^{-2}\pi^2/4$. Thus the flow enters the bend with no swirl. Other initial swirl conditions, and more general smooth cross-sections were considered in [77], although the zero initial swirl case above captured the essence of the flow structure. As the authors discussed, the specifics of the downstream flow are highly dependent on the intial conditions (a common feature, of course, of nonlinear systems), although the bulk development follows predictable paths of development. These predictions were obtained both from numerical experiments as detailed above and asymptotic analyses, for which the reader is referred to [77] as only the correspondence between the present numerical results and those in [77] will be examined here. We shall also consider a novel set of initial conditions to be described shortly.

Figure 2.5 presents the profiles of the four principal flow variables at the end of the bend. These second-order accurate profiles compare very favourably with the fourth-order accurate results presented in [77] in terms of their shape, sign, and magnitude. In Figure 2.6 we reproduce with kind permission of the authors the graph of $2W/\pi$ obtained in [77] which shows that the result computed here is very close to the result of [77].

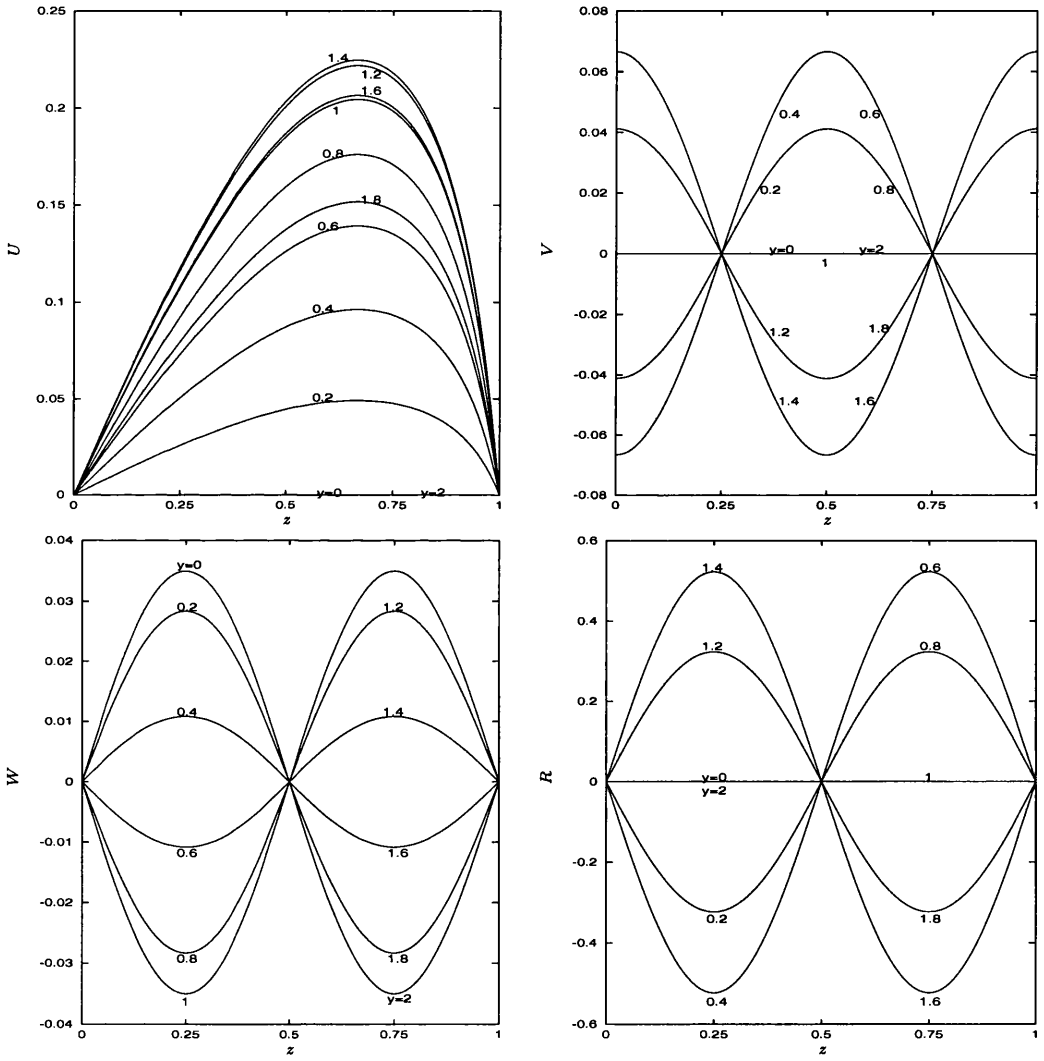

Figure 2.8: Plots of U_I, V_I, W_I, and R_I profiles for a 101×101 grid, from equations (2.40a–c).

In the caption of Figure 2.5 we mentioned that the results for W and R on the wall $y = 2$ were not shown because they diverged significantly from the corresponding results of [77]. Such numerical edge effects were absent in the results of the compact-differencing schemes of [77] and are also absent in the compact-differencing schemes presented in Chapter 5. As discussed above, further work to eliminate these effects was not undertaken here — the close comparisons possible between the current results and those of [77] were taken as a strong basis upon which to build the fourth-order accurate compact-differencing scheme for the compressible inviscid case, the method and results of which will be presented in Chapter 5.

It is important to demonstrate that the numerical results are virtually independent of the grid upon which they are computed. There are many techniques available to do this, and indeed this is almost an industry in itself, see for example [66], with some extremely sophisticated strategies now available (*e.g.* [86]). But the most common is grid refinement, whereby the grid is made successively finer, within the bounds of computational ability. A related method, naturally, is to coarsen the grid, the assumption being that once an upper bound is placed on the coarseness of the grid, the results of the finest grid will be presented. There are several ways to *quantify* the numerical uncertainty, but here we will satisfy ourselves that if the results visibly converge after grid refinement then the code is verified. The details of the quantification methods can be found in [66].

Thus Figure 2.7 presents the numerical evaluation of the double integral of R over three grids, with clear convergence of the data. Note that the computations were run beyond the bend ($\theta = 1$) and a flattening of the curve is apparent here in the absence of the bend effects. The observed linear growth

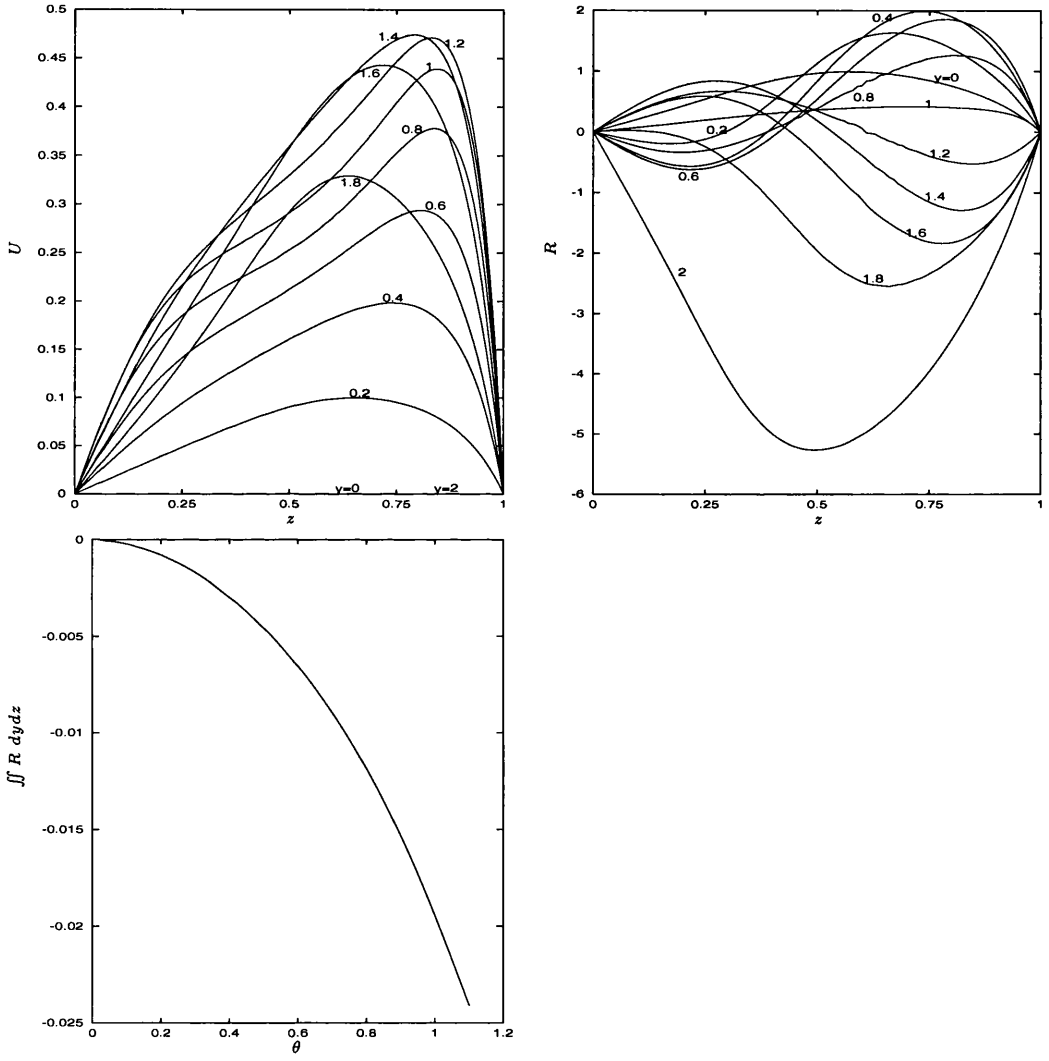

Figure 2.9: Plots of U and R profiles at $\theta = 1$, and the double integral of R, for a 101×101 grid, and a step size of 0.00001. The starting conditions are (2.40a–c).

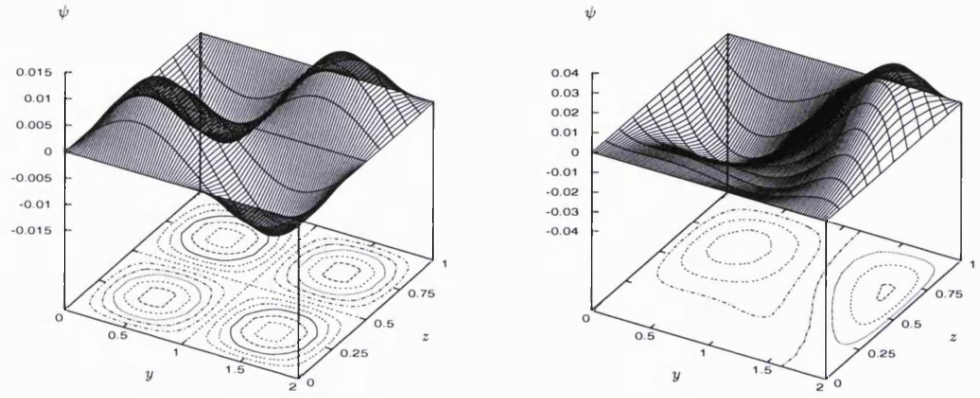

Figure 2.10: Surface plots of the stream-function ψ at $\theta = 0$ (left hand side) and $\theta = 1$ (right hand side). Solutions for the initial conditions (2.40a–c).

followed by a flattening is in line with one of the analytical results of [77] which predicted linear growth in the bend of the double integral of R when the inertial forces were small. This prediction is discussed in some detail in [77] and will also be considered in the compressible inviscid work of Chapters 4 and 5. The bending at $\theta = 1$ is numerically smooth and is physically smoothed by the mechanism described in §2.1.

A second set of solutions for the 2×1 duct was obtained for the following previously un-examined initial conditions. These conditions involve non-zero relatively large initial swirl:

$$U_I = a\frac{sin\left(\frac{\pi y}{2}\right) sin(\pi z)}{cos(2a\pi y)cos(4a\pi z)} \; ; \tag{2.40a}$$

$$V_I = -\frac{2a}{\pi} sin(\pi y)cos(2\pi z) \; ; \tag{2.40b}$$

$$W_I = \frac{a}{\pi} cos(\pi y)sin(2\pi z) \; ; \tag{2.40c}$$

here $a = 0.11$. These initial conditions are shown graphically in Figure 2.8.

We plot the profiles obtained numerically at $\theta = 1$ of U and R in Figure 2.9, along with the double integral of R. We note that the large negative value of R apparent on the line $y = 2$ is possibly a numerical effect as we have mentioned before, but we do not here have a higher-order scheme to establish this. The double integral of R does not appear to have grown linearly with θ which could serve to emphasise that the prediction of linear growth mentioned above on p.53 is only for small inertial forces and/or large distances downstream.

Figure 2.9 shows, in comparison with Figure 2.5, that the solutions are highly dependent on the initial conditions, as discussed above on p.43, although the bulk properties are maintained. For example, we note that the double integral of U is known to remain constant by (2.35b), and (2.37) implies that U is conserved following a particle, and so the change in the profile of U apparent between Figures 2.8 and 2.9 is due to the swirling motion of the fluid alone. Although this was also so in the case (2.39), the swirl-effect on U was less visible since the swirl was weaker. We also observe that the surface plots of Figure 2.10 show clearly how the "cellular" structure of the cross-flow at the onset of the bend (left-hand graph) becomes severely distorted at the end of the bend (right-hand graph). Indeed, the four-cell structure seen at $\theta = 0$ is mixed around through the length of the bend and is replaced by a two-cell structure at $\theta = 1$.

Finally here we reproduce a simple analytical solution from [77] which holds for both an arbitrary cross-section and arbitrary input conditions, when $\theta_1 \sim 1$. We assume that the inertial effects are small, which corresponds either to a low input swirl, and/or a small turning angle θ_1, and/or a small α. At the start of the bend, U is of order unity and since V, W are small in comparison with U, (2.37) implies that U remains close to its input value. Thus when V_I, W_I are

zero, (2.34b) implies

$$R \approx 2\Lambda\theta \frac{\partial U_I}{\partial y} \ . \tag{2.41}$$

For example, for any U_I and a rectangular 2×1 duct cross-section, we can derive:

$$[R, \psi, V, W] \sim 2\Lambda\theta[2(d_1 + d_2), d_1 d_2, (1 - 2z)d_1, 2(y - 1)d_2] \ , \tag{2.42}$$

where $d_1 \equiv y^2 - 2y, d_2 \equiv z^2 - z$, as reported in [77]. In [77] these predictions were shown to agree well with their more accurate numerical results. We observe that (2.42) suggests that particles on any one of the walls will remain there throughout the flow, gradually being advected into a corner, and that (of course) no particles are advected onto the walls to "replace" these particles.

Chapter 3

The Compressible Inviscid case

When compressibility is introduced the Euler equations are no longer closed, and we must obtain at least one more equation to close the system. To do this, we need to consider the thermodynamic aspects of the flow. In order to make any headway, further assumptions are made of the fluid, beyond the "dryness" or inviscidness already mentioned. As we shall see, these include a notion of "continuity" somewhat akin to that involving the *Knudsen number* in the problem of the applicability of the Navier-Stokes equations (see *e.g.* [78, p.7]), and great simplification of the atomic or molecular composition of the fluid enabling more concise descriptions to be obtained. Only as much detail as is immediately required can be entered into here, and the reader is referred to such texts as [22], [35], and [53]. Dimensional quantities are considered but without the subscript $_D$ for clarity.

The equations of direct interest to the present thesis are given in §3.3.

3.1 Thermodynamics

In the following discussion, a (thermodynamic) *system* is a quantity of matter separated from its *surroundings* by an *enclosure* which need not consist of a solid boundary, but need only be a closed surface. Heat and mass may be transferred through an enclosure. A system in which all macroscopically-measured quantities are independent of time is said to be in *equilibrium.* Equivalently, if we define a *current* as the flux of a quantity such as heat, then a system is in equilibrium if and only if there are no currents of any kind.

The foundations of all work in thermodynamics are the principal laws of thermodynamics, summarised in words as follows.

O^{th} Law : There exists a *variable of state*, the temperature θ.

1^{st} Law : Energy can be neither created nor destroyed; heat and mechanical work are equivalent.

2^{nd} Law : It is impossible in any closed system for heat to be conveyed from one body to another at higher temperature.

3^{rd} Law : It is impossible — by any procedure whatsoever — to reduce a system to *absolute zero* (0^{o}K/ $-$ 273.16^{o}C) in a finite number of operations.

Variables that depend only on the state of the system — and not the path taken between states — are referred to as *variables of state*, and include the pressure p and the volume V. By this definition, variables of state are perfect differentials. If the value of a variable of state depends on the mass of the system, then we refer to it as *extensive*, and denote it by an upper case letter. Otherwise it is *intensive* — in which case the quantity it refers to is called

a *specific* quantity — and is represented by a lower case letter. Variables of state are uniquely defined for any equilibrium state of the system, and indeed the difference in values of a variable of state between two equilibrium states is independent of the process by which the first state was transformed into the second. The 0^{th} Law introduces another variable of state unique to thermodynamics, the *temperature* θ. As we shall see, the 1^{st} and 2^{nd} Laws introduce and define the variables of state internal energy, E, and entropy, S, respectively.

The 1^{st} Law defines a variable of state E, the *internal energy.* The change in internal energy of a system is equal and opposite to the work done on and the heat added to a system. That is, if a system is transformed from a state of equilibrium A to that of B, by a process involving an amount of work W and in which a quantity of heat Q leaves the surroundings, then

$$E_B - E_A = Q + W \ . \tag{3.1}$$

By considering for example the work done on a cylinder of air by a moving piston (see [53, pp.5–6]) we can obtain the following equation:

$$de = dq - pdv \ . \tag{3.2}$$

Note that in this form, the mass-dependent, or extensive variables have been replaced by their intensive counterparts. By the definition of e, de is a perfect differential, whereas q and w depend on the process employed. To avoid confusion, some texts then write $de = \delta q - p\delta v$. The internal energy measures the energy of the fluid due to the molecular activity — it is proportional to the vibrational, rotational and translational (over the order of the mean free path) energies of the molecules. In this sense, it is also not surprising that de is path-independent.

Most natural processes do not pass through successive states of equilibria and are termed *non-static.* However, an infinitesimally slow process does pass through equilibria and is termed *quasi-static.* In the plane of any two state variables, a quasistatic process $A \rightarrow B$ is represented by a curve from point A to point B and conversely. The locus of the curve passes through all the intermediate states assumed in the process.

It is always possible for a process $A \rightarrow B$ to be reversed by a process $B \rightarrow A$, but this usually results in some global change to the system and its environment. Only if this change were absent would the process (and its inverse) be called *reversible.* Thus a process is reversible if W and Q are added in such a way that no currents are produced — the system remains in equilibrium throught the process of change of state (*i.e.* a process for which $\Delta E = Q + W$). As one would expect, most natural or "spontaneous" processes are *irreversible.* Paraphrasing [22, p.6] we say that whilst quasi-static processes may be either reversible or irreversible, a non-static process is always irreversible. A benefit of assuming a process to be reversible is that the equations derived for equilibrium conditions can be employed in an analysis at each stage in the process. If no heat is exchanged between system and surroundings at any point in a process then it is described as *adiabatic.*

Our aim in this Chapter is to provide additional equations to close the Navier-Stokes equations when compressibility and viscosity are taken into account. To do this, we need a way to equate other variables of state, such as temperature (a nebulous concept here, but effectively defined by the 2^{nd} Law and related to the internal motions of a fluid particle), pressure and density to our new variable of state, the internal energy. This is done in two stages.

Firstly, we note from experiment that at low densities (or rather, at densi-

ties typically found outside of shock regimes), gases approximate the behaviour of *thermally perfect* gases, which are defined as those satisfying

$$pv = R(\theta + \theta_0) \ , \tag{3.3}$$

where R is a characteristic constant of each gas known as the *species gas constant* ($R = 287$ J/(kg deg K) for air), and θ_0 is a characteristic temperature which is the same for all gases. To be more precise, (3.3) defines a family of perfect gases for each value of R, and any real gas will closely approximate its corresponding perfect gas at low enough densities[1]. Since θ_0 is the same for all gases (273.16°C) we define a new temperature T — measured in degrees Kelvin — by $T = \theta + \theta_0$. So then

$$p = \rho RT \ . \tag{3.4}$$

The second stage is to postulate a simple, linear relationship between the internal energy and the temperature. This seems like not too great a leap of faith, given the interpretation of the internal energy being a measure of the small-scale motion of the molecules, and the temperature being related similarly to molecular activity. In fact, if we define the *specific heat* to be the rate of heat addition q with respect to the temperature T, measured either at constant volume or constant pressure, then from (3.2) we obtain

$$c_v = \left(\frac{dq}{dT}\right)_v \ , \tag{3.5a}$$

$$c_p = \left(\frac{dq}{dT}\right)_p \ . \tag{3.5b}$$

[1] At very high densities — such as in strong shocks in a hypersonic regime — additional problems may also occur which will invalidate the assumptions of unconstrained equilibrium. See for example [49, p.8-3].

In these expressions, c_v is the specific heat measured at constant volume, and c_p is the specific heat measured at constant pressure. Then from (3.2) we obtain

$$c_v = \frac{\partial e}{\partial T} , \tag{3.6a}$$

$$c_p = \frac{\partial e}{\partial T} + \left(\frac{\partial e}{\partial v} + p\right)\left(\frac{\partial v}{\partial T}\right)_p . \tag{3.6b}$$

It is clear that v is a natural variable of state for e. Does there then exist another variable of state, related to e, for which p becomes the natural choice of independent variable? Indeed there does, and it is called the *enthalpy*, $h = h(p, T)$ given by

$$h = e + pv . \tag{3.7}$$

The quantity pv is known as the *displacement energy* or the *flow work*. Imagine a surface — the *control surface* — surrounding a particle of the fluid. When the control surface is deformed by the pressure on it, work is transferred to the unit mass contained within, and this change of energy is quantified by the flow work. See [35, p.7]. From this we can write the first law as

$$dh = dq + vdp , \tag{3.8}$$

whence

$$c_v = \frac{\partial h}{\partial T} + \left(\frac{\partial h}{\partial p} - v\right)\left(\frac{\partial p}{\partial T}\right)_v , \tag{3.9a}$$

$$c_p = \frac{\partial h}{\partial T} . \tag{3.9b}$$

For a perfect gas, it is possible in addition to obtain (see *e.g.* [53, p.12]):

$$\begin{aligned} c_p - c_v &= R , \\ e(T) &= \int c_v dT + \text{const.} , \\ h(T) &= \int c_p dT + \text{const.} \end{aligned} \tag{3.10}$$

The remaining assumption to make of our fluid is that it is *perfect*, which entails the gas being thermally perfect, continuous, homogeneous, and *calorically perfect*. This last is that c_v (and c_p) is constant, and hence by the above:

$$e = c_v T \ , \tag{3.11}$$

as required. The constant of integration has been taken such that $e(T = 0) = 0$, which conforms to a notion of absolute zero being the temperature at which all molecular activity ceases. When analysing flow where *dissociation* (the splitting of compounds into smaller products with much longer mean free paths) and other chemical processes do not occur, and for low-temperature, non-hypersonic flows, the assumption of a perfect gas is usually valid.

An interesting and important question remains. Given two equilibrium states of a system, is it possible — using *a priori* measurements of both states — to determine which will change into the other? A formal answer to this question is provided by the 2nd Law, which furnishes us with a new variable of state called the *entropy*, S. The definition proceeds as follows. It is possible to show that for a reversible change of state of an adiabatically closed system:

$$p = -\frac{\partial E}{\partial V} \ . \tag{3.12}$$

We now try to write E as a function of two variables — V as before and a new one, S — such that

$$\begin{aligned} -p &= \left(\frac{\partial E}{\partial V}\right)_S \ , \\ T &= \left(\frac{\partial E}{\partial S}\right)_V \ . \end{aligned} \tag{3.13}$$

By applying the chain rule to dE we find in comparison with the extensive version of (3.2) that

$$TdS = dQ \ . \tag{3.14}$$

Integrating bewteen two equilibrium states gives us

$$S_B - S_A = \int_A^B \frac{dQ}{T} \tag{3.15}$$

for a reversible process. Following [53, pp.17–20] we now re-define the 2nd Law as follows:

- There exists an extensive variable of state S, the entropy, and an intensive variable T, the absolute temperature. The entropy difference between two states A and B is given by

$$S_B - S_A = \int_A^B \frac{dQ}{T} \ , \tag{3.16}$$

  where the integral refers to any reversible process leading from A to B, and T is identical to the temperature defined by the perfect gas law, (3.4).

- For a *closed* system (*i.e.* one that exchanges neither heat nor work with the surroundings), S increases in any spontaneous process. The system reaches equilibrium when S is at a maximum.

Note that if we allow an arbitrary process, then (3.16) becomes

$$S_B - S_A \geqslant \int_A^B \frac{dQ}{T} \ . \tag{3.17}$$

In fact, if we transform a system from state A to state B by means of some process $A \rightarrow B$, then

$$S_B - S_A = \Delta S_o + \Delta S_i \ , \tag{3.18}$$

where ΔS_i is the entropy produced in the system by means of the process, and ΔS_o is that carried into the system through the walls (evaluated by some integral of dQ/T over the surface area of the walls of the system and throughout

the time of the process). For all processes, $\Delta S_i \geqslant 0$, but in a reversible process $\Delta S_i = 0$ in which case (3.18) reduces to (3.16). See [22, p.9]. Entropy measures the "quality" of the energy in the system or, equivalently, the system's disorder. As S increases, the distribution of the energy throughout the fluid increases and so the "useful" energy decreases (see [35, p.7]).

3.2 Equations of flow

We start with an inviscid, non-conducting fluid, and we attempt to derive an *Energy Equation*: an equation for the thermodynamic energy of the fluid in the same way that the Navier-Stokes equations describe the momentum.

To analyse the flow by following fluid particles we make two assumptions. The first of these is the grossly simplifying assumption that the moving gas particles are at all times in thermodynamic equilibrium, and so the thermodynamic properties of each are functionally related. In addition, we think of the fluid as a thermodynamic system, with the particles as self-contained thermodynamic entities, separated from the rest of the fluid (the surroundings) by perfectly heat-conducting walls. Thus wherever the word "system" has been used above, the arguments and results derived are now taken to apply to the fluid particles embedded in their surroundings. The surface of the arbitrary control volume defining a fluid particle must move with the local fluid velocity, and its size must be small enough so that the thermodynamic properties are invariant inside, but large enough to contain many millions of molecules so that those properties still have meaning. A molecule has no "temperature" because the definition relies on the mean motion of many millions of such molecules.

In summary, we require that a gas particle has no inhomogeneities; is large compared to the mean free path (in some kind of limiting sense); and that

local state variables do not change significantly over the order of the mean free path. In addition, D/Dt is taken over a time increment larger than that separating the collision between two molecules. These assumptions are violated for example in the upper atmosphere and in strong shock regimes, [22, p.43]. The assumptions are analagous to the result that the Navier-Stokes equations are valid only if the length scale L of the flow is much larger than the mean free path $\bar{l}$ of the molecules, that is the *Knudsen number* $Kn = \frac{\bar{l}}{L}$ is small. In practical terms, it is claimed in [48, p.6] that the continuum hypothesis holds for $Kn < 0.2$, with kinetic theory and the Maxwell-Boltzmann equations used for higher values of Kn. See also [78, p.7].

We expect the energy law to resemble

$$\text{heat added} + \text{work done on the fluid} = \text{increase in energy},$$

but for a fluid in motion it is more edifying to consider the rate of change of energy and expect an equation of the form

$$\begin{aligned}\text{rate of heat addition} + \text{rate of work on the fluid} \\ = \text{rate of increase of energy in the fluid.}\end{aligned}$$

The variable for the intensive heat addition is q, representing *only* heat absorbed by the volume of fluid by radiation or convection from the surroundings, but not latent heat caused by a transformation of the fluid. This latter is a *surface* term and will be included only when viscosity is considered. The *rate of work* on a fluid is caused by the pressure and any volume forces, and in future considerations, frictional forces. The *total energy* of all of the fluid is $\rho e + \frac{1}{2}\rho u^2$ per unit volume, and the energy equation is

$$\frac{D}{Dt}\left(\rho e + \frac{1}{2}\rho u^2\right) = \rho q + \rho f_i u_i - \frac{\partial}{\partial x_i}(p u_i) \ . \tag{3.19}$$

Subtracting $(e + \frac{1}{2}u^2)$ times the continuity equation from (3.19) we obtain

$$\rho\frac{De}{Dt} + \rho\frac{D}{Dt}\left(\frac{1}{2}u^2\right) = \rho q + \rho f_i u_i - \frac{\partial}{\partial x_i}(pu_i) \ . \tag{3.20}$$

Multiplying the Euler equations by u_i and subtracting the result and (3.20) from (3.19), and simplifying with the continuity equation, gives

$$\frac{De}{Dt} + p\frac{D}{Dt}\left(\frac{1}{\rho}\right) = q \ . \tag{3.21}$$

Equation (3.19) shows that kinetic energy is interchangeable with work done by the pressure and body forces. Equation (3.21) is the 1st Law of Thermodynamics for a system (here, a particle) in equilibrium. It implies that a particle moves only through successive states of equilibrium.

From (3.2) and (3.16) in differentials we have

$$de = Tds - pdv \ , \tag{3.22}$$

which together with (3.21) yields

$$\frac{Ds}{Dt} = \frac{q}{T} \ . \tag{3.23}$$

With no heat addition, changes in state of a fluid particle are *isentropic*:

$$\frac{Ds}{Dt} = 0 \ , \tag{3.24}$$

which is the case for adiabatic processes of the particle. These occur when the whole system is adiabatic, and the fluid is inviscid and not heat-conducting. These are sufficient but not necessary conditions for isentropy, as can be seen from the following discussion. When is a particle's process adiabatic? We want no heat addition or subtraction from the fluid particle — we require its processes to be adiabatic. This is achieved by firstly asserting that the whole system must be adiabatic, as any bulk heat addition will affect our particle.

This is not enough, however, as viscosity might still generate radiative heat, and so we insist that our fluid is inviscid. Finally, two neighbouring particles at different temperatures will, by dint of the 0^{th} Law, exchange heat through their diabatic "walls", and so we now need further that our fluid is non-conducting. When all these conditions are satisfied, then $q = 0$.

It is important to note that (3.24) does not imply that entropy is constant everywhere, but just for a particle, *i.e.* along particle paths. However, if the flow is steady then the streamlines coincide with the particle paths and s is constant along streamlines. The constant will in general vary from streamline to streamline. If it does not, and s is constant everywhere, then the flow is said to be *homentropic*, or *isentropic everywhere.* General conditions for homentropic flow are given by *Crocco's Theorem* — see [83, §1.3]. As above, these equations can be re-cast in terms of the enthalpy, such as in the well-known theorem of Bernoulli (see *e.g.* [83, §1.3]).

By substitution into (3.2) from equations (3.6a) and (3.4), and by equation (3.16) in differentials we obtain

$$ds = \frac{dq}{T} = c_v \frac{dT}{T} + R\frac{dv}{v} \ . \tag{3.25}$$

By defining the *adiabatic coefficient* (also known as the *isentropic exponent*) $\gamma := \frac{c_p}{c_v}$ we can rewrite R as $(\gamma - 1)c_v$, and hence

$$\frac{p}{\rho^\gamma} = K \exp\left(\frac{s}{c_v}\right) \ . \tag{3.26}$$

The isentropic condition is then

$$\begin{aligned} p &\propto \rho^\gamma \\ \text{or} \quad \frac{p}{\rho^\gamma} &= \frac{p_{\text{res}}}{\rho_{\text{res}}^\gamma} \ , \end{aligned} \tag{3.27}$$

where the constant of proportionality is usually non-invariant and in steady

flow depends on which reservoir (hence the subscript $_{\text{res}}$) the streamline originates from, so we can say

$$\frac{p}{\rho^\gamma} = f(\psi) \ , \tag{3.28}$$

where ψ is the streamfunction (if it exists).

The important relation

$$p = K\rho^\gamma \tag{3.29}$$

will be referred to as the *polytropic equation of state.* For homentropic flow, $f(\psi)$ is constant and so $p = k\rho^\gamma$ with k invariant. This is equivalent to there being just one reservoir from which all streamlines originate: that is, the flow is a "uniform stream at infinity".

The energy equation has many equivalent forms: it can be stated in terms of either the intensive internal energy e, the intensive enthalpy h or a combination of the two, and in integral or differential form. We shall here perform brief analyses on the full energy equation including the *dissipative terms* — those involving the dissipation of heat and consequent production of entropy, as these shall be required for §§4.3.1 and 4.3.2. The form to be used here is that found in [63, p.62]:

$$\rho\frac{De}{Dt} = -p\frac{\partial u_j}{\partial x_j} + \frac{\partial}{\partial x_j}\left(k\frac{\partial T}{\partial x_j}\right) + \Phi \ , \tag{3.30a}$$

$$\text{where } \Phi = \lambda\frac{\partial u_j}{\partial x_j}\frac{\partial u_k}{\partial x_k} + \mu\left(\frac{\partial u_i}{\partial x_j} + \frac{\partial u_j}{\partial x_i}\right)\frac{\partial u_j}{\partial x_i} \text{ is the } \textit{dissipation function.} \tag{3.30b}$$

Note that here the dissipation function has been given in terms of Cartesian velocity components u_i, $i = (1,2,3)$. More generally, the rate-of-strain dyadic $\underline{\underline{E}}$ satisfies $\underline{\underline{E}} = \epsilon_{ij}\hat{\boldsymbol{i}}_i\hat{\boldsymbol{i}}_j = e_{ij}\hat{\boldsymbol{a}}_i\hat{\boldsymbol{a}}_j$ where ϵ_{ij} is the Cartesian rate-of-strain tensor, $\hat{\boldsymbol{i}}_i$ $(i = 1,2,3)$ are the Cartesian unit vectors, and $\hat{\boldsymbol{a}}_i$ $(i = 1,2,3)$ are the unit vectors of an orthogonal curvilinear system, and $e_{ij} = \frac{1}{2}\hat{\boldsymbol{a}}_i \cdot \left[\boldsymbol{\nabla\mu} + (\boldsymbol{\nabla\mu})^{\mathrm{T}}\right] \cdot \hat{\boldsymbol{a}}_j$

(see *e.g.* [63, pp61ff]). Also note that no bulk heat addition (a volume term) has been included in (3.30a) since we have assumed the walls of the duct to be adiabatic, and hence there are no heat sources or sinks. Formally, this assumption fixes one wall boundary condition as the adiabatic condition $\frac{\partial T}{\partial y} = 0$ on the wall, where y is the coordinate normal to the wall. The term $\frac{\partial}{\partial x_j}\left(k\frac{\partial T}{\partial x_j}\right)$ is the surface heat term and comes from Fourier's law of heat conduction: k — the coefficient of *thermal diffusivity* — is zero in inviscid flow, and the dissipation function is also absent. Equation (3.30a) is true regardless of the presence of body forces as the momentum equations have been used in its derivation.

From the equation of state of a perfect gas (3.4):

$$c_p DT = c_v DT + D\left(\frac{p}{\rho}\right) . \tag{3.31}$$

Thereafter we apply the compressible continuity equation and so obtain

$$\rho\frac{De}{Dt} + p\boldsymbol{\nabla}\boldsymbol{.}\boldsymbol{u} \equiv \rho\left(\frac{De}{Dt} - \frac{p}{\rho^2}\frac{D\rho}{Dt}\right) . \tag{3.32}$$

Combining this identity with the perfect gas assumption (so that $e = c_v T$), and with (3.31), we find in our steady case that

$$\rho c_p(\boldsymbol{u}\boldsymbol{.}\boldsymbol{\nabla})T = (\boldsymbol{u}\boldsymbol{.}\boldsymbol{\nabla})p + \boldsymbol{\nabla}\boldsymbol{.}(k\boldsymbol{\nabla}T) + \Phi . \tag{3.33}$$

We discover in [63, p.61] that an equivalent form of Φ is

$$\Phi = 2\mu[\epsilon_{ij}]^2 + \lambda\left(\frac{\partial u_i}{\partial x_i}\right)^2 , \tag{3.34}$$

where ϵ_{ij} is the Cartesian rate-of-strain tensor, and we have the usual Stokes relation $\lambda + \frac{2}{3}\mu = 0$. However as above, the rate-of-strain dyadic $\underline{\underline{E}}$ satisfies $\underline{\underline{E}} = \epsilon_{ij}\hat{\boldsymbol{i}}_i\hat{\boldsymbol{i}}_j = e_{ij}\hat{\boldsymbol{a}}_i\hat{\boldsymbol{a}}_j$, where $\hat{\boldsymbol{a}}_i$, $(i = 1, 2, 3)$, are the unit vectors of an orthogonal curvilinear coordinate system, and e_{ij} depend only on finding the dyadic $\boldsymbol{\nabla u}$.

Consequently, we need only calculate the dyadic $\nabla \boldsymbol{u}$ in a curvilinear system, as is done in [63, p.66]. So in dyadic form, (3.33) becomes

$$\rho c_p(\boldsymbol{u} \cdot \nabla)T = (\boldsymbol{u} \cdot \nabla)p + \nabla \cdot (k\nabla T) + \Phi \ , \tag{3.35a}$$

$$\text{where } \Phi = 2\mu \left(\underline{\underline{E}} : \underline{\underline{E}} - \frac{1}{3}(\nabla \cdot \boldsymbol{u})^2 \right) \ , \tag{3.35b}$$

and $\underline{\underline{D}} : \underline{\underline{E}}$ denotes the *double dot product* of two dyadics ([63, p.33]).

We now apply the full non-dimensionalising factors, remembering that with our perfect gas assumption the specific heats are invariant, and we non-dimensionalise k and T on representative upstream values k_∞ and T_∞, and ρ on a representative value ρ_∞. We thus obtain the non-dimensional steady, viscous, compressible energy equation:

$$\rho(\boldsymbol{u} \cdot \nabla)T = Ec \left[(\boldsymbol{u} \cdot \nabla)p + \frac{1}{Se} \nabla \cdot (k\nabla T) + \frac{1}{Re}\Phi \right] \ , \tag{3.36}$$

where we have three dimensionless groups:

$$Ec = \frac{U_\infty^2}{c_p T_\infty} \quad , \quad Pr = \frac{\mu_\infty c_p}{k_\infty} \quad , \quad Re = \frac{\rho_\infty U_\infty h_D}{\mu_\infty} \ , \tag{3.37}$$

and we have formed the composite group $Se = Ec \cdot Pr \cdot Re$ for convenience. The groups in (3.37) are known as the *Eckert, Prandtl,* and *Reynolds* numbers, respectively.

The following results hold for incompressible fluids:

$$k = \text{constant} \quad ; \quad \mu = \text{constant} \quad ; \quad \rho = \text{constant} \tag{3.38}$$

such that Pr = constant. See *e.g.* [15, p.77]. The following broadbrush discussion should shed some light on these relationships. Consider two adjacent laminae of the fluid moving relative to one another. The shear stress at their mutual boundary is proportional to the velocity gradient normal to the boundary, and the constant of proportionality is the viscosity, μ. From a

kinetic theory point of view, the viscosity is a consequence of an exchange of molecules with kinetic energy surpluses or defecits between the laminae (*c.f.* Chapter 6). Thus the inviscid assumption is consistent with assuming no heat conduction in the fluid because conduction is also a product of molecular exchange. Since different fluids have different molecular compositions, it is clear that μ will depend on each fluid, but the density is also important in determining μ since this affects the number of molecules which can be exchanged per unit of time. Thus if density is invariant then μ must be also due to the above (in fact, in [22, p.232] this is quantified as $\mu \propto \rho \bar{v} l_F$ where $\bar{v}$ is the mean thermal speed and l_F is the mean free path). In a compressible fluid, raising the temperature increases the thermal velocity and increases the likelihood of exchange. In an incompressible fluid on the other hand, temperature merely increases the vibrational energy of the more-strongly bound molecules, meaning that μ is less dependent on T.

It should be noted that there is some discussion as to where one should take a representative upstream value of the temperature. In [67, p.210] we see a non-dimensional factor based on the difference between the wall and the free-stream temperature, and a scaling based solely on the wall temperature is not uncommon. However, in a system not dissimilar to ours, [37, pp.241–3] scales solely on the core temperature, as we have done. Certainly this is not a trivial decision, as we shall see later in Chapter 4 when we briefly discuss the Chapman-Rubesin constant, and the reader is referred to the discussions in [10].

Under the assumption of isentropy — which holds if the fluid is inviscid — so that $p = k\rho^\gamma$, then scaling on the core value, we find from the equation of

state that

$$\frac{\gamma p_\infty}{\rho_\infty} = c_p(\gamma - 1)T_\infty \ . \tag{3.39}$$

But then since also $a_\infty^2 = \frac{\gamma p_\infty}{\rho_\infty}$, we have

$$Ec = (\gamma - 1)M_\infty^2 \ , \tag{3.40}$$

if the fluid is compressible, where M_∞ is the upstream *Mach number.* Note that for incompressible flow, $a_D = \infty$ and so this form of the Eckert number is not valid. Since $\gamma - 1 = 0.4$ for air, and since our flow is not hypersonic (but sufficiently fast that M_∞ is of $\mathcal{O}(1)$), our Eckert number is of order unity. The Prandtl number is also of order unity for air from *e.g.* [67]. Consequently, S is of $\mathcal{O}(\epsilon^{-1})$.

By elementary kinetic theory, k must be a linear function of μ and so when c_p is constant (as in our calorically perfect gas assumption), the Prandtl number $\frac{c_p\mu}{k}$ must be invariant throughout the flow, and in [22, p.231] we find $Pr = \frac{4\gamma}{(9\gamma-5)}$, where γ as before is the adiabatic constant c_p/c_v.

With this formulation, we have:

$$k = c_p\mu\frac{(9\gamma - 5)}{4\gamma} \text{ (dimensional)}, \tag{3.41a}$$

$$\text{and so } k = \mu \text{ (dimensionless)}. \tag{3.41b}$$

Inserting (3.41b) into the energy equation, we finally write

$$\rho(\boldsymbol{u} \cdot \boldsymbol{\nabla})T = Ec\left[(\boldsymbol{u} \cdot \boldsymbol{\nabla})p + \frac{1}{Se}\boldsymbol{\nabla} \cdot (\mu\boldsymbol{\nabla}T) + \frac{1}{Re}\Phi\right] \ . \tag{3.42}$$

This form agrees with that found in [10, p.25] and elsewhere.

3.3 Summary of equations

The equations which we will use in Chapters 4 and 5 are summarised as follows. The steady energy equation is:

$$\rho(\boldsymbol{u}\,.\,\boldsymbol{\nabla})T = Ec\left[(\boldsymbol{u}\,.\,\boldsymbol{\nabla})p + \frac{1}{Se}\boldsymbol{\nabla}\,.\,(\mu\boldsymbol{\nabla}T) + \frac{1}{Re}\Phi\right] , \tag{3.43}$$

with the dimensionless groups Ec, Pr, Re, and Se defined on page 70, and the dissipation function Φ defined in equation (3.30b). In the compressible and inviscid case,

$$Ec = (\gamma - 1)M_\infty^2 , \tag{3.44}$$

where M_∞ is the upstream Mach number. The dimensionless equation of state of a perfect gas is

$$p = \frac{\gamma - 1}{\gamma Ec}\rho T , \tag{3.45}$$

and in the case of inviscid flows we can use the polytropic equation of state

$$p = K\rho^\gamma , \tag{3.46}$$

where K in general varies from stream line to stream line.

Chapter 4

The Compressible Inviscid case, continued

4.1 Introduction

In this chapter we formulate the Compressible Inviscid (CI) problem. This case is an extension to include compressibility of the work in [77] which was summarised in Chapter 2. Since the density ρ is no longer constant we have an additional unknown in the Euler equations and so need an extra equation to close the system. This equation is the inviscid form of the energy equation formulated in the preceding chapter. The analysis studies the downstream evolution of the perturbed flow variables. We will briefly discuss the inclusion of viscosity, though we will not draw any conclusions on the flow structure in such cases. However, the perturbation expansions in the viscous cases are essentially the same as those of a fully non-linear inviscid approach, subject to an assumption of attached flow, and so they will be useful in §§5.3 and 5.4. Finally, we will present asymptotic analyses of the governing equations,

studying the far-downstream effects of the bend as well as the influence of corners in the cross-sectional profile. These analytical results are found to show close correspondence with the numerical work to be presented in Chapter 5. Note that the full sets of governing equations for each case which we study in this chapter are summarised in Appendix A. In this chapter, dimensional quantities are once again indicated by the subscript $_D$.

4.2 Formulation of CI

The dimensionless incompressible continuity equation (2.1a) is now replaced by the compressible form $\boldsymbol{\nabla} \cdot (\rho \boldsymbol{u}) = 0$, which we consider together with the dimensionless Euler equations $\rho(\boldsymbol{u} \cdot \boldsymbol{\nabla})\boldsymbol{u} = -\boldsymbol{\nabla} p$. We also use the inviscid energy equation which we obtain by dropping Fourier's term and the dissipation term from (3.43), and replacing the dimensionless T by $(\gamma M_\infty^2 p)/\rho$ from (3.45) and (3.44) . This leads to the following form of the energy equation:

$$\rho(\boldsymbol{u} \cdot \boldsymbol{\nabla})p - \gamma p(\boldsymbol{u} \cdot \boldsymbol{\nabla})\rho = 0 \ . \tag{4.1}$$

As an aside, we note that this form is also attainable from the Bernoulli equation in terms of the total enthalpy $H = h + \frac{1}{2}u_i u_i$, which transforms to:

$$\frac{1}{2}u_i u_i + c_p T = \text{constant for a particle,} \tag{4.2}$$

since the total enthalpy is constant following a particle in inviscid, steady, adiabatic, non-conducting flow [49, p.8-7], and $h = c_p T$ if the fluid is calorically perfect. An ideal fluid has $e = c_v T$ and so $\frac{1}{2}u_i u_i + \gamma e$ remains constant following a particle. Finally, using the Euler equations and the standard relation $e = \frac{p}{(\gamma-1)\rho}$, we can confirm equation (4.1).

The discussion of the swirl-shear considerations immediately prior to equation (2.26) is still valid here since the duct geometry is the same and so we will

assume the same expansions of the velocities as Chapter 2. We assume that the pressure expansion is

$$p = p_0(\tilde{\theta}, y, z) + \epsilon p_1(\tilde{\theta}, y, z) + \epsilon^2 p_2(\tilde{\theta}, y, z) + \dots \ . \tag{4.3}$$

A leading order balance of the governing equations yields

$$p_{0\tilde{\theta}} \equiv p_{0y} \equiv p_{0z} \equiv 0 \ , \tag{4.4}$$

so that p_0 is a constant. Next, a balance of magnitudes implies that the leading-order size of the density is of $\mathcal{O}(1)$, and so we consider the density to be perturbed as follows:

$$\rho = \bar{\rho}(\tilde{\theta}, y, z) + \epsilon \tilde{\rho}(\tilde{\theta}, y, z) + \dots \ . \tag{4.5}$$

The relevant form of the energy equation (4.1) then yields

$$\frac{\bar{\rho}_{\tilde{\theta}}}{\alpha} + \tilde{V}\bar{\rho}_y + \tilde{W}\bar{\rho}_z = 0 \tag{4.6}$$

in the bend, suggesting that reservoir values of $\bar{\rho}$ are conserved for each particle. Consistent with our assumption of a uniform uni-directional upstream flow we take $\bar{\rho}$ to be uniform at $\tilde{\theta} = 0$, such that $\bar{\rho}$ is a constant for all $\tilde{\theta}$.

Examining the equations at the next highest order suggests that $p_{1y} \equiv 0 \equiv p_{1z}$, and furthermore that an $\mathcal{O}(\epsilon)$ centrifuging term needs to be absorbed into the pressure gradient in order to be able to balance the dynamics, analogously to the incompressible case. Thus the pressure expansion (cf. (2.27)) is:

$$p_0 + \epsilon \tilde{p}_1(\tilde{\theta}) + \Lambda \left(\frac{\bar{\rho} z}{a} - \frac{\bar{\rho} z^2}{2a^2} \right) + \epsilon^2 \tilde{p}_2(\tilde{\theta}, y, z) + \dots \ . \tag{4.7}$$

Note once again the appearance of the centrifuging parameter Λ, since the term of which it is a factor is absent when wall curvature is absent.

Since $\bar{\rho}$ is invariant we may set it to be unity since it is now the uniform "representative upstream value" $\rho_{D\infty}$ with which we non-dimensionalise the equations. That is, we now write

$$\rho = 1 + \epsilon\tilde{\rho} + \dots \ . \tag{4.8}$$

Note that although p_0 is similarly invariant, we cannot set it equal to unity without loss of generality, since we do not non-dimensionalise the pressure on a representative pressure "$p_{D\infty}$", but on twice the dynamic pressure-head $\rho_{D\infty}U_{D\infty}^2$. Unlike the incompressible case the constant p_0 will appear explicitly; in the energy equation.

After changing coordinates to the cylindrical polar coordinates introduced in §2.2, and examining the above governing equations to leading order in ϵ, we normalise the resulting equations. The normalisations of $\tilde{\theta}$ and of the velocity components remain the same as (2.30a) and (2.30b), but the pressure components are normalised differently, and we also introduce a normalisation of $\tilde{\rho}$:

$$\tilde{p}_1 = \frac{p_1}{\alpha\theta_1^2} \ , \tag{4.9a}$$

$$\tilde{p}_2 = \frac{p_2}{\alpha^2\theta_1^2} - \frac{\Lambda z^2}{\alpha^2} \ , \tag{4.9b}$$

$$\tilde{\rho} = \frac{\hat{\rho}}{\alpha^2\theta_1^2} \ . \tag{4.9c}$$

The governing equations are then:

$$V_y + W_z = 0 \ ; \tag{4.10a}$$

$$U_\theta + VU_y + WU_z = -p_1'(\theta) \ ; \tag{4.10b}$$

$$V_\theta + VV_y + WV_z = -p_{2y} \ ; \tag{4.10c}$$

$$W_\theta + VW_y + WW_z = -p_{2z} + \Lambda(2U + \hat{\rho}) \ ; \tag{4.10d}$$

$$\frac{\gamma p_0}{\alpha}\left(\hat{\rho}_\theta + V\hat{\rho}_y + W\hat{\rho}_z\right) = p_1'(\theta) + \Lambda W\theta_1^2 \ . \tag{4.10e}$$

The appearance of the normalising factors in the final equation is noted and apparently unavoidable here; it signals a strong dependence of the flow structure on these parameters, as described later in this chapter and in Chapter 5. The relative strength of $\alpha\theta_1^2$ to γp_0 will be taken as of order unity throughout, in keeping with realistic values for the physical duct in question and for air, although in §4.4.5 we will consider other balances.

We observe here that if there is no swirl at the entrance to the bend then in the absence of viscosity no vorticity is generated and the flow remains irrotational throughout. If in addition the static enthalpy is also uniform then the flow is homentropic by Crocco's theorem and so we then derive from the polytropic equation of state (3.46) the results

$$\bar{\rho} = (\gamma M_\infty^2)^{\frac{1}{\gamma}} , \tag{4.11a}$$

$$p_1 = \frac{\bar{\rho}^{\gamma-1}\hat{\rho}}{\alpha M_\infty^2} - \Lambda z\theta_1^2 , \tag{4.11b}$$

$$p_2 = \frac{1}{2}\left[\frac{(\gamma-1)\bar{\rho}^{\gamma-1}\hat{\rho}^2}{\alpha^2\theta_1^2 M_\infty^2} + z^2\theta_1^2(2\Lambda+1)\right] . \tag{4.11c}$$

However, in a discussion on the validity of these results, we first note the parabolic nature of the coupled set of equations. In this sense no information is passed upstream at this level, and so for example an initially homentropic flow would remain so throughout the bend. It should be noted that although there is only one physical reservoir — the expansion chamber behind the bursting diaphragm — this is not where we take the reservoir values. The bursting of a diaphragm creating a "... ragged initial wave" ([89, p.137]), the traversing of a precursor bend, and the possible passing of an (entropy-generating) shock all suggest the presence of inhomogeneities in the variables at the start of the bend where reservoir values are taken. Thus the quoted homentropic results (4.11a–c) are not physically realistic here, since at the very least Crocco's Theorem

would then require the flow to be uniform and irrotational everywhere at the start of the bend.

4.3 Viscous fluids

In this section we derive the governing equations which would hold should viscous effects become important in the core rather than being confined to thin wall layers. With the inclusion of viscosity, leading order variation in the velocity component u is required in order to satisfy the no-slip condition at the walls, and the polytropic equation of state (3.46) no longer holds since $e^{\frac{s}{c_v}}$ is not constant. Furthermore, the leading-order variation in u means that a new balance of swirl and curvature must be considered, as we will see below.

4.3.1 Incompressible Viscous flow (IV)

In this case we must use the steady Navier-Stokes equations

$$\rho_D(\boldsymbol{u}_D \cdot \boldsymbol{\nabla}_D)\boldsymbol{u}_D = -\boldsymbol{\nabla}_D p_D + \mu_D \nabla_D^2 \boldsymbol{u}_D \ , \tag{4.12}$$

and the incompressible continuity equation (2.1a). As in §2.2, the balance of swirl and curvature is dictated by the centrifuging term $\frac{u_D^2}{r_D}$. Since there is now leading order variation in u this centrifuging term is no longer a constant to leading order and so cannot be absorbed into the pressure expansion. It is necessary, therefore, to consider a new level of incident swirl. The radius of curvature is to be considered fixed throughout by the physical specifications of the motivating problem and is denoted by a, and we now take

$$\alpha \equiv a\epsilon^2 \tag{4.13}$$

to be of order unity. In §2.2 we mentioned that a in practice is typically 8, and thus that $\epsilon \sim \frac{1}{8}$ there. With the new balance (4.13) we now have $\epsilon \sim \frac{1}{2\sqrt{2}}$ being larger. Furthermore, we now consider a slightly shorter section of the bend (though still larger than the original entry flow problem considered in §2.1), such that the total angle turned through is smaller than before. Thus if θ is the angle appearing in the nondimensional equations, then $\theta = \epsilon\tilde{\theta}$, where now $\tilde{\theta}$ is order unity. (An alternative would be to consider the same level of swirl, but a larger radius of curvature.)

We non-dimensionalise exactly as before, and in addition the coefficient of viscosity μ_D — which remains constant here due to incompressibility (see the discussion in §3.2) — scales out of the equations. This introduces the Reynolds number

$$Re = \frac{\rho_D U_{D\infty} h_D}{\mu_D} , \tag{4.14}$$

and we will take ϵRe to be of order unity. Thus Re is typically large here.

As an aside, we note that the Görtler number based on the cross-sectional distance is defined in [36] as

$$G = 2\delta Re^2 , \tag{4.15}$$

where $\delta = h_D/a_D$ is a measure of curvature in the stream-wise direction. Here then $G \sim 1$, which is perhaps not surprising when one considers that the Görtler number is the ratio of the product of the inertial and centrifugal terms to the square of the viscous terms. Since Re was chosen to retain the leading order viscous terms — *i.e.* so that the leading order ratio of inertia to viscous terms was $\mathcal{O}(1)$ — an order unity Görtler number ensures that both centrifugal and viscous terms are retained in the governing equations.

We consider new perturbations of the flow quantities imposed by the ge-

ometry because our swirl-shear balance α has changed. The expansions are:

$$p = \tilde{p}_0(\tilde{\theta}) + \epsilon^2 \tilde{p}_2(\tilde{\theta}, y, z) + \dots \ ; \tag{4.16a}$$

$$\boldsymbol{u} = (\bar{U}, 0, 0)(\tilde{\theta}, y, z) + \epsilon(\tilde{U}, \tilde{V}, \tilde{W})(\tilde{\theta}, y, z) + \dots \ , \tag{4.16b}$$

with a leading-order variation in U to enable no-slip to be satisfied as discussed earlier. Since it is similar to the analysis showing that $p_0 \equiv 1$ in the CI case, we have omitted the work showing $p_1 \equiv 0$ in the above expansion.

Following the change of variables and substitution of the perturbed forms into the Navier-Stokes and continuity equations, we need to normalise the resulting equations. The direct introduction of a centrifugal variable Λ creates more problems than it solves, and so we normalise as follows:

$$\tilde{\theta} = \theta_1 \theta \ ; \tag{4.17a}$$

$$[\tilde{V}, \tilde{W}] = \frac{1}{\alpha\theta_1}[V, W] \ ; \tag{4.17b}$$

$$\tilde{p}_0 = p_0 \ ; \tag{4.17c}$$

$$\tilde{p}_2 = \frac{1}{\alpha^2\theta_1^2} p_2 \ ; \tag{4.17d}$$

$$\text{and } Re_{re} = \frac{\epsilon}{\alpha\theta_1} Re \ , \tag{4.17e}$$

where Re_{re} acts as a reduced Reynolds number. Note that once again the bend runs from $\theta = 0$ to $\theta = 1$.

The governing equations are thus reduced to

$$\bar{U}_\theta + V_y + W_z = 0 \ , \tag{4.18a}$$

$$\bar{U}\bar{U}_\theta + V\bar{U}_y + W\bar{U}_z = -p_0'(\theta) + \frac{1}{Re_{re}} \nabla_{2D}^2 \bar{U} \ , \tag{4.18b}$$

$$\bar{U}V_\theta + VV_y + WV_z = -p_{2y} + \frac{1}{Re_{re}} \nabla_{2D}^2 V \ , \tag{4.18c}$$

$$\bar{U}W_\theta + VW_y + WW_z - \bar{U}^2\alpha\theta_1^2 = -p_{2z} + \frac{1}{Re_{re}} \nabla_{2D}^2 W \ , \tag{4.18d}$$

where $\nabla_{2D}^2 = (\partial_y^2 + \partial_z^2)$. The appearance of the parameters α and θ_1 in (4.18d), similarly to the CI case, is again noted and apparently unavoidable. This problem did not arise in the II case because the analogue of the curvature term $-\bar{U}^2\alpha\theta_1^2$ was constant and absorbed into the pressure expansion.

It is important to note that the more strongly non-linear inviscid incompressible equations (to be referred to as the NLII case) can easily be derived from the above by omitting the viscous terms, since we have set the order unity part of the velocity expansion to be variable. More formally, if $Re \gg a^{\frac{1}{2}}$ then the viscous effects will be confined to a thin wall region until large distances are attained on this length scale. The core flow for order unity values of θ would thus remain inviscid and be treated by the large Reynolds number limit of the above fully non-linear equations. This will be considered in §5.4.

4.3.2 Compressible Viscous flow (CV)

We now come to the fullest case of this thesis. The steady, compressible viscous continuity and Navier-Stokes equations are ([63, pp.62-9]):

$$\boldsymbol{\nabla}_D \cdot (\rho_D \boldsymbol{u}_D) = 0 \,, \tag{4.19a}$$

$$\rho_D(\boldsymbol{u}_D \cdot \boldsymbol{\nabla}_D)\boldsymbol{u}_D = -\boldsymbol{\nabla}_D p_D + \boldsymbol{\nabla}_D(\lambda_D \boldsymbol{\nabla}_D \cdot \boldsymbol{u}_D) + \mu_D(\nabla_D^2 \boldsymbol{u}_D + \boldsymbol{\nabla}_D(\boldsymbol{\nabla}_D \cdot \boldsymbol{u}_D)) + 2(\boldsymbol{\nabla}_D \mu_D \cdot \boldsymbol{\nabla}_D)\boldsymbol{u}_D + \boldsymbol{\nabla}_D \mu_D \wedge (\boldsymbol{\nabla}_D \wedge \boldsymbol{u}_D) \,. \tag{4.19b}$$

For the reasons given in [63, §2.10 & §2.13], we assume that Stokes's relation holds and so take $\lambda_D = -\frac{2}{3}\mu_D$. The Navier-Stokes equations become:

$$\rho_D(\boldsymbol{u}_D \cdot \boldsymbol{\nabla}_D)\boldsymbol{u}_D = -\boldsymbol{\nabla}_D p_D - \frac{2}{3}\boldsymbol{\nabla}_D(\mu_D \boldsymbol{\nabla}_D \cdot \boldsymbol{u}_D) + \mu_D(\nabla_D^2 \boldsymbol{u}_D + \boldsymbol{\nabla}_D(\boldsymbol{\nabla}_D \cdot \boldsymbol{u}_D)) + 2(\boldsymbol{\nabla}_D \mu_D \cdot \boldsymbol{\nabla}_D)\boldsymbol{u}_D + \boldsymbol{\nabla}_D \mu_D \wedge (\boldsymbol{\nabla}_D \wedge \boldsymbol{u}_D) \,.$$

We retain the geometry introduced in the incompressible, viscous case where $\epsilon = \mathcal{O}(a^{-\frac{1}{2}})$. The variations and the non-dimensionalising factors of each flow quantity are obvious combinations of the above cases, with additionally the expansion of μ taken as

$$\mu = \bar{\mu}(\tilde{\theta}, y, z) + \epsilon\tilde{\mu}(\tilde{\theta}, y, z) + \dots \,, \tag{4.20}$$

and we consider the same swirl-shear conditions as the IV case. However, $\bar{\rho}$ is no longer conserved along streamlines because the polytropic equation of state (3.46) no longer holds. The expansion and normalisations of the pressure are those for the IV case — *i.e.* (4.16a) and (4.17c,d). The governing equations are then

$$(\bar{\rho}\bar{U})_\theta + (\bar{\rho}V)_y + (\bar{\rho}W)_z = 0 \,, \tag{4.21a}$$

$$\bar{\rho}(\bar{U}\bar{U}_\theta + V\bar{U}_y + W\bar{U}_z) = -p_0'(\theta) + \frac{1}{Re_{re}}\left[(\bar{\mu}\bar{U}_y)_y + (\bar{\mu}\bar{U}_z)_z\right] \,, \tag{4.21b}$$

$$\begin{aligned}\bar{\rho}(\bar{U}V_\theta + VV_y + WV_z) = -p_{2y} + \frac{1}{Re_{re}}\Big[&(\bar{\mu}\bar{U}_y)_\theta + (\bar{\mu}V_z + \bar{\mu}W_y)_z \\ &+ \frac{2}{3}(2\bar{\mu}V_y - \bar{\mu}W_z - \bar{\mu}\bar{U}_\theta)_y\Big] \,,\end{aligned} \tag{4.21c}$$

$$\begin{aligned}\bar{\rho}(\bar{U}W_\theta + VW_y + WW_z - \bar{U}^2\alpha\theta_1^2) = -p_{2z} + \frac{1}{Re_{re}}\Big[&(\bar{\mu}\bar{U}_z)_\theta + (\bar{\mu}V_z + \bar{\mu}W_y)_y \\ &+ \frac{2}{3}(2\bar{\mu}W_z - \bar{\mu}V_y - \bar{\mu}\bar{U}_\theta)_z\Big] \,.\end{aligned} \tag{4.21d}$$

The unknowns in this system are $\bar{U}, V, W, p_2, \bar{\rho}$, and $\bar{\mu}$, and so at least a further two equations must now be derived in order for this set of equations to be well-posed and solvable. To leading order, in the prescribed cylindrical polar coordinates with the given expansions — including $T = \bar{T}(\tilde{\theta}, y, z) + \epsilon\tilde{T}(\tilde{\theta}, y, z) + \dots$ since $\mu \propto T$ — and normalisations we obtain from the energy

equation (3.43):

$$\begin{aligned}\bar{\rho}\left(\bar{U}\bar{T}_\theta + V\bar{T}_y + W\bar{T}_z\right) =& Ec\Big[\bar{U}p_0'(\theta) + \frac{1}{Se_{re}}\left((\bar{\mu}\bar{T}_y)_y + (\bar{\mu}\bar{T}_z)_z\right) \\ &+ \frac{\bar{\mu}}{Re_{re}}\left(\bar{U}_y^2 + \bar{U}_z^2\right)\Big] .\end{aligned} \tag{4.22}$$

where we have reduced the group Se defined after equation (3.37) analogously to Re_{re}. We note in passing that the effects of viscous dissipation are likely to be small, and that this would influence a detailed study of this case.

The new variable T is functionally related to μ by various formulae (see for example [48, pp.22–23]) and an appropriate choice here is Chapman's Law $\mu_D = C_D T_D$, where C_D is the Chapman-Rubesin constant. The earlier discussion on page 71 about the choice of dimensional factor T_D now takes on even greater import, since it becomes clear that C_D cannot be chosen to simultaneously agree with the wall and free-stream values of T. This issue — and alternative relations of μ_D to T_D — is discussed in some detail in [10, p.28–33]. However, if we let the dimensionless Chapman-Rubesin constant be denoted by c_H, then we obtain:

$$\bar{\mu} = c_H \bar{T} . \tag{4.23}$$

As discussed in [10], in particular for large wall temperatures, the value of c_H can be chosen to agree with Sutherland's Law, but it often proves useful to an analysis to take c_H to be unity. A benefit of such a simple relationship is that T is usually easier to measure empirically than μ.

The final equation to complete the system is the equation of state of a perfect gas, $p_D = \rho_D R T_D$. When nondimensionalised for compressible fluids this equation takes the form (3.45). Substituting the given perturbation expansions, we have:

$$p_0 = \frac{(\gamma - 1)}{\gamma Ec}\bar{\rho}\bar{T} . \tag{4.24}$$

The more strongly non-linear compressible inviscid equations (which will be referred to as the NLCI case) can readily be derived from the above equations by neglecting the viscous terms. The formal reasoning behind this is the same as that on page 82. This case will be considered numerically in §§5.3 and 5.4.

4.4 Analysis of the CI case

In this section we derive results which further simplify the governing equations and provide useful predictions of the flow development. Some of these predictions will provide tests of the numerical accuracy in the subsequent chapter. We also consider simple analytical solutions to the equations. In §4.4.2 we analyse far-downstream limits of the CI case, and in §4.4.3 we examine the influence of sharp corners in the cross-sectional profile on the flow structure.

The following work features some novel arguments based on the approach of parts of [77], which we here extend to the CI case. It is interesting to note that some of the qualitative results of the II case reported in [77] carry over to the compressible case, and comparisons will be drawn where appropriate.

4.4.1 General flow properties for $\theta \sim 1$

For clarity, we indicate in Figure 4.1 the length scales of relevance to the weakly non-linear cases.

Two pressure components appear in the governing equations of the CI case (4.10a–e), and we make the assumption that p_1 is obtainable from a bulk integral. The second pressure term p_2 is eliminated by cross-differentiating equations (4.10c) and (4.10d) which introduces the streamwise vorticity $R = W_y - V_z$ as defined previously in §2.3. Thus equations (4.10c) and (4.10d)

reduce to:

$$R_\theta + VR_y + WR_z = \Lambda(2U_y + \hat{\rho}_y) \ . \tag{4.25}$$

Furthermore, in light of the continuity equation (4.10a) which implies mass conservation in the cross-section, we introduce the (two-dimensional) stream-function ψ such that

$$\psi_y = W \quad , \quad \psi_z = -V \ . \tag{4.26}$$

The introduction of ψ means that we also have the Poisson equation

$$\nabla^2_{2D}\psi = R \ , \tag{4.27}$$

where $\nabla^2_{2D} = \partial^2_y + \partial^2_z$ as before. Since the walls are impermeable (in addition to being adiabatic) we have as a boundary condition no normal flow at the walls and so we take $\psi \equiv 0$ on the walls. In more detail, we define the total stream-function as

$$\Psi = \psi_0 + \epsilon\psi_1 + \epsilon^2\psi_2 + \dots \ , \tag{4.28}$$

where ψ_0 is a constant and ψ_1 normalises to ψ defined by equation (4.26). The impermeability of the walls requires $\Psi =$ constant there, and thus that for all $i \geqslant 1$ we have $\psi_i \equiv 0$ on the walls.

Let us now examine the pressure component $p_1(\theta)$. The analagous term in the II case was shown in §2.2 to be a constant for all θ and we now prove that this result also holds in the CI case.

The leading-order balance (4.10a) of the continuity equation involved the $\mathcal{O}(\epsilon)$ terms. Examining at the ϵ^2-level yields:

$$\left(\frac{\tilde{\rho}_{\tilde{\theta}}}{\alpha} + (\tilde{V}\tilde{\rho})_y + (\tilde{W}\tilde{\rho})_z\right) + \left(\tilde{\tilde{V}}_y + \tilde{\tilde{W}}_z\right) + \frac{1}{\alpha}\left(\tilde{U}_{\tilde{\theta}} + \tilde{W}\right) = 0 \ , \tag{4.29}$$

before normalising. In this equation, the variables $\tilde{\tilde{V}}$ and $\tilde{\tilde{W}}$ are the $\mathcal{O}(\epsilon^2)$ terms in the expansions of v and w, and the expansion of the stream-function

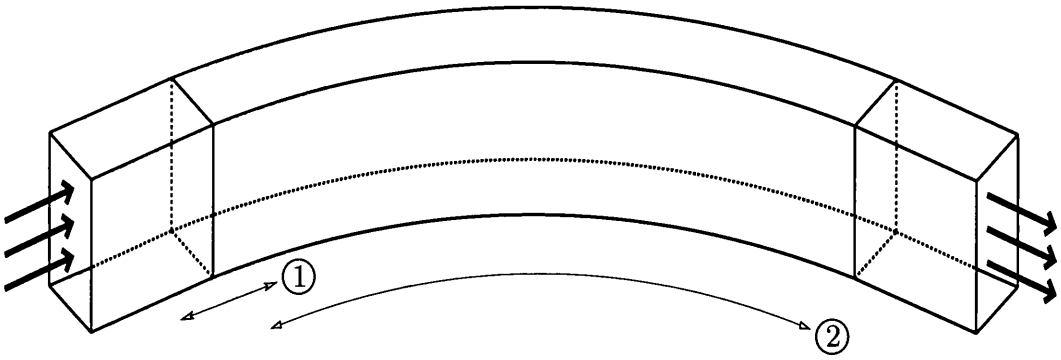

Figure 4.1: The different length scales. With a fixed, ① indicates the entry length scale ($x \sim 1$ or $\theta \sim a^{-1}$) while ② indicates the full bend length scale of the weakly non-linear inviscid work ($\theta \sim 1$). For a longer bend in which the viscous wall layers have a sufficient development distance to fill the duct, the strongly non-linear viscous cases of §4.3 might be seen far downstream on the full bend length scale.

(4.28) requires

$$\tilde{\tilde{V}}_y + \tilde{\tilde{W}}_z = -\psi_{2yz} + \psi_{2yz} = 0 \,. \tag{4.30}$$

With the result (4.30), a double integral of (4.29) across the plane of a cross-section yields:

$$\frac{1}{\alpha}\iint \tilde{\rho}_{\tilde{\theta}}\, dydz + \iint (\tilde{\rho}\tilde{V})_y + (\tilde{\rho}\tilde{W})_z\, dydz + \frac{1}{\alpha}\iint \tilde{U}_{\tilde{\theta}}\, dydz + \frac{1}{\alpha}\iint \tilde{W}\, dydz = 0 \,. \tag{4.31}$$

An application of Green's Theorem to the second integral above gives

$$\begin{aligned} \iint (\tilde{\rho}\tilde{V})_y + (\tilde{\rho}\tilde{W})_z\, dydz &= \oint_P (\tilde{\rho}\tilde{W})\, dy - (\tilde{\rho}\tilde{V})\, dz \\ &= 0 \,, \end{aligned} \tag{4.32}$$

where P is the perimeter of the duct cross-section, whilst the definition of the stream-function in the last integral in (4.31) yields

$$\iint \tilde{W}\, dydz = \iint \psi_{1y}\, dydz = \int [\psi_1]_{y=0}^{y=y_1}\, dz = 0 \,. \tag{4.33}$$

With the above results (4.31) becomes

$$\frac{d}{d\theta}\iint \hat{\rho}\; dydz + \alpha\frac{d}{d\theta}\iint U\; dydz = 0\;, \tag{4.34}$$

following normalising. A similar double integral and application of Green's Theorem to the leading order balances of the energy and θ-momentum equations (4.10e) and (4.10b) gives

$$\frac{d}{d\theta}\iint \hat{\rho}\; dydz = \frac{\alpha A}{\gamma p_0}\frac{dp_1}{d\theta} \quad \text{and} \quad \frac{d}{d\theta}\iint U\; dydz = -A\frac{dp_1}{d\theta}\;, \tag{4.35}$$

where A is the duct cross-sectional area. Combining these results with (4.34) shows that

$$\frac{dp_1}{d\theta}\left(\frac{1}{\gamma p_0} - 1\right) = 0 \quad \text{for all } \theta\;, \tag{4.36}$$

and since for full generality $p_0 \neq \frac{1}{\gamma}$, we conclude that

$$\frac{dp_1}{d\theta} = 0 \quad \text{for all } \theta\;. \tag{4.37}$$

Hence p_1 must be constant for all θ.

As a consequence of (4.37) the θ-momentum equation (4.10b) and the energy equation (4.10e) simplify to:

$$U_\theta + VU_y + WU_z = 0\;; \tag{4.38a}$$

$$\hat{\rho}_\theta + V\hat{\rho}_y + W\hat{\rho}_z = \Lambda\Upsilon W\;, \tag{4.38b}$$

where $\Upsilon = \frac{\alpha\theta_1^2}{\gamma p_0}$. As mentioned on page 78 above, we will take $\Upsilon \sim 1$ throughout, except in §4.4.4 where we consider other balances. We observe that since (4.38a) implies that U is conserved along streamlines, and that since we have just shown that the double integral of U is also conserved, then evolution of the profile of U will be due only to mixing by the swirl.

The Green's Theorem technique used above can be gainfully applied to the CI vorticity equation (4.25), with the result that

$$\frac{d}{d\theta}\iint R\; dydz = \Lambda\left(2\int (U_t - U_b)\; dz + \int (\hat{\rho}_t + \hat{\rho}_b)\; dz\right)\;, \tag{4.39}$$

where the subscripts $_t$ and $_b$ denote the values at the top and bottom of the duct, respectively. Equation (4.39) differs from the corresponding result (equation (4.5)) in [77] where $\iint R\, dydz$ was driven only by $2\Lambda \int (U_t - U_b)\, dz$. However, the prediction that $\iint R\, dydz$ is constant beyond the bend where $\Lambda = 0$ still holds. Extending the argument presented in [77] and described briefly on page 55, we note that when the inertial forces are small, due for example to low entrance swirl or small turning angle, then equations (4.38a) and (4.38b) respectively suggest that

$$U \approx U_I(y,z) \quad \text{and} \quad \hat{\rho} \approx \hat{\rho}_I(y,z)\ , \tag{4.40}$$

throughout the bend. Thus (4.39) predicts linear growth with θ of the double integral of R when inertial forces are small. In fact, equation (4.25) in this small-inertia case would explicitly imply linear growth, since it becomes

$$R \approx \Lambda\theta \left(2\frac{\partial U_I}{\partial y} + \frac{\partial \hat{\rho}_I}{\partial y} \right)\ . \tag{4.41}$$

This prediction of linear growth in the bend will be tested by the numerics in §5.2.

Finally in this section we note by the way that the following is an exact solution to the governing equations:

$$U \equiv U(z)\ ,\ \hat{\rho} \equiv \hat{\rho}(z)\ ,\ V \equiv W \equiv R \equiv \psi \equiv 0\ ,\ p_2 = \Lambda \int (2U + \hat{\rho})\, dz\ , \tag{4.42}$$

with $U(z)$ and $\hat{\rho}(z)$ arbitrary, and this also holds when $\Lambda = 0$ if we take $U(z) \equiv 1 \equiv \hat{\rho}(z)$ — that is, if uniform conditions hold in the upstream straight section. However, the preceding argument and the numerical results to be shown in §5.2 both seem to suggest that this form of solution in the bend is unlikely.

4.4.2 Predictions for large θ

In this section we analyse the full governing equations (4.10a, 4.38a, 4.25, 4.38b) in the limit $\theta \to \infty$ in order to study the downstream influence of the bend. We compare the predictions of the separate cases of Λ becoming zero at $\theta = 1$ and it remaining unity; that is, we compare the case when the bend ends at $\theta = 1$ to the case when it is maintained indefinitely. We will also compare the results with the analogues of [77] and in §5.2 we will show numerical support for the predictions.

Bend off

In this regime the bend ends at $\theta = 1$ and so the fluid then enters a straight section. We consider the effects of the bend on the flow structure far downstream in this straight section.

Consider a generic flow variable $F(\theta, y, z)$ and suppose that beyond the bend F satisfies

$$F_\theta + VF_y + WF_z = 0 \ , \tag{4.43}$$

which implies that F is conserved along particle paths (which here coincide with streamlines). Furthermore, a double integral of (4.43) combined with an application of Green's Theorem gives

$$\frac{d}{d\theta} \iint F \ dydz = 0 \ , \tag{4.44}$$

which suggests that beyond the bend the double integral remains constant for all θ. If F is of $\mathcal{O}(1)$ in the bend then as $\theta \to \infty$ we conclude that F must remain of order unity beyond the bend since it is conserved along streamlines and the double integral is constant. Therefore in the limit $\theta \to \infty$ the generic

variable F is independent of θ, that is:

$$F \to F_\infty(y,z) \quad \text{as} \quad \theta \to \infty \,, \tag{4.45}$$

and F_∞ then satisfies (4.43) with no θ-derivative. We observe from equations (4.38a, 4.25, 4.38b) that U, R, and $\hat{\rho}$ satisfy the above conditions on F when Λ is zero (*i.e.* beyond the bend termination) and hence we conclude that

$$U \to U_\infty(y,z) \quad , \quad R \to R_\infty(y,z) \quad , \quad \hat{\rho} \to \hat{\rho}_\infty(y,z) \quad , \quad \text{as} \quad \theta \to \infty \,. \tag{4.46}$$

Since the vorticity R is conserved along streamlines following the end of the bend, V and W must also reach a θ-invariant state, and thus p_2 tends to a constant. The constants $F_\infty(y,z)$ are strongly dependent on the initial conditions since it is the initial values which are evolved through the bend. This strong dependence on the initial conditions highlights the effects of the duct entry conditions even far downstream of the end of the bend.

With the additional result concerning $\hat{\rho}$, these results are the same as those for the II case in [77] and we conclude that at this level compressibility does not significantly affect the far-downstream behaviour of the velocities reported in [77], though it will differ in detail, since the evolution of $\hat{\rho}$ is coupled to that of R and hence U in the bend. This close correspondence in the straight section between the far-downstream bulk behaviours of the II and CI cases was not expected *a priori*.

Bend maintained

Since the continuity equation (4.10a) and the θ-momentum equation (4.38a) are independent of Λ,

$$U \to U_\infty(y,z) \quad \text{as} \quad \theta \to \infty \tag{4.47}$$

for the same reasons as above. Furthermore, a double integral of (4.38b) in the cross-section gives

$$\frac{d}{d\theta}\iint \hat{\rho}\; dydz = \Upsilon \iint W\; dydz\;, \tag{4.48}$$

since the double integrals of the inertial terms on the left hand side vanish through the usual application of Green's Theorem. Since we have already shown in equation (4.33) that the right hand side of (4.48) is zero, we conclude that

$$\frac{d}{d\theta}\iint \hat{\rho}\; dydz = 0\;, \tag{4.49}$$

which in fact holds true regardless of the value of Λ. The evolution following a particle of the quantity $(\hat{\rho} - \Lambda\Upsilon z)$, whether Λ is zero or unity, is

$$\begin{aligned}(\hat{\rho} - \Lambda\Upsilon z)_\theta + V(\hat{\rho} - \Lambda\Upsilon z)_y + W(\hat{\rho} - \Lambda\Upsilon z)_z & \\ = \hat{\rho}_\theta + V\hat{\rho}_y + W\hat{\rho}_z - \Lambda\Upsilon W & \\ = 0 &\end{aligned} \tag{4.50}$$

by equation (4.38b). Hence $(\hat{\rho} - \Lambda\Upsilon z)$ is conserved for particles, and remains of $\mathcal{O}(1)$ for all θ. This result, in combination with the conservation of the double integral in (4.49) suggests that

$$\hat{\rho} \to \hat{\rho}_\infty(y,z) \quad \text{as} \quad \theta \to \infty\;, \tag{4.51}$$

and $\hat{\rho}_\infty$ satisfies (4.38b) with no θ-derivative.

When the inertial forces are small the prediction of linear development of R from equation (4.41) still holds. However, initially small inertial forces may grow significantly when the bend is maintained. To investigate, we take the double integral of equation (4.25) and set $\Lambda = 1$:

$$\frac{d}{d\theta}\iint R\; dydz = 2\int (U_t - U_b)\; dz + \int (\hat{\rho}_t - \hat{\rho}_b)\; dz\;, \tag{4.52}$$

with the subscripts taking on the same meaning as before. Since $(U_t - U_b) \to (U_{\infty t} - U_{\infty b}) =$ constant by (4.47), and similarly for $\hat{\rho}$ from (4.51), we predict an eventual constant linear growth in R with θ, and similarly for V and W. We conclude that in the case of initially small inertial forces, R will grow linearly with θ until the inertial forces are sufficiently strong that the development becomes non-linear, just as it would be from $\theta = 0$ if the initial inertial forces were of $\mathcal{O}(1)$, as we saw with the development of the initial conditions (2.40a–c) in §2.3. However, we have also predicted that in the limit $\theta \to \infty$ the vorticity R will have a constant linear growth rate. This contrasts with the bend-off case, where all variables attained a θ-independent state beyond the bend. We note equation (4.25) implies that any initial U_I profile which has non-zero y-derivative U_{Iy} will generate vorticity, and this observation together with the numerical results in Chapter 5 seems to confirm these predictions, since they imply that $(U_t - U_b)$ and $(\hat{\rho}_t - \hat{\rho}_b)$ are in general non-zero, as required for the above linear growth prediction. Indeed, since no normal flow at the wall exists, and since the corners are stagnation points, a particle on a wall will remain there throughout the flow and be advected towards a corner. Since the fluid in general forms one large streamwise vortex (as shall be seen in Chapter 5) this argument lends physical credence to the notion that the right hand side of equation (4.52) tends to a non-zero constant. Furthermore, the numerical results in §5.2 also directly support the linear-growth prediction.

Once more we note that the θ-independent state of U and the linear growth of R were also predicted for the maintained bend in the II case considered in [77]. The distinction between the two cases is that in the CI case the double integral of the vorticity is additionally being driven by a density integral. Both integrals on the right hand side of equation (4.52) eventually become indepen-

dent of θ, and are effectively determined by the initial conditions set at $\theta = 0$ through the integral throughout the bend-length. It is interesting to note once again that the initial conditions affect the flow even far downstream.

Since we are currently assuming that the bend and its effects are maintained indefinitely, it is likely that as $\theta \to \infty$ some new flow structure will occur. To investigate this we set $\theta = \Delta\theta^*$, where $\Delta \gg 1$ and $\theta^* \sim 1$, and expand the principal variables as follows:

$$U = U_0 + \Delta^{-1}U_1 + \dots \; ; \tag{4.53a}$$

$$\hat{\rho} = \hat{\rho}_0 + \Delta^{-1}\hat{\rho}_1 + \dots \; ; \tag{4.53b}$$

$$R = \Delta R_0 + R_1 + \dots \; ; \tag{4.53c}$$

$$\psi = \Delta\bar{\psi}_0 + \bar{\psi}_1 + \dots \; , \tag{4.53d}$$

while V and W have a form similar to R. These expansions are suggested by the above results as $\theta \to \infty$. In fact, U_0 and $\hat{\rho}_0$ must match with U_∞ and $\hat{\rho}_\infty$ in the limit $\theta^* \to 0+$.

The leading-order balances of equations (4.38a), (4.25), and (4.38b) with $\Lambda = 1$ are the following quasi-planar equations:

$$V_0 U_{0y} + W_0 U_{0z} = 0 \; ; \tag{4.54a}$$

$$V_0 R_{0y} + W_0 R_{0z} = 0 \; ; \tag{4.54b}$$

$$V_0 \hat{\rho}_{0y} + W_0 \hat{\rho}_{0z} = \Upsilon W_0 \; . \tag{4.54c}$$

A higher-order examination of (4.25) with $\Lambda = 1$ gives

$$R_{0\theta^*} + (V_0 R_{2y} + V_1 R_{1y} + V_2 R_{0y}) + (W_0 R_{2z} + W_1 R_{1z} + W_2 R_{0z}) = 2U_{0y} + \hat{\rho}_{0y} \; . \tag{4.55}$$

Rewriting the inertial terms on the left hand side of equation (4.55) by means of the higher-order balances of the continuity equation, and with the given

terms in the expansion of the stream-function necessarily being zero on the boundaries, a double integral and application of Green's Theorem yields:

$$\frac{d}{d\theta^*}\iint R_0 \, dydz = 2\int U_{0t} - U_{0b} \, dz + \int \hat{\rho}_{0t} - \hat{\rho}_{0b} \, dz \; . \tag{4.56}$$

But since U_0 and $\hat{\rho}_0$ match with $U_\infty(y,z)$ and $\rho_\infty(y,z)$, respectively, as $\theta^* \to 0+$, equation (4.56) implies that R_0 grows linearly with θ^*. Thus if

$$R_0 = f(\theta^*)\bar{R}_0(y,z) \tag{4.57}$$

for some order unity $\bar{R}_0$ then $f(\theta^*) = b\theta^*$ for some order unity constant b. We conclude that for large θ

$$\begin{aligned} R \sim \Delta R_0 \sim \Delta\theta^* \bar{R}_0(y,z) = \theta \bar{R}_0(y,z) \; , \\ i.e. \; R \sim \theta \bar{R}_0(y,z) \; , \end{aligned} \tag{4.58}$$

and similarly for V and W, whilst $U = U_\infty(y,z)$ and $\hat{\rho} = \hat{\rho}_\infty(y,z)$. Thus at this large scale the flow behaviour for order unity θ continues as U and $\hat{\rho}$ no longer evolve downstream, but R, V, and W continue to do so and depend linearly on θ. Consequently, the cross-plane flow continues to grow and whilst the down-duct velocity u remains $1 + \mathcal{O}(\epsilon)$, the cross-plane velocities v and w become $\mathcal{O}(\epsilon \times \Delta)$ and we see the hint of a more strongly non-linear regime downstream. In addition, we note that the slopes of the streamlines are

$$\frac{dy}{d\theta} = V \quad \text{and} \quad \frac{dz}{d\theta} = W \; , \tag{4.59}$$

and so the slopes are increasing linearly with θ here. This also serves to highlight the ever-strengthening swirling motion of the fluid, and to suggest a more strongly non-linear regime to come: that regime is to be addressed in §§5.3 and 5.4.

4.4.3 The corners

The sharp corners in the duct cross-sectional profile are also of interest here. Novel arguments and results are presented below based on an approach given in [77] in which the flow near the corners was also of interest. The following work is in the bend with θ of $\mathcal{O}(1)$ and with $\Lambda = 1$.

Without loss of generality, at $\theta = 0$ we set the initial condition that $\hat{\rho} = 0$ on the walls and we observe that since $W \equiv 0$ for all θ on $z = 0$ and $z = z_1$ (as there is no normal flow), $\hat{\rho}$ remains zero on these two walls throughout the flow. In some sense these two walls do not "feel" the compressibility as the governing equations on these two walls reduce to those of the II case. We will refer to this fact in the "proofs" below.

After a sufficient development region — say when $\theta \sim 1$ — we assume that near any corner in the cross-section the behaviour of R is

$$R \sim s^{-n} \tag{4.60}$$

for some small azimuthal distance s from the corner and for some positive constant n to be found. Suppose that close to a corner we choose one wall, such that we take z constant and let $y \to 0$ (with $y = s$) on this wall and so the vorticity equation (4.25) becomes

$$R_\theta + VR_y = 2U_y \tag{4.61}$$

there. As discussed, this is equivalent to the II vorticity equation on this wall, and so we can use the result from [77] that $n = \frac{1}{3}$, *i.e.*

$$R \sim s^{-\frac{1}{3}} , \tag{4.62}$$

and thus R has singular behaviour near the corners.

We now assume that

$$\hat{\rho} \sim s^{-m} \tag{4.63}$$

for some unknown $m > 0$. Considering a side $y =$ constant and letting $z \to 0$ (with $z = s$) reduces equation (4.38b) to

$$\hat{\rho}_\theta + W\hat{\rho}_z = \Upsilon W \ , \tag{4.64}$$

and since we know the behaviour of R near the corner from (4.62) this in turn becomes:

$$\hat{\rho}_\theta - 3z^{\frac{2}{3}}\hat{\rho}_z = -3\Upsilon z^{\frac{2}{3}} \ . \tag{4.65}$$

For the homogeneous equation associated with (4.65) we have $\hat{\rho}_\theta$ effectively balancing $-3z^{\frac{2}{3}}\hat{\rho}_z$. More formally, we use the method of Lagrange to show that the complementary function is

$$\hat{\rho} = \hat{\rho}(\theta + z^{\frac{1}{3}}) \ . \tag{4.66}$$

A particular integral is $\hat{\rho} = \Upsilon z$ such that the general solution is

$$\hat{\rho}(\theta, z) = g(\theta + z^{\frac{1}{3}}) + \Upsilon z \tag{4.67}$$

for some function g. The initial conditions on the sides $y =$ constant are $\hat{\rho} = 0$ on $\theta = 0$, as set above, and so $g(z^{\frac{1}{3}}) = -\Upsilon z$ for all z. Thus:

$$\hat{\rho}(\theta, z) = \Upsilon(z - (\theta + z^{\frac{1}{3}})^3) \ . \tag{4.68}$$

Since we assumed in equation (4.63) that $\hat{\rho} \sim z^{-m}$, this is only consistent with (4.68) if $m < 0$ — a contradiction. Hence we conclude that there is no algebraic singularity in $\hat{\rho}$ close to the corners of the cross-section. It is therefore likely that $\hat{\rho}$ stays finite there.

4.4.4 The $\Upsilon - \epsilon$ balance

In this section we return briefly to the balance of terms in Υ defined on page 88. We first make the observation that if $\Upsilon \ll 1$ and if $\hat{\rho}_I \equiv 0$ then the CI case reduces to the II case, in effect, since equation (4.38b) suggests that $\hat{\rho}$ would be conserved along streamlines. On the other hand, let us consider the governing equations of the CI system if Υ is large. The definition of Υ on page 88 suggests that the case $\Upsilon \gg 1$ corresponds to either increased entry swirl, increased turning angle, a gas with a lower gas constant γ, a decreased leading-order pressure term p_0, or some combination of these. All of these possibilities suggest a greater significance for the inertial effects, which could increase the importance of the compressibility through the evolution given by (4.38b) and could lead to more strongly non-linear behaviour.

In order to investigate the case of $\Upsilon \gg 1$ we rescale the variables of the governing equations (4.10a, 4.38a, 4.25, 4.38b) as follows:

$$\begin{aligned} U &\to \Upsilon U & \tilde{\rho} &\to \Upsilon \tilde{\rho} \\ V &\to \Upsilon^{\frac{1}{2}} V & p_2 &\to \Upsilon p_2 \\ W &\to \Upsilon^{\frac{1}{2}} W & \theta &\to \Upsilon^{-\frac{1}{2}} \hat{\theta} \, . \end{aligned} \tag{4.69}$$

We allow for a smaller θ length scale because we expect the more influential inertial effects to dominate over a shorter length scale. The leading-order balances of the governing equations are:

$$V_y + W_z = 0 \, ; \tag{4.70a}$$

$$U_{\hat{\theta}} + VU_y + WU_z = 0 \, ; \tag{4.70b}$$

$$V_{\hat{\theta}} + VV_y + WV_z = -p_{2y} \tag{4.70c}$$

$$W_{\hat{\theta}} + VW_y + WW_z - 2\Lambda U = -p_{2z} + \Lambda\tilde{\rho} \, ; \tag{4.70d}$$

$$\tilde{\rho}_{\hat{\theta}} + V\tilde{\rho}_y + W\tilde{\rho}_z = \Lambda W \, . \tag{4.70e}$$

No normalisation factors appear explicitly in this system of equations, very much like the governing equations (2.31a–d) of the II case.

The parameter Υ cannot increase without bound, however, as we still wish to perturb about the straight-duct solution $(u, v, w) = (1, 0, 0)$. This suggests achieving a balance between Υ and ϵ. To do so, we let

$$\mathcal{B} = \Upsilon\epsilon \sim 1 \tag{4.71}$$

and when $\tilde{\theta} = \Upsilon^{-\frac{1}{2}}\hat{\theta}$ we perturb the straight-duct solution as follows:

$$u = 1 + \mathcal{B}\tilde{U} + \dots \; ; \tag{4.72a}$$

$$v = \mathcal{B}\Upsilon^{-\frac{1}{2}}\tilde{V} + \dots \; ; \tag{4.72b}$$

$$w = \mathcal{B}\Upsilon^{-\frac{1}{2}}\tilde{W} + \dots \; ; \tag{4.72c}$$

$$p = \tilde{p}_0 + \mathcal{B}\tilde{p}_1 + \epsilon\mathcal{B}\tilde{p}_2 + \dots \; ; \tag{4.72d}$$

$$\rho = \bar{\rho} + \mathcal{B}\tilde{\rho} + \dots \; , \tag{4.72e}$$

where all the variables given are functions of $(\hat{\theta}, y, z)$. Then upon substitution into the full, dimensionless continuity, Navier-Stokes, and energy equations we find that

$$\frac{1}{\alpha}\left[(\bar{\rho} + \mathcal{B}\tilde{\rho})(1 + \mathcal{B}\tilde{U})\right]_{\hat{\theta}} + \left((\bar{\rho} + \mathcal{B}\tilde{\rho})\tilde{V}\right)_y + \left((\bar{\rho} + \mathcal{B}\tilde{\rho})\tilde{W}\right)_z = 0 \; , \tag{4.73a}$$

$$(\bar{\rho} + \mathcal{B}\tilde{\rho})\left[\frac{1}{\alpha}(1 + \mathcal{B}\tilde{U})\tilde{U}_{\hat{\theta}} + \tilde{V}\tilde{U}_y + \tilde{W}\tilde{U}_z\right] = -\frac{1}{\alpha\mathcal{B}}(\tilde{p}_0 + \mathcal{B}\tilde{p}_1)_{\hat{\theta}} \; , \tag{4.73b}$$

$$(\bar{\rho} + \mathcal{B}\tilde{\rho})\left[\frac{1}{\alpha}(1 + \mathcal{B}\tilde{U})\tilde{V}_{\hat{\theta}} + \tilde{V}\tilde{V}_y + \tilde{W}\tilde{V}_z\right] = -\tilde{p}_{2y} \; , \tag{4.73c}$$

$$(\bar{\rho} + \mathcal{B}\tilde{\rho})\left[\frac{1}{\alpha}(1 + \mathcal{B}\tilde{U})\tilde{W}_{\hat{\theta}} + \tilde{V}\tilde{W}_y + \tilde{W}\tilde{W}_z - \frac{1}{\alpha\mathcal{B}}(1 + \mathcal{B}\tilde{U})^2\right] = -\tilde{p}_{2z} \; , \tag{4.73d}$$

$$\begin{aligned}\gamma(\tilde{p}_0 + \mathcal{B}\tilde{p}_1)\left[\frac{1}{\alpha}(1 + \mathcal{B}\tilde{U})(\bar{\rho} + \mathcal{B}\tilde{\rho})_{\hat{\theta}} + \tilde{V}(\bar{\rho} + \mathcal{B}\tilde{\rho})_y + \tilde{W}(\bar{\rho} + \mathcal{B}\tilde{\rho})_z\right] \\ = \frac{1}{\alpha}(\bar{\rho} + \mathcal{B}\tilde{\rho})(1 + \mathcal{B}\tilde{U})(\tilde{p}_0 + \mathcal{B}\tilde{p}_1)_{\hat{\theta}} \; .\end{aligned} \tag{4.73e}$$

In deriving the above equations leading-order balances also showed that $(\tilde{p}_0 + \mathcal{B}\tilde{p}_1)$ is a function of $\hat{\theta}$ only. We note that when $\mathcal{B} \sim 1$ the rescaling of the θ length scale brings us into the geometry discussed in §4.3. Furthermore when $\mathcal{B} \sim 1$, the above equations suggest that the flow becomes more fully non-linear. The geometry where $\tilde{\theta} \sim \epsilon^{\frac{1}{2}}$ in effect, combined with the more fully non-linear equations and expansions above, will be seen in §§5.3 and 5.4 when we study the fully non-linear scheme.

4.4.5 Discussion

In §4.4 we have reformulated the governing equations of the CI case in terms of the streamwise vorticity R and the stream-function ψ. By examining bulk integrals of the energy, θ-momentum, and higher-order continuity equations, we were able to show that the pressure term p_1 is a constant for all θ. We also predicted linear growth with θ for the double integral of R in the bend, and linear growth of R in the case of small inertial forces. Both predictions are found to be supported numerically in the next chapter. We observed that analogous results hold in the II case studied in [77]. These predictions require $\Lambda = 1$ and thus from an engineering standpoint it is clear that since the vorticity grows linearly whilst the bend is maintained, the bend-length should be minimised. The growth in vorticity is presumably detrimental to the efficacy of the resultant jet at the exit of the duct since energy must be extracted from the streamwise flow in order to generate the swirling motion, and because adjacent swirling external jets interact more strongly through the Coanda effect. Furthermore, the evolution of density variations means that the exit profile will not be the ideal uniform exit profile.

We also noted an exact, though physically unlikely, solution (4.42) to the

governing equations of the CI case. Though this "stratified" result seems unlikely given the physical conditions prior to the bend, at the very least it can be said to capture the idea of the radial centrifuging in the bend. We also gave a partial solution (4.11a–c) in the case of homentropy, a physical situation which we observed is perhaps unlikely to occur.

In order to study the far-downstream effects of the bend we considered the limit $\theta \to \infty$ of the governing equations in the two cases $\Lambda = 1$ for $0 \leqslant \theta \leqslant 1$ only, and $\Lambda = 1$ throughout. In the first case, the bend-off case, we showed that the principal flow variables attained θ-invariant states far downstream, whose values depended strongly on the initial conditions, suggesting that minimising disturbances prior to and at the onset of the bend are crucial to suppressing the evolution of swirl and density variations. We note here, for example, that initial profiles satisfying

$$U_{Iy} \equiv 0 \quad , \quad \hat{\rho}_{Iy} \equiv 0 \quad , \quad R_I \equiv 0 \tag{4.74}$$

imply that no swirl or density variations are generated in the bend. Hence suppressing initial swirl and variations in y of the density and down-duct velocity will reduce the detrimental growth of $\hat{\rho}$ and R.

In the second case, when the bend is maintained, we showed that U and $\hat{\rho}$ both attain θ-invariant states, but that the vorticity R grows linearly with θ. What is more, we showed that this linear growth continues for large θ. This result again stresses the importance of minimising the bend-length if the growth of R is considered undesirable. Again, the far-downstream behaviour was influenced by the initial conditions, effectively integrated throughout the bend. The continued linear growth also hints at a strongly non-linear regime far downstream which has connections with the work in §§5.3 and 5.4.

In a general discussion here, we note that in the balance (4.54c) the changes

in fluid particle density are simply advective, by which we mean that a particle responds to the local fluid conditions as it continues to swirl into regions of higher or lower density, but the density profile in the plane becomes constant in θ. Furthermore, the governing equations appear to be a special case, in the sense that if the driving term of (4.38b) involves derivatives of W (or of V) then linear growth in $\hat{\rho}$ occurs when $\Lambda = 1$. In a final point, we observe that when $\Lambda = 1$ it is tempting to analyse equation (4.38b) by solving along characteristics. In this case, the equation becomes

$$\frac{D\hat{\rho}}{D\theta} = \Upsilon W \ , \tag{4.75}$$

and the z-momentum equation is

$$\frac{DW}{D\theta} = -p_{2z} + 2U + \hat{\rho} \ . \tag{4.76}$$

Differentiating along the characteristic seems to suggest then that

$$\frac{D^2\hat{\rho}}{D\theta^2} - \Upsilon\hat{\rho} = \Upsilon(2U - p_{2z}) \ , \tag{4.77}$$

which in turn suggests that $\hat{\rho} \sim e^{\theta}$ as $\theta \to \infty$. Following this result, a similar analysis of equation (4.25) suggests that $R \sim e^{\theta}$ as $\theta \to \infty$ also whilst $U \sim 1$ still, implying that there is a new length scale to consider where $\theta \propto Ln(\Delta) + \theta^*$ for $\Delta \gg 1$ and $\theta^* \sim 1$. However, the formal change to characteristic coordinates by transforming $(\theta, y, z) \mapsto (\theta, \eta, \zeta)$ involves W and thus equation (4.77) would no doubt reduce to one in which the θ-invariant prediction would emerge.

The singularity in R close to the corners was an interesting result in [77] and was shown to hold in the CI case also. We were in addition able to demonstrate that no such singularity exists in the density $\hat{\rho}$ and this result will be tested numerically by the results in §5.2. The authors of [77] were aware that

corner singularities in R could possibly interfere with the far-downstream numerical work and so in some of their computations they smoothed the corners via conformal mappings. These smoother profiles eliminated the vorticity singularity but the authors noted that the bulk flow properties remained the same as those for a rectangular cross-section. At a boundary layer length scale in turbulent flow in a duct with sharp corners the corners introduce secondary flow patterns, as discussed in reference to the literature in Part II of the present thesis. From an engineering viewpoint, sharp corners in the duct cross-section are to be avoided.

Finally, in §4.4.4 we showed that when the parameter $\mathcal{B} = \Upsilon\epsilon$ is of order unity, *i.e.* Υ is large, then the inertial effects become more dominant and the equations become more fully non-linear over the length scale $\tilde{\theta} \sim \epsilon^{\frac{1}{2}}$. This observation provides a link between the CI study and the fully non-linear CI case, to be considered in §§5.3 and 5.4. We note in passing that when $\mathcal{B} \ll 1$ the equations of §4.4.4 reduce to the CI case studied in the rest of this chapter.

Chapter 5

Numerical solutions

Having formulated and made analytical predictions for the CI problem in Chapter 4, we will solve the coupled governing system of equations numerically in this chapter. The second-order accurate techniques presented briefly in §2.3 were first applied to the CI case but the results of that approach will not be shown here. Instead, the accuracy of the results is improved in this chapter by using fourth-order accurate techniques based on compact differencing for the derivatives in the cross-section and mid-point averaging for the θ-derivatives. These techniques are explained in §5.1 below. The strategy was to first extend the second-order accurate techniques to the CI case, building on the confidence in the second-order accurate techniques gained from their favourable comparison with the results of [77] in §2.3. These second-order accurate CI results supported the fourth-order accurate results and so only the fourth-order accurate results will be shown in §5.2 below. We note that throughout this chapter the parameter Υ is taken to be unity.

In §§5.3 and 5.4 we follow on from the work in §4.4.4 by tackling and solving numerically the fully non-linear compressible inviscid (NLCI) case. The

numerical scheme is run over a wide range of initial conditions and parameter values and we present analytical work to support the results, as well as numerical solutions to the fully non-linear incompressible inviscid (NLII) problem. We also demonstrate that the numerical scheme qualitatively connects with the CI results in certain limits.

The fully non-linear cases allow for a leading-order variation in the streamwise velocity u to account for a stronger interaction between the curvature-induced swirl and the streamwise motion.

5.1 Numerical strategy for the CI case

The finite-difference formulae for the derivatives of a variable X arise from rearrangements of a Taylor series expansion of X in terms of the grid sizes Δx_i. The accuracy of the finite-difference approximations is given by the power of the first term in the truncated part of the rearranged expansion. For example, the central-space difference expression

$$\frac{U_{j+1,k}^{(n+1)} - U_{j-1,k}^{(n+1)}}{2\Delta y} \tag{5.1}$$

for $\frac{\partial U}{\partial y}$ as given in §2.3 is second-order accurate because the expansion is truncated immediately prior to the term in $(\Delta y)^2$. In this chapter, we use fourth-order accurate techniques, based not on directly retaining more terms in the expansions but on treating derivatives as variables themselves. Solving second-order accurate finite-difference equations for the derivatives and then substituting these values into the finite-difference form of the equation we wish to solve is the essence of compact differencing, which we now explain in a little more detail.

The compact-differencing approach treats both dependent variables and

their derivatives as unknowns and tridiagonal formulae are set up to solve for them. Once these are solved the governing equations become effectively explicit. For example, for the equation

$$U_\theta + VU_y + WU_z = 0 \tag{5.2}$$

we define $A = U_y$ and $B = U_z$ and then solve

$$\frac{1}{3}A_{j-1,k}^{(n+1)} + \frac{4}{3}A_{j,k}^{(n+1)} + \frac{1}{3}A_{j+1,k}^{(n+1)} = \frac{1}{\Delta y}\left(U_{j+1,k}^{(n+1)} - U_{j-1,k}^{(n+1)}\right) \tag{5.3a}$$

$$\frac{1}{3}B_{j,k-1}^{(n+1)} + \frac{4}{3}B_{j,k}^{(n+1)} + \frac{1}{3}B_{j,k+1}^{(n+1)} = \frac{1}{\Delta z}\left(U_{j,k+1}^{(n+1)} - U_{j,k-1}^{(n+1)}\right). \tag{5.3b}$$

As with the numerical work of §2.3 we wish to avoid inverting block tridiagonal matrices and so employ an implicit-iterative approach. We solve (5.3a) "semi-implicitly" by sweeping in y as described on page 44 above and solve (5.3b) fully implicitly by solving the tridiagonal system directly. Since we now have A and B the following discretisation of (5.2),

$$\frac{U_{j,k}^{(n+1)} - U_{j,k}^{(n)}}{\Delta\theta} + V_{j,k}^{(n+1)}A_{j,k}^{(n+1)} + W_{j,k}^{(n+1)}B_{j,k}^{(n+1)} = 0\ , \tag{5.4}$$

becomes simply an explicit algebraic equation for $U_{j,k}^{(n+1)}$. This is done to all the computed equations, with iterations for convergence as before. We note that storage and running time savings compared with a second-order scheme can be substantial.

The second improvement in accuracy involves averaging the θ-derivatives at a mid-point $n + \frac{1}{2}$ which effectively makes these derivatives second-order accurate. This is done for the generic variable X by letting

$$\bar{X} = \frac{1}{2}\left(X_{j,k}^{(n+1)} + X_{j,k}^{(n)}\right)\ , \tag{5.5}$$

where $\bar{X}$ is the mean value at the mid-point. Then $X_{j,k}^{(n+1)} = 2\bar{X} - X_{j,k}^{(n)}$ and in the first-order backward difference formula for X_θ we get

$$X_\theta = \frac{\bar{X} - X_{j,k}^{(n)}}{\Delta\theta/2}\ . \tag{5.6}$$

We solve for all variables — including the derivatives treated as such — at the mid-points.

The compact-differencing approach effectively turns each of the governing equations (4.10a, 4.38a, 4.25, 4.38b) into a triple consisting of three triplets: two tridiagonal systems for the derivatives and one explicit system for the equation itself. The equations are solved in the following order. Firstly, we solve the triple associated with the θ-momentum equation (4.38a) for every point in the plane θ = constant. The density equation (4.38b) is solved next, followed by the vorticity equation (4.25). The triple associated with the Poisson equation (4.27) is then solved for ψ, but the solution technique is a little more involved, as we will now explain. Let $G_{j,k}$ denote ψ_{yy} at the grid-point (j,k) and the θ-level $n+\frac{1}{2}$. Similarly, let $H_{j,k}$ denote ψ_{zz} at the grid-point (j,k) and the θ-level $n+\frac{1}{2}$. The triple is then:

$$\frac{1}{12}G_{j-1,k}+\frac{5}{6}G_{j,k}+\frac{1}{12}G_{j+1,k}=\frac{1}{(\Delta y)^2}\left(\psi_{j-1,k}-2\psi_{j,k}+\psi_{j+1,k}\right)\ ; \tag{5.7a}$$

$$\frac{1}{12}H_{j,k-1}+\frac{5}{6}H_{j,k}+\frac{1}{12}H_{j,k+1}=\frac{1}{(\Delta z)^2}\left(\psi_{j,k-1}-2\psi_{j,k}+\psi_{j,k+1}\right)\ ; \tag{5.7b}$$

$$G_{j,k}+H_{j,k}=R_{j,k}\ . \tag{5.7c}$$

We sweep in lines of j = constant again, and so we sum the first two triplets above and rearrange to form the tridiagonal equation:

$$\begin{aligned}&\frac{1}{(\Delta z)^2}\psi_{j,k-1}-2\left(\frac{1}{(\Delta y)^2}+\frac{1}{(\Delta z)^2}\right)\psi_{j,k}+\frac{1}{(\Delta z^2)}\psi_{j,k+1}\\&=\frac{5}{6}R_{j,k}-\frac{1}{(\Delta y)^2}\left(\psi_{j-1,k}+\psi_{j+1,k}\right)+\frac{1}{12}\left(G_{j-1,k}+G_{j+1,k}+H_{j,k-1}+H_{j,k+1}\right)\ .\end{aligned} \tag{5.8}$$

In this equation as in all the others, we are solving on the line j whilst variables are known on the line $j-1$ and values from the previous iteration are used for the values on the line $j+1$. At this stage in the calculation, R has been found

at all (j,k) from the previous triple. After solving for $\psi_{j,k}$ we perform two additional calculations to update G and H. Having thus solved the Poisson equation it only remains to find the fourth-order accurate terms $\psi_z = -V$ and $\psi_y = W$ by solving two compact-differencing tridiagonal equations.

As in §2.3 the equations simplify on the walls of the duct, but also here one-sided derivatives have to be taken. The polynomial formulae for the derivatives at the boundary can be found by taking a Taylor expansion of the variable about the wall location, and then retaining as many terms as necessary for the required level of accuracy. This leads for example to the expression

$$\left(\frac{\partial^2 U}{\partial y^2}\right)\Bigg|_{y=0} = \frac{1}{12(\Delta y)^2}(-10U_{6,k}+61U_{5,k}-156U_{4,k}+214U_{3,k}-154U_{2,k}+45U_{1,k})\,. \tag{5.9}$$

Furthermore, the Dirichlet boundary condition $\psi \equiv 0$ is applied on the walls.

The coupled governing equations have an elliptic nature in the cross-plane, and so with the sweeping technique repeated iterations are necessary for information from the boundaries to diffuse through to the interior points. Thus at least ten iterations are carried out before convergence testing is performed. The greatest absolute difference in all variables between one iteration and the next is a measure of the convergence of the outputs, and the outputs are said to have converged when this maximum absolute difference is within some prescribed level of accuracy. All of the results in §5.2 are accurate to at least 10^{-8}. Since the iterative method leads to convergence here, relaxation as referenced on page 48 is not needed. Following convergence, we find the value for the generic variable X at the level $n+1$ from

$$X^{n+1} = 2X^{n+\frac{1}{2}} - X^n\,. \tag{5.10}$$

These values are stored as the solutions.

Finally here we note that $\iint R\, dydz$ will be denoted DD hereinafter. This integral was calculated by a compound application of Simpson's Rule, as given for example in [24, p.130].

5.2 Numerical results and discussion for the CI case

5.2.1 Zero initial swirl

The first computation we will present is for a 2×1 duct with the zero entry-swirl initial conditions (2.39). Three computational grids were considered. The *coarse* grid had the triple $(\Delta\theta, \Delta y, \Delta z)$ equal to $(\frac{1}{500}, \frac{1}{16}, \frac{1}{32})$. The other two grids were a *medium* grid at $(\frac{1}{1000}, \frac{1}{32}, \frac{1}{64})$, and a *fine* grid at $(\frac{1}{2000}, \frac{1}{48}, \frac{1}{96})$. As in §2.3 we generally present only the reults of the fine grid calculations, but following the discussion on page 51 we use the results over the other grids to show that the results are virtually grid-independent. Specifically, the left hand side of Figure 5.1 shows the computed values of DD against θ over the three grids, whilst the right hand side shows the computed values of $\hat{\rho}$ at the point $(0, 0.5)$ against θ. In both cases, significant grid effects can only be seen beyond $\theta = 30$ which we will later show is beyond the limit of accuracy. In all cases, we set the maximum allowable error as 10^{-8}. We note that the sudden bending seen in both graphs in Figure 5.1 are in fact numerically smooth transitions to a θ-invariant state caused by the end of the bend. Physically, the sudden bending is smoothed by the mechanism described in §2.1. The developments of DD and $\hat{\rho}$ in the bend $0 \leqslant \theta \leqslant 1$ are shown in more detail in Figure 5.4, and are described in the discussion accompanying that figure.

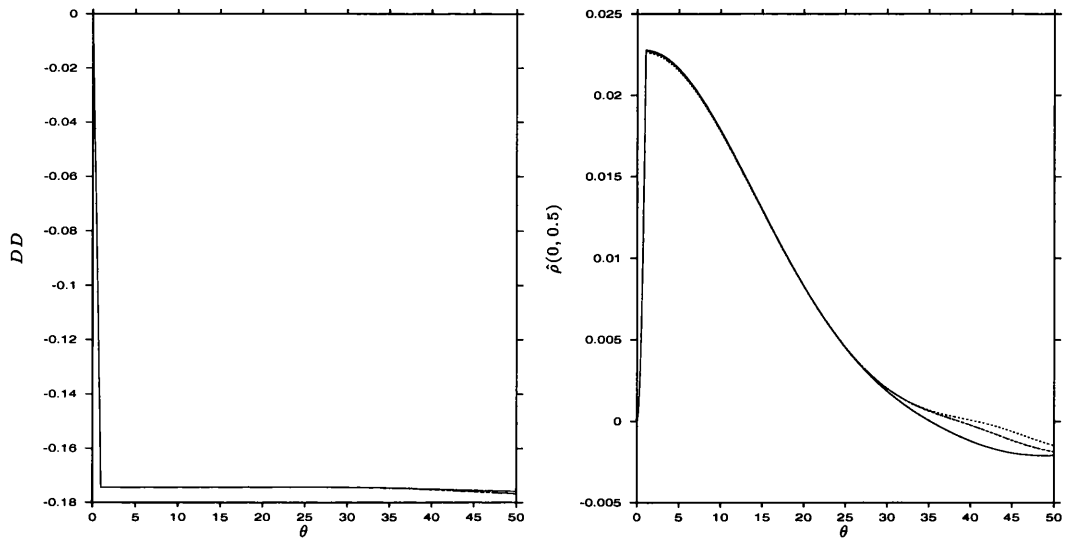

Figure 5.1: DD and $\hat{\rho}(0, 0.5)$ against θ, from three grids. The initial conditions are (2.39), and in both cases $\Lambda = 0$ for $\theta > 1$.

With the convergence testing and iterative procedure described in §5.1, the fine grid computation needed the fewest iterations — typically 20 in the bend, but increasing steadily with θ. In the straight section beyond the bend all three grids required no more than the 10 forced iterations, but when the bend was maintained the number of iterations required continued to grow.

Figure 5.2 shows the U-profile at $\theta = 1$ has changed little from the initial profile at $\theta = 0$ which is consistent with the analytical prediction (4.40) and the discussion accompanying (4.43). However, although the flow entered the bend with the swirl and $\hat{\rho}$ uniformly zero, a small swirl and variation in $\hat{\rho}$ have developed by $\theta = 1$ as shown in Figure 5.3. The effect of the small non-zero swirl can be seen in Figure 5.2: the U-profile has been slightly mixed around as is evident in the graphs of the values at $\theta = 1$. We observe also a slight off-symmetry in z of the profiles which corresponds to the streaming of the fluid towards the outside wall as a consequence of the centrifugal effects. This off-

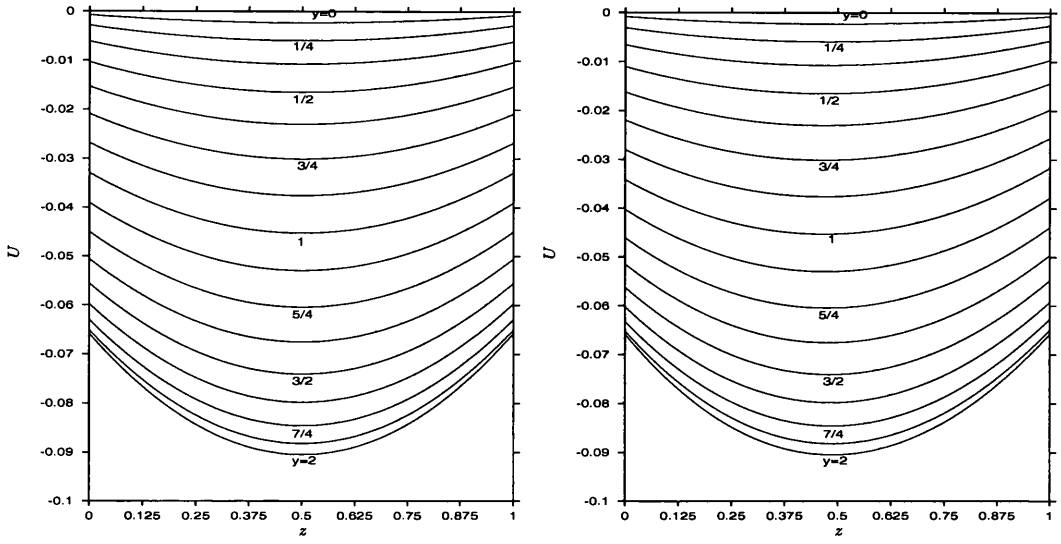

Figure 5.2: U at $\theta = 0$ (left hand side) and at $\theta = 1$. The initial conditions are (2.39).

symmetry was also seen in the II results of §2.3 but is more pronounced here. We also note that the improvement in accuracy in the compact-differencing approach has removed the numerical edge-effects discussed on page 51 which were apparent in the second-order accurate results of §2.3.

The left hand graph of Figure 5.4 shows linear growth of the swirl — measured by the double integral of the vorticity over the cross-plane — between $\theta = 0$ and $\theta = 1$ as predicted by (4.52) and the accompanying discussion. Since the evolution of $\hat{\rho}$ is driven by W the similarity between the two profiles seen in Figure 5.3 is to be expected. However, by considering a point in the cross-section we observe that in the bend W grows linearly (in keeping with the linear growth of the swirl) whilst $\hat{\rho}$ grows non-linearly, as shown in the graph on the right hand side of Figure 5.4.

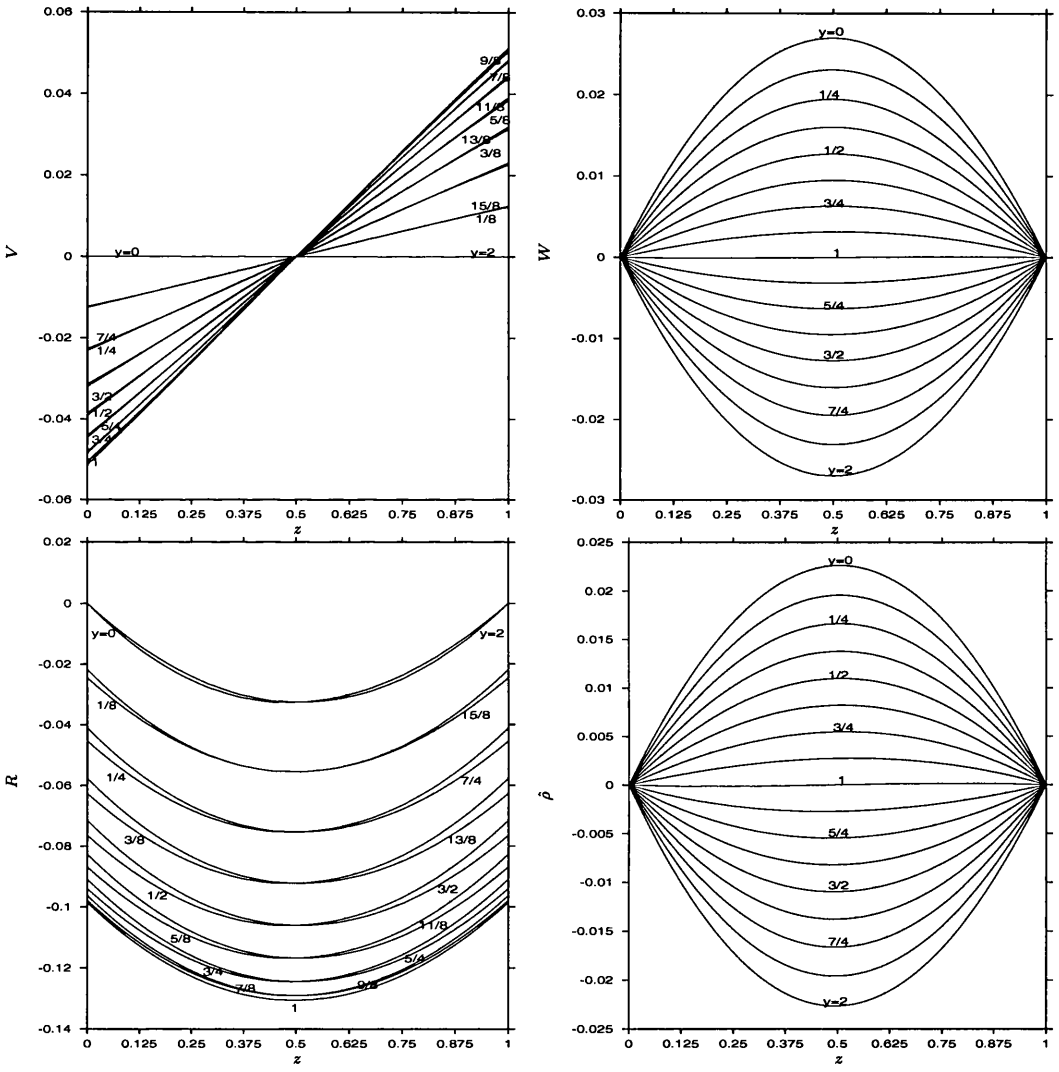

Figure 5.3: V, W, R, and $\hat{\rho}$ profiles at $\theta = 1$. Fine grid results, with the initial conditions (2.39).

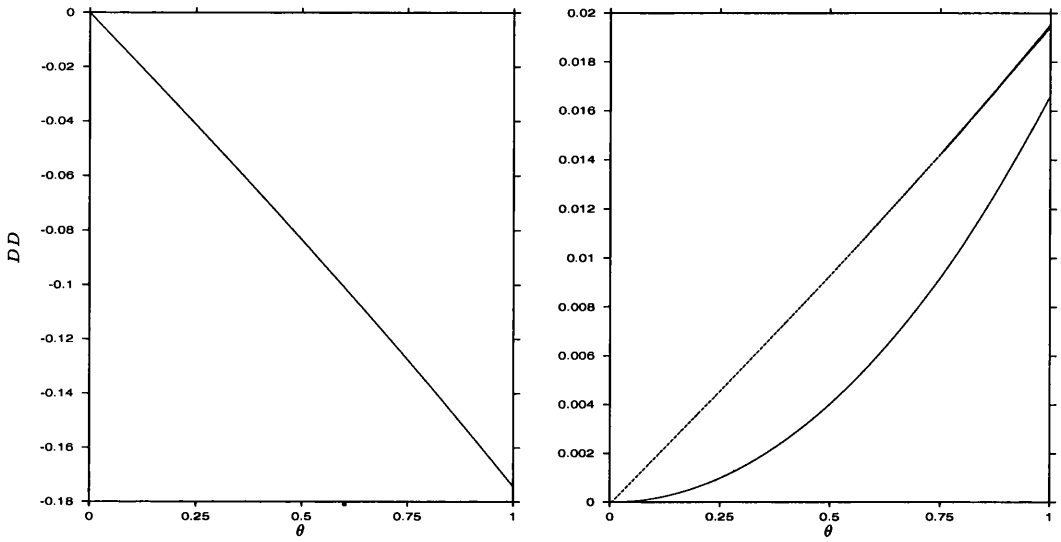

Figure 5.4: Left hand side: DD against θ. Right hand side: $W(0.5, 0.25)$ (dashed line) and $\hat{\rho}(0.5, 0.25)$ against θ. The initial conditions are (2.39).

Results for large θ

We first observe that the double integral of $\hat{\rho}$ in the plane of a cross-section can act as a test on numerical accuracy since the prediction is that the double integral remains zero from (4.49). Therefore, as soon as

$$\left| \iint \hat{\rho} \, dydz \right| > E \, , \tag{5.11}$$

where E denotes the defined level of accuracy (here, $E = 10^{-8}$), the numerical results are deemed no longer valid. Furthermore, since the double integral of $\hat{\rho}$ is zero for all θ regardless of the value of Λ, as $\hat{\rho}$ evolves it must do so anti-symmetrically to maintain this result, *i.e.* it is constrained to grow in a manner in which the volume beneath a surface plot of $\hat{\rho}$ is always zero.

Bend off

Using the test of accuracy effectively defined by equation (5.11) we observe that when $\Lambda = 0$ for $\theta > 1$, the numerics are valid up to $\theta = 30$ as shown in

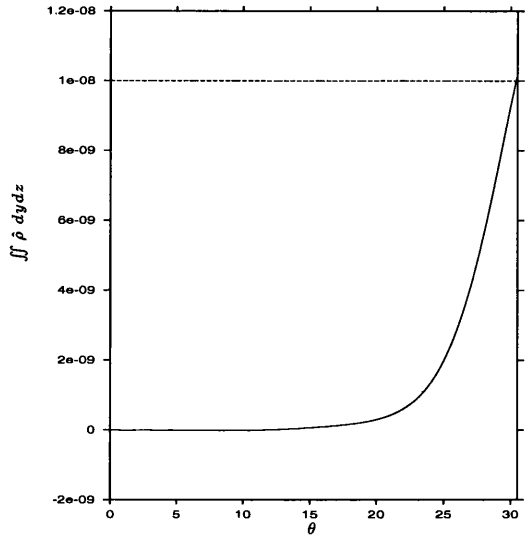

Figure 5.5: $\iint \hat{\rho}\ dydz$ against θ. The limit of numerical accuracy is reached at $\theta = 30.5$, beyond which the integral is greater than 10^{-8} for the first time. The initial conditions are (2.39).

Figure 5.5. No numerical results will be presented for $\theta > 30$.

A plot of DD in Figure 5.6 shows excellent agreement with the prediction in the discussion accompanying equation (4.39) that DD should grow linearly for $0 \leqslant \theta \leqslant 1$ when $\Lambda = 1$ and be constant thereafter where $\Lambda = 0$. We remark again that the sudden bending caused by the end of the bend is numerically smooth on a short length scale.

In line with the prediction from the energy equation (4.38b) when $\Lambda = 0$ that $\hat{\rho}$ is conserved along streamlines, the surface plots in Figure 5.7 suggest that $\hat{\rho}$ following a particle is not evolving, but that the profile is being swirled in line with the clockwise (looking downstream) helical motion suggested by Figure 5.3. We also predicted in (4.46) that all variables would attain a θ-invariant state by some large θ. Although, as shown in the top two graphs in Figure 5.8, the stream-lines in the cross-section change little between $\theta = 1$

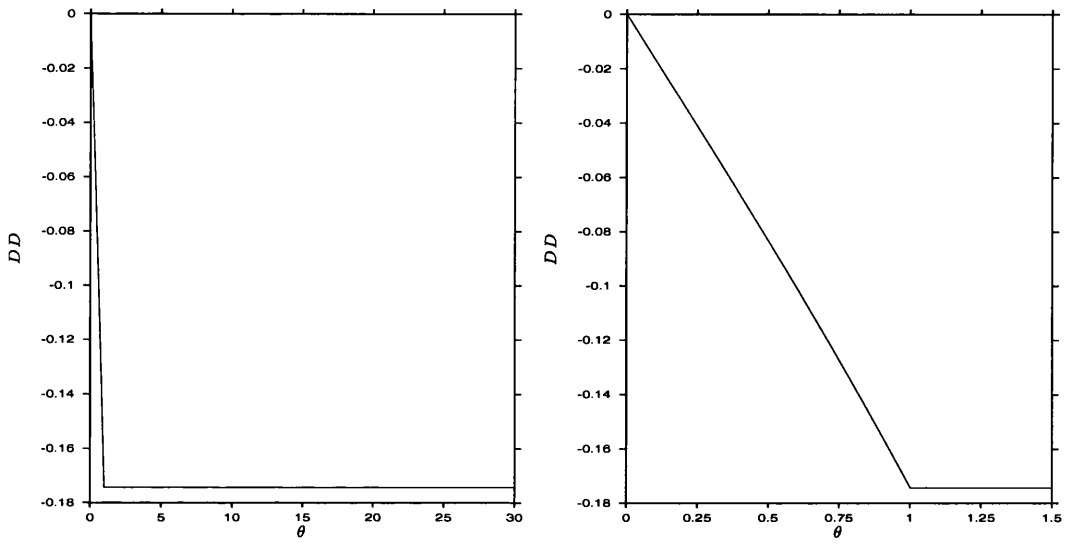

Figure 5.6: DD against θ. The initial conditions are (2.39).

and $\theta = 30$ in line with this prediction it seems apparent that the numerics cannot be run far enough to detect the θ-invariant state that would be the product of the mixing of the profiles seen between Figures 5.7 and 5.8.

In conclusion, the numerics appear to support the predictions related to the double integrals of R and $\hat{\rho}$ and suggest that the quantities are conserved along streamlines, supporting the predictions of §4.4.2. However, the prediction in (4.46) that after a sufficiently long downstream distance the effects of mixing would lead to θ-invariant states of the principal flow variables cannot be supported directly by the numerics, although they are in keeping with the logical steps taken to reach that prediction. If we define the turn-over distance as the downstream distance traversed by the flow whilst one complete rotation of the fluid in the plane takes place, then an approximate value for the turn-over distance can be found from the graphs of V and W in Figure 5.3. Even towards the centre of the duct the turn-over distance is greater than 100 and so the numerical restriction of $\theta = 30$ perhaps limits the chances of detecting

fully-mixed profiles.

Bend maintained

In this section $\Lambda = 1$ for all θ. In the bend-off case we argued from equation (5.11) and Figure 5.5 that the restriction of numerical accuracy was reached at $\theta = 30.5$. In the bend-maintained case a similar graph in Figure 5.9 suggests that the restriction of numerical accuracy is reached near $\theta = 3.9$.

The graph on the left hand side of Figure 5.10 shows the downstream development of the bulk swirl $DD = \iint R\, dydz$. The prediction from equation (4.52) and the accompanying discussion was of a linear increase in DD for as long as the inertial terms remain small, which we see between $\theta = 0$ and around $\theta = 2$ in Figure 5.10. By around $\theta = 2$ we can deduce from Figure 5.11 that the initially small inertial terms have grown significantly and are now comparable in magnitude to the non-zero initial R in (2.40a–c). As predicted for the larger swirl case in the discussion accompanying (4.52), DD appears to grow non-linearly between around $\theta = 2$ and the restriction of numerical accuracy $\theta = 3.9$. Furthermore, examination of W at some interior points in the right hand side of Figure 5.10 supports the claim that R, V, and W grow linearly whilst the inertial terms are small. In addition, the graphs of Figure 5.11 are plotted with a constant scale to demonstrate the anticipated continued growth and development of the stream-function ψ and the vorticity R.

As with R above, the surface plots of the density variation $\hat{\rho}$ shown in Figure 5.12 do not exhibit the far-downstream behaviour predicted in §4.4.2. The prediction for $\hat{\rho}$ was the emergence of a θ-invariant state as $\theta \to \infty$, but in fact $\hat{\rho}$ appears to be still evolving between $\theta = 1$ and $\theta = 3$. Once again

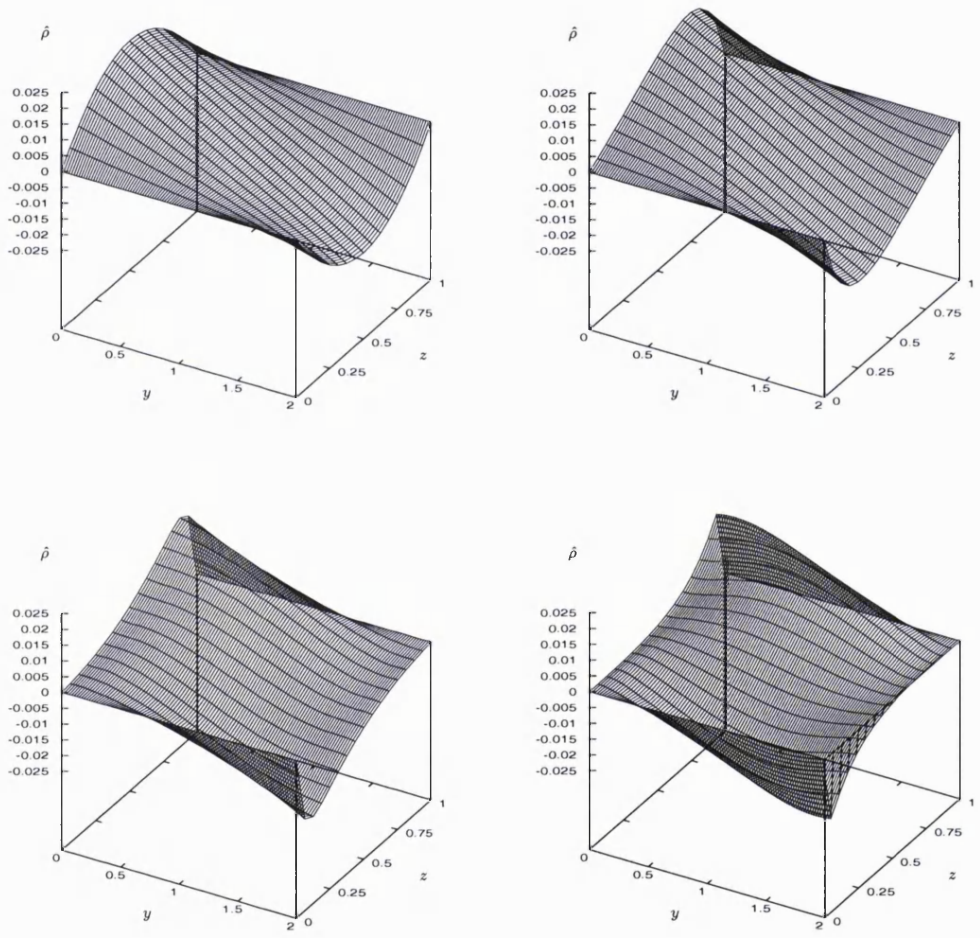

Figure 5.7: Surface plots of $\hat{\rho}$ at (left to right, top to bottom) $\theta = 1$, 10, 20, 30. Fine grid results, $\Lambda = 0$ for $\theta > 1$ and with the starting conditions (2.39).

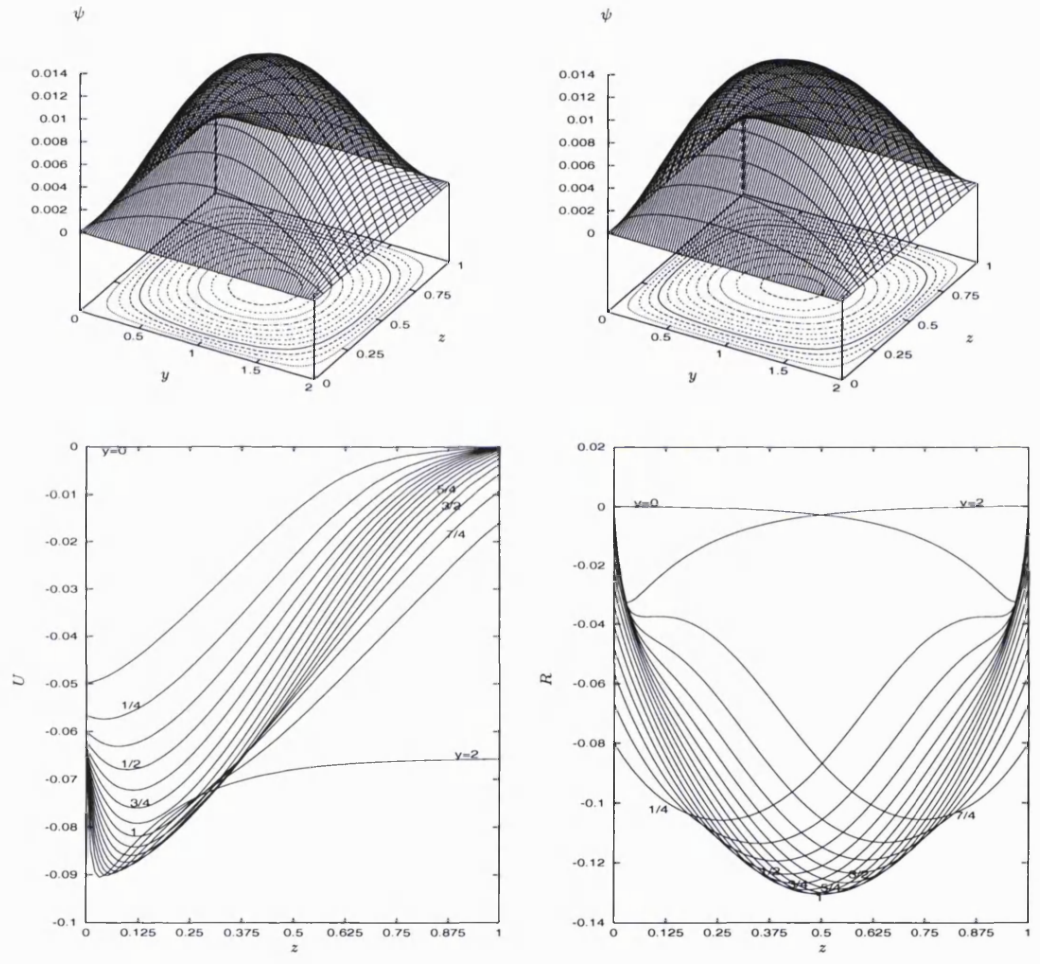

Figure 5.8: Surface plots of the stream-function ψ at (left to right) $\theta = 1$ and $\theta = 30$. Plots of U and R at $\theta = 30$. Fine grid results, $\Lambda = 0$ for $\theta > 1$ and with the starting conditions (2.39).

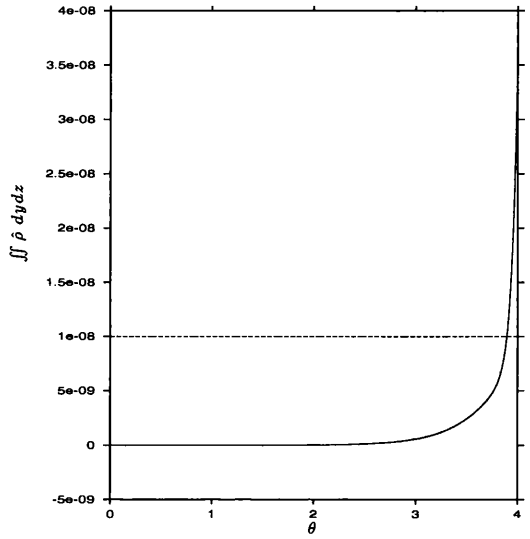

Figure 5.9: $\iint \hat{\rho}\ dydz$ against θ. The limit of numerical accuracy is reached near $\theta = 3.9$, beyond which the integral is greater than 10^{-8} for the first time. The initial conditions are (2.39).

we conclude that the numerics cannot run sufficiently far to detect the far-downstream predictions. We do, however, observe that the density profile is being swirled by the effects of R and that the growth in the values of $\hat{\rho}$ along the walls may be due to the accumulation of fluid near the corners, since as discussed in §2.3 particles on a given side are constrained to stay on that side. We also recall that the discussion on page 92 showed that $\hat{\rho}$ would remain of $\mathcal{O}(1)$ for all θ and we note that the numerics do not contradict this prediction.

Finally we mention that, in line with the prediction that U is conserved along streamlines, the results in Figure 5.13 show the U-profile being swirled in the cross-section.

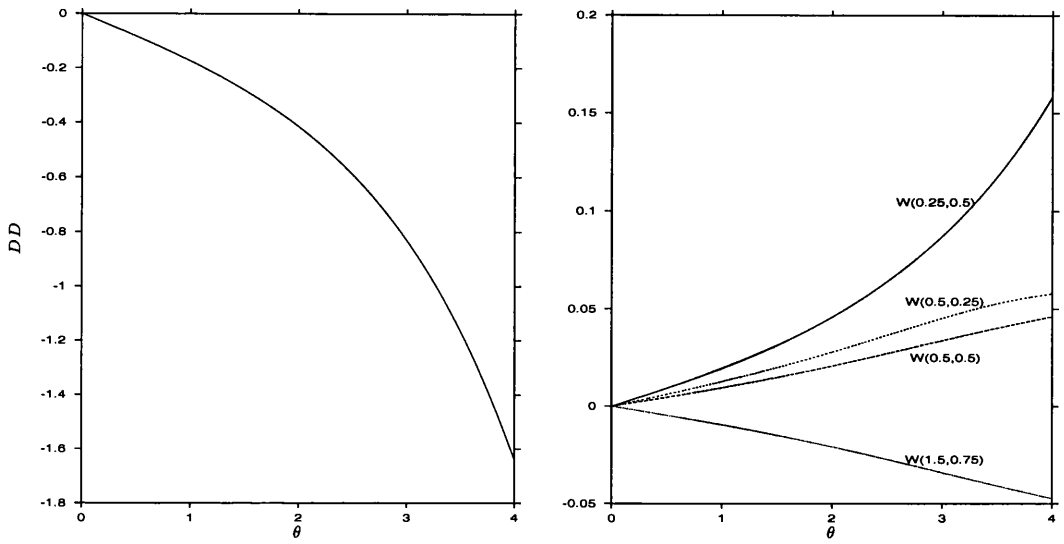

Figure 5.10: DD against θ and various W against θ. The initial conditions are (2.39).

The corners

We observed on page 116 that with the bend maintained beyond $\theta = 1$ the restriction of numerical accuracy was reached sooner than in the bend-off case. This earlier break-up of the results could be caused by a more rapid increase in the accumulation of truncation and rounding (*i.e.* numerical) errors. This greater accumulation of the inevitable numerical errors is perhaps due to the errors contributing to the driving terms in the governing equations. However, a physical candidate for the error-generation is the predicted singular response of the vorticity close to the corners of the duct cross-section after a sufficient development region shown by (4.62), which would be expected to continue to grow whilst $\Lambda = 1$. In fact, between $\theta = 3$ and $\theta = 4$ the magnitude of R close to two of the corners has become very large, as shown in Figure 5.14, supporting the prediction of a singular growth near the corners. The density variation $\hat{\rho}$ was predicted in equation (4.68) to grow no more strongly than θ^3,

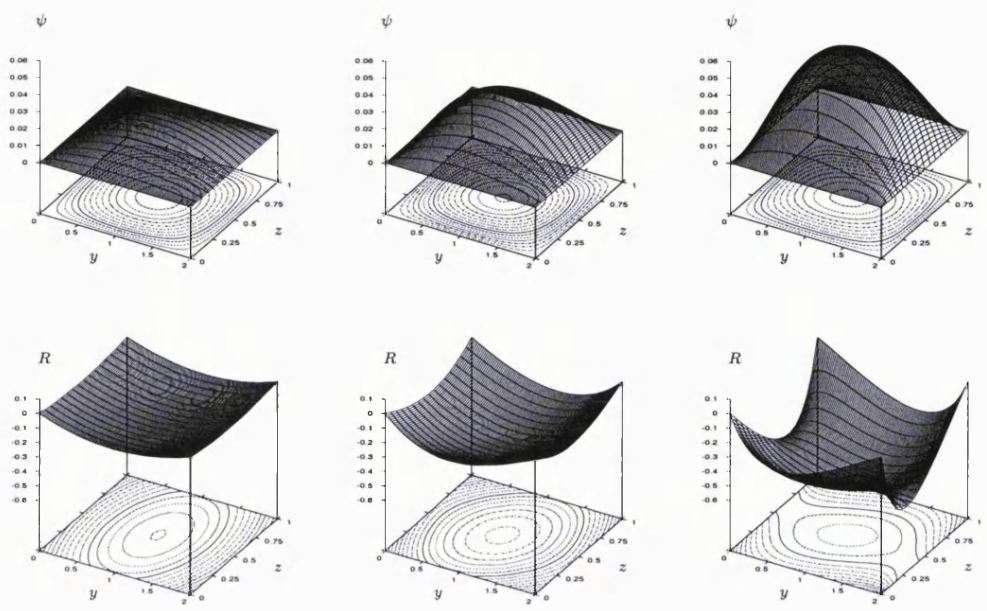

Figure 5.11: Constant-scale surface plots of the stream-function ψ and the vorticity R at (left to right) $\theta = 1$, 2, and 3. The initial conditions are (2.39).

and the graphs of Figure 5.12 appear to support this claim.

5.2.2 Non-zero initial swirl

In this section we briefly show some results of the numerical solutions for a 2×1 duct with the initial condtions (2.40a–c). The same grids as §5.2.1 were used and similar demonstrations of grid convergence were available which we will not reproduce here; only results from the fine grid will be shown. With the bend terminated at $\theta = 1$ the limit of accuracy was reached just beyond $\theta = 2$ only, whilst when the bend was maintained the limit of accuracy was reached by just before $\theta = 2$. In §5.2.1 the maximum distance the numerics could be run differed by an order of magnitude between the bend-off case and the bend-maintained case, but this is not so here. The strong growth of the already large

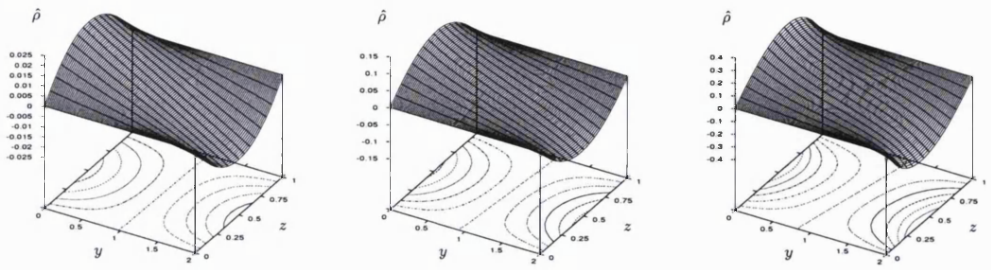

Figure 5.12: Surface plots of the density variation $\hat{\rho}$ at (left to right) $\theta = 1$, 2, and 3. The initial conditions are (2.39).

vorticity in the bend is thought to cause the blow up near $\theta = 2$ regardless of whether the bend has terminated or not. Since no large values of θ can be reached by the numerics we shall only present here solutions for the principal flow variables at the end of the bend at $\theta = 1$. We note that weaker initial swirl conditions such as those in [77] were considered: the numeric solutions were able to run further downstream and bulk predictions were supported, but again the far-downstream limits were not attained.

In Figure 5.15 we can see that once again, as in the incompressible solution shown in Figure 2.10, the four-cell structure of ψ has evolved to a two-cell structure by $\theta = 1$. The structure of R at $\theta = 1$ is perhaps less easy to describe qualitatively, but large values of R have evolved towards the top of the duct.

The left hand graph of Figure 5.16 shows the $\hat{\rho}$-profile at $\theta = 1$. Although $\hat{\rho}$ is clearly responding to the large values of R near the top of the duct, it is one order of magnitude smaller than R there and has quite a different overall form to R. The two remaining graphs in Figure 5.16 show the development of $\hat{\rho}$ and W at two sample points of the cross-section. The centre graph shows a

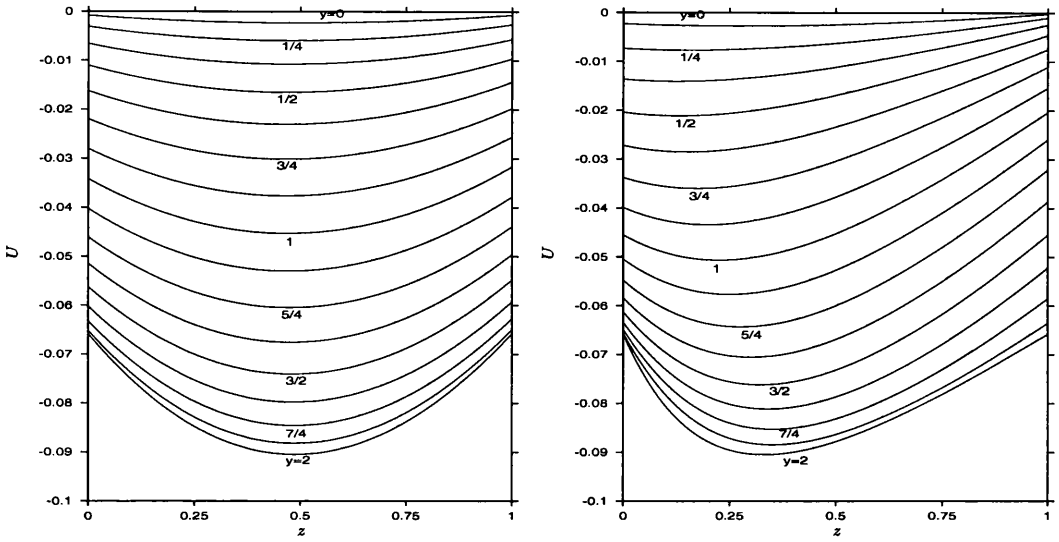

Figure 5.13: U at $\theta = 1$ (left hand side) and $\theta = 3$. The initial conditions are (2.39).

development familiar from the zero initial swirl case shown in Figure 5.4 with W growing linearly with θ. The right hand graph, however, shows that W may grow non-linearly at a fixed point; even though the evolution of $\hat{\rho}$ following a particle is driven by W, it is possible for $\hat{\rho}$ and W to behave very differently at a fixed point in the cross-section.

Finally, in Figure 5.17 we see that U has not grown in magnitude but the U-profile has been mixed by the action of the vorticity R in keeping with the predictions of §4.4.

5.2.3 General discussion

The work in §5.2 has provided specific numerical results to confirm many of the predictions of §4.4. It has shown that between $\theta = 0$ and $\theta = 1$ a non-zero swirl and density variation will in general develop and grow linearly even if the initial swirl and density variation are zero. The swirl distorts slightly

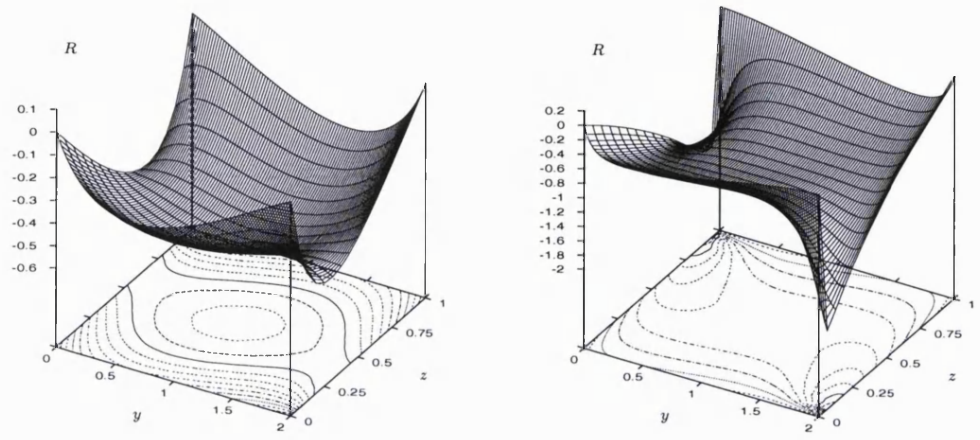

Figure 5.14: R at $\theta = 3$ and $\theta = 4$. The initial conditions are (2.39).

the profile of the downstream velocity U through a mixing mechanism. For those industrial applications seeking to minimise exit swirl the desirability of suppressing initial swirl was demonstrated by the solutions based on the initial conditions (2.40a–c): the non-zero initial swirl grew non-linearly in the bend and caused even greater distortion of the downstream velocity U.

In a straight section beyond $\theta = 1$ the bulk predictions of §4.4.2 were confirmed, but the numerical schemes were unable to run to sufficiently large θ to detect the far-downstream prediction of θ-invariant states of the principal flow variables. Although R and $\hat{\rho}$ were predicted to be constant following a particle beyond the bend, the continued swirling motion can distort the profiles to a significant extent suggesting that if close-to-uniform profiles are desired at the downstream duct exit, the length of any straight section beyond the bend should be minimised.

Maintaining the bend beyond $\theta = 1$ caused stronger growth in the swirling motion and led to more pronounced adverse effects on the density- and U-

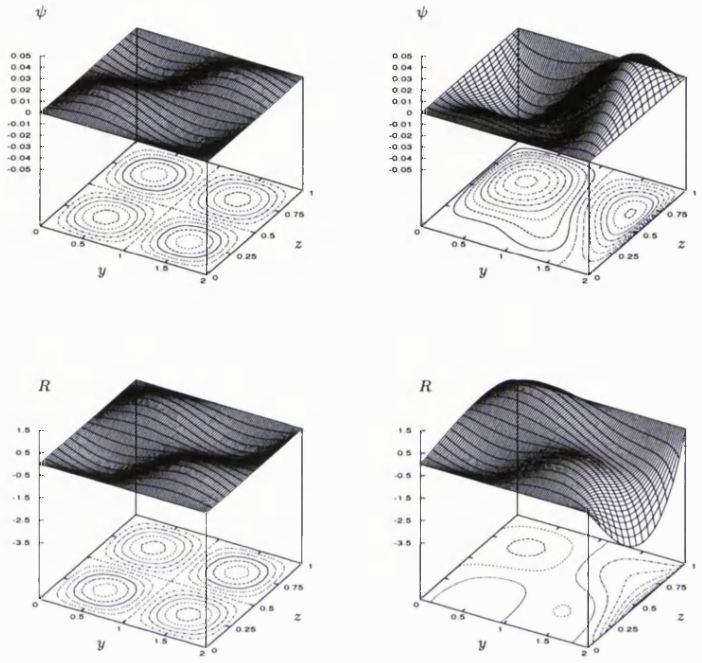

Figure 5.15: Constant-scale surface plots of the stream-function ψ and the vorticity R at $\theta = 0$ (left hand side) and $\theta = 1$. The initial conditions are (2.40a–c).

profiles, as predicted in §4.4.2. The far-downstream predictions of continued linear growth of R and the development of θ-invariant states for the other principal flow variables was again not detected before the restriction of numerical accuracy was reached, and we noted that this restriction arose at a smaller θ than in the bend-off case. However, the strong response of the vorticity and the density variations suggest that the bend length — and inertial forces in general — should be minimised if near-uniformity of profiles at the duct exit is required.

Finally, the predictions of a singular response in R close to the corners was

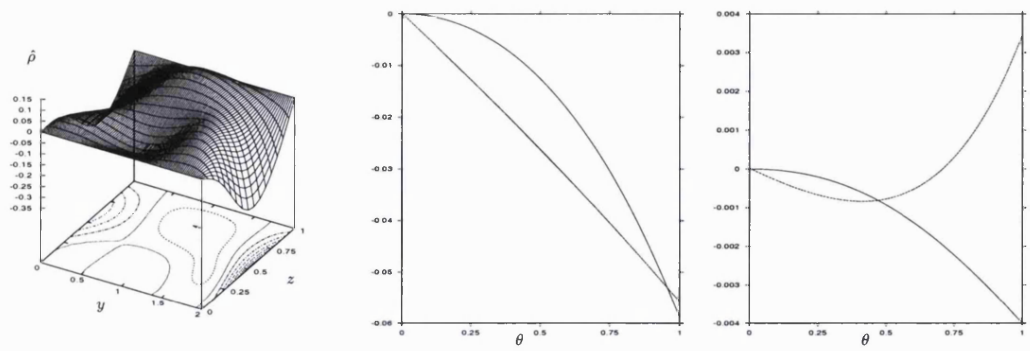

Figure 5.16: Left: $\hat{\rho}$ at $\theta = 1$. Centre: $\hat{\rho}$ (solid) and W at $(0.5, 0.25)$. Right: $\hat{\rho}$ (solid) and W at $(0.5, 0.5)$. The initial conditions are (2.40a–c).

confirmed and may even have been the cause of the break-up in the numerical solutions. The growth of this singular behaviour — becoming significant indeed by around $\theta = 4$ in the bend-maintained case — could cause adverse effects for industry. No singular response of $\hat{\rho}$ was detected near the corners in line with the predictions of §4.4.2.

We observe finally here that the current numerical scheme functions well over a wide range of parameter values and initial conditions.

5.3 The NLCI case

5.3.1 The governing equations of NLCI

Following on from the opening comments of this chapter on page 104 we will now formulate the fully non-linear compressible inviscid (NLCI) case.

We observed on page 85 that the governing equations of the CV case reduce to those of the NLCI case when $Re \gg a^{\frac{1}{2}}$. We recall the relevant streamwise length scale of this case in Figure 5.18. Although the momentum and continuity equations are the same, neglecting viscous effects changes the form of the

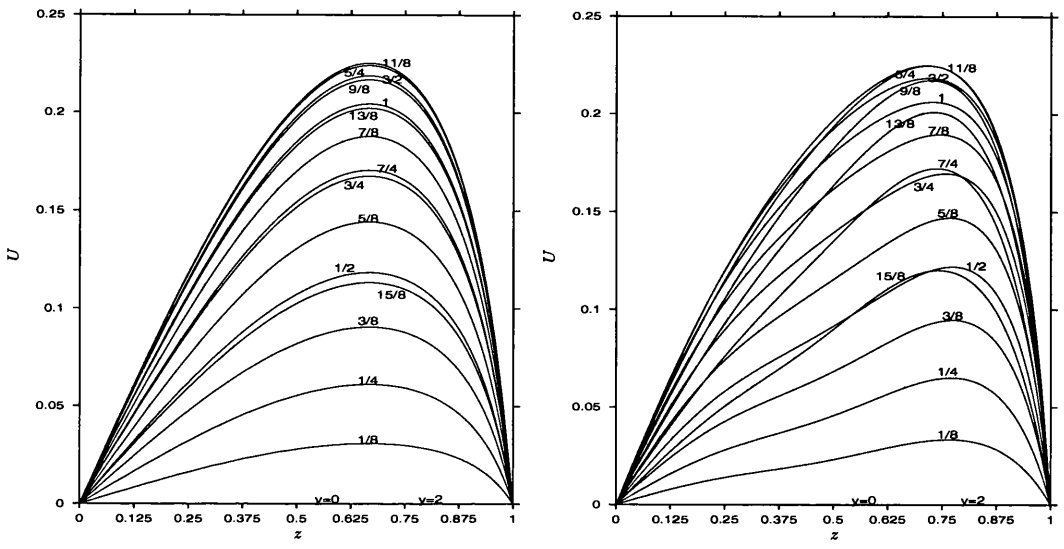

Figure 5.17: U-profiles at $\theta = 0$ (left hand side) and $\theta = 1$. The initial conditions are (2.40a–c).

energy and state equations. Let us then first write the NLCI continuity and momentum equations, which from (4.21a–d) are:

$$(\bar{\rho}\bar{U})_\theta + (\bar{\rho}V)_y + (\bar{\rho}W)_z = 0 \; ; \tag{5.12a}$$

$$\bar{\rho}(\bar{U}\bar{U}_\theta + V\bar{U}_y + W\bar{U}_z) = -p_0'(\theta) \; ; \tag{5.12b}$$

$$\bar{\rho}(\bar{U}V_\theta + VV_y + WV_z) = -p_{2y} \; ; \tag{5.12c}$$

$$\bar{\rho}(\bar{U}W_\theta + VW_y + WW_z - \Lambda\bar{U}^2\alpha\theta_1^2) = -p_{2z} \; . \tag{5.12d}$$

In §4.3.2 we did not introduce Λ into equation (5.12d) since we could not do so through a formal substitution. However, a derivation of the governing equations in the straight section (where $\Lambda = 0$ and $x = r\theta$) from first principles yields equations (5.12a–d) but without the final term on the left hand side of equation (5.12d). Consequently, we can include the parameter Λ in the governing equations and thus the equations will hold in both the straight and the curved sections of the duct. We recall that the expansions of the velocities,

pressure, and density are:

$$(u, v, w) = (\bar{U}, 0, 0) + \epsilon(\tilde{U}, \tilde{V}, \tilde{W}) + \dots \ ; \tag{5.13a}$$

$$p = p_0 + \epsilon p_1 + \epsilon p_2 + \dots \ ; \tag{5.13b}$$

$$\rho = \bar{\rho} + \epsilon\tilde{\rho} + \dots \ , \tag{5.13c}$$

where we have normalised the equations (5.12a–d). We emphasise that no factors of Λ appear in the expansions. Furthermore, leading order balances of the y- and z-momentum equations have led to the conclusion that

$$p_0 = p_0(\theta) \tag{5.14}$$

only. Similarly, we can show that p_1 is a constant which can be taken to be zero without loss of generality. Finally, we recall that we considered a new balance of swirl (measured by ϵ) and curvature (measured by the non-dimensional aspect ratio a of the bend), such that the parameter $\alpha = a\epsilon^2$ appearing in equation (5.12d) is of $\mathcal{O}(1)$. This new balance was chosen to ensure that some effects of the centrifuging experienced by the flow in the bend would appear to leading order in the equations. We noted on page 79 that this new swirl-curvature balance corresponded to a change in the level of swirl since throughout this thesis the geometry of the bend is fixed by the motivating physical set-up.

In the absence of viscosity we are able to use the polytropic equation of state (3.46), whose leading-order balance provides an equation coupling p_0 and $\bar{\rho}$:

$$p_0 = K\bar{\rho}^{\gamma} \ , \tag{5.15}$$

where K in general varies from streamline to streamline in steady flows but is uniform to leading order here due to assumptions of upstream homogeneity. Then equation (5.15) shows that

$$\bar{\rho} = \bar{\rho}(\theta) \ , \tag{5.16}$$

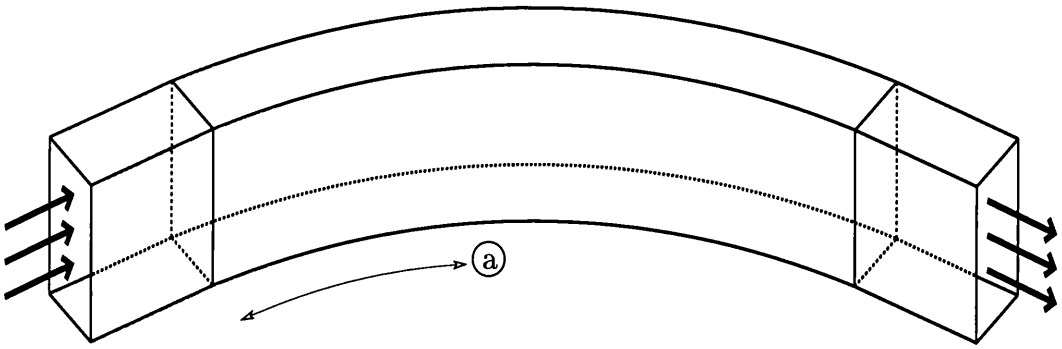

Figure 5.18: When $Re \gg a^{\frac{1}{2}}$ the core flow remains largely inviscid over the length scale ⓐ indicated, in which $\theta = \mathcal{O}(a^{-\frac{1}{2}})$. Far downstream the core viscous effects described by the equations of §4.3 might be seen.

which simplifies (5.12a). We note in passing that the same relation (5.15) can be derived by considering conservation of $\frac{p}{\rho^\gamma}$ following a particle.

The pressure term p_2 will be eliminated in the usual way by cross-differentiating equations (5.12c) and (5.12d) and introducing the vorticity R, and we will assume that p_0 is known from a conservation of mass flux in a manner to be described in the subsequent section. However, the normalised equations (5.12a–d,5.15) in their current form seem to exhibit a doubly-infinite range of initial values for the pair $(p_0, \bar{\rho})$. This problem suggests re-examining the normalising factors in light of the new balances available from the polytropic equation. A standard approach yields the normalisations:

$$\tilde{\theta} = \theta_1 \theta \ ; \tag{5.17a}$$

$$[\tilde{U}, \tilde{V}, \tilde{W}] = \left[U, \frac{V}{\alpha\theta_1}, \frac{W}{\alpha\theta_1}\right] \ ; \tag{5.17b}$$

$$[\bar{\rho}, \bar{p}_0, \bar{p}_2] = \left[\rho_n \rho, \pi_0 p_0, \frac{\pi_0}{\alpha^2 \theta_1^2} p_2\right] \ . \tag{5.17c}$$

The normalising factors ρ_n and π_0 are to be determined and we have the

relation

$$\rho_n = \pi_0 \tag{5.18}$$

from (5.12b) un-normalised. By choosing to normalise $\bar{\rho}$ and $\bar{p}_0$ on their initial values at the entrance to the bend we can reduce the doubly infinite range of (ρ, p_0) to a single computational case where the initial conditions on ρ and p_0 are that they are both unity at $\theta = 0$. More formally, we set

$$\rho_n = \bar{\rho}(0) \qquad \text{and} \qquad \pi_0 = \bar{p}_0(0), \tag{5.19}$$

which together with (5.18) yields the conclusions:

- $p_0(0) = 1 = \rho(0)$ as mentioned above, and
- $\bar{p}_0(0) = \bar{\rho}(0)$.

Substituting the normalising factors into the un-normalised equivalent of equation (5.15) gives

$$\frac{p_0}{\rho^\gamma} = K(\bar{\rho}(0))^{\gamma-1} \ . \tag{5.20}$$

Since this is true for all values of θ it is true at $\theta = 0$, which implies that $K(\bar{\rho}(0))^{\gamma-1} = 1$ and thus

$$p_0 = \rho^\gamma \ . \tag{5.21}$$

In summary, by normalising $\bar{\rho}$ and $\bar{p}_0$ on their initial values we have only one case to consider numerically where ρ and p_0 are coupled by equation (5.21) and are both unity at $\theta = 0$. We conclude this section by noting that the normalising factors and the non-dimensionalising factors for ρ and p_0 suggest that at the start of the bend the dimensional variables take the form:

$$\rho_D(0) = \rho_{D\infty}\bar{\rho}(0) \ ; \tag{5.22a}$$

$$p_D(0) = \rho_{D\infty}U_{D\infty}^2\bar{\rho}(0) = \rho_D(0)U_{D\infty}^2 \ . \tag{5.22b}$$

We present these relations to emphasise that under experimental conditions generality of the initial density and pressure is preserved.

5.3.2 The numerical strategy for NLCI

The NLCI case retains the parabolic nature of the previous cases, enabling us once again to march forward in θ. The equations in each plane θ = constant also retain their elliptic nature, requiring an implicit/iterative approach as previously employed in the II and CI cases and described in §5.1. The numerical scheme we will now describe is a fourth-order accurate compact differencing scheme as outlined in general in §5.1 but with some novel solution methods necessitated by several features of the NLCI governing equations. However, we note at the outset that a complete numerical solution of the coupled three-dimensional Euler equations is a difficult problem requiring other special computationally intensive techniques.

Firstly — as in all the previous numerical work in §§2.3, 5.1, and 5.2 — we eliminate p_2 and introduce the vorticity $R = W_y - V_z$ by cross-differentiating the y- and z-momentum equations. This converts the governing equations to:

$$(\rho U)_\theta + \rho(V_y + W_z) = 0 \; ; \tag{5.23a}$$

$$UU_\theta + VU_y + WU_z = -\frac{p_0'(\theta)}{\rho} \; ; \tag{5.23b}$$

$$UR_\theta + VR_y + WR_z = -R(V_y + W_z) + U_z V_\theta - U_y W_\theta + 2\Lambda U U_y \alpha \theta_1^2 \; ; \tag{5.23c}$$

$$\rho = p_0^{\frac{1}{\gamma}} \; . \tag{5.23d}$$

However, we cannot introduce a two-dimensional stream-function ψ as we did in the II and CI cases since this would not be consistent with the continuity equation (5.23a). Furthermore, in the II and CI cases we were able to show

that $p_0' = 0$ for all θ by a higher-order balance of the continuity equation combined with an integration of the θ-momentum equation. In the NLCI case each higher-order balance of the continuity equation (and other equations) is coupled non-linearly to the other balances in such a way that no simplifying result is forthcoming. Consequently another means of determining p_0 is used. The method within each iteration involves using the integrated continuity equation to optimise p_0 as it responds to the mass flux through the duct. In more detail, the strategy used at each θ-station is outlined as follows.

- The latest iterative value of $p_0(\theta)$ (on the first iteration at each θ-station, this is the value from the previous θ-station) is used as the initial estimate for p_0 at the current station.

- This value is substituted into equation (5.23d) to determine ρ at this station.

- Having determined p_0 and ρ we can solve equation (5.23b) for U using an implicit/iterative approach as described in §5.1, and employing streamwise lagging of U.

- A double integral in the cross-section of the continuity equation (5.23a) yields the result

$$\iint \rho U \; dydz = \text{constant} \; . \tag{5.24}$$

The current values of ρ and U are substituted into a Simpson's Rule integrating routine, and this latest-known value of the double integral at this θ-station is compared with the calculated value at $\theta = 0$. After two values of p_0 have been tried (the second value being the first value plus a small constant) an optimised value is determined via a Newton-Raphson

formula. The tolerance level for the test is:

$$\left| \iint \rho U \; dydz - \iint \rho_I U_I \; dydz \right| < 10^{-13} \; . \tag{5.25}$$

- A value of $p_0(\theta)$ which leads to the test being satisfied at the current iterative level implies that equations (5.23d & 5.23b) are satisfied to $\mathcal{O}(10^{-13})$.

- The vorticity equation (5.23c) is now solved for R.

- We then solve two Poisson equations: one for V and one for W as follows. Using the definition of R we write:

$$V_{yy} + V_{zz} = (V_y)_y + W_{yz} - R_z \; . \tag{5.26}$$

This equation requires knowledge of V_y which in the compact-differencing approach is treated as a dependent variable, but otherwise this equation is solved by the Poisson-solver used in §5.1. However, in §5.1 where we solved a Poisson equation for ψ with a known right hand side we had the boundary condition $\psi \equiv 0$ on the walls. In the present case we only know the latest-known values of R and that there is no normal flow at the walls. We combine these facts, the definition of R, and six-point one-sided polynomial discretisations of the derivatives to generate information at the walls. The implicit/iterative scheme for this Poisson equation is swept in the j-direction with the information we have just generated feeding in as the boundary conditions in the tridiagonal system. Sweeping in the k-direction such that the tridiagonal problem at each k involves 0 as the first and last elements in the array of values on the right hand side (since we know V is zero on $j = 0$ and $j = jj$) leads to greater numerical instability.

- The Poisson equation for W,

$$W_{yy} + W_{zz} = (W_z)_z + V_{yz} + R_y \ , \tag{5.27}$$

is solved in a similar fashion, with the implicit/iterative scheme swept in the k-direction.

- Having solved for the variables in equations (5.23a–d) we test the convergence error on R (since p_0, ρ, and U have already been optimised to $\mathcal{O}(10^{-13})$) to an accuracy of 10^{-8} and iterate until convergence is reached.

5.4 Results and discussion for NLCI

The parameters α and θ_1 are important to the flow development since they appear explicitly in equation (5.23c). The computations in this section were performed with

$$\alpha = 1 \quad , \quad \theta_1 = \frac{\pi}{2} \tag{5.28}$$

for consistency with the discussion in Chapter 1, where we explained that the typical angle the duct turns through is $\frac{\pi}{2}$, and that in Chapters 2 and 4 where we mentioned that α is of $\mathcal{O}(1)$. Varying α and/or θ_1 is analagous to varying the initial balance of the inertial forces as discussed for the II case on page 54, or to varying Υ in the CI case as discussed in §§4.4.4 and 4.4.5. Similar general conclusions hold here. As with the II and CI cases in §§2.3 and 5.2, respectively, we take a duct with a 2×1 rectangular cross-section.

The numerical scheme was sensitive to the initial conditions, and we found that the numerics reached their greatest extent downstream when the variation on U was relatively small. Thus we chose the initial condition:

$$U_I = 1 + 0.0025 \left(\frac{y^3}{3} - y^2 + yz^2 - yz \right) \ . \tag{5.29}$$

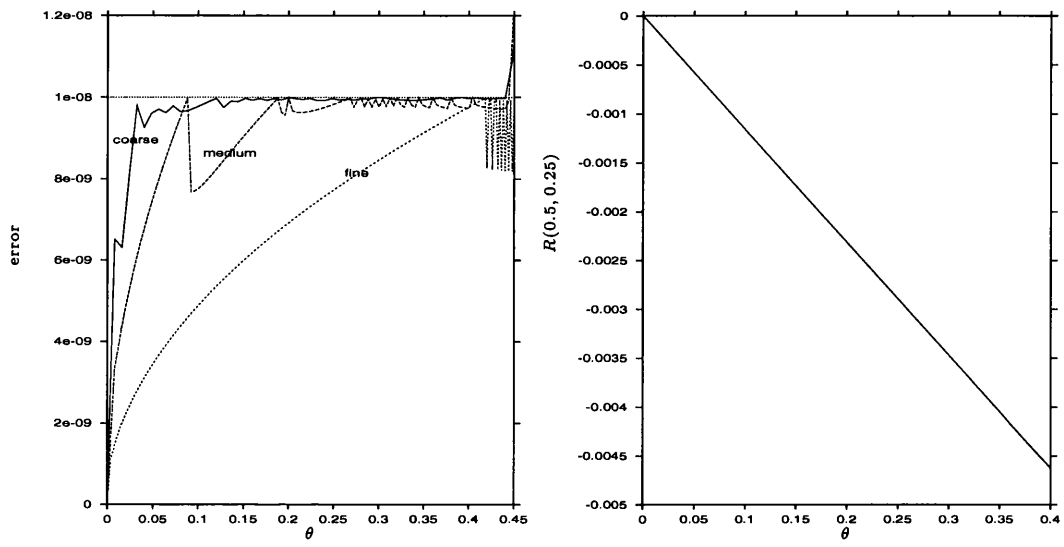

Figure 5.19: Left hand side: error (measured on R) over three grids. Right hand side: $R(0.5, 0.25)$ over three grids. The initial conditions were (5.29, 5.30).

The initial conditions on p_0 and ρ are that they are both unity as discussed in §5.3. With these initial conditions the computational scheme works over a wide range of parameter values: we will show how the magnitude of Λ affects the solutions, and also study both zero and non-zero initial swirl. Analytical work will also be presented which compares very well with the numerical results. With the above decision to fix α and θ_1 in mind, the principal parameter here is Λ, and we will present the results and discussions in sections concerning different values of Λ, beginning with the flow in the bend when $\Lambda = 1$.

5.4.1 Numerical results and discussion for $\Lambda = 1$

Zero initial swirl

In this case we take

$$V_I \equiv 0 \equiv W_I \tag{5.30}$$

in addition to (5.29). Computations were performed over three grids, defined as follows: the *coarse* grid had $(\Delta\theta, \Delta y, \Delta z) = (\frac{1}{125}, \frac{1}{16}, \frac{1}{32})$; the *medium* grid had $(\Delta\theta, \Delta y, \Delta z) = (\frac{1}{250}, \frac{1}{32}, \frac{1}{64})$; and the *fine* grid had $(\Delta\theta, \Delta y, \Delta z) = (\frac{1}{500}, \frac{1}{48}, \frac{1}{96})$. In each case the error terms measuring the rate of convergence between successive iterations grew to be larger than the prescribed level of accuracy (10^{-8}) beyond $\theta = 0.4$ as shown in the graph on the left hand side of Figure 5.19. We note that although the fine grid computation showed convergence beyond $\theta = 0.5$ we are unable to show that results between $\theta = 0.4$ and $\theta = 0.5$ are sufficiently grid-independent and consequently we will only present results up to $\theta = 0.4$. The graph on the right hand side of Figure 5.19 shows how closely the values of R at a point in the cross-section agree over the three grids. We observe that although $\mathcal{O}(1)$ values of θ are reached by the NLCI numerics the scheme is not sufficiently accurate to run for the entire length of the bend from $\theta = 0$ to $\theta = 1$. Nevertheless, the results obtained are interesting and useful, as we shall see. We will discuss the limitations of the numerics in §5.4.8. Similar comparisons over three grids were also made in each of the subsequent sections of this chapter. In each case the numerical results were accurate to at least $\theta = 0.4$ and only the finest grid results will be presented.

We observe from the graph on the right hand side of Figure 5.19 that in the NLCI case as in the II and CI cases we see linear growth of the vorticity R in the bend. With the scaling $\tilde{\theta} = \epsilon\theta$ — where on page 80 we mentioned that $\epsilon \approx (2\sqrt{2})^{-1}$ — we deduce that the real growth rate is of $\mathcal{O}(10^{-2})$ from the graph, and in the CI case it was also of $\mathcal{O}(10^{-2})$ from Figure 5.11.

The numerical solutions for U are plotted in Figure 5.20. There is almost no mixing effect of the swirl apparent at this level, which we attribute to the extremely weak swirl which we will shortly plot. Correspondingly weak

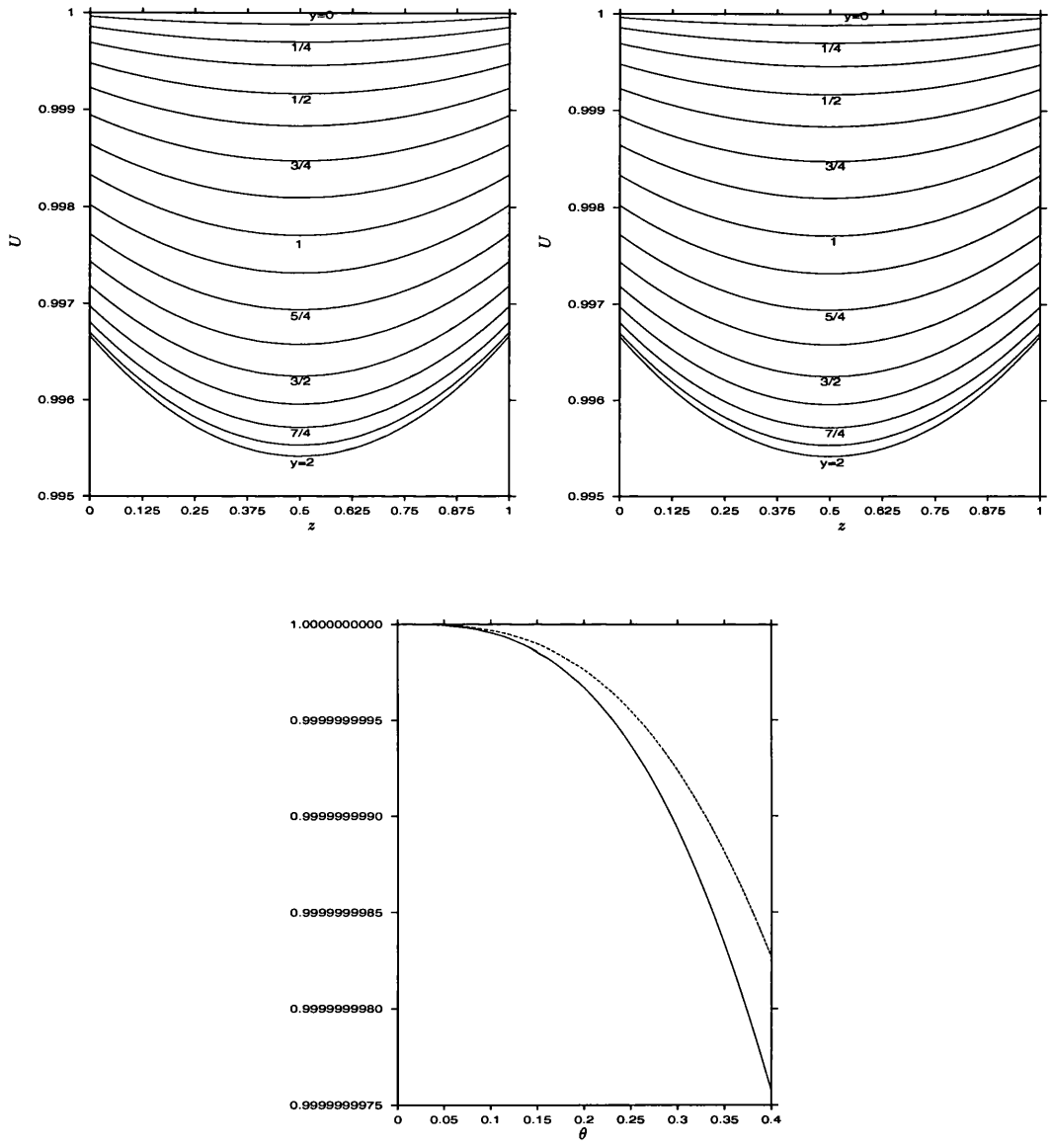

Figure 5.20: Top: U at $\theta = 0$ (left hand side) and $\theta = 0.4$ (right hand side), plotted on lines of constant y. Bottom: p_0 (solid line) and ρ against θ. The initial conditions were (5.29, 5.30).

evolution of the pressure term p_0 and the density ρ can also be seen in Figure 5.20. However, both p_0 and ρ appear to be exhibiting at least linear growth by $\theta = 0.4$.

The form of the evolution of V, W, and R from their zero initial values is interesting. The basic shape of the profile is established early, with the subsequent development being essentially one of magnitude. We also note that the results shown in Figure 5.21 are more symmetrical in the z-direction than their analogues in the CI and II cases shown in Figures 5.3 and 2.5, respectively, but perhaps less symmetrical in the y-direction. Furthermore, the profiles in Figure 5.21 are more greatly distorted than the CI and II analogues, especially near the inner and outer walls $z = 0$ and $z = 1$. Put another way, the form of the profiles in Figure 5.21 more closely resemble the form of the profiles in the CI case in the central region of the duct, and this could be because the magnitude of U is smallest there — for a given y — which brings the NLCI case closer to the CI case.

One simple analytical solution in the current parameter regime with $\Lambda = 1$ and zero initial swirl is found by assuming that the initial U-profile is an arbitrary funtion, $U_I(z)$. Then a solution of the governing equations (5.23a–d) is:

$$U \equiv U_I(z) \text{ for all } \theta \quad ; \quad p_0 \equiv 1 \equiv \rho \text{ for all } \theta \quad ; \quad R \equiv R_I \equiv 0 \text{ for all } \theta \,. \tag{5.31}$$

We note that when V_I or W_I is not zero the above prediction that $R \equiv R_I$ for all θ is not valid. Running the numerical scheme with

$$U_I = 1.05 - 0.1(z-1)^2 \tag{5.32}$$

and zero initial swirl indeed reveals no evolution of any quantities. The numerics in this case can continue indefinitely, so we have here decided simply

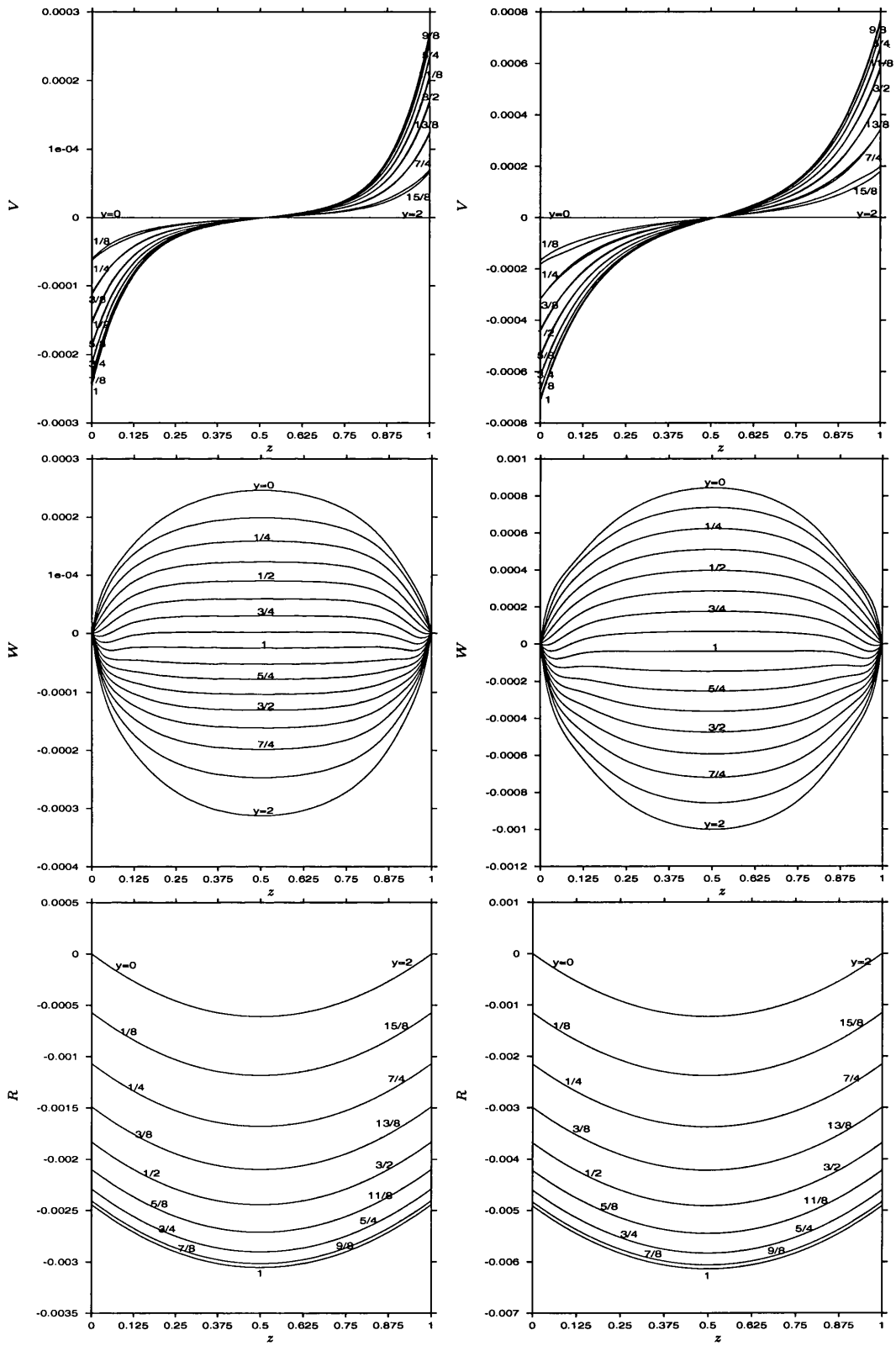

Figure 5.21: V, W, and R at $\theta = 0.2$ (left hand side) and $\theta = 0.4$ (right hand side), plotted on lines of constant y. The initial conditions were (5.29, 5.30).

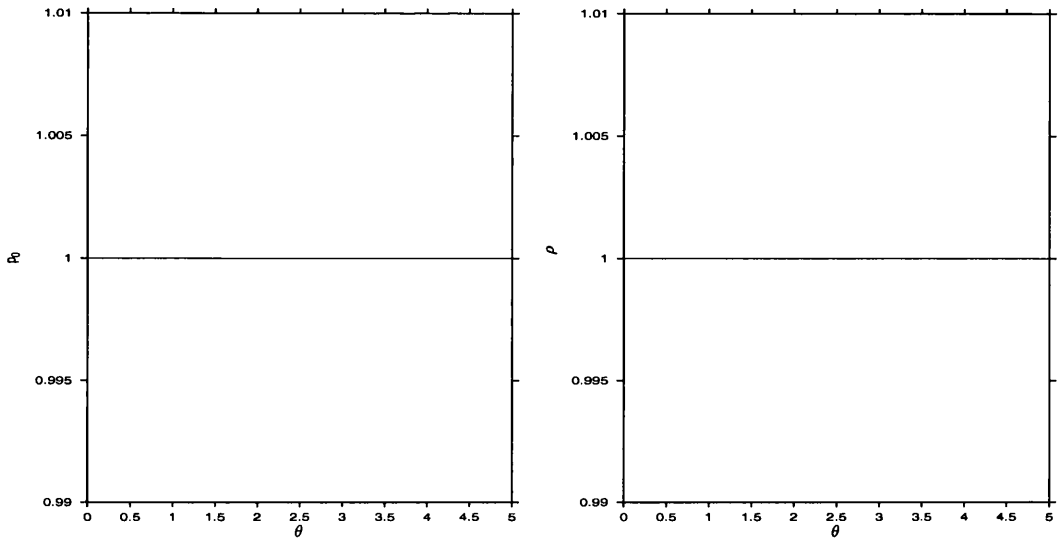

Figure 5.22: p_0 (left hand side) and ρ against θ. The initial conditions were (5.32, 5.30).

to show in Figure 5.22 that ρ and p_0 do not evolve between $\theta = 0$ and $\theta = 1$.

Non-zero initial swirl

In this parameter regime, we take U_I as defined by (5.29) and V_I,W_I, and R_I as:

$$V_I = -2\bar{a}sin\left(\frac{\pi y}{2}\right)cos(\pi z)\ ; \tag{5.33a}$$

$$W_I = \bar{a}cos\left(\frac{\pi y}{2}\right)sin(\pi z)\ ; \tag{5.33b}$$

$$R_I = -\frac{5\pi}{2}\bar{a}sin\left(\frac{\pi y}{2}\right)sin(\pi z)\ , \tag{5.33c}$$

where $\bar{a} = 0.0001$. We note that the numerics do not work satisfactorily for $\bar{a} > 0.0001$ and this was also true in subsequent sections of this thesis where we vary the size of Λ. Smaller values of $\bar{a}$ were also considered with the largest possible value taken to study the most interesting case. However, with the relatively weak level of swirl defined in (5.33a–c) the numerical scheme

performed at least as well in terms of the maximum downstream distance attainable as the zero initial swirl case. Three different computational grids were compared to establish grid convergence and the results we present are for the finest grid, defined as $(\Delta\theta, \Delta y, \Delta z) = (\frac{1}{250}, \frac{1}{32}, \frac{1}{64})$. We note that the V_I and W_I defined in equations (5.33a) and (5.33b) were chosen such that

$$V_{Iy} + W_{Iz} = 0 \ , \tag{5.34}$$

which from equation (5.23a) imposes:

$$(\rho U)_\theta\big|_{\theta=0} = 0 \ . \tag{5.35}$$

This result implies that particles are simply being swirled around in the straight section immediately prior to the onset of the bend.

Figure 5.23 shows the evolution of U between $\theta = 0$ and $\theta = 0.4$. As in the zero initial swirl case above U shows very little effects of the mixing induced by R since R remains weak throughout. However, the evolution of ρ and p_0 is stronger than was the case with zero initial swirl as we can see by comparing the relevant graphs in Figures 5.23 and 5.20.

The evolution of V and W as shown in Figure 5.24 seems strongest towards the inner and outer walls $z = 0$ and $z = 1$. In greater detail, we first recall that the particles on the inner and outer walls are constrained to stay on those walls since there is no normal flow. However, at small distances from the inner and outer walls the normal flow W is growing rapidly in magnitude. This could perhaps be hinting at the appearance of edge layers on these walls across which W develops rapidly. The parallel flow V is also growing strongly close to the inner and outer walls implying that the strength of the swirl is large there. The flow parallel to the bottom and top of the duct, measured by W there, is correspondingly large. Overall, the solutions hint at relatively rapid rotation

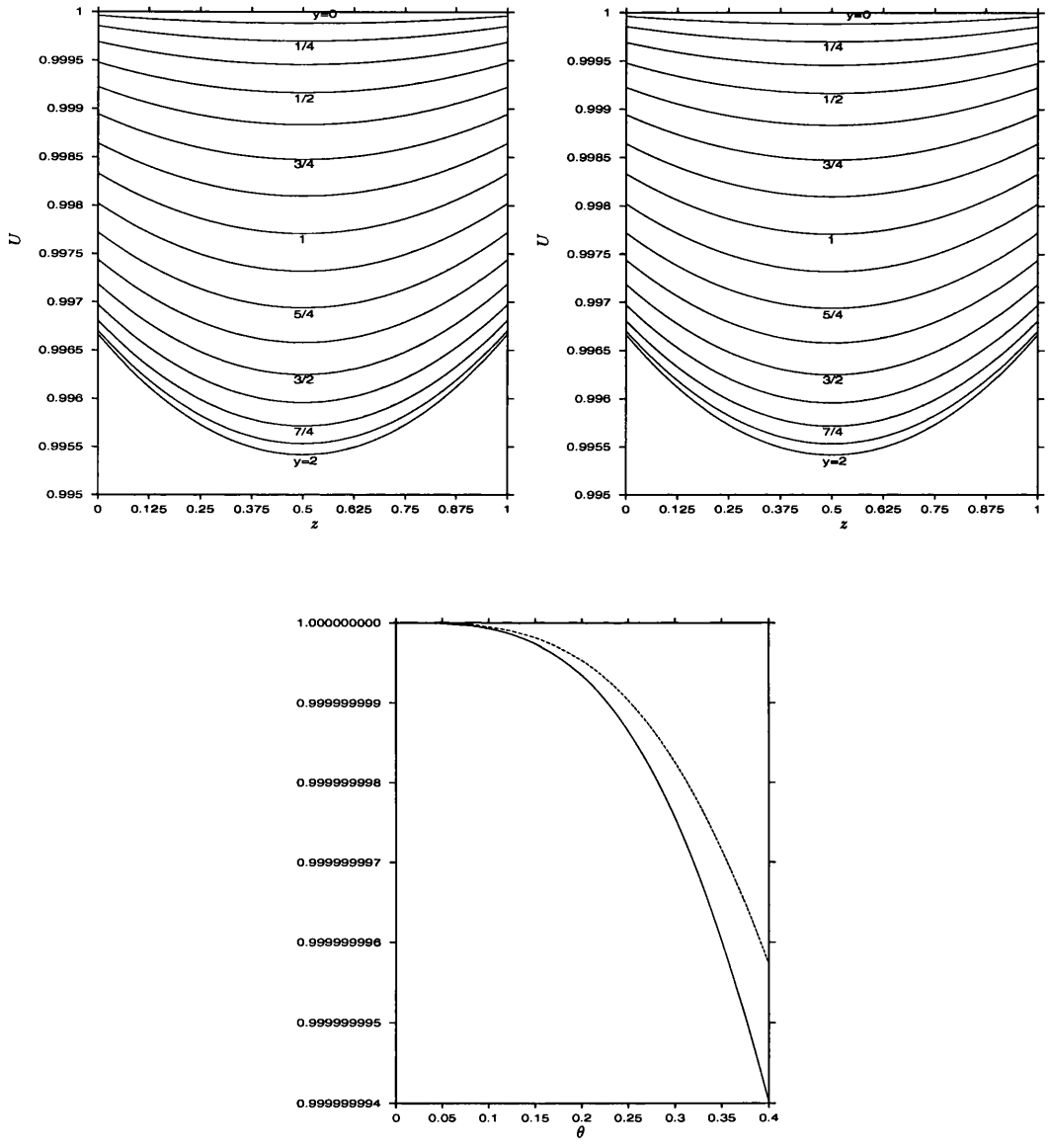

Figure 5.23: Top: U at $\theta = 0$ (left hand side) and $\theta = 0.4$ (right hand side), plotted on lines of constant y. Bottom: p_0 (solid line) and ρ against θ. The initial conditions were (5.29, 5.33a–c).

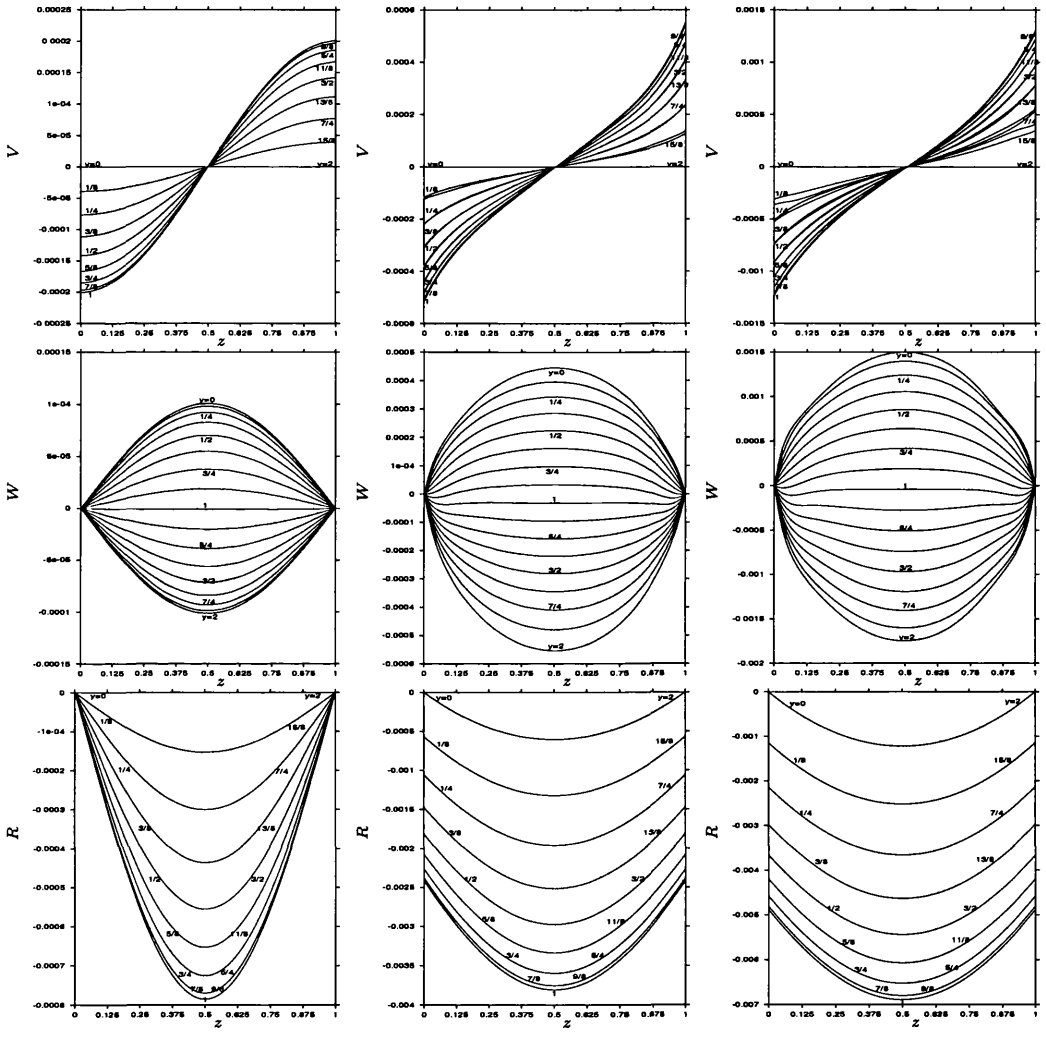

Figure 5.24: V, W, and R at $\theta = 0$ (left hand side), $\theta = 0.2$ (centre) and $\theta = 0.4$ (right hand side), plotted on lines of constant y. The initial conditions were (5.29, 5.33a–c).

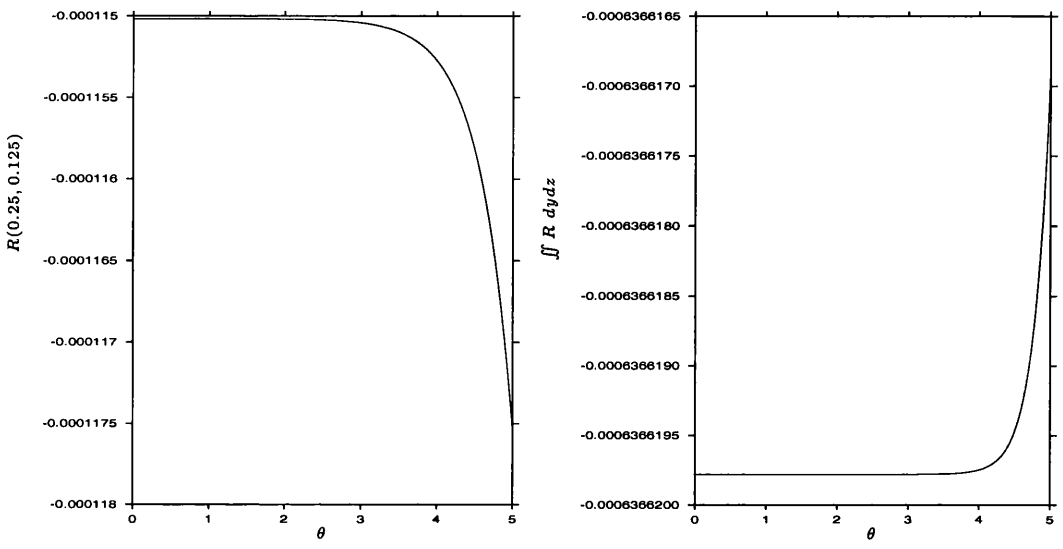

Figure 5.25: Left hand side: $R(0.25, 0.125)$ against θ. Right hand side: $\iint R\ dydz$ against θ. The initial conditions were $U_I \equiv 1$ and (5.33a–c).

of the fluid close to the walls combined with a comparitively slowly rotating central region.

One simple analytical solution is given by

$$U \equiv 1 \text{ for all } \theta \quad ; \quad p_0 \equiv 1 \equiv \rho \text{ for all } \theta \quad . \tag{5.36}$$

Under these conditions (5.23c) reduces to

$$R_\theta + VR_y + WR_z = 0 \ , \tag{5.37}$$

since the continuity equation (5.23a) reduces to

$$V_y + W_z = 0 \ . \tag{5.38}$$

Equation (5.37) suggests that R is conserved along streamlines. The prediction at any fixed point in the cross-section would thus be that the value of R at such a point changes only very slowly as the weak swirl brings different particles onto that point. We note that if V_I and W_I were zero then R would remain

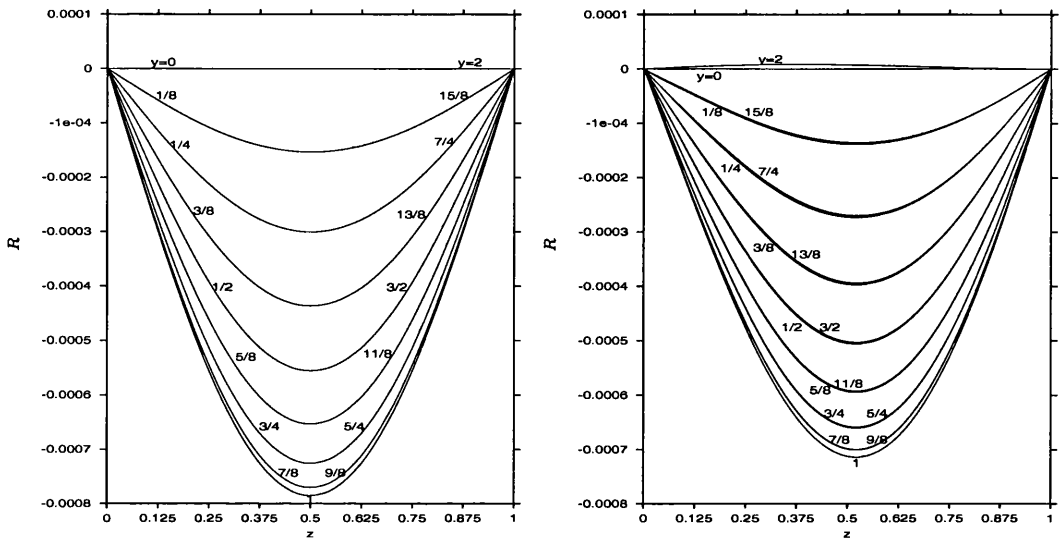

Figure 5.26: Left hand side: R at $\theta = 0$. Right hand side: R at $\theta = 1.4$. The initial conditions were (5.32,5.33a–c).

zero. Furthermore, by integrating (5.37) over the plane of a cross-section and with the usual application of Green's theorem we predict that

$$\iint R \, dydz = \text{constant for all } \theta \, . \tag{5.39}$$

Running the numerics under these conditions the analytical predictions (including no evolution of U, p_0, and ρ from (5.36)) are upheld, as we see in Figure 5.25. Specifically, the left hand side of Figure 5.25 shows R visibly evolving only after a downstream distance sufficient for the swirl to have advected particles with different values of R onto those points, whilst the right hand side shows $\iint R \, dydz$ remaining constant to within the prescribed level of accuracy as predicted. We note that the numerics are able to run reliably to $\theta = 5$ under these conditions.

Finally, we recall that on page 138 we predicted that if the initial swirl is non-zero then R would evolve in the case that $U_I = U_I(z)$ only, whilst U, p_0, and ρ would be conserved. The numerical results, which run as far as $\theta = 1.4$

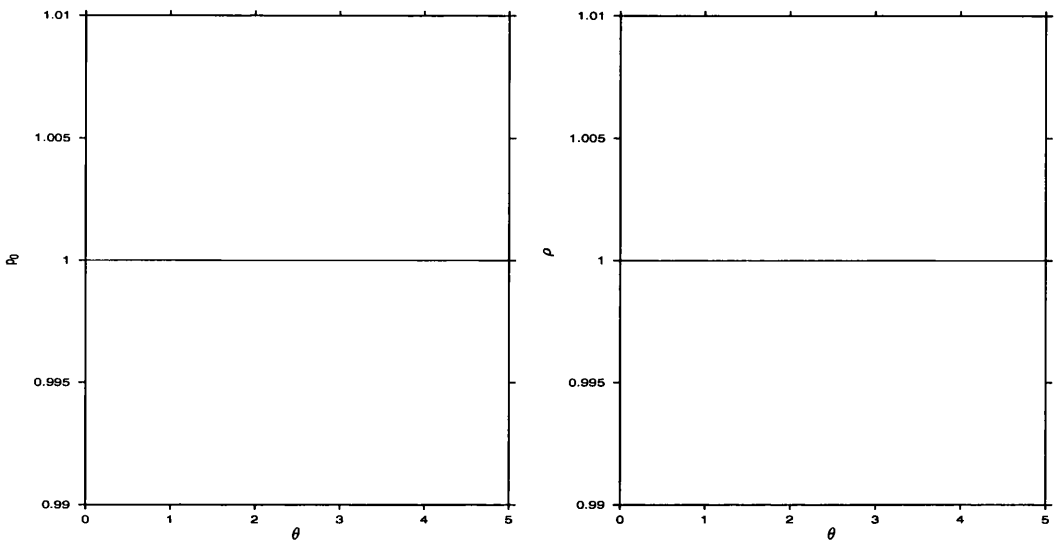

Figure 5.27: p_0 (left hand side) and ρ against θ. The initial conditions were (5.32, 5.30).

downstream, are shown in Figure 5.26 and confirm this prediction.

5.4.2 Numerical results and discussion for $\Lambda = 0$

Zero initial swirl

The prediction for this case from equations (5.23a–d) is that — regardless of the form of U_I — there will be no evolution of any of the flow variables in equations (5.23a–d) throughout the flow. This is because the driving terms in the vorticity equation (5.23c) are zero at $\theta = 0$ and remain so. The numerics run as far as desired with no evolution in any variables as predicted. For example, in Figure 5.27 we see p_0 and ρ remaining constant at their initial values of unity between $\theta = 0$ and $\theta = 5$. The general conclusion is that if the flow enters a straight section with zero initial swirl and any p_0 and ρ of $\mathcal{O}(1)$ then no evolution of the principal variables occurs.

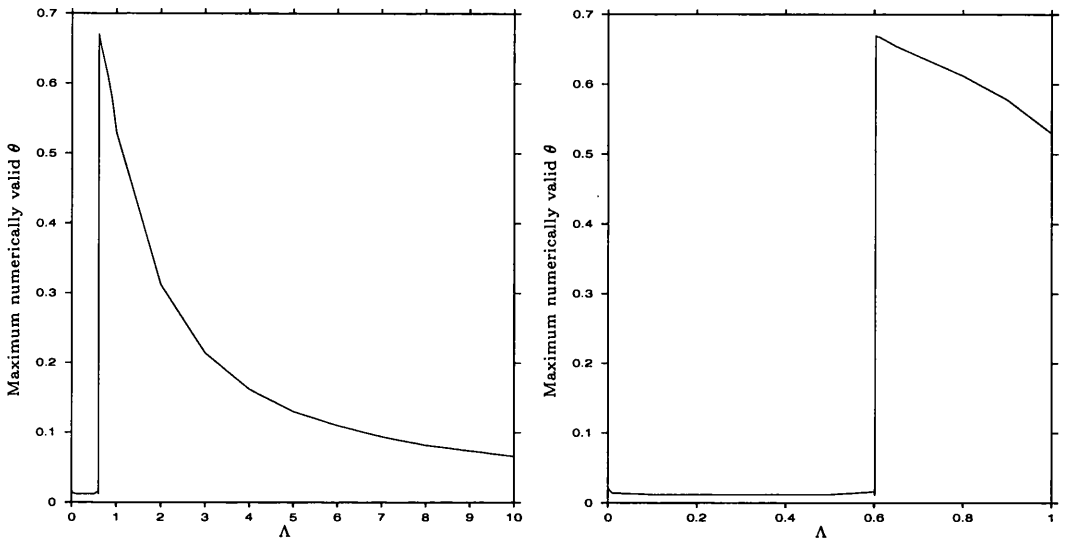

Figure 5.28: The effects of the value of Λ on the maximum numerically valid θ. The initial conditions were (5.29, 5.30).

Non-zero initial swirl

For a range of non-zero initial swirl conditions the numerical solutions ceased to be physical — by which we mean that $\iint \rho U \, dydz > 10^{-13}$ — by θ of $\mathcal{O}(10^{-1})$. It seems as if the numerical scheme is unable to work under conditions of zero Λ when evolution occurs, and a discussion of this problem is contained in §5.4.3. Equations (5.23a–d) suggest that in this case evolution would in general occur, although we are unable to offer any numerical evidence for this.

5.4.3 Discussion of the numerical limitations imposed by the size of Λ

The numerical difficulties encountered in the non-zero initial swirl case of §5.4.2 suggest examining the stability of the numerical scheme for various values of Λ. We use the phrase "maximum numerically valid θ" to indicate either the last θ for which the error is smaller than 10^{-8} (indicating that beyond this θ

the results will no longer converge) or the last θ for which $\iint \rho U \, dydz < 10^{-13}$ (indicating that beyond this θ the results will no longer be deemed physically valid), whichever of the two is the smaller.

Figure 5.28 shows that the numerical scheme depends very strongly on $\mathcal{O}(\Lambda)$. Specifically, it appears that the scheme works only for Λ of $\mathcal{O}(1)$ — say for $0.7 < \Lambda < 5$. Since the computational equations (5.23a–d) were derived with the assumption that Λ is of $\mathcal{O}(1)$ it is perhaps no surprise that the numerical scheme does not work outside of this restriction. However, we note that the CI numerical scheme was also derived with the assumption that Λ is of $\mathcal{O}(1)$, and the fact that the CI scheme worked for a range of Λ serves to emphasise once more the versatility of that numerical scheme. A similar numerical comparison of the effects of $\mathcal{O}(\Lambda)$ on the stability of the scheme with various non-zero initial swirls yields the same conclusions.

5.4.4 The NLII case

The fully non-linear incompressible inviscid (NLII) case is obtained by omitting the viscous terms from the IV case governing equations (4.18a–d) for the reasons discussed on page 82. This leads to the NLII governing equations:

$$U_\theta + V_y + W_z = 0 \; ; \tag{5.40a}$$

$$UU_\theta + VU_y + WU_z = -p_0'(\theta) \; ; \tag{5.40b}$$

$$UV_\theta + VV_y + WV_z = -p_{2y} \; ; \tag{5.40c}$$

$$UW_\theta + VW_y + WW_z - \Lambda U^2 \alpha \theta_1^2 = -p_{2z} \; . \tag{5.40d}$$

We note that we have introduced the centrifugal parameter Λ into (5.40d) as we did in (5.12d) for similar reasons to those given in the discussion following (5.12a–d). It is apparent that equations (5.40a–d) are simply the NLCI equa-

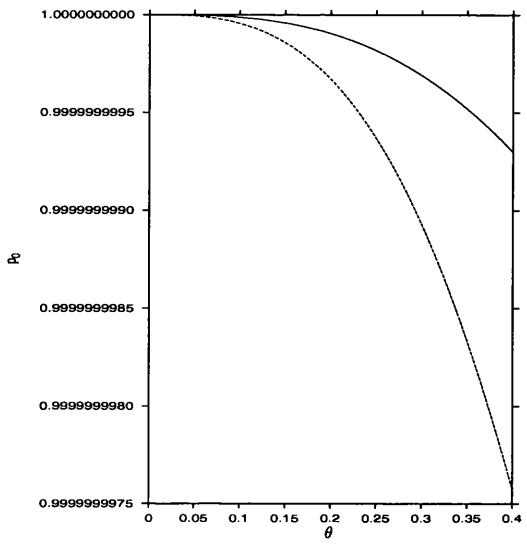

Figure 5.29: The NLII p_0 (solid) and the NLCI p_0 against θ. The initial conditions were (5.29, 5.30).

tions with $\rho \equiv 1$ for all θ. This observation provides a method of solution: simply set $\rho \equiv 1$ in the NLCI scheme. Having made the necessary change to the numerical scheme the computation was performed over three grids and virtual grid-indpendence was once again established to at least $\theta = 0.4$. We will show results from calculations with the fine grid $(\Delta\theta, \Delta y, \Delta z) = (\frac{1}{500}, \frac{1}{48}, \frac{1}{96})$.

For zero initial swirl Figure 5.29 shows the evolution in the NLII case of p_0 with θ and contrasts it with p_0 for the NLCI case. It is apparent that p_0 grows less strongly in the NLII case than in the NLCI case.

The graphs in Figure 5.30 show that at this level the NLII results are quantitatively very close to the NLCI results shown in Figure 5.21. We saw previously in §5.2 that the CI results were qualitatively similar to the II case. The quantitative differences between CI and II which are not so apparent between NLCI and NLII are perhaps attributable to the longer distances through which the weakly non-linear numerics are able to run.

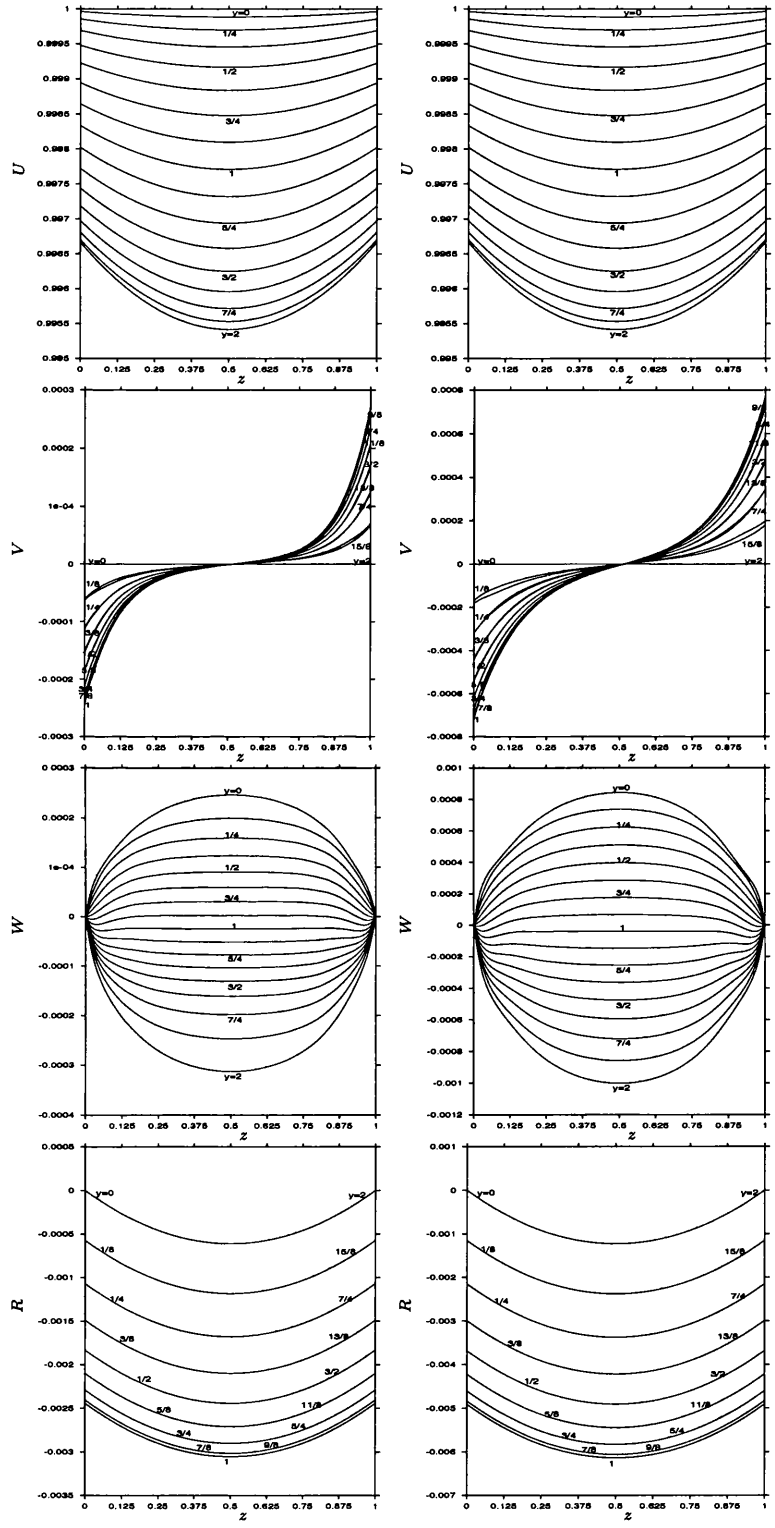

Figure 5.30: The NLII U, V, W, and R at $\theta = 0.2$ (left hand side) and $\theta = 0.4$ (right hand side). The initial conditions were (5.29, 5.30).

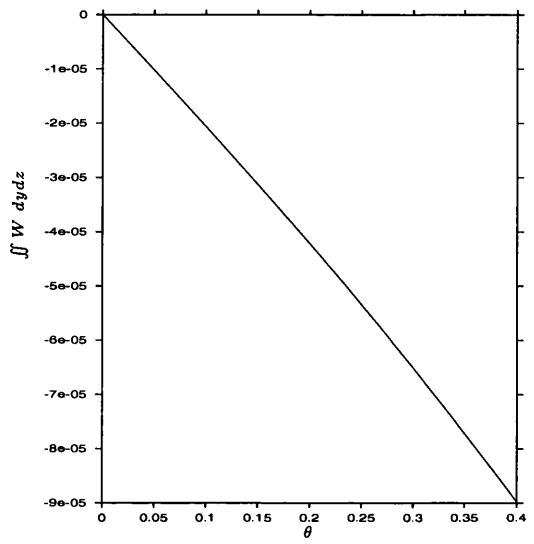

Figure 5.31: The NLII $\iint W\ dydz$ against θ. The initial conditions were (5.29, 5.30).

We observe once again that U has not evolved between $\theta = 0$ and $\theta = 0.4$ and that it has not visibly responded to the weak swirl. The swirl is growing linearly in the bend, however, and to illustrate this we show in Figure 5.31 that $\iint W\ dydz$ grows linearly with θ. Other important aspects of the solution are similar to those of the NLCI solution with which the NLII solution so closely corresponds.

5.4.5 A link between NLCI and CI

In another validation of the numerical scheme we now investigate whether the NLCI numerics are able to qualitatively recreate the CI results of §5.2. This should occur in the regime:

$$\theta \to \infty \quad ; \quad \Lambda \to 0 \quad ; \quad (U_I - 1) \to 0\ . \tag{5.41}$$

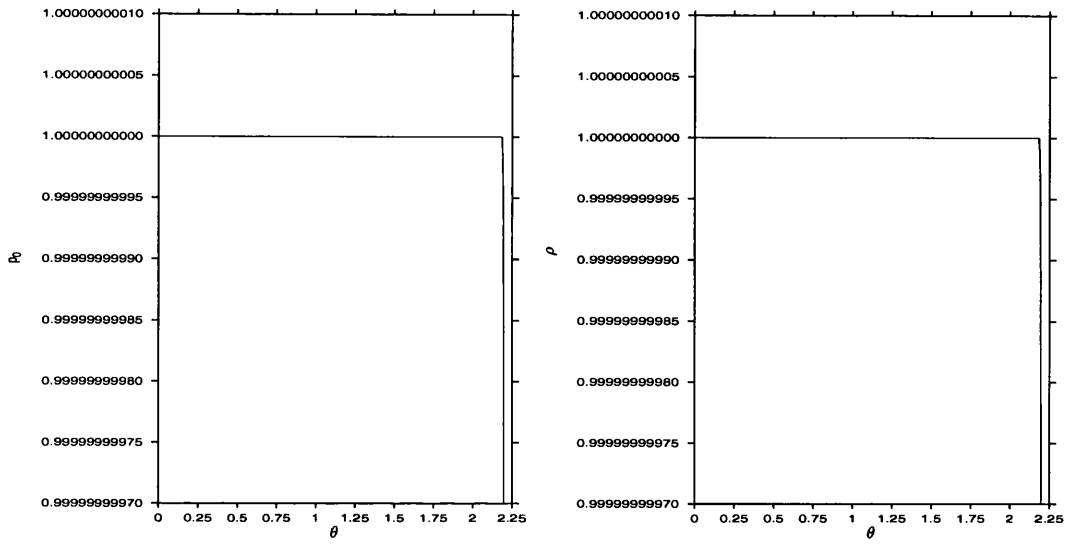

Figure 5.32: p_0 and ρ against θ for the initial conditions (5.42a, 5.30).

Consequently, we set:

$$U_I = 1 + (2.5 \times 10^{-6}) \left(\frac{y^3}{3} - y^2 + yz^2 - yz \right) \; ; \tag{5.42a}$$

$$\Lambda = 10^{-5} \; ; \tag{5.42b}$$

$$E = 10^{-13} \; , \tag{5.42c}$$

where E is the maximum allowable error (previously set at 10^{-8}). We will perform the computation over the fine grid defined in §5.4.1.

Figure 5.32 shows that in the regime (5.42a–c) the pressure term p_0 and the density term ρ both remain at unity until relatively large values of θ are reached. This agrees with the CI case where the leading order components of the pressure and density were fixed at unity and only the higher order components evolved. In Figure 5.33 we show that $\iint R \; dydz$ grows linearly with θ as was predicted (and confirmed numerically) in the CI case. We also note that the magnitude of R is consistent with the CI case given the change in length scale and size of ϵ.

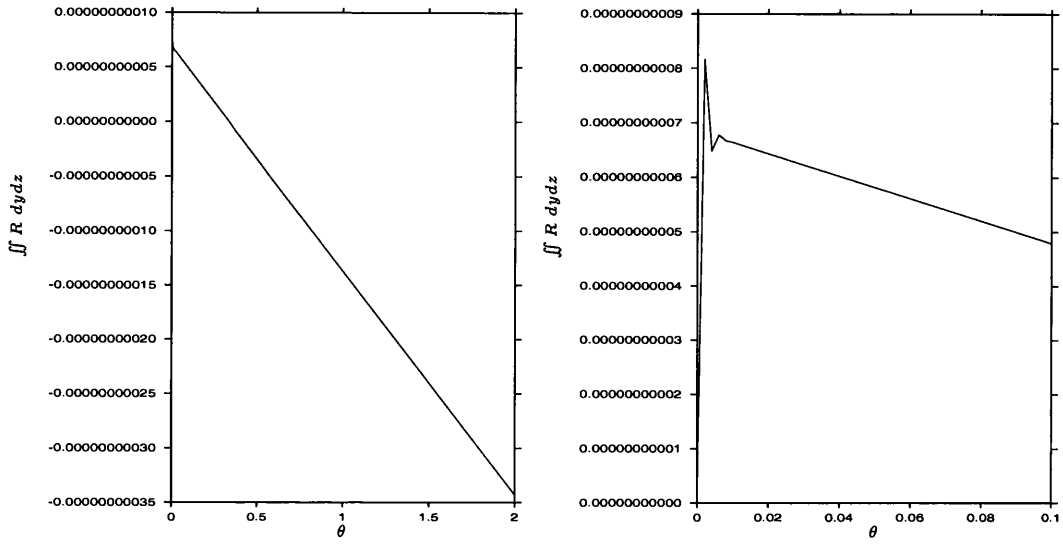

Figure 5.33: $\iint R\, dydz$ against θ for the initial conditions (5.42a, 5.30).

In an observation unrelated to a connection with the CI case we note that very close to the bend entry it appears that the total integrated vorticity over the plane of a cross-section is briefly positive before beoming negative downstream, perhaps hinting at strong initial asymmetry in the vorticity.

A final analytical correspondence between the CI and NLCI cases is to note that when $U_I \equiv 1$, then for general V_I, W_I and for any Λ:

$$U \equiv 1 \text{ for all } \theta \quad \text{and} \quad p_0 \equiv 1 \equiv \rho \text{ for all } \theta \; ; \tag{5.43}$$

$$R_\theta + VR_y + WR_z = 0 \; . \tag{5.44}$$

That is, the system reduces to the CI or II case with $\Lambda = 0$. In words, a fully non-linear description of compressible inviscid flow with a uniform entry U-profile, general entry swirl, and any Λ corresponds to a weakly non-linear description of either compressible or incompressible flow with uniform entry U-profile, general entry swirl and zero Λ. This fact serves to emphasise the importance of the initial non-uniformities of U in driving the evolution of the flow.

5.4.6 Further analytical support for the NLCI numerics

More confidence in the numerical solutions is implied by the following analytical work.

Small Λ, order unity θ

We first suppose that as Λ becomes small the response of the principal flow variables over $\mathcal{O}(1)$ values of θ will be correspondingly small. Thus when

$$\Lambda = \delta\tilde{\Lambda} \ , \ \text{where } \delta \ll 1 \ , \tag{5.45}$$

we assume:

$$U = U_0 + \delta U_1 + \dots \ ; \tag{5.46a}$$

$$R = R_0 + \delta R_1 + \dots \ ; \tag{5.46b}$$

$$\rho = \rho_0 + \delta\rho_1 + \dots \ ; \tag{5.46c}$$

$$p_0 = p_{00} + \delta p_{01} + \dots \ , \tag{5.46d}$$

and similarly for V and W from equation (5.46b). Examining the computational equations (5.23a–d) to leading order yields:

$$(\rho_0 U_0)_\theta + \rho_0 \left(V_{0y} + W_{0z}\right) = 0 \ ; \tag{5.47a}$$

$$U_0 U_{0\theta} + V_0 U_{0y} + W_0 U_{0z} = -\frac{p_{00\theta}}{\rho_0} \ ; \tag{5.47b}$$

$$U_0 R_{0\theta} + V_0 R_{0y} + W_0 R_{0z} = -R_0 \left(V_{0y} + W_{0z}\right) + V_{0\theta} U_{0z} - W_{0\theta} U_{0y} \ ; \tag{5.47c}$$

$$p_{00} = \rho_0^\gamma \ . \tag{5.47d}$$

Thus the leading order components of the principal flow variables satisfy the straight-duct equations when Λ is of $\mathcal{O}(\delta)$. This suggests that as in the II and CI cases, we can linearise the governing equations (5.23a–d) about the

straight-duct solution, which in the case of zero-initial swirl we demonstrated in §5.4.2 featured no evolution of U with θ. Therefore, for θ of $\mathcal{O}(1)$ and $\Lambda = \delta\tilde{\Lambda}$ we take:

$$U = U_0(y,z) + \delta U_1(\theta,y,z) + \mathcal{O}(\delta^2) \; ; \tag{5.48a}$$

$$R = \delta R_1(\theta,y,z) + \mathcal{O}(\delta^2) \; ; \tag{5.48b}$$

$$\rho = \rho_0(\theta) + \delta\rho_1(\theta,y,z) + \mathcal{O}(\delta^2) \; ; \tag{5.48c}$$

$$p_0 = p_{00}(\theta) + \delta p_{01}(\theta,y,z) + \mathcal{O}(\delta^2) \; , \tag{5.48d}$$

and similarly for V and W from equation (5.48b). The leading order balance of the U-equation (5.23b) is $p_{00\theta} = 0$ which implies that $p_{00} = 1$ for all θ. The polytropic equation of state (5.23d) then implies that $\rho_0 \equiv 1$ for all θ also, and thus:

$$\rho = 1 + \delta\rho_1(\theta,y,z) + \mathcal{O}(\delta^2) \; ; \tag{5.49a}$$

$$p_0 = 1 + \delta p_{01}(\theta,y,z) + \mathcal{O}(\delta^2) \; . \tag{5.49b}$$

Then the leading order balances of the remaining equations (5.23a–c) are:

$$(U_1 + U_0\rho_1)_\theta + V_{1y} + W_{1z} = 0 \; ; \tag{5.50a}$$

$$U_{1\theta} + V_1\frac{U_{0y}}{U_0} + W_1\frac{U_{0z}}{U_0} = -\frac{p_{01\theta}}{U_0} \; ; \tag{5.50b}$$

$$R_{1\theta} = 2\tilde{\Lambda}U_{0y}\alpha\theta_1^2 - W_{1\theta}\frac{U_{0y}}{U_0} + V_{1\theta}\frac{U_{0z}}{U_0} \; . \tag{5.50c}$$

By eliminating U_1 from equations (5.50a) and (5.50b) we obtain

$$-U_0(U_0\rho_{1\theta} + V_{1y} + W_{1z}) + V_1U_{0y} + W_1U_{0z} = -p_{01\theta} \; , \tag{5.51}$$

and by integrating equation (5.50c) with respect to θ we obtain:

$$R_1 = (2\tilde{\Lambda}U_{0y}\alpha\theta_1^2)\theta - W_1\frac{U_{0y}}{U_0} + V_1\frac{U_{0z}}{U_0} \; , \tag{5.52}$$

which implies linear growth in θ of the leading-order vorticity when Λ is small. Alternatively, we note that equation (5.52) can be rearranged to give:

$$(U_0 W_1)_y - (U_0 V_1)_z = (2\tilde{\Lambda} U_0 U_{0y} \alpha \theta_1^2)\theta \tag{5.53}$$

which suggests that W_1,$V_1 \propto \theta$, and thus that $R_1 \propto \theta$. This set of analytical conclusions is consistent with the small-Λ numerical results shown in §5.4.5.

The predicted linear growth in R_1 suggests that $(U_1 + U_0\rho_1)$ will grow in proportion to θ^2 from the balance of the continuity equation given by (5.50a). Therefore we consider a new length scale when θ is of $\mathcal{O}(\delta^{-\frac{1}{2}})$ since $(U_1 + U_0\rho_1)$ will have grown to be of $\mathcal{O}(\delta^{-1})$ at this stage. This suggests we consider the following expansions when $\theta = \delta^{-\frac{1}{2}}\bar{\theta}$ and $\Lambda = \delta\tilde{\Lambda}$:

$$U = U_0(\bar{\theta}, y, z) + \dots \ ; \tag{5.54a}$$

$$R = \delta^{\frac{1}{2}} R_0(\bar{\theta}, y, z) + \dots \ ; \tag{5.54b}$$

$$\rho = \rho_0(\bar{\theta}, y, z) + \dots \ ; \tag{5.54c}$$

$$p_0 = p_{00}(\bar{\theta}, y, z) + \dots \ . \tag{5.54d}$$

The expansion (5.54d) comes from the behaviour of p_{01} implied by (5.51), expansion (5.54c) comes from (5.54d) together with the polytropic equation (5.23d) and is consistent with $\rho_1 \propto \theta^2$ as above, and similar expansions to (5.54b) exist for V and W.

Examining (5.23a) to leading order in δ yields

$$(\rho_0 U_0)_{\bar{\theta}} + \rho_0 (V_{0y} + W_{0z}) = 0 \ , \tag{5.55}$$

while (5.23b) becomes

$$U_0 U_{0\bar{\theta}} + V_0 U_{0y} + W_0 U_{0z} = -\frac{p_{00\bar{\theta}}}{\rho_0} \tag{5.56}$$

to leading order. The leading order balance of (5.23c) gives

$$U_0 R_{0\bar{\theta}} + V_0 R_{0y} + W_0 R_{0z} = -R_0 \left(V_{0y} + W_{0z}\right) + U_{0z} V_{0\bar{\theta}} - U_{0y} W_{0\bar{\theta}} + 2\tilde{\Lambda} U_0 U_{0y} \alpha \theta_1^2 \,. \tag{5.57}$$

The polytropic equation of state (5.23d) becomes:

$$p_{00} = \rho_0^{\gamma} \,. \tag{5.58}$$

Furthermore, leading order balances of (5.12c) and (5.12d) yield $p_{00} = p_{00}(\bar{\theta})$ only, and similarly for ρ_0 from (5.58). We note that there must be matching of the leading order components as $\bar{\theta} \to 0+$ with the previous case as $\theta \to \infty$.

The above equations imply that at this new stage, the leading order components of the principal variables are governed by the same coupled set of equations as the leading order components in the case when Λ and θ are of order unity. The results and predictions for that regime, which was the main focus of §§5.3 and 5.4, will carry over to this regime. Thus for example there would be continued linear growth of the vorticity at this new stage, whilst the streamwise velocity would be weakly mixed. Physically, we have considered here the effects of a weaker bend over a longer development distance, so the connection with the previous case is perhaps to be expected. We note that the numerical solutions do not extend far enough downstream to test these analytical results when θ is of $\mathcal{O}(\delta^{-\frac{1}{2}})$, and are not generally reliable unless Λ is of order unity.

Small θ, order unity Λ

In final support of the numerics which, when Λ is of $\mathcal{O}(1)$ only extend to relatively small θ, we examine the entry region where θ is small and Λ is of $\mathcal{O}(1)$. We aim to show, for example, that $R \propto \theta$ here since this is the numerical

prediction seen in §5.4.2. Thus when $\theta = \delta\tilde{\theta}$ for $\delta \ll 1$, we take

$$R = \delta\tilde{R} + \mathcal{O}(\delta^2) \ , \tag{5.59}$$

and similarly for V and W, in order to match as $\tilde{\theta} \to \infty$ with the θ of $\mathcal{O}(1)$, Λ of $\mathcal{O}(1)$ prediction of linear growth as $\theta \to 0+$. We take U to be of order unity and similarly for ρ and p_0, that is:

$$U = U_0(\tilde{\theta}, y, z) + \mathcal{O}(\delta) \ ; \tag{5.60a}$$

$$\rho = \rho_0(\tilde{\theta}) + \mathcal{O}(\delta) \ ; \tag{5.60b}$$

$$p_0 = p_{00}(\tilde{\theta}) + \mathcal{O}(\delta) \ . \tag{5.60c}$$

The leading order balance of continuity (5.23a) is

$$(\rho_0 U_0)_{\tilde{\theta}} = 0 \ , \tag{5.61}$$

whilst the leading order balance of the U-equation (5.23b) is:

$$\rho_0 U_0 U_{0\tilde{\theta}} = -p_{00\tilde{\theta}} \ . \tag{5.62}$$

Expanding (5.61) gives $\frac{\rho_{0\tilde{\theta}}}{\rho_0} = -\frac{U_{0\tilde{\theta}}}{U_0}$, suggesting that

$$U_0 = F(\tilde{\theta})G(y, z) \tag{5.63}$$

where $F(\tilde{\theta} = 0) = 1$. Then (5.61) implies $\rho_0 F = 1$ for all $\tilde{\theta}$. Substituting for ρ_0 into (5.62) and letting $'$ denote differentiation with respect to $\tilde{\theta}$ yields

$$\frac{F'}{p'_{00}} = -\frac{1}{G^2} \tag{5.64}$$

which is a contradiction unless (5.62) is satisfied trivially, that is unless $p'_{00} \equiv 0 \equiv F'$. Thus, using also the polytropic equation:

$$p_{00} \equiv 1 \equiv \rho_0 \text{ for all } \tilde{\theta} \ ; \tag{5.65a}$$

$$U_0 = U_I(y, z) \text{ for all } \tilde{\theta} \ . \tag{5.65b}$$

The leading order balance of the R-equation (5.23c) together with the above results (5.65a,b) yields:

$$(U_I\tilde{W})_y - (U_I\tilde{V})_z = (2\Lambda U_I U_{Iy}\alpha\theta_1^2)\tilde{\theta} \ . \tag{5.66}$$

Thus the dominant behaviour is $\tilde{R} \propto \tilde{\theta}$. These conlcusions are consistent with the numerics in §5.4.1 since in that section we saw $U \approx U_I$ for all θ studied, p_0 and ρ staying very close to their initial values of unity, and R growing linearly with θ.

5.4.7 Re-examination of the fully non-linear results

In the fully non-linear schemes of §5.4 we optimised p_0, and therefore also ρ, to within 10^{-13} while solving all other variables to within an accuracy of 10^{-8}. We note that the calculated pressure and density variations are less than 10^{-8}, which suggests that the other variables experience p_0 and ρ as unity throughout the calculation. Indeed, optimising p_0 and ρ to 10^{-13} when U, V, and W are known only to within an accuracy of 10^{-8} may not be a workable approach. The numerical results thus appear to suggest that p_0 and ρ remain constant in both the NLCI and the NLII cases. By running the numerical schemes for NLCI and NLII with p_0 and ρ prescribed as unity throughout we can show that the numerical predictions for the other computed variables in both cases remain the same as reported. In particular for the NLCI case, we show in Figure 5.34 the profiles of U, V, W, and R at $\theta = 0.4$ generated with a prescribed p_0 and ρ (left hand side) and with p_0 and ρ allowed to vary (right hand side). We observe that they correspond very closely with each other, in line with the above discussion. The same is also true of the NLII case, as shown in Figure 5.35. The results in Figures 5.34 and 5.35 were computed over a fine grid.

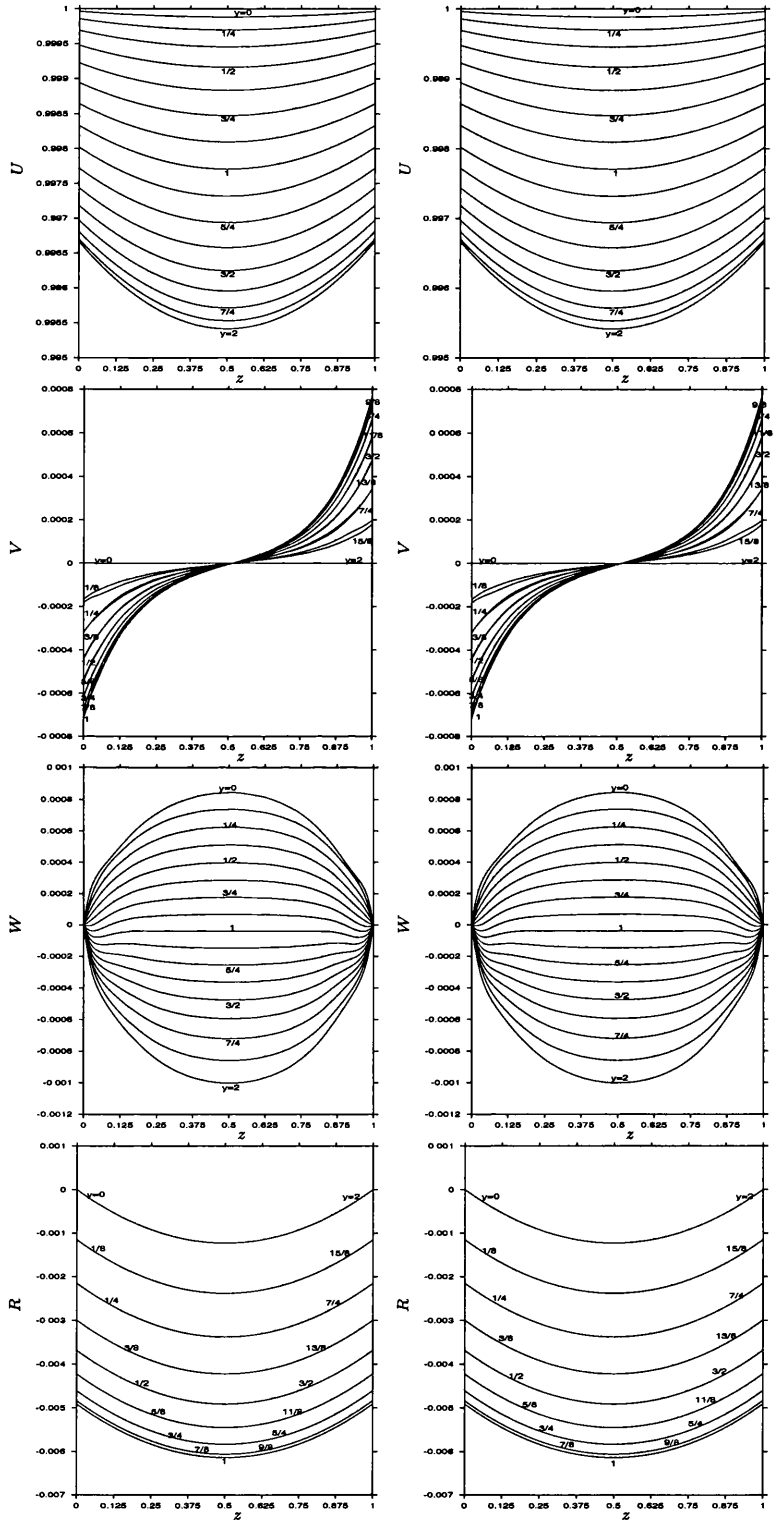

Figure 5.34: NLCI: U, V, W, R at $\theta = 0.4$, on lines of constant y. Left hand side: p_0, ρ prescribed as unity throughout. Right hand side (first shown in Figures 5.20 & 5.21): p_0, ρ permitted to vary. Initial conditions: (5.29, 5.30).

Significantly, when p_0 and ρ are prescribed the numerical blow-up occurs at the same θ-station as when they are allowed to vary in both the NLCI and the NLII cases. This also seems to support the above discussion in which we suggested that p_0 and ρ remain unity in both cases.

We observe that when $p_0 \equiv 1 \equiv \rho$ the NLCI case reduces to the NLII case, since then (5.23a–d) reduce to (5.40a–d) (with (5.40c) and (5.40d) replaced by a single equation for R). We note that this is in marked contrast to the weakly non-linear CI case of §§4.4 and 5.2 in which a definite compressibility factor $\hat{\rho}$ was present, evolved significantly throughout the bend, and was coupled with the flow development, distinguishing the CI case from the II case. We also showed in §4.4.2 that this varying $\hat{\rho}$ influenced the far-downstream behaviour of the flow in the weakly non-linear study — an important role for compressibility not apparent in the fully non-linear study.

Analytically, we observe that in the NLII case the θ-momentum equation (5.40b) can be written as

$$(U\partial_\theta + V\partial_y + W\partial_z)\left(p_0 + \frac{1}{2}U^2\right) = 0 \,. \tag{5.67}$$

Furthermore, a double integral of the NLII continuity equation (5.40a) gives

$$\iint U \; dydz = \text{constant for all } \theta \,. \tag{5.68}$$

Equation (5.67) implies that the quantity $p_0 + \frac{1}{2}U^2$ is conserved following a particle, such that if p_0 decreases, $\frac{1}{2}U^2$ increases and conversely. But since $p_0 = p_0(\theta)$ only, any evolution of p_0 away from unity is the same for all particles. In this way, a decrease, say, in p_0 leads to an increase in $\frac{1}{2}U^2$ for *all* particles. But this is clearly in contradiction with (5.68) since $\frac{1}{2}U^2$ cannot increase for all particles whilst $\iint U \; dydz$ remains constant. This argument suggests that p_0 is constant for all θ in line with the above arguments based on the numerical

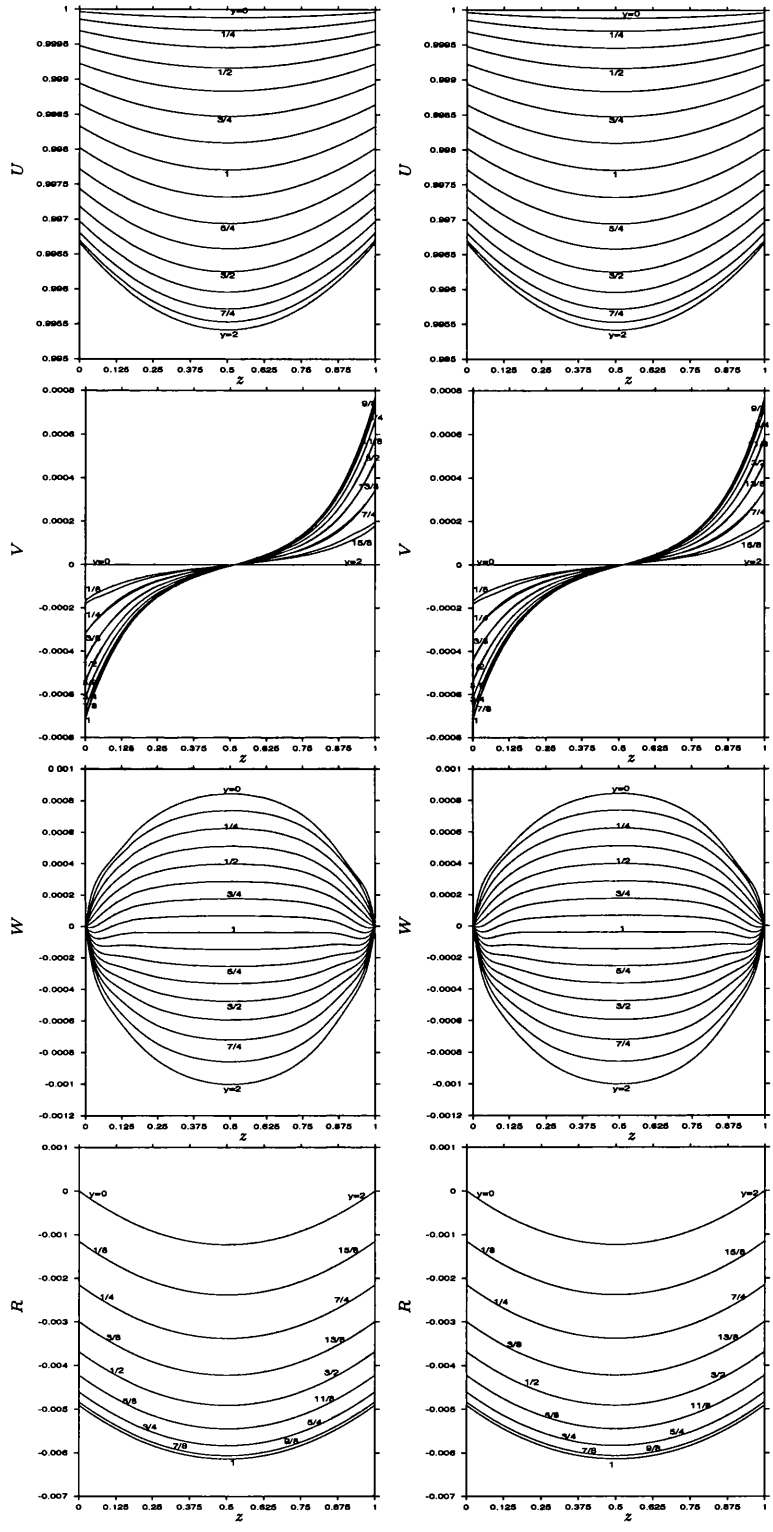

Figure 5.35: NLII: U, V, W, R at $\theta = 0.4$, on lines of constant y. Left hand side: p_0 prescribed as unity throughout. Right hand side (first shown in Figure 5.30): p_0 permitted to vary. Initial conditions: (5.29, 5.30).

work. We observe that the continuity equation is in effect a compatibility condition which provides a test to ensure that the flow remains source-free.

For the NLCI case the conserved quantity following a particle is

$$\frac{\gamma}{\gamma-1}p_0^{\frac{\gamma-1}{\gamma}}+\frac{1}{2}U^2 \tag{5.69}$$

from (5.23b) and (5.23d). Once more we see that if p_0 decreases then $\frac{1}{2}U^2$ increases and conversely. The NLCI continuity equation (5.23a) suggests that

$$\iint p_0^{\frac{1}{\gamma}}U\ dydz = \text{constant for all } \theta\ , \tag{5.70}$$

which is not immediately in contradiction with a falling p_0 and rising U (or *vice versa*). However, the (y,z)-invariant change in p_0 forces a response in $\frac{1}{2}U^2$ which differs between particles with different U. This suggests that the change induced in $\iint U\ dydz$ cannot simply be scaled by the (y,z)-invariant factor $p_0^{\frac{1}{\gamma}}$ in such a way that $p_0^{\frac{1}{\gamma}}\iint U\ dydz$ remains constant. This argument suggests that p_0 and ρ remain unity for the NLCI case as was suggested by the numerical arguments given above. This line of reasoning also implies that U is conserved following particles, which combined with the above result that the double integral of U is also conserved, suggests that U evolves only through a mixing mechanism as in the weakly non-linear cases.

5.4.8 Final discussion of the NLCI results

In §§5.3 and 5.4 we have solved numerically the governing equations of the NLCI case, (5.12a–d), and those of the NLII case, (5.40a–d), over a wide range of parameter values. As in the II and CI cases, the entry profile of U has been shown to be very important in the downstream evolution of the flow since it is conserved for the $\mathcal{O}(1)$ values of θ considered here. Furthermore, in another feature of the fully non-linear results which is in qualitative agreement

with the weakly non-linear results, U_I drives the evolution of the vorticity R in the bend even when $R_I \equiv 0$. Various non-zero values of initial swirl give qualitatively similar results which, in combination with U driving the evolution of R, highlights the desirability of suppressing variations in the initial profile of U.

The numerical schemes perform well for $\mathcal{O}(1)$ values of θ when the important parameter Λ is of $\mathcal{O}(1)$, and are stable for both zero and non-zero initial swirl. For example, when $\Lambda = 1$ and the variations in U_I, V_I, and W_I are relatively large numerical restrictions are reached by around $\theta = 0.4$. In this final section of §5.4 we will discuss the possible causes of the break-up in the results.

The first point we note is that the analytical work for small Λ in §5.4.6 shows no hint of an analytical blow-up, and thus it is likely that the difficulties experienced by the numerical scheme as Λ becomes small — which occured regardless of the size of the initial swirl — are numerical blow-ups rather than physical ones. In an effort to minimise in all parameter regimes the accumulation of numerical errors we advanced the schemes in θ once the results at the current θ-station had converged to within the prescribed level of accuracy without forcing a minimum number of iterations as we did in §§2.3 and 5.1.

Of the candidates which we shall discuss for the general break-up in the solutions when Λ is of $\mathcal{O}(1)$, some are numerical whilst others are physical. In the former category is the solution method for the Poisson equations (5.26) and (5.27). As we discussed on page 133 we do not have accurate boundary information for V and W on all the walls and this could lead to the accumulation of errors as they are diffused through the computational domain from the boundaries. Another potential source of numerical errors is the size of the

variations in U_I. As $|U_{Iy}|$ and $|U_{Iz}|$ are allowed to increase, the numerics break up for smaller values of θ. However, this occurs only when the curvature is present, since even when $|U_{Iy}|$ and $|U_{Iz}|$ are of $\mathcal{O}(1)$ the numerics are able to run for long downstream distances when Λ is zero. Another possible numerical source of the break-up is the development of the higher-order velocity components. In particular, if we consider the expansion of the non-dimensional streamwise velocity u given in (5.13a) and extend it to

$$u = \bar{U} + \epsilon\tilde{U} + \epsilon^2\tilde{\tilde{U}} + \dots \ , \tag{5.71}$$

then examining the continuity equation to higher orders in ϵ yields in the NLII case:

$$\frac{d}{d\theta}\iint \tilde{U}\ dydz = 0 \ ; \tag{5.72a}$$

$$\frac{d}{d\theta}\iint \tilde{\tilde{U}}\ dydz + \iint W\ dydz = 0 \ , \tag{5.72b}$$

after normalising. Equation (5.72a) suggests that the initially $\mathcal{O}(\epsilon)$ part of u remains of $\mathcal{O}(\epsilon)$ throughout the bend, whilst (5.72b) suggests that the growth of the $\mathcal{O}(\epsilon^2)$ part of u is proportional to $\iint W\ dydz$. Since we saw in Figure 5.31 that $\iint W\ dydz$ grows linearly with θ it is possible that $\tilde{\tilde{U}}$ is growing sufficiently strongly to interfere with the leading order solutions as θ increases.

Amongst physical sources of the break-up is the possibility that the flow is becoming supercritical, *i.e.* there is a change of type. At the onset of the bend the Mach number $M = \frac{u}{a}$, where $a^2 = \gamma\rho^{\gamma-1}$, is approximately 0.85. Although the leading-order part of the density remains unity it is possible that if strong growth in the higher-order components occurred then the total density could decrease with increasing θ. This would bring the Mach number M closer to unity, perhaps suggesting that the flow is becoming supercritical. We note in

this context that a higher-order balance of the continuity equation yields

$$\frac{d}{d\theta}\iint \tilde{\rho}\, dydz = 0\ , \tag{5.73}$$

where $\tilde{\rho}$ is the $\mathcal{O}(\epsilon)$ part of the density. Since (5.73) suggests that $\tilde{\rho}$ remains of order unity throughout the bend, a decrease in density would have to come from the significant growth of a higher-order density component.

It is also possible that thin edge layers are generated near the walls to allow for significant θ-variation, as descibed in [77, pp.336–337]. It is thought that the emergence of such layers could interfere with the numerical schemes which do not account for their presence.

Furthermore, we cannot rule out the possibility of a physical singularity downstream.

A final suggestion for the cause of the break-up is to draw a loose analogy with the reversed-flow singularity mechanism reported in [73]. In this mechanism, non-zero values of the viscosity are required for the singularity to occur. The analogy is that curvature acts like viscosity here, in the sense that when Λ is zero the break-up is absent.

Finally for this discussion, we repeat that a complete numerical solution of the three-dimensional Euler equations is a difficult problem requiring other special computationally intensive techniques. Even when such techniques are used in commercial CFD packages, the schemes work well in one dimension but are described as having "horrible performance" and being "uncodable" in three dimensions [39]. The long length scale θ in the present study renders the coupled governing equations parabolic, simplifying the computational approach as the numerics can be marched forward in θ. However, numerical errors due to truncation and lack of detailed boundary information will still be accumulated throughout the computational domain.

In conclusion, we note that the aim of the numerical work in this chapter and the thesis in general is to generate data which interact with the analytical work, and conversely. The numerical schemes used in §§5.3 and 5.4 certainly generate interesting data for $\mathcal{O}(1)$ values of θ which we have shown to be consistent with the analytical work of §5.4. We do observe, however, that from a purely numerical point of view supposedly more advanced techniques do exist, although whether they would work well under the conditions relevant to this thesis is not known. For example, multigrid and unstructured grid approaches appear to be quite successful, as shown by [86] and [12]. In a vorticity-dominated flow through a duct — a case not considered in the present thesis — [61] suggests that rotational Euler solvers work well.

Part II

The effects of turbulence

Chapter 6

Introduction to the turbulent boundary layer

Consider a fluid-conveying duct whose cross-section is not strongly curved (in a sense we will define more precisely later in this chapter), and suppose we are sufficiently far away from the complicating effects of corners in the duct cross-sectional profile. At sufficiently small distances from the interior wall, the turbulent boundary layer (TBL) becomes our object of study, where the effects of inertia, viscosity, and turbulence all come into play as the fluid is brought to rest over a very short distance normal to the wall. This part of the thesis models the behaviour of the TBL in a duct, including the effects of duct curvature in the streamwise direction.

In the first section of this chapter, we present a brief history of the description and modelling of turbulence, introducing concepts which are formalised in §6.2. We define the geometry and velocity perturbations of the problem in a form consistent with the results of Part I of this thesis. The rest of this chapter is concerned with the discussion of the relevant physics and the formulation of

the governing equations, with reference also to Appendix B.

6.1 History and overview

Experimental results are of course very important in seeking to understand the structure and behaviour of turbulence in general, and this understanding is essential in building models of the turbulent effects on the governing equations. Such models are hybrids of two approaches, one based on physical understanding, and the other on analyses of empirical data. Thus we see physical ideas — building on an understanding of the fundamental nature of turbulence — creating the framework in which an engineering approach seeks to curve-fit formulae to experimental data. We shall consider a representative model, the Cebeci-Smith model, though other models exist with the same or similar basis. The creators of the Cebeci-Smith model freely admit that it "... [does] not improve any fundamental understanding of turbulence" ([15, p.255]). However, the Cebeci-Smith model is in reality a very successful engineering model based on a long history of physical ideas extending back to the 19^{th} century, as we shall see in the following discussion, which is based on that in [15].

As discussed in [15, §2.3], the apparently randomly fluctuating variables of turbulent flows suggest an approach based on mean quantities. Since turbulence is inherently unsteady, time-averaging of the data seems appropriate. This approach has the added benefit that fluctuating variables can now be written as the sum of the time average and a fluctuation, as the following example for the velocity component u_i shows:

$$u_i(x_i, t) = \overline{u}_i(x_i) + u_i''(x_i, t) \ , \tag{6.1}$$

where a bar denotes the time average and the double prime denotes the imposed

fluctuation. Upon substitution into the unsteady Navier-Stokes and continuity equations, this formulation generates extra terms which are not present in the laminar case. These terms either involve the transport of turbulence, or are density-generated terms. Consequently, the system of equations has been "re-opened" in the sense that there are now fewer equations than there are dependent variables. Physically, the turbulent transport terms appear because of the strong coupling of the velocity fluctuations to the mean flow and the re-opening is to be expected *a priori*, since averaging implies a loss of information. However, the appearance of source terms in the continuity equation leads to a contradiction with respect to the (mean) streamlines, since it implies mass is exchanged across them.

The resolution of this problem is mass-weighted averaging, first employed in this context by Van Driest. In essence, the mass-weighted average of a quantity takes the time average of the density and the quantity measured together, and divides it by the time average of the density:

$$\tilde{u}_i = \frac{\overline{\rho u_i}}{\overline{\rho}} \ . \tag{6.2}$$

The variable is then re-written as a mass-weighted average plus a superimposed velocity fluctuation. That is:

$$u_i(x_i, t) = \tilde{u}_i(x_i) + u_i'(x_i, t) \ , \tag{6.3}$$

where the single prime denotes the imposed fluctuation (and similarly for other variables).

The mass-weighted average formulation has the added advantage of making the variables more readily measurable in the laboratory (see [15, p.53]). Formal relationships between time-averaged and mass-weighted averaged quantities exist, but these will not concern us here (the interested reader is referred to

[15, §2.4] and elsewhere).

As we shall see in more detail in §6.2, the mass-weighted average approach removes the source term from the continuity equation, but still re-opens the system of equations as other turbulent transfer terms are still present. A description of these terms is therefore called for to close the system of equations — this is the so-called closure problem.

A reply came from Boussinesq, who in 1877 suggested that the turbulent transfer terms should be modelled after the viscous transfer terms as being proportional to a local velocity gradient. The turbulent transfer terms are often referred to as Reynolds stress terms as a consequence of the analogy between Boussinesq's formulation and the Newton laminar stresses. The constant of proportionality — whose form would occupy the modellers from then until the present day — became known as the eddy viscosity. In effect, the eddy-viscosity formulation reinstates a constant of proportionality between the anisotropic component of the turbulent stresses with the anisotropic part of the mean rate-of-strain, as explained in [64, p.102]. The proposal is thus that the effective viscosity μ_{eff} of the fluid is

$$\mu_{\text{eff}} = \mu_L + \mu_T \ , \tag{6.4}$$

where μ_L is the laminar (molecular) viscosity, and μ_T is the turbulent viscosity. Note that in practice $\mu_T \gg \mu_L$. Both the eddy-viscosity and the molecular (laminar) viscosity have units of length×velocity. In the case of μ_L, the characteristic length is the distance of the mean free path of a molecule and the characteristic velocity is the mean molecular velocity. The characteristic velocity for μ_T can be taken as $\sqrt{K}$ where $K = \frac{1}{2}\overline{u_i' u_i'}$ is the turbulent kinetic energy. With this formulation, the choice of length scale is not yet clear, since the eddy viscosity could also be local. After all, even 500 years ago Leonardo

da Vinci had some intuition of the cascade structure of eddies — an observation of a multitude of length scales which would seem to prohibit the notion of a single representative length.

In 1926, Prandtl assumed that there is a characteristic length when he proposed the concept of the mixing length, which is in effect the small distance between eddies. In this formulation, the eddy viscosity μ_T is given by

$$\mu_T = l_m^2 \left| \frac{\partial u}{\partial y} \right| , \tag{6.5}$$

where l_m denotes the as-yet unknown mixing length.

The mixing-length hypothesis (MLH) of Prandtl can be seen as an extension of one explanation of the effects of Newton stresses. The effects of laminar viscosity can be derived as a result of the interchange of fluid particles of different speeds between adjacent laminae moving relative to one another.However the laminar viscosity is molecular — a property of the fluid unaffected by motion. This is not true for μ_T. By extension, for the turbulent part Prandtl proposed a mechanism whereby the fluctuating component of the velocities carried particles between various loci of mean velocity, assuming again that a characteristic length l_m exists, but without suggesting what l_m might be.

Van Driest suggested modelling l_m as

$$l_m = \kappa y[1 - e^{-\frac{y}{A}}] , \tag{6.6}$$

with κ (the von Kármán constant, an important parameter, as we shall see later in Chapter 8) and A (a damping parameter) being empirically determined, and this suggestion was later improved by several authors. Prominent amongst them in relation to this thesis was Tuncer Cebeci's improvement in [13]. This model was gradually improved and its utility was shown in many regimes (such as external flows with curvature in [16] and references therein, unsteady flows

with fluctuations in the external velocity in [14], and more besides), driven and quantified by the experiments of his collaborator A.M.O. Smith. This led to the Cebeci-Smith model which we shall employ in this thesis and which is explained in great detail with many examples in [15]. An excellent introduction to the nature of turbulence, and to the development of the MLH, is given in [15, §§1–6].

The composite nature of TBLs is shown in Figure 6.1, which is adapted from [17, Fig.6.6]. The flows in the inner and outer layers merge smoothly via a thin logarithmic layer. As will be seen, the Cebeci-Smith model is a two-tier mixing length model, in which the TBL is treated as a two-tiered object, with the eddy-viscosity having a different formulation in each tier. The velocity profiles along with the eddy viscosity and stresses merge smoothly across the unknown junction between the two tiers of the model.

The Cebeci-Smith model itself was chosen because it is "...particularly successful" ([64, p.108]) in terms of engineering predictions. It has also shown itself to be widely applicable (see the above discussion, and *e.g.* [60]), as well as extendable. Other two-tier mixing-length models exist, for example involving the outer layer improvements to Cebeci-Smith by Baldwin and Lomax, the model of Johnson and King, and so on, the details of which can be found in [64], for example. Of these, Cebeci-Smith is probably the simplest and performs well under a wide regime of physical configurations, and so it will suffice here, where the finest details tend not to be required yet. Indeed, it is an important point that the results obtained in this thesis are valid for any two-tier mixing-length model — choosing a specific model enables us to obtain numerical answers, and to make comparisons with experiment (where of course data is model-invariant).

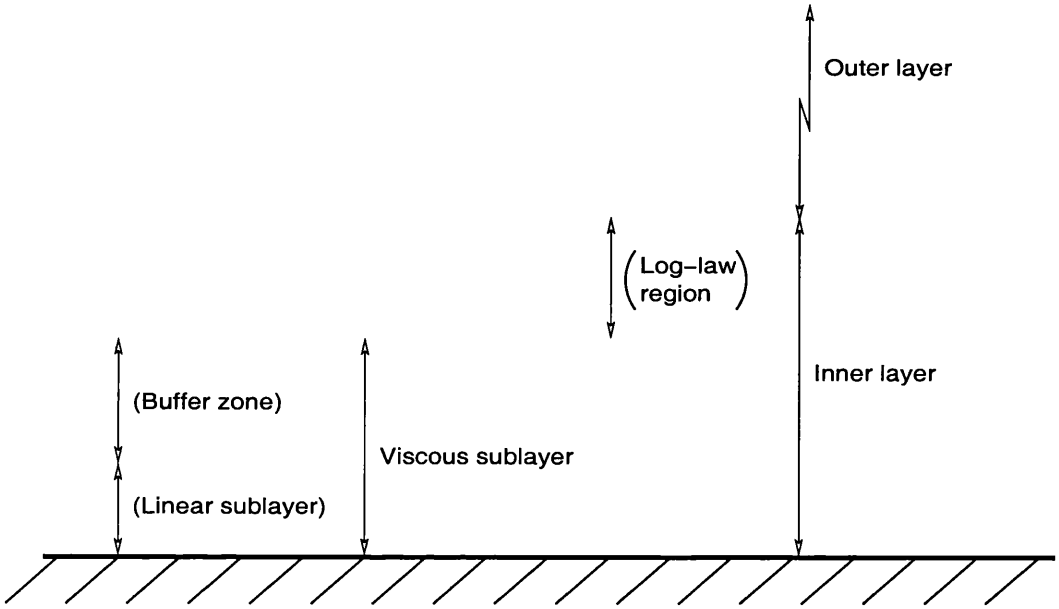

Figure 6.1: Schematic of the layers of a high Reynolds number TBL, drawn to a scaled wall normal coordinate on a logarithmic scale (not indicated). The outer layer, which typically accounts for 90% of the thickness of the TBL, is not drawn to scale. In low Reynolds number flow there will be a viscous superlayer between the outer layer and the external flow ([67, p.556]). The detailed structure of the inner layer is not a part of the analysis of this thesis.

There are reasoned objections to the eddy-viscosity/mixing-length approach, since it assumes a local equilibrium of transport coefficients, as discussed in [64, p.107]. A more general, but analytically and numerically harder[1], approach is to use extra equations to model the turbulent transport of energy, and so on. Such approaches are called one- or two-equation closure models, since they close the system by the introduction of one or two additional partial differential equations; our algebraic approach is sometimes referred to as a zero-equation closure model. We note that $\frac{1}{2}$, $1\frac{1}{2}$, and other hybrid models are

[1]The computational advantage of an algebraic model is quantified in [18].

also possible and can work well, see *e.g.* [3]. One- and two-equation closure models — outlined for example in considerable detail in [64, §5] — will not be used here, since the physical situation differs sufficiently from those in previous studies that an understanding of the basic mechanisms should first be sought.

Since the details of a two-tier mixing-length model depend on experimental data, it is natural to compare any analytical or numerical results with experiment. Perhaps surprisingly, there appears to be little empirical data for TBLs in ducts with the particular level of duct curvature assumed throughout this thesis. One experimental investigation which studied a similar level of curvature to the present motivating problem is [30]. However, the experiment involved a rectangular duct of much larger aspect ratio than we consider in this thesis (the height of the duct was 33 inches (83.8cm) whilst the width was 2.5 inches (6.4cm)) which effectively excludes any secondary flow in the cross-section. Furthermore, measurements are made only further downstream than is considered in the forthcoming work. As a result, no comparisons with the data in that study can be made.

The apparent lack of empirical work for TBLs in ducts with the curvature considered herein may be due to the duct curvature of interest lying somewhere between strongly curved, such as an elbow in a duct, and weakly curved, which is several orders of magnitude weaker than the strong case. Experiments in these two regimes have been performed, for example by [68] in the first instance, and [42] in the second. However, the present study is aimed not at confirming experimental results, nor at proving the utility of a particular model (as is the case for example in the useful contribution [60]), but at investigating a physical situation commonly arising in industrial settings. An additional challenge when trying to make comparisons with experimental data is that

experimentalists often measure higher-order statistical quantities such as the double-correlation terms, which are important in understanding the turbulent transport of energy but are not considered herein. Additionally, both experimentalists and theorists are interested in coherent and transient structures in TBLs (see for example [43] and references therein). The work in this thesis, on the other hand, is largely concerned with the development of velocity and pressure profiles, and how, for example, these influence the core flow, since it is the bulk behaviour of the whole duct flow which is of importance to the motivating industrial problem.

In the introduction to §5.4 of [64], Piquet discusses the various caveats to bear in mind when consulting experimental pipe-flow data. For example, the Reynolds number can be defined in several ways; the question of whether the flow is fully developed; the presence of secondary flows due for example to a small aspect ratio of the cross-section; and the reliability of measuring techniques. He also questions the accuracy of DNS simulations as they are not free of scale effects. A particular example of a DNS comparison with experiment is [29], in which the comparison with experiment on some computed quantities is only "... reasonably good". [64] also provides some interesting comparisons of the performance of various models.

In contrast to our specific level of curvature, there is an abundance of data for straight-duct flows in two and three dimensions (see for example [59, 56, 20, 51, 52]) in the region downstream of that where the TBLs develop and start to merge. This region is studied analytically and numerically for straight ducts in two and three dimensions in our Chapter 8 below and favourable comparisons with the aforementioned empirical data are found. Since the approach to Chapter 8 is an extension of that used in Chapter 7

below, some confidence in the results of that chapter is also implied. In the absence of experimental comparisons for the results of Chapter 7, every effort both analytical and numerical has been undertaken to show strong consistency between the sometimes surprising analytical predictions and the numerical results.

Given the obvious significance to airfoil performance, the TBLs over flat plates and thin airfoils, and questions of the turbulent wake structure and separation conditions have received much attention, both analytical and numerical. Though questions concerning the stability, transition, and separation of the boundary layer, and their influence on growth and development, will not be discussed here — the boundary layer is instead assumed to be turbulent from the start (in line with the discussion in [91, §D2.1]) and to remain attached throughout — representative work in these areas can be found in [72, 15, 79, 9, 50, 95]. The last two of these include work on how curvature affects transition (see also [67, pp.500–8]).

Important theoretical work on the two-tiered asymptotic structure in the limit of large Reynolds number can be found in [26] and references therein. This reference is important to the present study, since it shows that the two-tier mixing-length formulation is valid for three-dimensional flows in general, since previous work had concentrated on three-dimensional axisymmetrical flows at best.

The appearance of [26] came at a time when the increasing power and availability of computers meant that complex three-dimensional TBL flowfields were being computed. The impetus for these numerical studies — in the absence of sure theoretical footing — was the relatively frequent appearance of three-dimensional TBLs in industrial applications.

The introduction to [26] contains a review of the outstanding contemporary "controversial" issues with regard to the three-dimensional TBL structure. The controversies seemed mainly to hinge around the frequently-encountered polarisation of views on the interpretation of data, as either the "absence of evidence" or the "evidence of absence". The paper resolves these important issues raised by the empiricists, and it provides firm footing for the present thesis.

As the above discussion and the novel work below in Chapters 7 and 8 hopefully show, industry can provide interesting situations in this area which have not been considered in sufficient depth and which yield exciting new science.

6.2 Modelling and other considerations

The full, dimensional continuity and Navier-Stokes equations are

$$\text{Cty:} \qquad \frac{\partial \rho_D}{\partial t_D} + \frac{\partial}{\partial x_{Dj}}(\rho_D u_{Dj}) = 0 \; ; \tag{6.7a}$$

$$\text{Mtm:} \qquad \frac{\partial}{\partial t_D}(\rho_D u_{Di}) \frac{\partial}{\partial x_{Dj}}(\rho_D u_{Di} u_{Dj}) = -\frac{\partial p_D}{\partial x_{Di}} + \frac{\partial \tau_{Dij}}{\partial x_{Dj}} \; . \tag{6.7b}$$

As alluded to in §6.1, we split the stress tensor τ_{Dij} into a laminar part and turbulent part. The laminar part $(\tau_L)_{Dij}$ is the usual stress dyadic containing the divergence and the deformation terms:

$$(\tau_L)_{Dij} = \lambda_D \delta_{ij} \frac{\partial u_{Dl}}{\partial x_{Dl}} + \mu_D \left(\frac{\partial u_{Di}}{\partial x_{Dj}} + \frac{\partial u_{Dj}}{\partial x_{Di}} \right) \; . \tag{6.8}$$

The modelling of the turbulent or Reynolds stress $(\tau_T)_{Dij}$ is of great import as we have discussed above.

We consider the flow to be steady and, in order to make some headway,

incompressible and hence obtain

$$\text{Cty:} \qquad \frac{\partial u_{Dj}}{\partial x_{Dj}} = 0 \; ; \tag{6.9a}$$

$$\text{Mtm:} \qquad u_{Dj}\frac{\partial u_{Di}}{\partial x_{Dj}} = -\frac{1}{\rho_D}\frac{\partial p_D}{\partial x_{Di}} + \frac{1}{\rho_D}\frac{\partial \tau_{Dij}}{\partial x_{Dj}} \; , \tag{6.9b}$$

$$\text{where now} \qquad (\tau_L)_{Dij} = \mu_D \left(\frac{\partial u_{Di}}{\partial x_{Dj}} + \frac{\partial u_{Dj}}{\partial x_{Di}} \right) \; . \tag{6.9c}$$

At this point, we recall that a turbulent flow is characterised by random fluctuations about a mean flow, and that we seek to predict the mean flow by casting the equations in terms of the mass-weighted averages as defined on p.171 above. All the terms in the governing equations (6.9a–c) involve mass-weighted averages and so the tildes are omitted.

The issue at hand is the turbulence closure problem of §6.1: having introduced an unknown quantity, the Reynolds stress, how now to describe it in order to close the equations? Beyond the many excellent discussions on this problem referenced in §6.1, the choice boils down to the number of additional equations to introduce in order to model the double correlation terms such as $\overline{u_i' u_j'}$ which appear in $(\tau_T)_{Dij}$. For example, we could introduce a transport equation for the Reynolds stress but, as discussed in [15], although the equation highlights the way in which the Reynolds stress is transferred, it confers no knowledge of its distribution. Note that in the core we shall take for any i, j

$$\frac{\tau_{Dij}}{u_{Di}\partial_{Di}u_{Dj}} \ll 1 \; , \tag{6.10}$$

meaning that the inertia terms dominate there as in Part I.

The length scales and length functions are non-dimensionalised on the width of the duct, h_D, the velocities on the typical centreline velocity in the duct, $U_{D\infty}$, and pressure and the Reynolds stress on twice the dynamic pressure head, $\rho_D U_{D\infty}^2$. Finally, the laminar stresses are non-dimensionalised as usual

on $\frac{U_{D\infty}}{h_D}$ which eventually leads to the introduction of the Reynolds number Re, here defined as

$$Re = \frac{\rho_D U_{D\infty} h_D}{\mu_D} \,. \tag{6.11}$$

As mentioned in §6.1, care must be taken when comparisons are drawn with other studies as various length scales and velocities can be taken to define Re in a duct TBL.

It is known (see *e.g.* [81]) that in the limit of large Reynolds number the TBL has a two-tiered structure (a common feature of singular perturbation problems — see *e.g.* [67, pp.519–20]) and that this also holds for three-dimensional TBLs ([26]). Furthermore, the work in [26] confirms the defect-function form of the velocity in the outer layer of a three-dimensional TBL, whilst [67, p.548] proves that the universal law of the wall holds in the case of duct flow. We will therefore consider two-tier algebraic models. Most of these assume Prandtl's mixing-length hypothesis as described in §6.1 and are extensions of the work of Van Driest in 1956 as discussed above. In such formulations there is an outer layer, where the main balance of forces is between inertia and turbulence, and an inner layer where turbulent and laminar viscous stresses balance. The layers merge in a logarithmic zone, and in fact even finer layer structure is apparent on smaller length scales (see *e.g.* [15]). In order to use a forward-marching numerical scheme in Chapters 7 and 8, we must also assume that there does not exist any reverse flow. A final implicit assumption is that the walls of the duct are perfectly smooth. In reality, of course, all physical surfaces have non-zero roughness, and this roughness influences not only the transition to turbulence of a TBL, but also the turbulent flow development, see [67, pp.526ff].

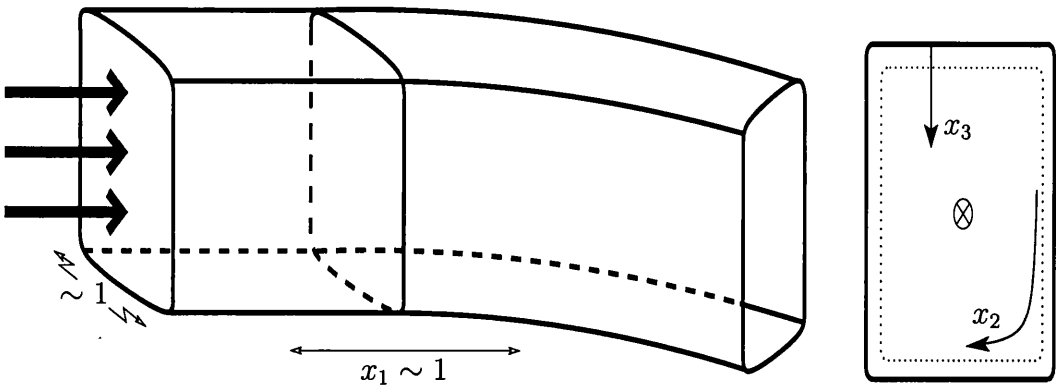

Figure 6.2: Coordinate configuration. The thin dotted line in the right hand diagram indicates the boundary layer.

6.3 Derivation of equations

Consider a duct at rest, lying such that the bulk flow is in a horizontal direction, with two coordinate directions in the wall and one normal to the wall. With reference to Figure 6.2, the direction in the wall running downstream (*i.e.* in the direction of monotonically increasing duct length) we will denote x_1 with corresponding velocity u_1. The other wall direction which runs around the wall in a cross-section normal to x_1 we will denote x_2 with velocity component u_2. This direction is periodic and runs in the negative orientation, that is, clockwise looking in the direction of increasing x_1. Let the circumference of the duct at any x_1-station be $C(x_1)$. Then the periodicity of x_2 ensures that

$$\boldsymbol{\xi}(x_2 + nC) = \boldsymbol{\xi}(x_2) \ , \tag{6.12}$$

for all x_2, where $n \in \mathcal{Z}$ and $\boldsymbol{\xi}$ is any variable. Finally, the wall-normal coordinate will be x_3 with velocity component u_3. It is oriented to point towards the interior of the duct, thus completing the orthogonal right-handed triad. Implicit in this definition is that on a boundary-layer length scale, x_3 is "short",

and thus that we avoid problems arising from different values of x_3 from different points.

The derivation of the governing equations involves determining the non-dimensionalising factors, and considering the relative orders of magnitude of each term in the continuity and Navier-Stokes equations. This can be a lengthy process, particularly when curvature is present. In order not to unduly weigh-down this section of the thesis, the detailed derivation can be found in Appendix B, whilst here we present the results of that derivation.

In the following set of equations we use the metrics h_i of the orthogonal curvilinear system which are defined by the length-segment

$$(ds)^2 = h_1(dx_1)^2 + h_2(dx_2)^2 + h_3(dx_3)^2 \tag{6.13}$$

and whose nature is discussed in Appendix B. The curvature terms K_1 and K_2 defined formally in equation (B.5b) also appear. In essence, K_1 measures the rate of change with x_1 of the circumference of the duct, whilst K_2 measures the streamwise curvature of the duct.

The full non-dimensional formulation is:

$$\frac{1}{h_1}\frac{\partial u_1}{\partial x_1} + \frac{1}{h_2}\frac{\partial u_2}{\partial x_2} + \frac{\partial u_3}{\partial x_3} - K_1 u_1 - K_2 u_2 = 0 \; ; \tag{6.14a}$$

$$\frac{u_1}{h_1}\frac{\partial u_1}{\partial x_1} + \frac{u_2}{h_2}\frac{\partial u_1}{\partial x_2} + u_3\frac{\partial u_1}{\partial x_3} - K_2 u_1 u_2 + K_1 u_2^2 = -\frac{1}{h_1}\frac{\partial p}{\partial x_1} + \frac{1}{Re}\frac{\partial^2 u_1}{\partial x_3^2} + \frac{\partial}{\partial x_3}\left(B\frac{\partial u_1}{\partial x_3}\right) \; ; \tag{6.14b}$$

$$\frac{u_1}{h_1}\frac{\partial u_2}{\partial x_1} + \frac{u_2}{h_2}\frac{\partial u_2}{\partial x_2} + u_3\frac{\partial u_2}{\partial x_3} - K_1 u_1 u_2 + K_2 u_1^2 = -\frac{1}{h_2}\frac{\partial p}{\partial x_2} + \frac{1}{Re}\frac{\partial^2 u_2}{\partial x_3^2} + \frac{\partial}{\partial x_3}\left(B\frac{\partial u_2}{\partial x_3}\right) \; ; \tag{6.14c}$$

where in the above equations we have

$$B = \begin{cases} a_2 x_3^2 \left[1 - exp\left(-\frac{Re_\tau^{\frac{1}{2}}}{26} x_3 \left[\left(\frac{\partial u_1}{\partial x_3}\right)_w^2 + \left(\frac{\partial u_2}{\partial x_3}\right)_w^2\right]^{\frac{1}{4}}\right)\right]^2 \\ \qquad \times \left[\left(\frac{\partial u_1}{\partial x_3}\right)^2 + \left(\frac{\partial u_2}{\partial x_3}\right)^2\right]^{\frac{1}{2}} & , \; x_3 < x_{3J} \; , \\ a_1 u_t \delta_1 & , \; x_3 > x_{3J} \; , \end{cases} \tag{6.15a}$$

where

$$\begin{gathered} a_1 = 0.0168 \; , \quad a_2 = 0.16 \\ \delta_1 = \int_0^\infty 1 - \frac{(u_1^2 + u_2^2)^{\frac{1}{2}}}{u_t} \, dx_3 \; , \quad u_t = (u_1^2 + u_2^2)^{\frac{1}{2}}|_{x_3 = x_{3e}} \; . \end{gathered} \tag{6.15b}$$

The boundary conditions are:

$$\boldsymbol{u} = (u_1, u_2, u_3) \equiv \mathbf{0} \quad \text{on} \quad x_3 = 0 \; ; \tag{6.16a}$$

$$\text{non-wall stresses} \; = 0 \quad \text{at} \quad x_3 = 0, \quad \text{all stresses} \; = 0 \quad \text{at} \quad x_3 \geqslant x_{3e} \; ; \tag{6.16b}$$

$$\boldsymbol{u} = \boldsymbol{u}_\infty \quad \text{at} \quad x_3 = x_{3e} \; , \tag{6.16c}$$

where $\boldsymbol{u}_\infty$ is the core flow. Finally, we require continuity of eddy viscosity B, velocity components u_i , $i = 1, 2$, and the shears $\frac{\partial u_i}{\partial x_3}$, $i = 1, 2$ across the unknown junction $x_3 = x_{3J}$. Note that u_3 matches automatically with the core flow as in [78, p.20].

Having derived the full equations, we can now apply them to specific situations. In all the subsequent work we will assume that the duct has constant cross-sectional area[2] which implies

$$K_1 \equiv 0 \; . \tag{6.17}$$

[2]For a demonstration of the effects of sudden changes in cross-sectional area, see *e.g.* [59].

In §6.4 we examine the inlet flow in a straight duct, and in §6.5 we formulate the problem for the entry flow in a curved duct, which is to be analysed in the subsequent chapter.

6.4 Inlet flow in a straight duct

Following [15, p.780], we see that if $K_2 = 0$, a solution of the x_2-momentum equation which satisfies the boundary conditions is

$$u_2 \equiv 0 \quad , \quad p = p(x_1) \; . \tag{6.18}$$

The condition $K_2 = 0$ corresponds to a straight duct, hence in a straight duct the TBLs are two-dimensional. More formally, the problem of a straight, constant cross-section duct with inlet flow is formulated as follows. When

$$K_1 \equiv K_2 \equiv 0 \quad , \quad u_2 \equiv 0 \quad , \quad h_1 \equiv h_2 \equiv h_3 \equiv 1 \quad , \quad p \text{ known}, \tag{6.19}$$

we have:

$$\text{Cty:} \qquad \frac{\partial u_1}{\partial x_1} + \frac{\partial u_3}{\partial x_3} = 0 \; ; \tag{6.20a}$$

$$x_1\text{-mtm:} \qquad u_1 \frac{\partial u_1}{\partial x_1} + u_3 \frac{\partial u_1}{\partial x_3} = - \frac{\partial p}{\partial x_1} + \frac{1}{Re} \frac{\partial^2 u_1}{\partial x_3^2} + \frac{\partial}{\partial x_3} \left(B \frac{\partial u_1}{\partial x_3} \right) \; ; \tag{6.20b}$$

where in the above

$$B = \begin{cases} a_2 x_3^2 \left[1 - exp \left(- \frac{Re^{\frac{1}{2}}}{26} x_3 \left(\left| \left(\frac{\partial u_1}{\partial x_3} \right)_w \right| \right)^{\frac{1}{2}} \right) \right]^2 \left| \frac{\partial u_1}{\partial x_3} \right| & , \; x_3 < x_{3J} \; , \\ a_1 \delta_1 & , \; x_3 > x_{3J} \; , \end{cases} \tag{6.21}$$

where $a_1 = 0.0168$, $a_2 = 0.16$ and $\delta_1 = \int_0^\infty (1 - u_1) \, dx_3$.

The boundary conditions are:

$$\boldsymbol{u} = \mathbf{0} \quad \text{on} \quad x_3 = 0 \; ; \tag{6.22a}$$

$$\text{non-wall stresses } = 0 \quad \text{at} \quad x_3 = 0 \quad \text{and all stresses } = 0 \quad \text{at} \quad x_3 \geqslant x_{3e} \; ; \tag{6.22b}$$

$$u_1 = 1 \quad \text{at} \quad x_3 = x_{3e} \; ; \tag{6.22c}$$

and continuity of eddy viscosity B, u_1, and $\frac{\partial u_1}{\partial x_3}$ across the unknown junction $x_3 = x_{3J}$.

The layered structure of the TBL has a thickness of the outer tier of $\mathcal{O}(\hat{\epsilon})$, for $\hat{\epsilon} \ll 1$, with a defecit from freestream velocity also of $\mathcal{O}(\hat{\epsilon})$. The inner tier is of $\mathcal{O}(Re^{-1}\hat{\epsilon}^{-1})$ thick, and in this layer u_1 is now of $\mathcal{O}(\hat{\epsilon})$. The two tiers merge via a logarithmic behaviour in the velocity *defecit* in the outer layer and the *velocity* in the inner layer. It is also known (see *e.g.* [81]) that

$$\hat{\epsilon} \equiv (Ln(Re))^{-1} \; , \tag{6.23}$$

where we are taking $Re \gg 1$ such that $\hat{\epsilon} \ll 1$ as above.

Let us first examine the small defecit in the outer layer. In this layer, the major balance of forces is between inertia and the Reynolds stresses. Following [60] we expand as follows:

$$u_1 = 1 + \hat{\epsilon} u_{11} + \hat{\epsilon}^2 (Ln(\hat{\epsilon})) u_{12L} + \hat{\epsilon}^2 u_{12} + \dots \; ; \tag{6.24a}$$

$$u_3 = \hat{\epsilon}^2 u_{31} + \hat{\epsilon}^3 (Ln(\hat{\epsilon})) u_{32L} \dots \; . \tag{6.24b}$$

In this expression, u_{11} is the "small defecit" discussed above, and the subscript $_L$ denotes the logarithmic term. The expansion for u_3 comes from balancing continuity, after the usual setting $x_3 = \hat{\epsilon}\bar{x}_3$ where $\bar{x}_3$ is of $\mathcal{O}(1)$. This allows us to find the displacement thickness to leading order (and in fact to some higher orders), but more formally and for higher order determination of the flow

field and displacement thicknesses, the unknown junction position x_{3J} should also be expanded asymptotically, as discussed briefly in [60, p.20]. These expansions and length scales suggest that δ_1 is of $\mathcal{O}(\hat{\epsilon}^2)$, and thus the expansion will be

$$\delta_1 = \hat{\epsilon}^2\hat{\delta}_1 + \hat{\epsilon}^3(Ln(\hat{\epsilon}))\hat{\delta}_{2L} + \hat{\epsilon}^3\hat{\delta}_2 + \dots \ . \tag{6.25}$$

Under the inlet conditions, we are sufficiently close to the entrance that the only change in pressure comes about locally due to an external displacement of the potential flow field. By the definition of δ_1, the slope of the TBL — and hence the displacement of the external flow field — is of $\mathcal{O}(\hat{\epsilon}^2)$. Therefore the external induced pressure near the edge must be of $\mathcal{O}(\hat{\epsilon}^2)$. Since pressure does not vary across the height of the TBL by (B.14), this is also the size of the internal flow field pressure, and hence:

$$p = \hat{\epsilon}^2 p_1 + \dots \ . \tag{6.26}$$

Armed with this information, the leading order balance of the x_1-momentum equation is:

$$\frac{\partial u_{11}}{\partial \bar{x}_3} = \begin{cases} a_2 \frac{\partial}{\partial \bar{x}_3}\left(\bar{x}_3^2\left(\frac{\partial u_{11}}{\partial \bar{x}_3}\right)^2\right) & \text{for } \bar{x}_3 < \bar{x}_{3J} \ , \\ a_1\hat{\delta}_1\frac{\partial^2 u_{11}}{\partial \bar{x}_3} & \text{for } \bar{x}_3 > \bar{x}_{3J} \ . \end{cases} \tag{6.27}$$

With the exception of a difference in normalising, (6.27) is the same as [60, (3.3b)], and we are thus able to quote the principal result: $\hat{\delta}_1 \propto x_1$. In fact, the prediction is that

$$\delta_1(x_1, x_2) = \hat{\epsilon}^2 x_1 + \mathcal{O}(\hat{\epsilon}^2 Ln(\hat{\epsilon})) \ , \tag{6.28}$$

from ([60, (3.18)]). Therefore — at the very least in an axisymmetric duct — we can suppose that the TBL will have grown to fill the duct by a distance of $\mathcal{O}(\hat{\epsilon}^{-2})$ downstream.

The correspondence between the inlet flow in a straight duct and the flow over a flat plate aligned with the flow is due in part to the simplicity of the duct cross-section and its straightness in this example, which together make the duct developable, as formally defined in Appendix B. The same is not true of a curved duct. Furthermore, interaction with the external flow will happen earlier than for a flat plate, as effectively any edge effects (from core turbulence, or centrifuging, *etc.*) are amplified as the edges approach one another towards the centre of the duct (see *e.g.* [67, p.605] and [82]).

Note that the neighbourhood of a corner in the cross-section has very strong curvature, breaking our assumptions, and leading to more complex behaviour than this essentially two-dimensional result, as mentioned in Appendix B.

6.5 Entry flow in a curved duct

Let us now return to the curved duct case, and consider the entry region. The short-scale analysis here deliberately omits the upstream influence effect described in §2.1 because our current concern is more with the flow properties relatively far downstream (at large x_1) on the short length scale. Further, we reiterate that the cross-sectional curvature is taken small in relation to the the boundary layer thickness, such that $h_3 \equiv 1$ and $K_3 \equiv 0$. Maintaining a constant, regular cross-section such that $K_1 = 0$ then ensures $h_2 = h_2(x_2)$ only. An axisymmetric duct would furthermore take $h_2 \equiv c \in \Re$. It is worth noting that though the duct will be assumed to have constant curvature, this is not to say that K_2 is constant. For example, in a duct of simple cross-section bending in a horizontal plane through the centre of each cross-section, it can

be shown that

$$K_2 = -\frac{f(x_2)}{R + f(x_2)} \,, \tag{6.29}$$

where R is the radius of curvature of the inside bend, and $f(x_2)$ is the unambiguous projection of the duct wall onto a horizontal plane through the centre of the duct. It is clear that in general K_2 will be a non-constant function of x_2 for such a duct. Note also that for a circular cross-section, the sign of (6.29) ensures that should Dean-type counter-rotating vortices with allied boundary layers exist, then they would have the correct orientation (see *e.g.* [7]).

With the above discussion in mind, the governing equations are:

$$\text{Cty:} \qquad \frac{1}{h_1}\frac{\partial u_1}{\partial x_1} + \frac{1}{h_2}\frac{\partial u_2}{\partial x_2} + \frac{\partial u_3}{\partial x_3} - K_2 u_2 = 0 \;; \tag{6.30a}$$

$$x_1\text{-mtm:} \quad \frac{u_1}{h_1}\frac{\partial u_1}{\partial x_1} + \frac{u_2}{h_2}\frac{\partial u_1}{\partial x_2} + u_3\frac{\partial u_1}{\partial x_3} - K_2 u_1 u_2 = -\frac{1}{h_1}\frac{\partial p}{\partial x_1} + \frac{1}{Re}\frac{\partial^2 u_1}{\partial x_3^2} + \frac{\partial}{\partial x_3}\left(B\frac{\partial u_1}{\partial x_3}\right) \;; \tag{6.30b}$$

$$x_2\text{-mtm:} \quad \frac{u_1}{h_1}\frac{\partial u_2}{\partial x_1} + \frac{u_2}{h_2}\frac{\partial u_2}{\partial x_2} + u_3\frac{\partial u_2}{\partial x_3} + K_2 u_1^2 = -\frac{1}{h_2}\frac{\partial p}{\partial x_2} + \frac{1}{Re}\frac{\partial^2 u_2}{\partial x_3^2} + \frac{\partial}{\partial x_3}\left(B\frac{\partial u_2}{\partial x_3}\right) \;; \tag{6.30c}$$

where B is given by equation (6.15a) and the equations are subject to the boundary conditions (6.16) and the junction boundary conditions previously described.

A simple solution when $K_2 = 0$ is $u_2 = 0$ and p known by mass-conservation. However, when $K_2 \neq 0$, it is clear that $u_2 = 0$ is no longer a solution, that is:

$$\text{duct curvature} \quad \Longrightarrow \quad \text{three-dimensional TBLs.} \tag{6.31}$$

It is also reasonable to wonder if $u_2 = u_1$ is a solution when there is a core flow such that $\boldsymbol{u}_\infty = (1, 1, 0)$. Some simple algebra shows that this is possible if and only if $K_2 = 0$. However, we shall later see that in the straight section

of the entry region, u_2 differs only by a multiplicative constant from u_1 in the outer layer.

6.5.1 The core flow perturbations

Knowledge of the form of the core flow in the entry region is also required for the matching as $\bar{x}_3 \to \infty$. Previously when studying the flow in the bend, we used cylindrical polar coordinates $(\tilde{\theta}, y, z)$ where: $\tilde{\theta} = 0+$ corresponds to the start of the bend and $\tilde{\theta}$ was considered to be of $\mathcal{O}(1)$; y is a vertical $\mathcal{O}(1)$ direction in the duct cross-section; and $z = r - a$ is an $\mathcal{O}(1)$ radial direction in the duct cross-section, where $a \gg 1$. Thus the distance traversed in the streamwise direction was of $\mathcal{O}(r \cdot \tilde{\theta}) = \mathcal{O}(a)$ and the duct was much longer than it was wide and tall (that is, it was slender). This geometry — and the velocity perturbations given for it below — will be referred to as "the full bend case".

To re-consider the entry section, we must take $\tilde{\theta} \ll 1$. However, as discussed in Part I, the entry section of the curved duct includes the end of the adjoining straight section where cylindrical polar coordinates are not necessarily a good choice of coordinates. To overcome this we will write all of our equations in terms of $\tilde{\theta}$ but declare that in the straight section, $x = \tilde{\theta}$ in effect where $\tilde{\theta}$ has been written as $\tilde{\theta} = \epsilon\theta$, $\epsilon \sim a^{-1}$ and velocities have been suitably normalised with terms of $\alpha \equiv a\epsilon \sim 1$. We note that $x \sim 1$ where $\tilde{\theta} \sim \epsilon$, and upstream influence is again omitted for the reason stated earlier. The normalisations and centrifuging terms in the equations will carry Λ terms, where $\Lambda \equiv 1$ in the bend and $\Lambda \equiv 0$ in the straight section, just as in Part I. Thus the derived and stated equations will hold in both the far-upstream and far-downstream parts of the entry region.

In the core flow when $\tilde{\theta} \sim 1$ we had the results that when

$$\begin{aligned} \tilde{U} &= 1 + \epsilon U + \dots \ , \\ \tilde{V} &= \epsilon V + \dots \ , \\ \tilde{W} &= \epsilon W + \dots \ , \end{aligned} \tag{6.32}$$

then the following are true:

- U is $\mathcal{O}(1)$ for all $\tilde{\theta}$;
- V, W, and the vorticity $R = W_y - V_z$ are proportional to $\tilde{\theta}$ for all $\tilde{\theta}$.

Thus as $\tilde{\theta} \to 0+$ we expect $\tilde{V} \sim \epsilon^2$, $\tilde{W} \sim \epsilon^2$ and $\left(\tilde{U} - 1\right) \sim \epsilon$. That is, we expect $V \to \epsilon \bar{V}$, $W \to \epsilon \bar{W}$ and $U = \bar{U}$ when $\tilde{\theta} \sim \epsilon$. Then the asymptotic limit as $\tilde{\theta} \to 0+$ of the core equations (2.31a–d) from the full $\tilde{\theta} \sim 1$ system is:

$$V_y + W_z = 0 \ ; \tag{6.33a}$$

$$U_\theta = 0 \ ; \tag{6.33b}$$

$$V_\theta = -p_{2y} \ ; \tag{6.33c}$$

$$W_\theta - 2\Lambda U = -p_{2z} \ . \tag{6.33d}$$

Now let us consider the core equations in the entry region, where we take:

$$\tilde{\theta} = \epsilon \bar{\theta} \ ; \tag{6.34a}$$

$$\tilde{U} = 1 + \epsilon \bar{U} + \dots \ ; \tag{6.34b}$$

$$\tilde{V} = \epsilon^2 \bar{V} + \dots \ ; \tag{6.34c}$$

$$\tilde{W} = \epsilon^2 \bar{W} + \dots \ ; \tag{6.34d}$$

$$\tilde{p} = 1 + \epsilon \bar{p}_1(\bar{\theta}) + \Lambda \frac{z}{a} \left(1 - \frac{z}{2a}\right) + \epsilon^2 \bar{p}_2(\bar{\theta}, y, z) + \dots \ , \tag{6.34e}$$

with the form of $\tilde{p}$ chosen to absorb some of the lower-order centrifuging terms, as we did in Part I. Substituting into the full Navier-Stokes equations we

obtain:

$$\bar{U}_{\bar{\theta}} = -\bar{p}_{1\bar{\theta}} \; ; \tag{6.35a}$$

$$\bar{V}_{\bar{\theta}} = -\bar{p}_{2y} \; ; \tag{6.35b}$$

$$\bar{W}_{\bar{\theta}} - 2\Lambda\bar{U} = -\bar{p}_{2z} \; . \tag{6.35c}$$

Recall that upstream influence is omitted, which accounts for the relative smallness of the $\bar{V}, \bar{W}$ effects. Furthermore, the continuity equation reduces to $\bar{U}_{\bar{\theta}} = 0$ which implies $-\bar{p}_{1\bar{\theta}} = 0$ in agreement with the above and ensures consistency of the continuity equation. We stress once more that our attention is on large values of $\bar{\theta}$, far downstream. The governing equations become:

$$\bar{U}_{\bar{\theta}} = 0 \; ; \tag{6.36a}$$

$$\bar{V}_{\bar{\theta}} = -\bar{p}_{2y} \; ; \tag{6.36b}$$

$$\bar{W}_{\bar{\theta}} - 2\Lambda\bar{U} = -\bar{p}_{2z} \; . \tag{6.36c}$$

Equation (6.36a) suggests that $U = U_I(y, z)$ over the entry region and the equation $\bar{U}_{\bar{\theta}} = 0$ as $\bar{\theta} \to \infty$ is consistent with $U_\theta = 0$ as $\theta \to 0$. This suggests that the weak θ-dependence of U in the bend emerges only as the swirl becomes comparable to the streamwise velocity perturbation. Matching also requires that

$$\lim_{\bar{\theta}\to\infty} \bar{p}_2 = \lim_{\theta\to 0} p_2 \quad , \quad \lim_{\bar{\theta}\to\infty} \bar{R} = \lim_{\theta\to 0} R \; , \tag{6.37}$$

where $\bar{R} = \bar{W}_y - \bar{V}_z$. Furthermore, since $\bar{U}$ is of $\mathcal{O}(1)$ for all $\bar{\theta}$, the term $\bar{W}_{\bar{\theta}}$ is effectively driven by a term of $\mathcal{O}(1)$, and so $\bar{W}$ is of $\mathcal{O}(\bar{\theta})$ as $\bar{\theta} \to \infty$. More formally, by cross-differentiation from (6.36b,c):

$$\bar{R}_{\bar{\theta}} - 2\Lambda\bar{U}_y = 0 \; , \tag{6.38}$$

and since $\bar{U}_y$ is of $\mathcal{O}(1)$ for all $\bar{\theta}$ we have $\bar{R}_{\bar{\theta}} \sim 1$ for all $\bar{\theta}$ as soon as $\Lambda \equiv 1$, *i.e.*:

$$\bar{R} \sim \bar{\theta} \quad \text{for all } \bar{\theta} \; . \tag{6.39}$$

Thus we see that the swirl increases linearly downstream of the entry region after the bend is entered, prior to which it remains constant. Consequently as $\bar{\theta} \to \infty$, the velocity components $\bar{V}, \bar{W} \to \infty$ in proportion to $\bar{\theta}$ and so the matching with the full bend case where $\tilde{V}, \tilde{W} \sim \epsilon$ is satisfied. Of course, since $\bar{U}_{\bar{\theta}} = 0$, the matching with $\tilde{U} = 1 + \epsilon U + \ldots$ is also assured.

It is worth noting that a perturbation of the order of ϵ^2 to the uniform streamwise flow (whilst retaining $\mathcal{O}(\epsilon^2)$ forms for $\tilde{V}$ and $\tilde{W}$) can easily be shown to be incorrect, since this yields potential flow equations far upstream of the entry region with no driving terms, and although $\bar{U}$ can grow sufficiently here to match with the full bend case, the downstream asymptotic matching for the swirl is impossible. The swirl grows linearly to match the next regime, and $\bar{U}$ remains of $\mathcal{O}(1)$. Equations (6.34a–e) are useful here because they determine the form of the external matching for the TBL in the entry region.

6.5.2 The boundary layer perturbations

Recalling the small parameter $\hat{\epsilon} = (Ln(Re))^{-1}$ in the TBL, we perturb the boundary layer velocities as follows:

$$u_1 = 1 + \hat{\epsilon}\hat{u}_1 \ldots \; ; \tag{6.40a}$$

$$u_2 = \hat{\epsilon}^2\hat{u}_2 \ldots \; ; \tag{6.40b}$$

$$u_3 = \hat{\epsilon}^2\hat{u}_3 \ldots \; . \tag{6.40c}$$

The form of the perturbations arise by considering an imposed disturbance about a uniform streamwise flow. We regard $\hat{\epsilon}, \epsilon$ as being comparable, at least in the initial argument, and then generalise this later. The $\mathcal{O}(\hat{\epsilon}^2)$ magnitude of the swirl (the magnitude of u_2 in effect) is taken to facilitate the eventual matching of u_2 with the external $\mathcal{O}(\epsilon^2)$ swirl, as will be described below. The

magnitude of u_3 stems from a balance of continuity.

We recall that $x_3 = \hat{\epsilon}\bar{x}_3$ and so as $\bar{x}_3 \to \infty$ we have $u_2 \to \tilde{Q}$, where $\tilde{Q}$ is either $\tilde{V}$ or $\tilde{W}$ in the previous formulation depending on location. Thus

$$\hat{u}_2 \to \beta^2 \bar{Q} \ , \tag{6.41a}$$

$$\text{where} \quad \beta = \hat{\epsilon}^{-1}\epsilon \ . \tag{6.41b}$$

The balancing parameter β, which here emerges naturally in the matching of the TBL velocities with the core flow, will be shown to be a vital parameter in the development of the TBL in the curved duct, leading to quantitatively different behaviour depending on its magnitude.

As above, we will impose the condition of constant cross-section as we run downstream — our duct is a prism, curved into a bend. This assumption of constant cross-section suggests that $h_2 = h_2(x_2)$ only, in which case $K_1 \equiv 0$. By definition (see Appendix B) therefore, x_2 has zero geodesic curvature, and as a consequence x_2 is a geodesic. Since the triad $(x_1, x_2, \bar{x}_3)$ is orthogonal, x_2 being a geodesic implies that the lines of x_1 are the geodesic parallels of x_2. A theorem of Gauss, quoted in [54, p.293], then yields the convenient result:

$$\begin{aligned} &h_2 \equiv 1 \ , \\ &\text{such that} \quad ds^2 = h_1^2 dx_1^2 + dx_2^2 + d\bar{x}_3^2 \ , \end{aligned} \tag{6.42}$$

which we shall use henceforth.

The size of the curvature term K_2 is important here. We have been careful throughout to ensure that the forms of the velocity expansions agree with the level of curvature. By reference to the fixed geometry of the duct in question — and by considering the fact that the core flow (at the wall) must satisfy the TBL equations (at the edge)— we conclude that $K_2 \sim \epsilon$. Note that this is a result of the magnitude of the radius of curvature of the duct inner wall which

serves as an order of magnitude for $K_2 = K_2(x_2)$. We will write

$$K_2 = \epsilon \hat{K}_2 \ . \tag{6.43}$$

What does this equation imply for the nature of h_1? Since by equation (B.11) h_1 is of $\mathcal{O}(1)$ (and clearly it must be by its definition) then equation (6.43) suggests

$$h_1 = 1 + \epsilon \bar{h}_1 \ . \tag{6.44}$$

In this way, for example,

$$K_2 = -\frac{1}{h_1 h_2}\frac{\partial h_1}{\partial x_2} = -\frac{1}{(1+\epsilon\bar{h}_1)\cdot 1}\epsilon\frac{\partial \bar{h}_1}{\partial x_2} = -\epsilon\frac{\partial \bar{h}_1}{\partial x_2} + \dots \ , \tag{6.45a}$$

that is:

$$\hat{K}_2 = -\frac{\partial \bar{h}_1}{\partial x_2} \ , \tag{6.45b}$$

and all occurences of h_1 will vanish from the leading order equations. This is really no different from the way in which the $\frac{1}{r}$ disappeared (or rather, was constant) to leading order in the equations in Part I.

The leading order balance of the continuity equation (6.30a) is then:

$$\frac{\partial \hat{u}_1}{\partial x_1} + \frac{\partial \hat{u}_3}{\partial \bar{x}_3} = 0 \ . \tag{6.46}$$

Note that the core flow satisfies this equation as $\bar{x}_3 \to \infty$.

Let us consider the order of magnitude of each of the terms in the x_1-

momentum equation (6.30b), based on the above discussion. We find that

$$\begin{aligned}
\tfrac{u_1}{h_1}\tfrac{\partial u_1}{\partial x_1} &\sim \hat{\epsilon}\ , \\
u_2\tfrac{\partial u_1}{\partial x_2} &\sim \hat{\epsilon}^3\ , \\
u_3\tfrac{\partial u_1}{\partial x_3} &\sim \hat{\epsilon}^2\ , \\
K_2 u_1 u_2 &\sim \epsilon\hat{\epsilon}^2\ , \\
\tfrac{1}{h_1}\tfrac{\partial p}{\partial x_1} &\sim \hat{\epsilon}\ \text{(to retain)}\ , \\
\tfrac{1}{Re}\tfrac{\partial^2 u_1}{\partial x_3^2} &\sim \hat{\epsilon}^{-1}Re^{-1} \ll \hat{\epsilon}\ , \\
\tfrac{\partial}{\partial x_3}\left(B\tfrac{\partial u_1}{\partial x_3}\right) &\sim \hat{\epsilon}^{-1}\mathcal{O}(B)\ .
\end{aligned} \tag{6.47}$$

Additionally, we must assume that $\frac{\partial u_1}{\partial x_2} \ll \hat{\epsilon}^{-1}$. We do not know at this stage the form of the pressure perturbation, but we do know that the pressure gradient must be retained here. We also must find the order of magnitude of the eddy viscosity, B, and expect it to be of $\mathcal{O}(\hat{\epsilon}^2)$ in order for it to balance the dominant inertia term on the left hand side, in which case we will write $B = \hat{\epsilon}^2\hat{B}$. Considering first the order of magnitude of the inner tier form of B from equation (6.15a) we see that

$$B \sim \hat{\epsilon}^2\left[1 - e^{-\text{large}}\right]\left[\left(\frac{\hat{\epsilon}}{\hat{\epsilon}}\right)^2 + \left(\frac{\hat{\epsilon}^2}{\hat{\epsilon}}\right)^2\right]^{\frac{1}{2}}\ , \tag{6.48a}$$

$$i.e.:\quad B \sim \hat{\epsilon}^2\ , \tag{6.48b}$$

$$\text{and}\quad \hat{B} = a_2\bar{x}_3^2\frac{\partial\hat{u}_1}{\partial\bar{x}_3} \qquad \text{for}\quad \bar{x}_3 < \bar{x}_{3J}\ . \tag{6.48c}$$

In the outer tier, we note that the factor u_t is of $\mathcal{O}(1)$ and consider δ_1:

$$\delta_1 = \int_0^\infty 1 - \frac{(u_1^2 + u_2^2)^{\frac{1}{2}}}{(u_{1e}^2 + u_{2e}^2)^{\frac{1}{2}}}\,dx_3\ . \tag{6.49}$$

The denominator is of $\mathcal{O}(1)$, x_3 is of $\mathcal{O}(\hat{\epsilon})$, the velocity expansions ensure the terms of $\mathcal{O}(1)$ cancel, and so we conclude that:

$$\delta_1 = \hat{\epsilon}^2\hat{\delta}_1 + \mathcal{O}(\hat{\epsilon}^2 Ln(\hat{\epsilon}))\ . \tag{6.50}$$

Thus in the outer layer we have confirmed that $B = \hat{\epsilon}^2 \hat{B}$ with

$$\hat{B} = a_1 \hat{\delta}_1 \qquad \text{for} \quad \bar{x}_3 > \bar{x}_{3J} \ . \tag{6.51}$$

The leading order balance of the x_1-momentum equation is thus:

$$\frac{\partial \hat{u}_1}{\partial x_1} = -\frac{\partial p}{\partial x_1} + \frac{\partial}{\partial \bar{x}_3} \begin{cases} a_2 \bar{x}_3^2 \left(\frac{\partial \hat{u}_1}{\partial \bar{x}_3} \right)^2 & , \quad \bar{x}_3 < \bar{x}_{3J} \ , \\ a_1 \hat{\delta}_1 \frac{\partial \hat{u}_1}{\partial \bar{x}_3} & , \quad \bar{x}_3 > \bar{x}_{3J} \ . \end{cases} \tag{6.52}$$

Since the core flow, where all stresses vanish, must satisfy these equations, we can conclude that

$$-\frac{\partial p}{\partial x_1} = \frac{\partial \hat{u}_{1e}}{\partial x_1} \ , \tag{6.53}$$

because the pressure field p does not vary across the height of the TBL from (B.14). Although in general this matching involves a factor of β, we know that

$$\frac{\partial \hat{u}_{1e}}{\partial x_1} \equiv 0 \tag{6.54}$$

in the entry region because $\bar{U}_{\bar{\theta}}|_{y,z \to 0} = 0$ there. The pressure gradient thus disappears at this level, and we are left with:

$$\frac{\partial \hat{u}_1}{\partial x_1} = \begin{cases} a_2 \frac{\partial}{\partial \bar{x}_3} \left(\bar{x}_3 \frac{\partial \hat{u}_1}{\partial \bar{x}_3} \right)^2 & , \quad \bar{x}_3 < \bar{x}_{3J} \ , \\ a_1 \hat{\delta}_1 \frac{\partial^2 \hat{u}_1}{\partial \bar{x}_3^2} & , \quad \bar{x}_3 > \bar{x}_{3J} \ . \end{cases} \tag{6.55}$$

The x_2-momentum equation is complicated by the retention of the $K_2 u_1^2$ term to leading order. In the core flow, the analagous term was $\Lambda \frac{\tilde{U}^2}{a}$ which, since $\tilde{U} = 1 + \ldots$, yielded a term of $\mathcal{O}(a^{-1}) = \mathcal{O}(\epsilon)$, whilst the rest of the equation was of $\mathcal{O}(\epsilon^2)$. This necessitated including a $\Lambda \frac{z}{a}$ term in the pressure expansion in order that the momentum equation could be balanced to leading order in ϵ^2. A naïve examination of the x_2-momentum equation (6.30c) gives:

$$\hat{\epsilon}^2 \left[\frac{\partial \hat{u}_2}{\partial x_1} \right] + \epsilon [\hat{K}_2] + \hat{\epsilon} [2 \epsilon \hat{K}_2 \hat{u}_1] + \mathcal{O}(\epsilon \hat{\epsilon}^2) = -\frac{\partial p}{\partial x_2} + \hat{\epsilon}^2 \left[\frac{\partial}{\partial \bar{x}_3} \left(\hat{B} \frac{\partial \hat{u}_2}{\partial \bar{x}_3} \right) \right] \tag{6.56}$$

Once again we need to incorporate a curvature term into the pressure expansion. This was relatively easy in the core since we had a specific wall geometry, and with the result (6.44) it is easy here also. Firstly, it is clear that the pressure gradient in the x_2-direction must be of $\mathcal{O}(\hat{\epsilon}^2)$ in order to be retained to leading order. Then, recalling that $\bar{h}_1 = \bar{h}_1(x_2)$ only, the expansion for the pressure p is

$$p = \hat{p}_0 + \hat{\epsilon}\hat{p}_1(x_1) + \epsilon\bar{h}_1 + \hat{\epsilon}^2\hat{p}_2(x_1, x_2) + \dots \ , \tag{6.57}$$

where the constant $\hat{p}_0$ is known from the straight section upstream, and we have already shown that $\frac{d\hat{p}_1}{dx_1} = \frac{\partial \hat{u}_{1e}}{\partial x_1} \equiv 0$. Furthermore, since the core flow satisifies the equations at the edge, we observe that

$$-\frac{\partial \hat{p}_2}{\partial x_2} = \frac{\partial \hat{u}_{2e}}{\partial x_1} + 2\beta\hat{K}_2\hat{u}_{1e} \ . \tag{6.58}$$

Note here the explicit appearance of β and its implicit influence in both terms involving edge values. Hence p is known to all relevant orders, and the x_2-momentum equation becomes:

$$\frac{\partial \hat{u}_2}{\partial x_1} + 2\beta\hat{K}_2\hat{u}_1 = \left(\frac{\partial \hat{u}_{2e}}{\partial x_1} + 2\beta\hat{K}_2\hat{u}_{1e}\right) + \begin{cases} a_2 \frac{\partial}{\partial \bar{x}_3}\left(\bar{x}_3^2 \frac{\partial \hat{u}_1}{\partial \bar{x}_3}\frac{\partial \hat{u}_2}{\partial \bar{x}_3}\right) & , \quad \bar{x}_3 < \bar{x}_{3J} \ , \\ a_1\hat{\delta}_1 \frac{\partial^2 \hat{u}_2}{\partial \bar{x}_3^2} & , \quad \bar{x}_3 > \bar{x}_{3J} \ . \end{cases} \tag{6.59}$$

It is clear that the governing equations have become quasi-two dimensional, in the sense that we can independently solve (6.55) for $\hat{u}_1$, before solving (6.59) for $\hat{u}_2$ with known $\hat{u}_1$ (consistent with this cross-flow being an order of magnitude smaller than the main flow), before finally solving the continuity equation (6.46) for $\hat{u}_3$.

However, the appearance of β in the equations, its hidden influence through the pressure gradients, and such equations as (6.41a,b), seem to suggest the

existence of at least three regimes of interest — $\beta \ll 1$, $\beta \sim 1$, $\beta \gg 1$ — and that three different sets of equations, with three different sets of boundary conditions, will need to be considered in the entry region. This *is not the case*, as we will see in our analysis of the governing equations (6.55) and (6.59) in the next chapter.

Chapter 7

Analysis of the turbulent boundary layer in a curved duct

In this chapter we explore the solutions of the governing equations of the three-dimensional TBLs in a curved duct, (6.55) and (6.59), in a variety of parameter regimes via analytical and numerical methods. The numerical strategies in Chapter 7, which involve no more than standard finite-differencing, show that surprising results are obtained for the cross-flow.

The numerical computation of TBLs in three dimensions has been much studied. Various approaches are possible with two alternatives being direct computation from either the Navier-Stokes equations or from the boundary layer equations. An improvement to both is the "wall function method" developed in [90] from earlier work. The benefits of such an approach can be seen in computations of the near-wall flow, since perhaps a 50% reduction (claimed by [90]) in the grid refinement required in this region is attainable. Although we do not consider a numerical evaluation in this region, we should mention that the wall function method was put on an important footing by [26].

7.1 The β-split

As we discussed at the end of the previous chapter, it seems that to solve the governing equations (6.55) and (6.59) three different regimes corresponding to the order of magnitude of β need to be considered. One possibility to resolve this predicament is a scaling of $\bar{x}_3$. However, it is fairly easy to show that this leads to a contradiction on the size of $\hat{\delta}_1$ in different β-regimes. In fact, we can find *exact* solutions — not just asymptotic expansions — which enable us to study but one solution space for all three different regimes in the entry region.

We will refer to the following exact solutions of equations (6.55 & 6.59) as the *β-split*:

$$\hat{u}_1 = \beta\tilde{u}_1 + 1 \cdot \tilde{\tilde{u}}_1 \; ; \tag{7.1a}$$

$$\hat{u}_2 = \beta^2\tilde{u}_2 + \beta\tilde{\tilde{u}}_2 \; , \tag{7.1b}$$

where $\tilde{\tilde{u}}_i \to 0$ for $i = 1, 2$ as $\bar{x}_3 \to \infty$ such that the upper boundary conditions on $\hat{u}_i$ are satisfied by $\tilde{u}_i$. That is, $\hat{u}_{1e} = \beta\tilde{u}_1|_{\bar{x}_3 \to \infty}$ and similarly for $\hat{u}_{2e}$. However, we have already seen that $\hat{u}_{1e} = \beta U|_{\text{wall}}$ such that the edge value of $\tilde{u}_1$ identifies very naturally and simply with $U|_{\text{wall}}$, and similarly for $\tilde{u}_2$ and Q. Furthermore, $\tilde{\tilde{u}}_i$ will accommodate the lower boundary conditions, as will be discussed below.

The β-split emerges naturally when one considers the nature of the matching of $\hat{u}_1$ and $\hat{u}_2$ with the core flow. We know that $\hat{u}_1 \sim \beta$ at the edge, and that it is a function of x_2 only there, by the nature of the core flow. But it is clear that $\hat{u}_1$ must also have an $\mathcal{O}(1)$ component to account for the lower boundary condition on u_1 of no slip. Similarly, a consideration of (6.59) shows that $\hat{u}_2$ is driven by $\beta^2 \left(\frac{\partial Q}{\partial x_2}\Big|_{\text{wall}} + 2\hat{K}_2 U\Big|_{\text{wall}} \right)$ and also by $2\beta\hat{K}_2\hat{u}_1$, suggesting that $\hat{u}_2$ is driven by an $\mathcal{O}(\beta^2)$ term and an $\mathcal{O}(\beta)$ term, prompting the form of

(7.1b).

The full benefits of this approach have yet to be described here, and at first sight it appears to be an added complication, as we have replaced two variables by four. However, we claim the following simplification of (7.1a,b):

$$\tilde{u}_1 \equiv \tilde{u}_{1e} \; ; \tag{7.2a}$$

$$\tilde{u}_2 \equiv \tilde{u}_{2e} \; . \tag{7.2b}$$

In other words, $\tilde{u}_1$ and $\tilde{u}_2$ are independent of $\bar{x}_3$, and we are left with only two variables to solve for, namely $\tilde{\tilde{u}}_1$ and $\tilde{\tilde{u}}_2$. In the process of examining the various β-balances of the equations, we will prove (7.2a,b) and examine the consequences of substituting the solution (7.1a,b) into (6.55 & 6.59).

Checking on (7.2a,b)

The $\mathcal{O}(1)$ balance of (6.55) is:

$$\frac{\partial \tilde{\tilde{u}}_1}{\partial x_1} = \begin{cases} a_2 \frac{\partial}{\partial \bar{x}_3} \left(\left(\bar{x}_3 \frac{\partial \tilde{\tilde{u}}_1}{\partial \bar{x}_3} \right)^2 \right) & , \quad \bar{x}_3 < \bar{x}_{3J} \; , \\ a_1 \hat{\delta}_1 \frac{\partial^2 \tilde{\tilde{u}}_1}{\partial \bar{x}_3^2} & , \quad \bar{x}_3 > \bar{x}_{3J} \; , \end{cases} \tag{7.3}$$

while the $\mathcal{O}(\beta)$ balance is:

$$\frac{\partial \tilde{u}_1}{\partial x_1} = \begin{cases} a_2 \frac{\partial}{\partial \bar{x}_3} \left(2 \bar{x}_3^2 \frac{\partial \tilde{u}_1}{\partial \bar{x}_3} \frac{\partial \tilde{\tilde{u}}_1}{\partial \bar{x}_3} \right) & , \quad \bar{x}_3 < \bar{x}_{3J} \; , \\ a_1 \hat{\delta}_1 \frac{\partial^2 \tilde{u}_1}{\partial \bar{x}_3^2} & , \quad \bar{x}_3 > \bar{x}_{3J} \; , \end{cases} \tag{7.4}$$

and the $\mathcal{O}(\beta^2)$ balance is:

$$0 = \begin{cases} a_2 \frac{\partial}{\partial \bar{x}_3} \left(\left(\bar{x}_3 \frac{\partial \tilde{u}_1}{\partial \bar{x}_3} \right)^2 \right) & , \quad \bar{x}_3 < \bar{x}_{3J} \; , \\ 0 & , \quad \bar{x}_3 > \bar{x}_{3J} \; . \end{cases} \tag{7.5}$$

Before we examine the x_2-momentum equations, notice that β is still not appearing explicitly in the equations governing $\hat{u}_1$. In addition, equation (7.3) is

implying that $\tilde{\tilde{u}}_1$ is slowed by the stress at the wall. In reality, the stress will vary due to curvature, and this is linked with the buoyancy idea discussed in Appendix B. Furthermore, in an effort to establish (7.2a), let:

$$\tilde{u}_1 = \tilde{u}_{1e} + \tilde{u}_{1b} \ , \tag{7.6a}$$

$$\text{where clearly} \quad \frac{\partial \tilde{u}_{1e}}{\partial \bar{x}_3} \equiv 0 \quad \text{by definition,} \tag{7.6b}$$

$$\text{and} \quad \frac{\partial \tilde{u}_{1e}}{\partial x_1} \equiv 0 \quad \text{by the matching with the core flow,} \tag{7.6c}$$

and $\tilde{u}_{1b} \to 0$ as $\bar{x}_3 \to \infty$. This form — with an $\mathcal{O}(1)$ variation from the edge value — is consistent with the claim that $\tilde{u}_1$ is part of an *exact* solution for $\hat{u}_1$. Consequently, equation (7.4) becomes:

$$\frac{\partial \tilde{u}_{1b}}{\partial x_1} = \begin{cases} a_2 \frac{\partial}{\partial \bar{x}_3} \left(2\bar{x}_3^2 \frac{\partial \tilde{u}_{1b}}{\partial \bar{x}_3} \frac{\partial \tilde{\tilde{u}}_1}{\partial \bar{x}_3} \right) & , \quad \bar{x}_3 < \bar{x}_{3J} \ , \\ a_1 \hat{\delta}_1 \frac{\partial^2 \tilde{u}_{1b}}{\partial \bar{x}_3^2} & , \quad \bar{x}_3 > \bar{x}_{3J} \ , \end{cases} \tag{7.7}$$

and equation (7.5) becomes:

$$0 = \begin{cases} a_2 \frac{\partial}{\partial \bar{x}_3} \left(\left(\bar{x}_3 \frac{\partial \tilde{u}_{1b}}{\partial \bar{x}_3} \right)^2 \right) & , \quad \bar{x}_3 < \bar{x}_{3J} \ , \\ 0 & , \quad \bar{x}_3 > \bar{x}_{3J} \ . \end{cases} \tag{7.8}$$

The inner part of equation (7.8) has the solution

$$\tilde{u}_{1b} = c_1 \cdot Ln(\bar{x}_3) \ , \tag{7.9}$$

for some function $c_1(x_1, x_2)$, for all $\bar{x}_3$ in the inner layer. We will now show that this leads to a contradiction on the no-slip condition at the lower boundary unless $c_1 \equiv 0$, in which case we will have proved (7.2a).

As $\bar{x}_3 \to 0+$ we enter the lower tier when $\bar{x}_3 \to Re^{-1}\hat{\epsilon}^{-2}\tilde{x}_3$ (see for example [60, p.23]), and the above equation then suggests

$$\tilde{u}_{1b} \sim -c_1 Ln(Re) - 2c_1 Ln(\hat{\epsilon}) + c_1 Ln(\tilde{x}_3) \ . \tag{7.10}$$

This means that, from the original expansion of u_1,

$$\begin{aligned} u_1 &= 1 + \hat{\epsilon}(\beta\tilde{u}_1 + \tilde{\tilde{u}}_1) + \dots \ , \\ &= 1 + \epsilon\tilde{u}_1 + \hat{\epsilon}\tilde{\tilde{u}}_1 + \dots \ , \\ &\sim 1 + \epsilon\tilde{u}_{1e} - c_1\beta - 2c_1\epsilon Ln(\hat{\epsilon}) + \epsilon c_1 Ln(\tilde{x}_3) + \dots \quad \text{as we enter the inner tier.} \end{aligned} \tag{7.11}$$

But if $\beta \gg 1$ we have a contradiction as then $u_1 \nrightarrow 0$ as $x_3 \to 0+$ whenever $c_1 \not\equiv 0$. Since we require the solutions (7.2a,b) to work for all orders of β, we must take $c_1 \equiv 0$, giving the solution $\tilde{u}_{1b} \equiv 0$ in the inner layer. Clearly, the solution $\tilde{u}_{1b} \equiv 0$ also satisfies trivially the outer part of (7.7), and also all the boundary conditions, including matching across the junction with the zero form in the inner part. Hence we have established (7.2a). As an aside, let us note that we will shortly show that

$$\tilde{\tilde{u}}_1 \sim Ln(\bar{x}_3) - \beta\bar{U}_w(x_1, x_2) \ , \tag{7.12}$$

as $\bar{x}_3 \to 0+$, where $\bar{U}_w$ is the streamwise core flow at the wall, as usual. Consequently, together with (7.2a) we see that:

$$u_1 \sim 1 - \hat{\epsilon}Ln(Re) - 2\hat{\epsilon}Ln(\hat{\epsilon}) + \hat{\epsilon}Ln(\tilde{x}_3) - \epsilon\bar{U}_w + \epsilon\bar{U}_w \dots \ , \tag{7.13}$$

with the first two terms (as presented) cancelling since $\hat{\epsilon} = (Ln(Re))^{-1}$, and the last two terms (as presented) also clearly cancelling, as are required to satisfy the no-slip condition.

We next examine the various balances of the x_2-momentum equations (6.59), after making the substitutions (7.1a,b). There is now no longer any higher order balance analagous to (7.5) to give us the behaviour of $\tilde{u}_2$. Instead, we obtain the following balances.

First, to $\mathcal{O}(\beta)$:

$$\frac{\partial \tilde{\tilde{u}}_2}{\partial x_1} + 2\hat{K}_2 \tilde{\tilde{u}}_1 = \begin{cases} a_2 \frac{\partial}{\partial \bar{x}_3}\left(\bar{x}_3^2 \frac{\partial \tilde{\tilde{u}}_1}{\partial \bar{x}_3} \frac{\partial \tilde{\tilde{u}}_2}{\partial \bar{x}_3}\right) & , \quad \bar{x}_3 < \bar{x}_{3J} \ , \\ a_1 \hat{\delta}_1 \frac{\partial^2 \tilde{\tilde{u}}_2}{\partial \bar{x}_3^2} & , \quad \bar{x}_3 > \bar{x}_{3J} \ ; \end{cases} \tag{7.14}$$

and to $\mathcal{O}(\beta^2)$:

$$\frac{\partial \tilde{u}_2}{\partial x_1} = \frac{\partial \tilde{u}_{2e}}{\partial x_1} + \begin{cases} a_2 \frac{\partial}{\partial \bar{x}_3}\left(\bar{x}_3^2 \frac{\partial \tilde{\tilde{u}}_1}{\partial \bar{x}_3} \frac{\partial \tilde{u}_2}{\partial \bar{x}_3}\right) & , \quad \bar{x}_3 < \bar{x}_{3J} \ , \\ a_1 \hat{\delta}_1 \frac{\partial^2 \tilde{u}_2}{\partial \bar{x}_3^2} & , \quad \bar{x}_3 > \bar{x}_{3J} \ . \end{cases} \tag{7.15}$$

Note that there has been some cancellation of the terms on the righthand side, and that, importantly, β no longer appears explicitly in the equations. Also note that both equations are satisfied at the edge of the TBL as $\bar{x}_3 \to \infty$ where all stresses are zero. In order to establish (7.2b) we postulate, analogously to the earlier (7.6a), that

$$\tilde{u}_2 = \tilde{u}_{2e} + \tilde{u}_{2b} \ , \tag{7.16a}$$

$$\text{where} \quad \frac{\partial \tilde{u}_{2e}}{\partial \bar{x}_3} \equiv 0 \quad \text{by definition,} \tag{7.16b}$$

and $\tilde{u}_{2b} \to 0$ as $\bar{x}_3 \to \infty$. The postulate encompasses the assumption that $\tilde{u}_{2b}$ is not a constant, and we will now derive a contradiction to this assumption. The $\mathcal{O}(\beta^2)$ balance then yields:

$$\frac{\partial \tilde{u}_{2b}}{\partial x_1} = \begin{cases} a_2 \frac{\partial}{\partial \bar{x}_3}\left(\bar{x}_3^2 \frac{\partial \tilde{\tilde{u}}_1}{\partial \bar{x}_3} \frac{\partial \tilde{u}_{2b}}{\partial \bar{x}_3}\right) & , \quad \bar{x}_3 < \bar{x}_{3J} \ , \\ a_1 \hat{\delta}_1 \frac{\partial^2 \tilde{u}_{2b}}{\partial \bar{x}_3^2} & , \quad \bar{x}_3 > \bar{x}_{3J} \ . \end{cases} \tag{7.17}$$

This equation suggests that as $\bar{x}_3 \to 0+$:

$$0 = \frac{\partial}{\partial \bar{x}_3}\left(\bar{x}_3^2 \frac{1}{\bar{x}_3} \frac{\partial \tilde{u}_{2b}}{\partial \bar{x}_3}\right) \ . \tag{7.18}$$

We can then conclude that

$$\tilde{u}_{2b} \sim c_2 Ln(\bar{x}_3) \quad \text{as} \quad \bar{x}_3 \to 0+ \ , \tag{7.19}$$

where $c_2 \neq 0$. This leading order behaviour near the wall, upon substitution into the original expansion of u_2, gives:

$$u_2 \sim \epsilon^2 \tilde{u}_{2e} + \epsilon^2 c_2 Ln(\bar{x}_3) + \epsilon\hat{\epsilon}\tilde{\tilde{u}}_2 + \dots \,, \tag{7.20}$$

and to satisfy the no-slip condition we require $u_2 \equiv 0$ on $\bar{x}_3 = 0$. Since $c_2 \neq 0$ then $u_2 \to \epsilon^2 c_2 Ln(\bar{x}_3)$ as $\bar{x}_3 \to 0+$, leading to a contradiction. That is, if $\tilde{u}_{2b}$ is not a constant, then it satisfies nontrivially (7.17), which predicts a leading order behaviour for $\tilde{u}_{2b}$ which contradicts the no-slip condition. Therefore, we conclude $\tilde{u}_{2b} \equiv 0$, as although any constant satisfies the equations (7.17), only $\tilde{u}_{2b} \equiv 0$ satisfies also the boundary condition as $\bar{x}_3 \to \infty$. Hence:

$$\tilde{u}_2 \equiv \tilde{u}_{2e} \quad \text{exactly.} \tag{7.21}$$

Again, we will later show that

$$\tilde{\tilde{u}}_2 \sim \frac{2}{a_2}\hat{K}_2 \bar{x}_3 Ln(\bar{x}_3) - \beta\tilde{u}_2 \quad \text{as} \quad \bar{x}_3 \to 0+ \,, \tag{7.22}$$

such that

$$u_2 = \epsilon^2 \tilde{u}_2 + \epsilon\hat{\epsilon}\frac{2}{a_2}\hat{K}_2 \bar{x}_3 Ln(\bar{x}_3) - \epsilon^2\tilde{u}_2 + \dots \,, \tag{7.23}$$

with the first and last terms, as presented here, cancelling in order that u_2 satisfies the no-slip condition.

We have thus established that throughout the outer layer $\tilde{u}_1$ and $\tilde{u}_2$ simply retain their edge values — where they identify exactly with the values of the core flow at the wall — and our task is reduced to solving (7.3) for $\tilde{\tilde{u}}_1$ and (7.14) for $\tilde{\tilde{u}}_2$. The main factor β has completely disappeared from the equations, as have the pressure terms, the matching with the core is accommodated, the lower boundary conditions will be considered shortly, and (7.14) retains its nontriviality since a term in $\hat{K}_2$ is still present (so that $\tilde{\tilde{u}}_2 \equiv 0$ is not a solution).

Further analysis

Before we go on to solve the equations, we have to specify the lower boundary conditions. Returning for a moment to the equations (6.55) and (6.59) we can determine the lower boundary conditions on $\hat{u}_1$ and $\hat{u}_2$. As $\bar{x}_3 \to 0+$, the inertia and pressure terms are small in comparison with the turbulent stress terms. Starting with (6.55), this yields the equation:

$$0 = \frac{\partial}{\partial \bar{x}_3}\left(\left(\bar{x}_3 \frac{\partial \hat{u}_1}{\partial \bar{x}_3}\right)^2\right) . \tag{7.24}$$

This equation gives the following near-wall asymptote, after solving and examining balances as $\bar{x}_3 \to \hat{\epsilon}^{-2} Re^{-1} \tilde{x}_3$:

$$\hat{u}_1 \sim c_3 Ln(\bar{x}_3) + k_1(x_1, x_2) , \tag{7.25}$$

where $c_3 \equiv 1$ so that as the inner tier is entered the leading order identically unity part of the velocity expansion is cancelled, and where the unknown deficit function k_1 of $\mathcal{O}(1)$ can be determined at a later stage by expanding in the inner tier. Equation (6.59) behaves slightly differently as the wall is approached, because the centrifuging term also remains, given that we now know $\hat{u}_1$ is large as $\bar{x}_3 \to 0+$. That is we have:

$$2\hat{K}_2 \hat{u}_1 = a_2 \frac{\partial}{\partial \bar{x}_3}\left(\bar{x}_3^2 \frac{\partial \hat{u}_1}{\partial \bar{x}_3}\frac{\partial \hat{u}_2}{\partial \bar{x}_3}\right) . \tag{7.26}$$

With the asymptotic behaviour of $\hat{u}_1$ from (7.25), equation (7.26) yields the behaviour

$$\hat{u}_2 \sim \frac{2\hat{K}_2}{a_2}((\bar{x}_3 + c_4)Ln(\bar{x}_3) + (d_1 - 2)\bar{x}_3 + d_2) , \tag{7.27}$$

involving the unknown constants c_4, d_1, d_2.

Then the asymptote for $\tilde{\tilde{u}}_1$ is:

$$\tilde{\tilde{u}}_1 \sim Ln(\bar{x}_3) + k_1(x_1, x_2) - \beta \bar{U}_w(x_2) , \tag{7.28}$$

which can be tidied up by setting $\bar{k}_1 = k_1 - \beta \bar{U}_w$, if desired. Later on, we shall further determine k_1. In a similar fashion, we have:

$$\tilde{\tilde{u}}_2 \sim \frac{2\hat{K}_2}{a_2} \bar{x}_3 Ln(\bar{x}_3) + k_2(x_1, x_2) - \beta^2 \bar{Q}_w \ . \tag{7.29}$$

The interpretation of (7.28) and (7.29) is that the deficit functions k_i are influenced by the edge values, and that these influenced $\mathcal{O}(1)$ parts are what the inner tier feels when examined on a smaller length scale. This suggests that there will be some edge effects, x_2-dependence, and some cancelling of the edge values, even on the shorter length scale much closer to the wall. The viscous sublayer has been shown elsewhere to be more sensitive to external influences in other respects, such as the sensitivity of A^+ (see *e.g.* [41]).

The spatial growth rate of the TBL, measured to an extent by $\hat{\delta}_1$ as introduced in equation (6.50), is as follows. Expanding the integrand of (6.49) we see that

$$\hat{\delta}_1 = \int_0^\infty (\hat{u}_{1e} - \hat{u}_1) \ d\bar{x}_3 \ . \tag{7.30}$$

But then the β-split has $\hat{u}_1 = \beta \tilde{u}_1 + \tilde{\tilde{u}}_1$, where $\hat{u}_{1e} \equiv \beta \tilde{u}_1$, so that

$$\hat{\delta}_1 = \int_0^\infty (-\tilde{\tilde{u}}_1) \ d\bar{x}_3 \ . \tag{7.31}$$

Then an integration of (7.3) across the layer proceeds as follows:

$$\int_0^\infty \frac{\partial \tilde{\tilde{u}}_1}{\partial x_1} \ d\bar{x}_3 = a_1 \hat{\delta}_1 \left(\frac{\partial \tilde{\tilde{u}}_1}{\partial \bar{x}_3} \right) \Big|_{\bar{x}_3 \to \infty} - a_2 \left(\bar{x}_3 \frac{\partial \tilde{\tilde{u}}_1}{\partial \bar{x}_3} \right) \Big|_{\bar{x}_3 \to 0+} \ . \tag{7.32}$$

Since $\tilde{\tilde{u}}_1 \to 0$ on approach to the edge of the TBL, and since we have the lower boundary condition (7.28) as well as continuity of $\tilde{\tilde{u}}_1$ across the junction, we can establish from the definition (7.30) that

$$\frac{\partial \hat{\delta}_1}{\partial x_1} = a_2 \cdot (1) \tag{7.33a}$$

$$\Longrightarrow \ \hat{\delta}_1 = a_2 x_1 \ . \tag{7.33b}$$

We are now in a position to solve equations (7.3) and (7.14) and we have noted that they are independent of β and so we need only search in one solution space. However, the *interpretation* of (7.3 & 7.14) together with the β-split (7.1a,b) is of course dependent on the size of β and yields three interpretations in the entry region, and three qualitatively and quantitatively different regimes far downstream, as follows.

- If $\beta \ll 1$ the solutions from equations (7.3) and (7.14) dominate, and the edge effects are weak since the curvature-induced swirl is weak in comparison to the magnitude of the turbulent fluctuations. The scalings in (7.1a,b) ensure that the curvature is driving only a relatively small cross-flow. The result (7.33b) suggests that a new stage will develop at $\hat{\epsilon}^{-1}$ ($\ll \epsilon^{-1}$) when the TBL grows to fill the duct. This merged or merging case will be the subject of the subsequent chapter.

- If $\beta \sim 1$, both curvature and turbulence are important and the behaviour of the TBL in the entry region depends on the solution of equations (7.3) and (7.14) and on the $\bar{x}_3$-independent core terms carried down from the edges. There will be a new stage at $\hat{\epsilon}^{-1} \sim \epsilon^{-1}$ when interaction of the TBL and the core occurs. This is a *weak* form of interaction as defined by [67, p.377]. It is likely that at this stage an amendment to the Cebeci-Smith model would need to be considered in order to account for the interaction, and the influence of the curvature at this new length scale. It is at present unclear what form such a modification would take, but likely candidates involve modified buoyancy-like terms as mentioned in Appendix B and expanded upon briefly here. The inner and outer expressions for the eddy-viscosity can be modified by multiplying each

by S^2, where

$$S = \frac{1}{1+jRi} \quad , \quad Ri = \frac{2u_1}{a}\left(\frac{\partial u_1}{\partial y}\right)^{-1} \tag{7.34}$$

where a is the radius of curvature as before, and $j = 7$ for convex walls and $j = 4$ for concave walls. This modification was introduced in [11] wherein also it was found experimentally that modification is required when the streamline curvature exceeds a certain threshold in relation to the total boundary layer thickness δ_{99}; in particular when $\frac{\delta_{99}}{a} > \frac{1}{300}$. This is certainly not the case in the entry region where the threshold is exceed only if the Reynolds number is of $\mathcal{O}(10^2)$, but would become important further downstream in the $\beta \sim 1$ case.

- Finally, if $\beta \gg 1$ the core flow dominates the TBL solutions (from (7.1a,b)), which is to be expected, since in this case the interpretation is that the turbulence is weak. There will be a new stage at ϵ^{-1} ($\ll \hat{\epsilon}^{-1}$) when the core becomes fully developed and the TBL remains thin. In this case, there will be no real impact on the core flow results presented in Chapter 2 since the TBL is thin throughout the bend under consideration.

In the next section, we present similarity solutions of (7.3) and (7.14) for $\tilde{\tilde{u}}_1$ and $\tilde{\tilde{u}}_2$.

7.2 Similarity solutions

7.2.1 Solution for $\tilde{\tilde{u}}_1$

In the far field downstream, beyond any entry effects near the start of the bend (see *e.g.* [67, pp658ff]), similarity solutions can be expected for $\tilde{\tilde{u}}_1$ and $\tilde{\tilde{u}}_2$. We

suppose that

$$\begin{aligned} \tilde{\tilde{u}}_1 &= \tilde{\tilde{u}}_1\,(y, x_2)\ , \\ \text{where we define} \quad y &= \frac{\bar{x}_3}{x_1}\ , \end{aligned} \tag{7.35}$$

and furthermore that the x_2-dependence is separable from the y-dependence. Therefore we have:

$$\tilde{\tilde{u}}_1 = \bar{f}(x_2) f(y)\ . \tag{7.36}$$

This change of variables yields:

$$\frac{\partial \tilde{\tilde{u}}_1}{\partial x_1} = -\frac{1}{x_1} \bar{f} y f'\ ; \tag{7.37a}$$

$$\frac{\partial \tilde{\tilde{u}}_1}{\partial \bar{x}_3} = \frac{1}{x_1} \bar{f} f'\ ; \tag{7.37b}$$

$$\frac{\partial^2 \tilde{\tilde{u}}_1}{\partial \bar{x}_3^2} = \frac{1}{x_1^2} \bar{f} f''\ , \tag{7.37c}$$

where $'$ denotes differentiation with respect to y. Substitution into (7.3), together with the result (7.33b), gives:

$$-yf' = \begin{cases} 2a_2 y \bar{f} f'(f' + yf'') & ,\quad y < y_J\ ; \\ bf'' & ,\quad y > y_J\ , \end{cases} \tag{7.38}$$

where $b = a_2 a_1$ for clarity, and where $y_J = \frac{\bar{x}_{3J}}{x_1}$.

Inner part of (7.38)

By separation of variables, we see that

$$\bar{f}(x_2) = K\ , \tag{7.39}$$

for some generally non-zero constant K. Then a rearrangement of the inner part yields:

$$yf'(2a_2 K(f' + yf'') + 1) = 0\ , \tag{7.40a}$$

$$\text{such that} \quad yf' = 0 \quad \text{or} \quad f' + yf'' + \frac{1}{2a_2 K} = 0\ . \tag{7.40b}$$

The first option in (7.40b) suggests that $f' = 0$ and hence that $\tilde{\bar{u}}_1$ is a constant. This solution has to be rejected, as the logarithmic merging with the inner tier would not then be possible. We therefore consider only the second option in (7.40b), and set $h = yf'$, so that:

$$h' = -\frac{1}{2a_2K} \ , \tag{7.41a}$$

$$\text{whereby} \quad h = -\frac{1}{2a_2K}y + \frac{c_5}{K} \ , \tag{7.41b}$$

for some constant c_5. Therefore

$$f' = -\frac{1}{2a_2K} + \frac{c_5}{Ky} \quad (\text{since } y \neq 0), \tag{7.42a}$$

$$\text{hence:} \quad f = -\frac{1}{2a_2K}y + \frac{c_5}{K}Ln(y) + \frac{d_3}{K} \ , \tag{7.42b}$$

for some scaled constant d_3.

The lower boundary condition requires

$$\tilde{\bar{u}}_1 \sim 1 \cdot Ln(\bar{x}_3) + \mathcal{O}(1) \quad \text{as } \bar{x}_3 \to 0+ \ , \tag{7.43a}$$

$$\text{and therefore that} \quad f \sim 1 \cdot Ln(y) + \mathcal{O}(1) \quad \text{as } \bar{x}_3 \to 0+ \ . \tag{7.43b}$$

Hence we must take $c_5 = 1$. Finally then, in the inner layer we have:

$$\tilde{\bar{u}}_1 = K \cdot f = -\frac{1}{2a_2}y + Ln(y) + d_3 \ . \tag{7.44}$$

Outer part of (7.38)

The outer part of equation (7.38) is

$$f'' + \frac{y}{b}f' = 0 \ . \tag{7.45}$$

Solving by means of the integrating factor $e^{\frac{y^2}{2b}}$ gives

$$f' = \frac{\bar{c}_6}{K}e^{\frac{(y_J^2 - y^2)}{2b}} \ , \tag{7.46a}$$

$$\text{such that} \quad \int_y^\infty f' \, d\bar{y} = \frac{\bar{c}_6}{K}\int_y^\infty e^{\frac{(y_J^2 - \bar{y}^2)}{2b}} \, d\bar{y} \ , \tag{7.46b}$$

where $\bar{y}$ is a dummy variable, and $\bar{c_6}$ is an unknown constant c_6 scaled on $e^{\frac{y_J^2}{2b}}$. Scaling on the integrating factor ensures that numerical work concerning $\tilde{\tilde{u}}_1$ involves finite values. Using the upper boundary condition $\tilde{\tilde{u}}_1 \to 0$ as $\bar{x}_3 \to \infty$ yields the solution:

$$\tilde{\tilde{u}}_1 = K \cdot f = \bar{c_6} \int_{\infty}^{y} e^{\frac{(y_J^2 - \bar{y}^2)}{2b}} \, d\bar{y} \; . \tag{7.47}$$

As discussed above, it is perhaps no surprise that the downstream streamwise behaviour is very similar to that for flow over a flat plate at zero incidence, as described in [60].

Matching

The remaining unknown constants $\bar{c_6}, d_3$, and y_J are determined by the three junction conditions of continuity of f, f' and the stress — *i.e.* $y^2 f' = a_1$ — across y_J. That is, we require:

$$f: \quad -\frac{1}{2a_2} y_J + Ln(y_J) + d_3 = \bar{c_6} \int_{\infty}^{y_J} e^{\frac{(y_J^2 - \bar{y}^2)}{2b}} \, d\bar{y} \; ; \tag{7.48a}$$

$$f': \quad -\frac{1}{2a_2} + \frac{1}{y_J} = \bar{c_6} e^{\frac{(y_J^2 - y_J^2)}{2b}} = \bar{c_6} \; ; \tag{7.48b}$$

$$\text{stress:} \quad -\frac{1}{2a_2} y_J^2 + y_J = a_1 \; . \tag{7.48c}$$

The solutions[1] to these three equations are:

$$y_J = 0.3022 \; ; \tag{7.49a}$$

$$\bar{c_6} = 0.184 \; ; \tag{7.49b}$$

$$d_3 = 2.14 \; . \tag{7.49c}$$

[1] We take the larger of the two values of y_J obtained from (7.48c) since otherwise the junction is not in the outer layer.

Note that once y_J and $\bar{c_6}$ have been determined from (7.48c) and (7.48b), we have to solve the rather more involved (7.48a) for d_3. To do so, we either note that

$$\begin{aligned}\int_y^\infty e^{-t^2}\,dt &= \int_0^\infty e^{-t^2}\,dt - \int_0^y e^{-t^2}\,dt\ , \\ &= \frac{\sqrt{\pi}}{2}\left(\frac{1}{\sqrt{2}} - erf(y)\right)\ ,\end{aligned} \tag{7.50a}$$

where $erf(y)$ is the error function at y, and therefore that

$$\int_y^\infty e^{\frac{(y_J^2-\bar{y}^2)}{2b}}\,d\bar{y} = \frac{\sqrt{\pi}e^{\frac{y_J^2}{2b}}}{4\sqrt{b}}\left[1-\sqrt{2}erf\left(\frac{y}{\sqrt{2b}}\right)\right]\ . \tag{7.50b}$$

At this point, we know y_J and b and so can calculate the integral and hence d_3 from (7.48a), after looking up the requisite values of erf either in tables, or by calculating from a commercial program such as *Mathematica*. In fact, the value quoted above was further validated by a simple integration program based on Simpson's Rule.

In summary:

$$\tilde{\bar{u}}_1 = \begin{cases} -\frac{1}{2a_2}y + Ln(y) + 2.14 & ,\quad y < 0.3022\ ; \\ 0.184\int_\infty^y e^{\frac{(0.3022^2-\bar{y}^2)}{2b}}\,d\bar{y} & ,\quad y > 0.3022\ . \end{cases} \tag{7.51}$$

Near-wall asymptote of $\tilde{\bar{u}}_1$

We consider in a little more detail the near-wall asymptote of $\tilde{\bar{u}}_1$. Currently, we know from equation (7.28) that

$$\begin{aligned}\tilde{\bar{u}}_1 &\sim Ln(\bar{x}_3) + k_1(x_1,x_2) - \beta\bar{U}_w(x_2)\ , \\ \text{or equivalently}\quad \tilde{\bar{u}}_1 &\sim Ln(\bar{x}_3) + \bar{k}_1(x_1,x_2)\ ,\end{aligned} \tag{7.52}$$

where $\bar{k}_1 = k_1 - \beta\bar{U}_w$ as before. But we have also derived the similarity solution

$$\tilde{\bar{u}}_1 = -\frac{1}{2a_2}y + Ln(y) + 2.14 \tag{7.53}$$

for $y < 0.3022$. Recall that the coefficient of 1 for the Ln term was determined by the requirement that (7.53) has the same behaviour as (7.28) near the wall. Continuing this idea, we insist that:

$$Ln(\bar{x}_3) + \bar{k}_1(x_1, x_2) = Ln(\bar{x}_3) - Ln(x_1) - \frac{\bar{x}_3}{2a_2x_1} + 2.14 \ , \tag{7.54a}$$

and therefore that

$$k_1(x_1, x_2) = \beta\bar{U}_w(x_2) + 2.14 - Ln(x_1) \ . \tag{7.54b}$$

It is interesting to note that the effects of the core flow — carried down through the layer by the $\bar{x}_3$-independent term $\beta\bar{U}_w$ — will be felt by the inner tier of the TBL through the action of the deficit function k_1. In a similar fashion, it is clear that $\beta^2\bar{Q}_w$ will contribute to the $\mathcal{O}(1)$ deficit function $k_2(x_1, x_2)$, and we can expect to see some x_2-dependence emerging in the inner layer.

7.2.2 Solution for $\tilde{\tilde{u}}_2$

The similarity form of $\tilde{\tilde{u}}_2$ is the following:

$$\tilde{\tilde{u}}_2 = x_1^{\Lambda}\bar{g}(x_2)g(y) \ , \tag{7.55}$$

where as before Λ is identically zero in the straight section, and identically unity in the curved section, and $y = \frac{\bar{x}_3}{x_1}$ as before. Note that once again we have separated the x_1- and x_2-dependence. Analagously to $\tilde{\tilde{u}}_1$, we now substitute into (7.14) after making the change of variables and obtain:

$$x_1^{\Lambda-1}\bar{g}(\Lambda g - yg') + 2\hat{K}_2(\Lambda)f = \begin{cases} a_2x_1^{\Lambda-1}\bar{g}(y^2f'g')' & , \quad y < y_J \ ; \\ bx_1^{\Lambda-1}\bar{g}g'' & , \quad y > y_J \ , \end{cases} \tag{7.56}$$

where we recall that f is known as the equations are quasi-two dimensional ($\tilde{\tilde{u}}_1$ can be found independently of $\tilde{\tilde{u}}_2$), and $\hat{K}_2(\Lambda = 0) = 0$ by definition. Note

that when $\Lambda = 0$ the unknown x_2-dependence $\bar{g}(x_2)$ will disappear from the equations.

Then in the absence of curvature, the equations become:

$$-yg' = \begin{cases} a_2(y^2 f' g')' & , \quad y < y_J \ ; \\ bg'' & , \quad y > y_J \ . \end{cases} \tag{7.57}$$

The inner part here has the form

$$a_2(y^2 f')\bar{h}' + y(1 + 2a_2 f' + a_2 y f'')\bar{h} = 0 \ , \tag{7.58}$$

where $\bar{h} = g'$ and f is known in effect from (7.51). Thus the equation to solve in the inner layer is:

$$y(1 - \frac{1}{2a_2}y)\bar{h}' + \bar{h} = 0 \ . \tag{7.59}$$

So

$$\bar{h} = c_7 \left(\frac{1}{y} - \frac{1}{2a_2} \right) \ , \tag{7.60a}$$

and thus

$$g = c_7 Ln(y) - \frac{c_7}{2a_2} y + c_8 \ , \tag{7.60b}$$

involving the unknown constants c_7 and c_8.

Thus

$$\tilde{\bar{u}}_2 = \bar{g}(x_2) \left(c_7 Ln(y) - \frac{c_7}{2a_2} y + c_8 \right) \ , \tag{7.61}$$

that is, $\tilde{\bar{u}}_2$ appears to behave like $\tilde{\bar{u}}_1$ in the absence of curvature. However, $\tilde{\bar{u}}_2$ is asymptotically $yLn(y)$ near the wall, suggesting at the very least that $c_7 = 0$ in the above. The outer part of (7.57) is the same as that for f, and so again an analagous result holds for $\tilde{\bar{u}}_2$ here. The usual matching across the junction, as well as with the lower boundary conditions, would supply values for the unknown constant of integration.

Considering now the general curved case, where $\Lambda \equiv 1$ and $\hat{K}_2 \not\equiv 0$[2], the equations to solve are:

$$\bar{g}(g - yg') + 2\hat{K}_2 f = \begin{cases} a_2\bar{g}(y^2 f'g')' & , \quad y < y_J \ ; \\ b\bar{g}g'' & , \quad y > y_J \ , \end{cases} \tag{7.62}$$

where this time $\bar{g}$ is retained in the equations.

Inner part of (7.62)

Substitution of (7.51) into (7.62) yields the governing equation for g in the inner part:

$$\bar{g}g - a_2\bar{g}g' - a_2 y\bar{g}g''(1 - \frac{1}{2a_2}y) + \hat{K}_2(-\frac{1}{a_2}y + 2Ln(y) + 4.28) = 0 \ . \tag{7.63}$$

By the usual methods associated with separation of variables, we can rearrange this equation until one side involves a ratio of x_2-dependent terms and the other a ratio of y-dependent terms, and thus both sides must be equal to the same constant. Thus

$$\bar{g}(x_2) \propto \hat{K}_2 \ , \tag{7.64}$$

and the magnitude of the constant of proportionality can always be absorbed into the scalings of $\tilde{\tilde{u}}_2$ such that $\tilde{\tilde{u}}_2$ is independent of it. However, an advantageous choice for the magnitude of the constant is 2 in order to cancel the factor of 2 in the driving term in (7.62). The sign of the solution depends on the sign of the separation constant, which we shall determine as follows. Suppose

$$\begin{aligned} \tilde{\tilde{u}}_2 &= x_1\bar{g}g = 2p\hat{K}_2 x_1 g(y) \ , \\ \text{where} \quad p &= \pm 1 \quad \text{to be determined,} \end{aligned} \tag{7.65}$$

[2]Note, however, that $\hat{K}_2$ may be 0 at certain points of the cross-section — say at the inside and outside of the duct of circular cross-section.

and let us examine the behaviour of (7.63) near the lower wall. We know that as $y \to 0+$, $\bar{g}g \sim 2p\hat{K}_2 yLn(y)$. Substituting this form into (7.63) and gathering terms of like order, we see that in the limit:

$$\text{Left hand side} \sim [-2a_2p+2.14]+[-a_2pLn(y)+Ln(y)]+[0.5py-\frac{1}{2a_2}y]+[pyLn(y)]\,, \tag{7.66}$$

which ~ 0 in the limit only if $p = +1$. Hence

$$\tilde{\tilde{u}}_2 = 2\hat{K}_2 x_1 g(y)\ . \tag{7.67}$$

The associated homogeneous equation of (7.63) is:

$$a_2 y(1-\frac{1}{2a_2}y)(\bar{g}g)'' + a_2(\bar{g}g)' - (\bar{g}g) = 0\ , \tag{7.68a}$$

$$\text{or} \quad \bar{g}\cdot\mathcal{L}(g) = 0$$
$$\text{where} \quad \mathcal{L}(g) = a_2 y(1-\frac{1}{2a_2}y)g'' + a_2 g' - g\ , \tag{7.68b}$$

and since we know $\bar{g}(x_2) \not\equiv 0$ we conclude that here we must — for the complementary function — solve $\mathcal{L}(g) = 0$. One possible solution method is to expand about y_J, supposing that the equation is analytic everywhere, *i.e.*, to let:

$$g = \sum_{n=0}^{\infty} f_n (y-y_J)^n\ . \tag{7.69}$$

This yields an infinite regression of recursion relations of the form

$$\begin{aligned}
&-f_0 + a_2 f_1 + a_2 y(1-\frac{1}{2a_2}y)(2f_2) = 0\ ;\\
&-f_1 + 2a_2 f_2 + a_2 y(1-\frac{1}{2a_2}y)(6f_3) = 0\ ;\\
&-f_2 + 3a_2 f_3 + a_2 y(1-\frac{1}{2a_2}y)(12f_4) = 0\ ;
\end{aligned} \tag{7.70}$$

.

.

.

If we knew *a priori* the behaviour of $\tilde{u}_2$ at the junction — specifically, if we knew $g(y_J) = f_0$ and $g'(y_J) = f_1$ — then we would have the complementary function. Since we do not, we have to consider another approach.

With the substitution $z = \frac{1}{2a_2}y$, (7.68) is transformed to

$$z(1-z)g'' + g' - 2g = 0 \,, \tag{7.71}$$

where $'$ now denotes differentiation with respect to z. We next compare this equation to the general hypergeometric equation

$$z(1-z)w'' + [\alpha_3 - (\alpha_1 + \alpha_2 + 1)z)]w' - \alpha_1\alpha_2 w = 0 \,, \tag{7.72}$$

whose solution is given in [27, p.310]. We find that:

$$\begin{aligned} \alpha_1 &= -\frac{1}{2} - \imath\frac{\sqrt{7}}{2} \,; \\ \alpha_2 &= -\frac{1}{2} + \imath\frac{\sqrt{7}}{2} \,; \\ \alpha_3 &= 1 \,, \end{aligned} \tag{7.73}$$

such that the formula yields one solution, namely

$$g_1 = \frac{1}{\Gamma(\alpha_1)\Gamma(\alpha_1 + \imath\sqrt{7})} \sum_{k=0}^{\infty} \frac{\Gamma(\alpha_1 + k)\Gamma(\alpha_1 + \imath\sqrt{7} + k)}{k!} \frac{z^k}{k!} \,. \tag{7.74}$$

Here Γ is the Gamma function. Substitution of this formula into (7.71) yields the coefficient of z^n as:

$$\begin{aligned} &\frac{\Gamma(\alpha_1 + n + 1)\Gamma(\alpha_1 + \imath\sqrt{7} + n + 1)}{(n+1)!} \frac{1}{2(n-1)!} \\ &\quad - \frac{\Gamma(\alpha_1 + n)\Gamma(\alpha_1 + \imath\sqrt{7} + n)}{n!} \frac{1}{2(n-2)!} \\ &\quad + \frac{\Gamma(\alpha_1 + n + 1)\Gamma(\alpha_1 + \imath\sqrt{7} + n + 1)}{(n+1)!} \frac{1}{2(n)!} \\ &\quad - \frac{\Gamma(\alpha_1 + n)\Gamma(\alpha_1 + \imath\sqrt{7} + n)}{n!} \frac{1}{n!} \end{aligned} \tag{7.75}$$

Simplifying this coefficient, we find that it involves a factor of

$$[(n^2 - n + 2) - (n^2 - n + 2)] \tag{7.76}$$

and is thus 0. At this stage, we have found one solution to the associated homogeneous equation. Furthermore, numerical values for the above, obtained from either *Mathematica* or *NAG*[3] routines, give the first few terms in the series as:

$$g_1 = 1 + 2z + z^2 + 0.445z^3 + 0.222z^4 + 0.125z^5 + \dots \ . \tag{7.77}$$

It is a straightforward exercise to check that these first few terms satisfy the equation. A second, linearly independent solution can be found by a reduction of order, with the substitution

$$g(z) = G(z)g_1(z) \ . \tag{7.78}$$

Once the second solution g_2 is found, a particular integral can also be determined by considering a linear combination of g_1 and g_2 and then employing the Wronskian and Green's Functions (see for example [27, pp308ff]). By the above technique, we can demonstrate that

$$G = c \int_y^{y_J} \frac{8 - 25\bar{y}}{\bar{y} g_1^2} \, d\bar{y} \ , \tag{7.79}$$

based on $a_2 = 0.16$. Note that the singularity is at $y = 0.32 = 2a_2$ and since $y_J = 0.3022$, setting y_J as an upper limit is perfectly acceptable, in order to fix the constant. The value of c would come from matching with the outer solution as usual. It is also possible to verify — analagously to above — that

$$g_2(y) = \left(c \int_y^{y_J} \frac{8 - 25\bar{y}}{\bar{y} g_1^2(y)} \, d\bar{y} \right) g_1(y) \tag{7.80}$$

satisfies the equation.

[3]The Numerical Algorithms Group, Ltd.: http://www.nag.co.uk.

For a particular integral of (7.63) we consider by inspection

$$g(y) = pLn(y) + qy + r \ , \tag{7.81}$$

for $p, q, r \in \Re$. By identifying like terms, the solution is:

$$p = -1 \quad ; \quad q = \frac{1}{2a_2} \quad ; \quad r = -2.14 \ . \tag{7.82}$$

Let us then write down the putative general solution of equation (7.63):

$$\begin{aligned}
&\tilde{\tilde{u}}_2 = 2\hat{K}_2 x_1 g(y) \ , \\
\text{where} \quad &g(y) = \left(1 + c\int_y^{y_J} \frac{8 - 25y}{y g_1^2}\, dy\right) g_1(y) - Ln(y) + \frac{1}{2a_2} y - 2.14 \ , \\
\text{where} \quad &g_1(y) = \frac{1}{\Gamma(\alpha_1)\Gamma(\alpha_1 + \imath\sqrt{7})} \sum_{k=0}^{\infty} \frac{\Gamma(\alpha_1 + k)\Gamma(\alpha_1 + \imath\sqrt{7} + k)}{k!} \left(\frac{1}{2a_2}\right)^k \frac{y^k}{k!} \ , \\
&\alpha_1 = -\frac{1}{2} - \imath\frac{\sqrt{7}}{2} \ .
\end{aligned} \tag{7.83}$$

However, we offer no proof that the above expression converges or can be made to match with the outer layer solutions which we find next, and indeed we will seek a numerical solution to the inner part of (7.63) in §7.3.

Outer part of (7.62)

The equation for the outer part is

$$\bar{g}(g - yg') + 2\hat{K}_2 f = b\bar{g}g'' \ , \tag{7.84}$$

where once again we stress that f is known from the outer part of (7.51). Furthermore, the result $\bar{g} = +2\hat{K}_2$ can similarly be derived here. Equation (7.84) has the associated homogeneous equation

$$bg'' + yg' - g = 0 \ , \tag{7.85}$$

where we have disallowed the solution $\hat{K}_2 \equiv 0$ as above. Again, *a priori* knowledge of $\tilde{\tilde{u}}_2$ at $y = y_J$ — or any other point in the outer part — would enable a solution method based on that on page 218. In the absence of such knowledge, we pursue other methods.

In fact, the outer part of equation (7.62) in its full form, namely

$$g'' + \frac{y}{b}g' - \frac{g}{b} = \frac{0.184}{b}\int_{\infty}^{y} e^{\frac{y_J^2 - \bar{y}^2}{2b}}\, d\bar{y} \,, \tag{7.86}$$

is relatively straightforward to solve. Upon differentiation we see that

$$g''' + \frac{y}{b}g'' = \gamma e^{-\frac{y^2}{2b}} \,, \tag{7.87}$$

where we have introduced the convenient notation $\gamma = \frac{0.184}{b}e^{\frac{y_J^2}{2b}}$. Considering this as a linear first order ODE in g'', the complementary function is

$$g''_{CF} = \bar{A}\gamma e^{-\frac{y^2}{2b}} \tag{7.88}$$

for some constant $\bar{A}$. The factor γ acts to reduce the order of magnitude of $\bar{A}$, rendering the subsequent computation somewhat easier. It is not difficult to find a particular integral,

$$g''_{PI} = \gamma y e^{-\frac{y^2}{2b}} \,, \tag{7.89}$$

leading to the general solution:

$$g'' = \gamma(\bar{A} + y)e^{-\frac{y^2}{2b}} \,. \tag{7.90}$$

Integrating once gives:

$$\begin{aligned} g' &= \bar{A}\gamma I - b\gamma e^{-\frac{y^2}{2b}} + c_9 \,, \\ \text{where} \quad I &= \int_{\infty}^{y} e^{-\frac{\bar{y}^2}{2b}}\, d\bar{y} \,. \end{aligned} \tag{7.91}$$

But the edge condition $g' = 0$ at $y \to \infty$ implies the constant of integration c_9 is zero, since the integrands are everywhere bounded. A final integration yields

$$g = \bar{A}\gamma \int_{\infty}^{y} I \, d\bar{y} - b\gamma I + c_{10} \, , \tag{7.92}$$

where $c_{10} = 0$ since $g = 0$ at the edge (the matching with the core is via $\tilde{u}_2$).

Hence the solution of the outer part of (7.62) is:

$$g = \bar{A}\gamma \int_{\infty}^{y} I \, d\bar{y} - b\gamma I \, , \tag{7.93}$$

with $\bar{A}$ currently unknown. This expression involves a term analogous to the complementary error function. Once again, recourse to tables of functions, *Mathematica*, or the aforementioned integration routine based on Simpson's Rule — which for example agrees with *Mathematica* to four decimal places for $\int_{\infty}^{y} I \, d\bar{y}$ — is necessary for progress to be made.

Comments on x_2-dependence

Before moving on, it is worthwhile spending a moment examining the origin of the x_2-dependence in the velocity components. This dependence arises as follows.

- $\tilde{u}_1$:— from the matching with the core flow's x_2-dependence (carried down across the whole layer).
- $\tilde{\tilde{u}}_1$:— defined $\tilde{\tilde{u}}_1 = \bar{f}(x_2)f(y)$ but showed that $\bar{f}$ is in fact a constant. This can be scaled out of the equations to leave us with $\tilde{\tilde{u}}_1 = f(y)$ — that is, there is no x_2-dependence.
- $\tilde{u}_2$:— from the matching with the core flow's x_2-dependence (carried down across the whole layer).

- $\tilde{\tilde{u}}_2$:— defined $\tilde{\tilde{u}}_2 = x_1\bar{g}(x_2)g(y)$ and showed that $\bar{g} = 2\hat{K}_2$ after a similar scaling-out as above. The solution will be $\tilde{\tilde{u}}_2 = 2\hat{K}_2 x_1 g(y)$, where note that in a duct of circular cross-section with circumference C, $\hat{K}_2$ may well be $\Lambda x_2(x_2 - \frac{1}{2}C)$, by inspection.

7.3 Numerical solutions

We have found in §7.2.2 an analytical solution to the *outer* part of (7.62), satisfying the upper boundary conditions and involving an unknown constant $\bar{A}$. Having formulated a putative analytical solution to the inner part of (7.62), but in the absence of any proof of convergence, we now attempt to solve the *inner* ODE numerically. Recall that the inner ODE has a singularity at $y = 2a_2 = 0.32$ which is just outside the computational range $y < y_J = 0.3022$.

There are three junction conditions to satisfy: continuity of g; continuity of g'; and continuity of stress. The last is satisfied automatically here once the first two hold, even before we know what the solution is in the inner part. This is because stress continuity here means:

$$a_2 y^2 f'\big|_{y=0.3022} = b\big|_{y=0.3022} \tag{7.94}$$

$$\text{Left hand side} = a_2 y_J^2 \left(-\frac{1}{2a_2} + \frac{1}{y_J}\right) = 0.0168 a_2 \ , \tag{7.95a}$$

whilst

$$\text{right hand side} = a_1 a_2 = 0.0168 a_2 \ . \tag{7.95b}$$

That is, continuity of stress across y_J is satisfied automatically to our level of working, which can be traced to our assumption of isotropic eddy viscosity.

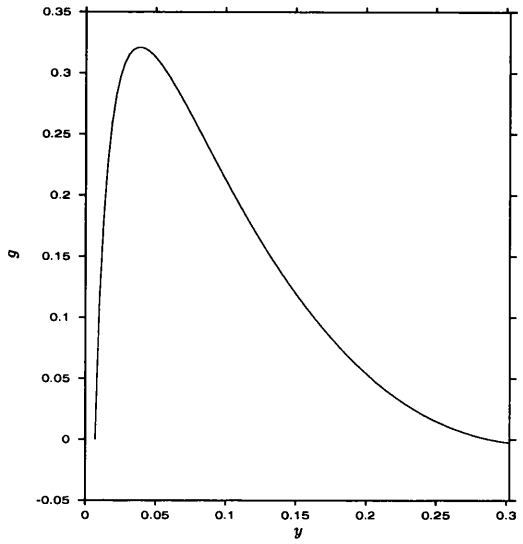

Figure 7.1: The Runge-Kutta solution for g. Computed with the methodology described in the text, and over 100 points, with $\Delta = 0.007$.

First study

The numerical problem for the inner part is a boundary value problem, running from the lower boundary (the wall) to the upper boundary (the junction). However, we start the computation slightly away from the wall (at $y = \Delta \ll 1$) because the driving term $Ln(y)$ is singular there. The equation is of second order, and so we require two boundary conditions each at both $y = \Delta$ and at $y = y_J$. However, although the lower boundary condition on g is known because $g = 0$ there to satisfy the no-slip condition, $g'(\Delta)$ is not known, since the deficit function for g has not been determined. Our first attempt is therefore to treat the problem as an initial value problem and linearly optimise guesses of $g'(\Delta)$ by seeking to satisfy the junction conditions. Note that the junction conditions involve matching with the outer solution which brings in the unknown constant $\bar{A}$. We therefore have two degrees of freedom — $g'(\Delta)$

and $\bar{A}$ — and two constraints — continuity of g and g' across the junction.

The overall method is as follows:

- set $g(\Delta) = 0$ and $g'(\Delta) = \alpha$ for some estimated constant α of $\mathcal{O}(1)$;
- solve between $y = \Delta$ and $y = y_J$ using a Runge-Kutta technique;
- at the junction, compare the Runge-Kutta solution $g_{RK}(y_J)$ with the outer solution $g_{\text{outer}}(y_J)$ to fix $\bar{A}$;
- next compare $g'_{RK}(y_J)$ with $g'_{\text{outer}}(y_J)$ and store this difference;
- repeat each step above with a second α;
- with now two points on a linear graph of $g'_{\text{diff}} := g'_{RK}(y_J) - g'_{\text{outer}}(y_J)$ against α, interpolate using Newton-Raphson to obtain the optimal value α^*;
- finally, run the routine with α^*.

The Runge-Kutta technique is used to solve a system of linear, first-order ODEs. Setting

$$\begin{aligned} z_1 &= g \ , \\ z_2 &= g' \ , \end{aligned} \tag{7.96}$$

the system of equations to solve becomes:

$$z_1' = z_2 \ ; \tag{7.97a}$$

$$z_2' = \frac{1}{4y(8-25y)}(200Ln(y) - 625y + 428 - 32z_2 + 200z_1) \ , \tag{7.97b}$$

based on $a_2 = 0.16$.

We used a commercially-avaliable *NAG* Runge-Kutta routine integrated into our own program. The routine is called "DO2PCF" and also calls on

another *NAG* routine "DO2PVF". The latter enables the user to specify the number of pairs to be used in the Runge-Kutta method, and our program ran with three different pair numbers: a 2(3) pair (quoted accuracy 10^{-2}–10^{-4}); a 4(5) pair (quoted accuracy 10^{-3}–10^{-6}); and a 7(8) pair (quoted accuracy better than 10^{-5}). A comparison was made between all three levels of accuracy which showed the results to have converged. Furthermore, in a bid to increase accuracy, we used a *NAG* complementary error-function routine to find the integral I, by writing:

$$I = \int_{\infty}^{y} e^{-\frac{\bar{y}^2}{2b}}\, d\bar{y} = -\sqrt{\frac{\pi b}{2}} erfc\left(\frac{y}{\sqrt{2b}}\right) . \tag{7.98}$$

The integration of $\int_{\infty}^{y} I\, d\bar{y}$ was by our own Simpson's Rule integrator.

The solution in the outer tier was not considered important here, since it can be shown from equation (7.93) that the solution tends monotonically to zero as $y \to \infty$. All that is important is the value of the unknown constant $\bar{A}$ in solving the inner part, and this is found as a stage of the above strategy. Whatever the value of $\bar{A}$, the inner solution automatically adjusts smoothly to it at the junction 0.3022, and thereafter the outer solution decays to zero.

In the above discussion we overlooked another degree of freedom — Δ, the distance offset from the wall. This was to be fixed by a comparison of the computed results with the known asymptote at the wall, namely

$$g \sim \frac{1}{a_2} yLn(y) . \tag{7.99}$$

However, it was at this point that an apparent paradox emerged. The computed results, shown in Figure 7.1, seemed to be of the wrong sign — the solutions were positive whilst the asymptote at $y \to 0+$ is negative.

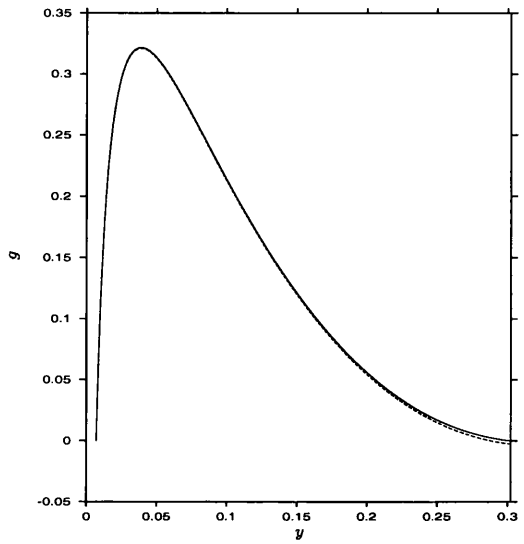

Figure 7.2: The directly computed solution for g (solid line) shown together with the curve of Figure 7.1.

Second study

Suspecting a user error in the implementation of the *NAG* routines, a direct computation of g was attempted. For this, the initial value problem was treated as a boundary value problem, with a "known" junction value for g of zero, since it is certainly close to zero there. This direct computation followed a straight-forward finite-differencing scheme as introduced in Chapters 2 and 5, with second-order accurate central-differences, and simple first-order accurate differences at the boundaries. However, this computation also produced a positive solution, as shown in Figure 7.2, where it is plotted together with the curve of Figure 7.1 for comparison. The results correspond closely, differing only near the junction, where the Runge-Kutta method matches to the external solution, whilst the direct computation simply sets g zero there.

Boundary condition

The paradox concerns the asymptote of g (or of $\tilde{\tilde{u}}_2$) derived from the governing equation as $y \to 0+$. There seems to be no denying that the controlling behaviour of the asymptote is $\frac{1}{a_2} y Ln(y)$ as can be confirmed by analysing the inner part of equation (7.62), recalling that we have taken $\bar{g} = 2\hat{K}_2$ and that we anticipate the inertia terms to tend to zero in the limit. We consequently seek to balance the curvature and viscous terms (*c.f.* equations (7.27) and (7.29)).

Considering the steps of this analysis, or those taken to derive equation (7.27), we see that the prediction that the controlling behaviour of the asymptote is $\frac{1}{a_2} y Ln(y)$ comes from the driving term f, *i.e.*, it comes from the behaviour of the particular integral of the solution of the ODE. The question then emerges, how does the complementary function behave in the limit $y \to 0+$?

The associated homogeneous equation to the inner part of equation (7.62) is:

$$y(2a_2 - y)g'' + 2a_2 g' - 2g = 0 \ . \tag{7.100}$$

Supposing now that

$$g \sim \lambda y^m \tag{7.101}$$

for some $m \geqslant 0$ and $\lambda \neq 0$ as $y \to 0+$, then the controlling behaviour in the limit comes from the y^{m-1} term whose coefficient is

$$2a_2\lambda m(m-1) + 2a_2\lambda m = 0 \ , \tag{7.102}$$

that is, m has the repeated root of 0. Thus the complementary function g_{CF} is

$$g_{CF} = A + BLn(y) \ , \tag{7.103}$$

for some constants A and B. Hence the full behaviour as $y \to 0+$ combining the controlling behaviours of the complementary function and the particular integral is:

$$g \sim A + BLn(y) + CyLn(y) + Dy + \mathcal{O}(y^2 Ln(y)) \quad \text{as } y \to 0+. \tag{7.104}$$

Substituting (7.104) into the full equation and balancing to each order yields the following relations:

$$\mathcal{O}(y^{-1}): \qquad -2a_2B + 2a_2B = 0 \qquad \text{— satisfied;} \tag{7.105a}$$

$$\mathcal{O}(Ln(y)): \qquad 2a_2C - 2B = 2 \qquad \Longrightarrow C \text{ given } B; \tag{7.105b}$$

$$\mathcal{O}(1): \quad B + 4a_2C + 2a_2D - 2A = 4.28 \quad \Longrightarrow D \text{ given } A, B, C. \tag{7.105c}$$

We recall that previously we had $A = 0 = B$, which in the above relations gives $C = \frac{1}{a_2}$ as required.

As the inner tier is entered, $y \to \hat{\epsilon}^{-2} Re^{-1} \tilde{y}$ such that $Ln(y)$ becomes $-2Ln(\hat{\epsilon}) - Ln(Re) + Ln(\tilde{y})$. We must in general insist that $B = 0$ otherwise the $Ln(y)$ term becomes too large as the inner tier is entered — no term in the inner expansion will be sufficiently large to cancel it as is required to satisfy the no-slip condition at the wall. Hence using the relations (7.105a–c) we claim that:

$$g \sim A + \frac{1}{a_2} yLn(y) + \frac{1}{a_2}(A + 0.14)y \quad \text{as } y \to 0+, \tag{7.106}$$

where the constant A is arbitrary. The appearance of A and its arbitrary nature resolves the paradox. Since we have a new degree of freedom, yet no new information, the programs are unable to satisfy the boundary conditions. That is, by setting $g = 0$ at the wall, we are setting a false condition, and yet we cannot set a non-zero value there (corresponding to A) since it is not fixed

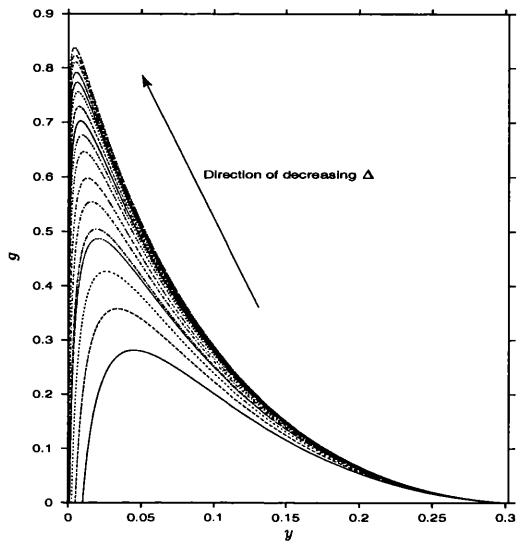

Figure 7.3: The appearance of a numerical boundary layer. 17 datasets are shown with Δ ranging from 0.01 to 0.0000001. Note that in each case, the uniform grid was adjusted to ensure that the distance between two compuational-grid points was at least an order of magnitude less than Δ.

by the equations. Furthermore, we see that on this length scale, the solution should asymptote to a constant at the wall, with the $yLn(y)$-behaviour occuring extremely close to the wall. Presumably, the constant term is cancelled by a corresponding term in the inner tier expansion.

Final study

In order to see some numerical confirmation of the above explanation, an alternative to the direct computation of g was sought. A strategy — dubbed the "S-method" — in which the governing equation was recast in terms of a new variable S defined by

$$S := \frac{g}{Ln(y)} \tag{7.107}$$

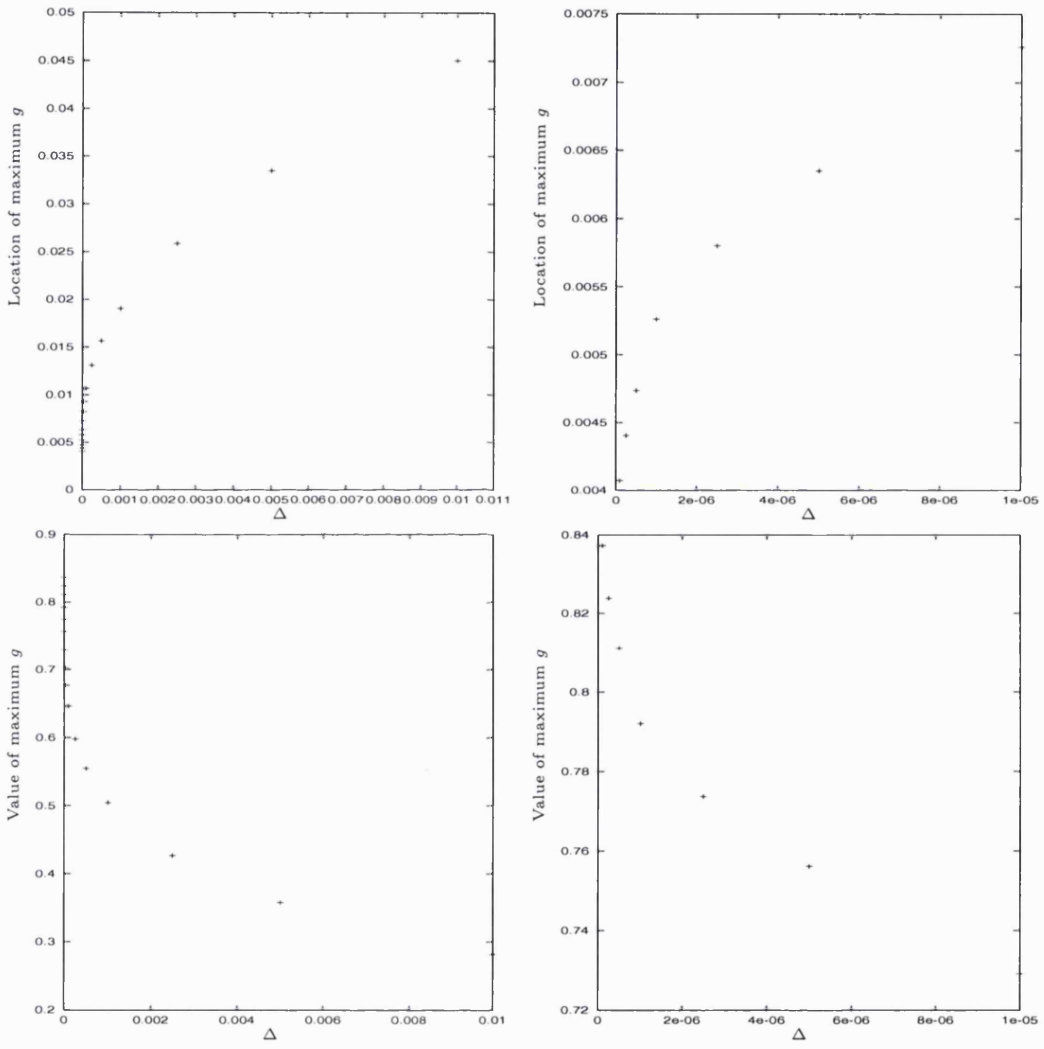

Figure 7.4: The effects of varying Δ on the location of maximum g and its value. (Magnified on right hand side)

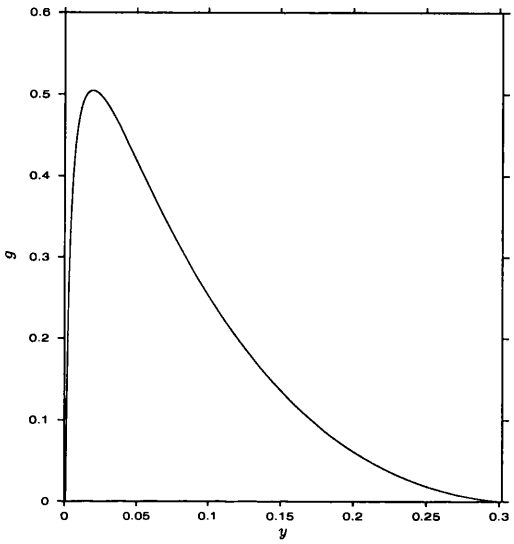

Figure 7.5: A plot of g computed directly and via the S-method. Both data sets begin from $\Delta = 0.001$ and are over 10,000 points.

was formulated. The boundary condition at the "wall" $y = \Delta$ would be $S(\Delta) = 0$, with the definition of S suggesting that the adjustment to this boundary condition should happen over a sufficiently short length scale so as to be practically invisible, and thus the asymptote to a constant value at the wall would be apparent.

At first, this did not seem to be the case, though as Δ was allowed to get ever closer to the wall, a numerical boundary layer did seem to appear with the solutions tending to a universal curve, as shown in Figure 7.3. This was also borne out by plotting the variation with Δ of both the location of the maximum point of g and its value in Figure 7.4.

Although this was persuasive, the large y-range over which g adjusted was puzzling, and of the same order as that for a direct computation of g. Indeed, the two methods agreed extremely closely, as is shown in Figure 7.5.

In order to feed more detailed information into the system over the crucial

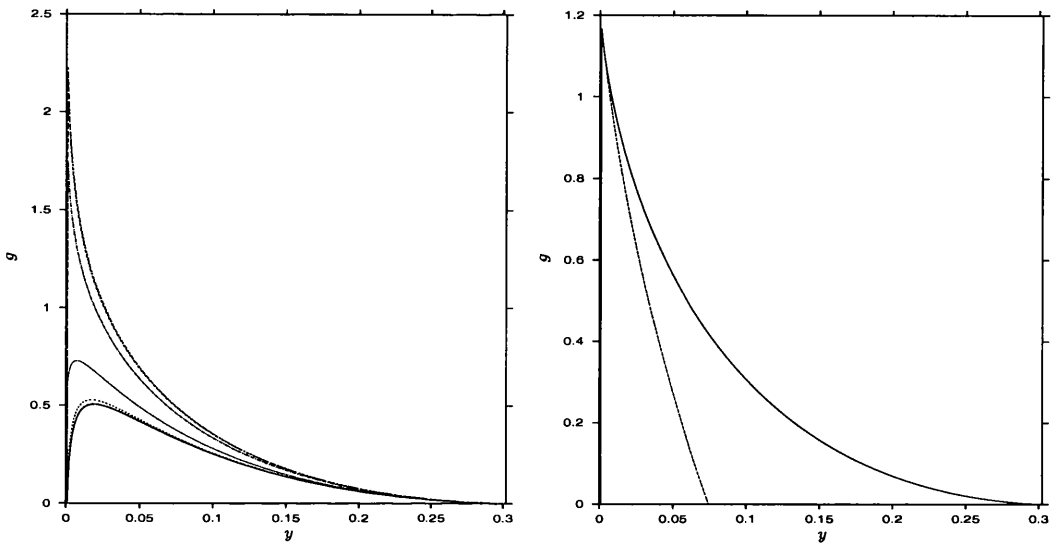

Figure 7.6: The left hand graph plots curves generated by successive refinements of the grid between $\Delta = 0.001$ and the second point of the standard grid of 100,000 points. Increasing the refinement increases monotonically the maximum value of g. The lowermost curve has no refinement, whilst the uppermost features an additional 1,000,000 points. The right hand graph shows the solution parallel to the quoted near-wall asymptote, and the asymptote itself (dotted line) with $A = 1.21$.

adjustment region near the wall, we use grid refinement between the first two computational-grid points of a standard grid with a constant spacing δ of grid points. The grid spacing δ was one order of magnitude less than Δ. Earlier work on the direct computation of g showed that grid refinement beyond this did not improve the results and we have seen in Figure 7.5 the close correspondence between the results of the S-method and the direct-computation method. Increasing the refinement with Δ fixed generates an adjustment over a short distance and gives a variety of curves, as shown on the left hand side of Figure 7.6. We choose the level of refinement which generates a curve par-

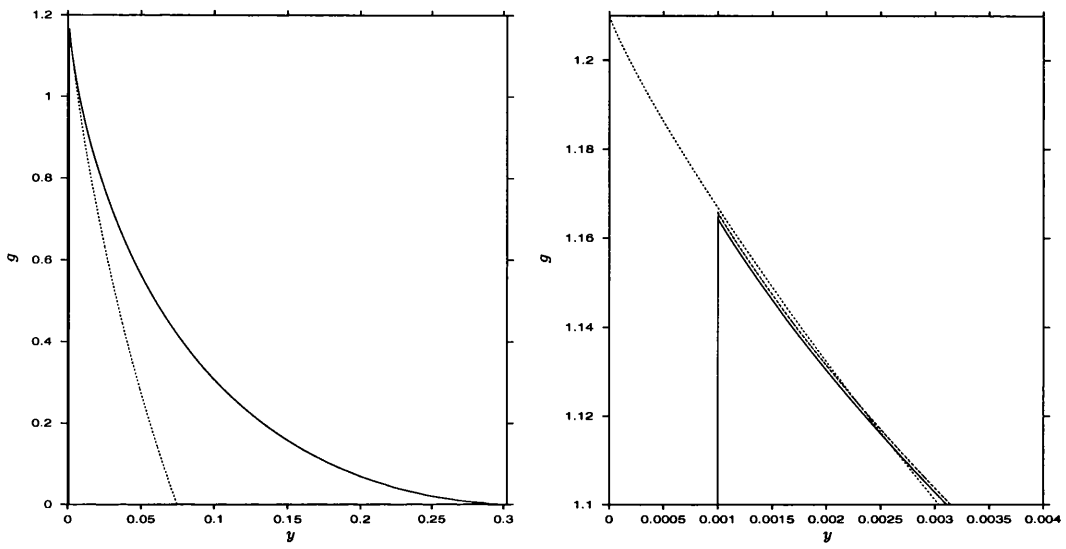

Figure 7.7: The solid line in the graph on the left hand side is in fact two lines; the solutions from both grids coincide at this scale. The dotted line is the asymptote. In the magnified view on the right hand side, a small difference can be seen between the two solutions.

allel to the asymptote $A + \frac{1}{a_2} yLn(y)$ near the wall, and then fix A such that the curve of the solution and the curve of the asymptote coincide there. This solution and the asymptote are shown on the right hand side of Figure 7.6.

We now show that this result is not an artefact of the grid nor an artifice of the user, by showing that the result is independent of the computational grid. With $\Delta = 0.001$, the solution shown on the right hand side of Figure 7.6 has a standard grid of 100,000 points between Δ and y_J with a 3,000-point refinement near the wall. If we define the grid refinement density as $\frac{N_r+N_s}{N_s}$ where N_r is the number of refinement points between two standard points and N_s is the number of standard points, then this grid has a grid refinement density of 103%. A second computation with the same refinement density between points 1 and 2 of the standard grid was performed with a 500,000-

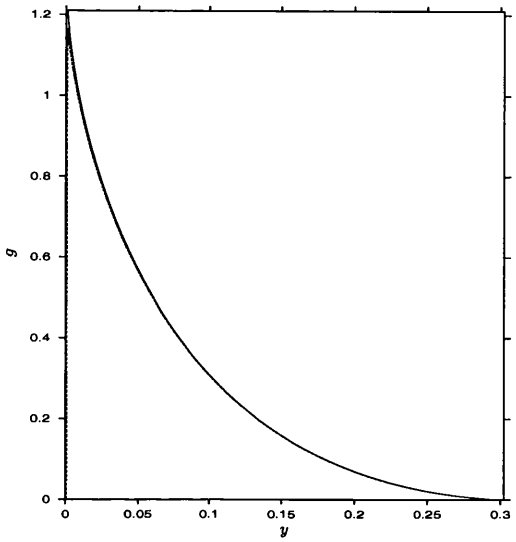

Figure 7.8: A comparison of the S-method results of Figure 7.7 (dotted line) with those of a direct computation of g after setting $g(\Delta) = 1.21$.

point standard grid, and the two sets of results are compared in Figure 7.7, together with the asymptote. The results compare very favourably indeed, suggesting that the behaviour is not simply a product of the grid.

A final assurance comes from a direct computation of g with the forcing $g(\Delta = 0.001) = 1.21$ over the 100,000-point standard grid (with no refinement) used above. The result is very close to that for the S-method with grid refinement, as shown in Figure 7.8.

7.3.1 A final note on the numerical solutions

The junction boundary condition on g has been set as zero throughout this section, since the analytical solution in the outer part contains an unknown constant $\bar{A}$. However, we noted on page 227 that g decays monotonically to zero in the outer part and that the numerical solution in the inner part can adjust itself smoothly to a non-zero g at y_J without difficulty. Hence we can

declare that the above work confirms the principal result that

$$g \sim A + \frac{1}{a_2} y Ln(y) + \frac{1}{a_2}(A + 0.14)y \quad \text{as } y \to 0+, \tag{7.108}$$

though not the precise value of A nor the precise form of g close to the junction. Since g decays so rapidly in the outer region, in a direct computation of the outer solution, g at the junction cannot be optimised to generate $g(\text{“}\infty\text{”}) = 0$ (given $g'(\text{“}\infty\text{”}) = 0$) since almost any value of g at y_J satisfies these conditions.

Finally, we draw attention to [97] which studied the TBLs over curved turbomachinery blades. Experimental data is shown in Figure 3 of that paper for the cross-flow over such a blade and it can be seen that the maximum of the cross-flow velocity is very close indeed to the blade surface. Although the experimental study is for an external flow with wall curvature, we note that flows such as that considered in this chapter in which the cross-flow involves a maximum velocity very close to the surface have been observed experimentally.

Chapter 8

The merged turbulent boundary layer in a curved duct

In the discussion on page 209 we noted that when β is small the turbulent boundary layers (TBLs) grow to merge and fill the duct by a distance of $\mathcal{O}(\hat{\epsilon}^{-1})$ downstream, and so in this chapter we consider the merged (or merging) TBLs in quasi-straight two-dimensional or three-dimensional axisymmetric ducts, primarily over the $\mathcal{O}(\hat{\epsilon}^{-1})$ length scale. In the overlap between the entry region and the merged region the dominant velocity perturbations in the core are due to the blocking effect of the growing TBLs. This is because the distance of $\mathcal{O}(\hat{\epsilon}^{-1})$ is much less than the distance of $\mathcal{O}(\epsilon^{-1})$ at which the curvature effects in the core grow in significance. Wall frictional effects caused by the TBL are compared with Fanno flow in Appendix C.

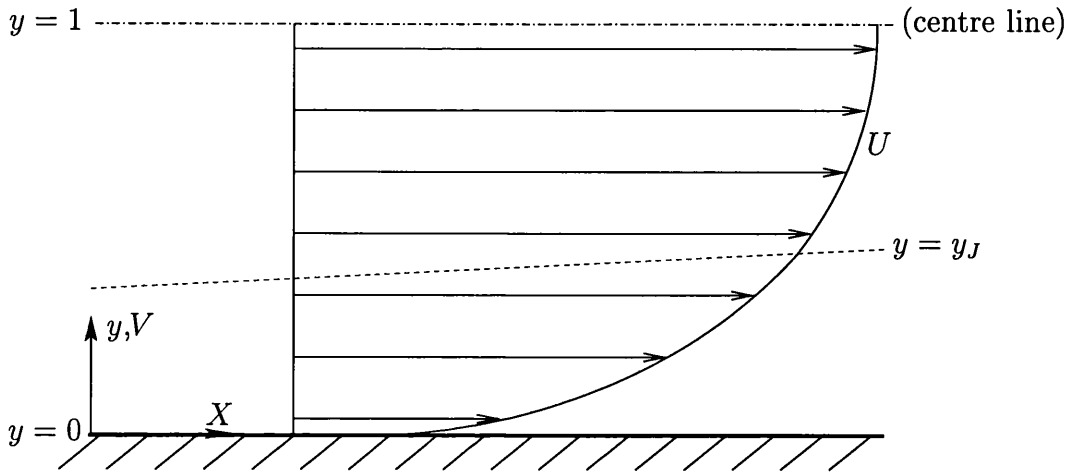

Figure 8.1: Coordinate configuration.

8.1 The quasi-straight two-dimensional duct

8.1.1 Governing equations

Since this case is symmetrical about the centre-line of the two-dimensional duct, we non-dimensionalise the length scales on the half-width of the duct and study the flow development between the wall and the centre-line. The other non-dimensionalising factors are the same as those in Chapter 6.

Determining the perturbed forms

With reference to Figure 8.1 the length scales of this new stage have x of $\mathcal{O}(\hat{\epsilon}^{-1})$ and y of $\mathcal{O}(1)$ and as a consequence we set

$$x = \hat{\epsilon}^{-1} X \ , \tag{8.1}$$

where X is of $\mathcal{O}(1)$. We note that the slender layer approximation also holds at this stage since $y \ll x$.

We denote the full velocities in this new stage by U and V, and then an integration of the two-dimensional continuity equation — which from (6.20a)

is $U_x + V_y = 0$ — between $y = 0$ and $y = 1$ yields

$$\int_0^1 U_x \, dy + [V]_0^1 = 0 \, , \tag{8.2}$$

with $[V]_0^1 = 0$ since there is no normal flow at the wall or across the centre-line here. Hence if

$$U = \bar{U}(X) + \hat{\epsilon}\hat{U}(X, y) + \dots \, , \tag{8.3}$$

then examining (8.2) to leading order in $\hat{\epsilon}$ suggests that

$$\frac{\mathrm{d}\bar{U}}{\mathrm{d}X} \equiv 0 \tag{8.4}$$

and as a consequence we have

$$U = 1 + \hat{\epsilon}\hat{U}(X, y) + \dots \, . \tag{8.5}$$

In order to find the perturbed form of V we next consider the overlap between the entry region and the present new stage. This overlap region is where the matching of the double limit $x \to \infty$ and $X \to 0+$ takes place, and the configuration of this region is shown in Figure 8.2. We introduce a stream function ψ in the TBL defined by

$$\psi_y = U \quad , \quad \psi_x = -V \, , \tag{8.6}$$

with ψ being zero at the wall. In order to match with the TBL velocity perturbations of Chapters 6 and 7 when examining the overlap region we must have

$$\psi = \hat{\epsilon}Y + \hat{\epsilon}^2\psi_1 + \dots \, . \tag{8.7}$$

Furthermore, we can also introduce a streamfunction Ψ in the core of the overlap region, defined by

$$\Psi_y = U_c \quad , \quad \Psi_x = -V_c \, , \tag{8.8}$$

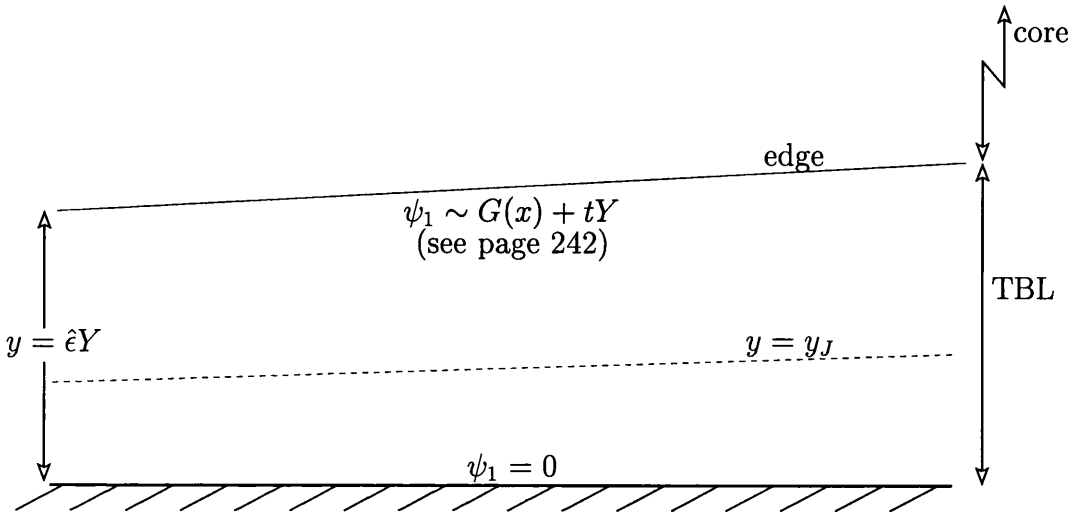

Figure 8.2: Configuration in the overlap region.

with Ψ being zero at the wall and where the subscript $_c$ denotes core velocities. The uniform core flow in the overlap region is perturbed by the conservation of mass responding to the significant blocking effect of the now large TBL, and so we expand

$$\Psi = y + \hat{\epsilon}\Psi_1 + \hat{\epsilon}^2\Psi_2 + \dots \ . \tag{8.9}$$

For a smooth matching process with the flow in the TBL, and for further reasons which we will describe later in this section, we must take $\Psi_{1x} \equiv 0$ so that $\Psi_1 = ty$ for some constant t. Therefore in the core we have

$$\Psi = y + \hat{\epsilon}ty + \hat{\epsilon}^2\Psi_2 + \dots \ . \tag{8.10}$$

In terms of the matching in the double limit $y \to 0+$ and $Y \to \infty$ we note that y matches with $\hat{\epsilon}Y$, and $\hat{\epsilon}ty + \hat{\epsilon}^2\Psi_2$ matches with $\hat{\epsilon}^2\psi_1$. Furthermore, the core flow has an effective slip condition at the wall and so

$$\Psi_2|_{\text{wall}} = G(x) \tag{8.11}$$

for some function $G(x)$, such that

$$\psi_1 \sim G(x) + tY \quad \text{as} \quad Y \to \infty \tag{8.12}$$

(and hence $\hat{U} \to t$ as $Y \to \infty$).

Thus where $X = \hat{\epsilon}x$ is of $\mathcal{O}(1)$ again, which is the main stage of present concern, the above work shows that

$$U = 1 + \hat{\epsilon}\hat{U}(X, y) + \dots \,, \tag{8.13a}$$

$$V = \hat{\epsilon}^2\hat{V}(X, y) + \dots \,. \tag{8.13b}$$

Governing equations

To leading order in $\hat{\epsilon}$, the two-dimensional continuity equation $U_x + V_y = 0$ is:

$$\hat{U}_X + \hat{V}_y = 0 \,. \tag{8.14}$$

We remark that this leading order form is related to the streamfunction component ψ_1 via $\psi_{1y} = \hat{U}$ and $\psi_{1X} = -\hat{V}$, where ψ_1 is zero on $y = 0$ and ψ_1 is constant on $y = 1$. The value of ψ_1 on $y = 1$ is to be determined by the conservation of mass across the width of the duct and by symmetry. With an initially uniform flow of unit velocity in the duct of width 2 the total non-dimensional mass flux is 2, and so by symmetry there is a non-dimensional mass flux of 1 in each half of the duct. Thus either from (8.13a) or from the full two-dimensional continuity equation we have

$$1 = 1 + \hat{\epsilon} \int_0^1 \hat{U}(X, y)\, dy + \dots \text{ for all } X \,, \tag{8.15a}$$

that is,

$$\int_0^1 \hat{U}(X, y)\, dy = 0 \text{ for all } X \,. \tag{8.15b}$$

Furthermore, the mass flux across any line joining $y = 0$ and $y = 1$ is equal to $\psi(y = 1) - \psi(y = 0)$, which yields:

$$\psi_1(y = 1) = 0 \ . \tag{8.16}$$

Since the non-dimensionalisations (other than the length scale factor) are the same as those in Chapter 6, and since also the slender layer approximation still holds at this new stage, we can quote the two-dimensional form of the TBL x-momentum equation without curvature from equation (6.20b):

$$UU_x + VU_y = -p_x + \frac{1}{Re}\nabla^2 U - (U'V')_y \ . \tag{8.17}$$

We recall that we take $Re \gg 1$ and that we model $-(U'V')_y$ with the Cebeci-Smith model, although we reiterate that much of what follows depends only on assuming the mixing-length hypothesis, with a specific choice of two-tier mixing-length model providing specific quantitative predictions. The Cebeci-Smith model has $-(U'V')_y = (BU_y)_y$ where

$$B = \begin{cases} a_2 y^2 \left[1 - exp\left(-\frac{Re^{\frac{1}{2}}}{26} y \left(\left|(U_y)_w\right|\right)^{\frac{1}{2}}\right)\right]^2 |U_y| & , \ y < y_J \ , \\ a_1 U_{\mathcal{L}} \delta_1 & , \ 1 > y > y_J \ , \end{cases} \tag{8.18}$$

and $a_1 = 0.0168$ and $a_2 = 0.16$.

In this formulation the quasi-displacement δ_1 is given by

$$\delta_1 = \int_0^1 \left(1 - \frac{U}{U_{\mathcal{L}}}\right) \, dy \ , \tag{8.19}$$

where $U_{\mathcal{L}}$ is the streamwise centre-line velocity. In fact

$$\delta_1 = \frac{1}{U_{\mathcal{L}}} \int_0^1 (U_{\mathcal{L}} - U) \ dy \tag{8.20a}$$

$$= \int_0^1 \left[\left(1 + \hat{\epsilon}\hat{U}_{\mathcal{L}} + \ldots\right) - \left(1 + \hat{\epsilon}\hat{U} + \ldots\right)\right]\left(1 - \hat{\epsilon}\hat{U}_{\mathcal{L}} + \ldots\right) \ dy \tag{8.20b}$$

$$= \hat{\epsilon} \int_0^1 \left(\hat{U}_{\mathcal{L}} - \hat{U}\right) \ dy + \ldots \tag{8.20c}$$

$$= \hat{\epsilon}\hat{\delta}_1 + \ldots \ , \tag{8.20d}$$

with:

$$\hat{\delta}_1 = \hat{U}_{\mathcal{Q}} - \int_0^1 \hat{U}\, dy = \hat{U}_{\mathcal{Q}} \ , \tag{8.20e}$$

by (8.15b). Since $\hat{U}_{\mathcal{Q}}$ appears in the outer part of (8.18) it is clear that $\hat{U}_{\mathcal{Q}}$ is an important parameter in the merged two-dimensional quasi-straight regime.

A leading order examination of the x-momentum equation (8.17) and the associated form of the y-momentum equation shows that the pressure p is perturbed as

$$p = 1 + \hat{\epsilon} p_1(X) + \hat{\epsilon}^2 p_2(X, y) + \dots \ . \tag{8.21}$$

Here $p_1(X)$ is independent of y while $p_2(X, y)$ is expected in general to be dependent on both X and y. Thus to leading order in $\hat{\epsilon}$, in the limit of large Re, the streamwise-momentum equation is:

$$\hat{U}_X = -p_{1X} + \begin{cases} a_2 \left(y^2 \hat{U}_y^2 \right)_y & , y < y_J \ , \\ \bar{a}_1 \hat{U}_{yy} & , y_J < y < 1 \ , \end{cases} \tag{8.22}$$

where $\bar{a}_1 = a_1 \hat{U}_{\mathcal{Q}}$. The lower boundary condition on $\hat{U}$ remains

$$\hat{U} \sim 1 \cdot Ln(y) \quad \text{as} \quad y \to 0+ \ . \tag{8.23}$$

By integrating (8.22) across the half-width of the duct we then obtain

$$\int_0^1 \hat{U}_X \, dy = -\int_0^1 p_{1X} \, dy + \left[\bar{a}_1 \, \hat{U}_y \Big|_{y=1} - a_2 \left(y^2 \hat{U}_y^2 \right) \Big|_{y \to 0+} \right] \ . \tag{8.24}$$

Using now (8.15b), symmetry at $y = 1$, and (8.23), yields

$$p_{1X} = -a_2 \quad \text{for all } X, \tag{8.25}$$

and as a consequence we have:

$$\hat{U}_X = a_2 + \begin{cases} a_2 \left(y^2 \hat{U}_y^2 \right)_y & , y < y_J \ , \\ \bar{a}_1 \hat{U}_{yy} & , y_J < y < 1 \ . \end{cases} \tag{8.26}$$

The non-linear partial differential equation (8.26) and the corresponding boundary conditions are central to this rest of this chapter.

Since we have shown that $p_{1X} = -a_2$ it is worth noting immediately here the origin of the parameter a_2 in the Cebeci-Smith model. With reference to the discussion in §6.1, we recall that Van Driest improved Prandtl's mixing-length model of Boussinesq's original eddy-viscosity assumption. After setting

$$\mu_T = \rho l_m^2 \left| \frac{\partial u}{\partial y} \right| , \tag{8.27}$$

the Van Driest mixing-length l_m has a factor of κ which is experimentally determined as being close to 0.4. The Cebeci-Smith model is in turn a modification of Van Driest's but with the same limit near the wall, namely $l_m^2 = 0.16y^2$. Furthermore, Nikuradse's formula for turbulent pipe flow (as given for example in [15, pp 111–112]) also has a near-wall asymptote of $l_m = 0.4y$. Hence the result that

$$p_{1X} = -a_2 = -0.16 \tag{8.28}$$

depends only on the assumption of the mixing-length hypothesis and *not* on the choice of model.

Finally in this section we examine (8.26) in the limit $X \to 0+$ with y remaining of $\mathcal{O}(1)$ in order to determine the core flow behaviour near the start of the new stage. The leading order suggests that $\mathcal{O}(\hat{U}) = \mathcal{O}(X)$ in the limit, and in fact we deduce that

$$\hat{U} = a_2 X + \mathcal{O}(X^2) . \tag{8.29}$$

Then we note that with the core streamfunction definition (8.9) we must have

$$\Psi_{1y} = a_2 = t , \tag{8.30}$$

which validates the earlier argument that Ψ_{1y} is constant.

8.1.2 Numerical study

Inner part of (8.26)

Taking first the inner part of (8.26), we differentiate with respect to y to obtain

$$\hat{U}_{yX} = a_2 \left(y^2 \hat{U}_y^2 \right)_{yy} . \tag{8.31}$$

We set $\tau = \hat{U}_y$ and $T = (y\tau)^2$, so that the inner part of (8.26) becomes

$$T^{-\frac{1}{2}} T_X = 2a_2 y T_{yy} , \tag{8.32}$$

which is a non-linear diffusion equation. By defining the junction-fitted inner coordinate $\eta = \frac{y}{f}$ equation (8.32) becomes

$$T_X = \frac{\eta}{f} \left(f' T_\eta + 2a_2 T^{\frac{1}{2}} T_{\eta\eta} \right) . \tag{8.33}$$

The wall boundary condition on $\hat{U}$ is $\hat{U} \sim 1 \cdot Ln(y)$ and so for T it is:

$$T(\eta = 0) = 1 . \tag{8.34}$$

The junction condition of continuity of stress yields

$$T(\eta = 1) = \left(\frac{\bar{a}_1}{a_2 f} \right)^2 . \tag{8.35}$$

The main equations here are therefore (8.33)–(8.35).

Outer part of (8.26)

Turning now to the outer part of (8.26), we differentiate with respect to y to obtain the linear diffusion equation

$$\hat{U}_{yX} = \bar{a}_1 \hat{U}_{yyy} , \tag{8.36}$$

and we also define the junction-fitted outer coordinate $\hat{\eta} = \left(\frac{y-1}{f-1}\right)$ such that $\hat{\eta} = 0$ at the centre-line and $\hat{\eta} = 1$ at the junction. With this change of coordinates in (8.36) we have

$$\tau_X = \frac{1}{(f-1)^2}\left((f-1)f'\hat{\eta}\tau_{\hat{\eta}} + \bar{a}_1\tau_{\hat{\eta}\hat{\eta}}\right) \ . \tag{8.37}$$

Symmetry across the centre-line yields the requirement

$$\tau(\hat{\eta} = 0) = 0 \ , \tag{8.38}$$

while continuity of $\hat{U}_y$ across the junction, together with (8.35), gives

$$\tau(\hat{\eta} = 1) = \frac{\bar{a}_1}{a_2 f^2} \ . \tag{8.39}$$

Thus the main equations in the outer part are (8.37)–(8.39).

Numerical scheme

The governing equations (8.33) and (8.37) are parabolic in X and so we discretise each equation with nominally first-order accurate backward differencing formulae for the X-derivatives, with second-order accurate central-space difference formulae for the η and $\hat{\eta}$ derivatives. The computational grids are fitted to the unknown curve $y_J = f(X)$ by use of $\eta, \hat{\eta}$; then $f(X)$ is linearly optimised at each X-station in a manner to be described shortly.

A compact differencing scheme was not applied here, for the following reasons. Firstly, we recall that the compact-differencing approach treats derivatives of the dependent variables as variables in their own right. Yet, although the leading order behaviour of $\hat{U}$ near the wall is $\hat{U} \sim 1 \cdot Ln(y)$, the higher order terms are unknown here. Written in terms of $y\tau = y\hat{U}_y$, which is of order unity near the wall, a compact-differencing approach would require solving a tridiagonal matrix for $(y\tau)_y$ involving the unknown part of $y\tau$ near the

wall. Secondly, $\hat{U}_{yy}$ can be shown to be discontinuous at $y = y_J$. Thus the tridiagonal problem for $(y\tau)_y$ is not obviously well-posed.

Given the junction position, the inner equation (8.33) and the outer equation (8.37) together with their associated boundary and junction conditions each forms a closed boundary value problem. We can solve each boundary value problem independently before comparing values across $\eta = 1 = \hat{\eta}$ to determine the junction position, as follows.

With an initial guess for f we solve (8.33) for T and (8.37) for τ, with the current guess for f diffusing through the computational domain of each boundary value problem via the computational boundaries. The important parameter $\hat{U}_{\mathcal{Q}}$ is updated from

$$\left(\hat{U}_{\mathcal{Q}}\right)_X = a_2 + \bar{a}_1 \hat{U}_{yy}\Big|_{y=1} . \tag{8.40}$$

With the change of coordinates $(X, y) \mapsto (X, \hat{\eta})$ we can thus update $\hat{U}_{\mathcal{Q}}$ by:

$$\left(\hat{U}_{\mathcal{Q}}\right)_X = a_2 + \frac{\bar{a}_1 \tau_{\hat{\eta}}}{f-1}\Big|_{\hat{\eta}=1} . \tag{8.41}$$

The non-linearity of (8.33) and (8.37) requires lagging of some of the variables and so iteration is used until convergence is reached to within a prescribed level of accuracy. At this stage we have employed two of the three junction conditions (namely, continuity of τ and of B) and we next optimise f based on the third junction condition, continuity of $\hat{U}$ (or equivalently of $\hat{U}_X$), as follows. Consider the absolute difference

$$E = \left| \frac{\bar{a}_1 \tau_{\hat{\eta}}}{f-1}\Big|_{\hat{\eta}=1} - \frac{a_2 T_\eta}{f}\Big|_{\eta=1} \right| . \tag{8.42}$$

By comparing converged values of τ and T from two different values of f we can optimise f to minimise E. The computation is then repeated with this optimised value of f with iteration to convergence, before advancing to

the next X-station. The results of this scheme were compared with those of a predictor-corrector approach. The solution method described above has higher-order accuracy than a predictor-corrector approach, and we will present only the high-order accurate results.

We observe that, if required, $\hat{U}$ can be determined by integrating with respect to y the computed values of τ and T between 1 and y since we know $\hat{U}_{\mathcal{Q}}$. Continuing, ψ can be found from an integration with respect to y from either 1 to y or 0 to y.

Initial conditions

The initial conditions for the numerical scheme are determined by considering the governing equations (8.33) and (8.37) in the regime where X is small.

By connecting with the previous regime where $x \to \infty$ we assume that in the inner region:

$$f = d_1 X + \dots \; ; \tag{8.43a}$$

$$T = T_0(\eta) + \dots \; , \tag{8.43b}$$

with the constant d_1 and the function T_0 to be determined. Then (8.33) becomes

$$d_1 T_0' + 2a_2 T_0^{\frac{1}{2}} T_0'' = 0 \tag{8.44}$$

to leading order. To solve this non-linear ordinary differential equation, if we first let $T_0' \equiv H(T_0)$ then we find

$$H = -\left(\frac{d_1 T_0^{\frac{1}{2}}}{a_2} + d_2 \right) \tag{8.45}$$

where d_2 is an unknown constant. Equation (8.45) has the solution

$$2(T_0^{\frac{1}{2}} - DLn(T_0^{\frac{1}{2}} + D)) = -\frac{d_1}{a_2}\eta + d_3 \; , \tag{8.46}$$

where $D = \frac{d_2 a_2}{d_1}$ is unknown and d_3 is another unknown constant. Employing the boundary condition (8.34) in the form $T_0(0) = 1$ then gives us

$$d_3 = 2(1 - DLn(1 + D)) \,, \tag{8.47}$$

where we have yet to determine D. The junction condition (8.35) yields

$$T_0(1) = \left(\frac{\bar{a}_1}{a_2 d_1 X}\right)^2 \tag{8.48}$$

but since $T_0 = T_0(\eta)$ only, we rescale $\bar{a}_1$ by $\bar{a}_1 = \tilde{a}_1 f$ and then

$$T_0(1) = \left(\frac{\tilde{a}_1}{a_2}\right)^2 \,. \tag{8.49}$$

Substituting expression (8.49) into (8.46) yields

$$\frac{2\tilde{a}_1}{a_2} + \frac{d_1}{a_2} - 2 = DLn\left(\frac{\tilde{a}_1}{a_2} + D\right) - 2DLn(1 + D) \tag{8.50}$$

at the junction, which we shall later use in determining the unknown constants.

For the variable τ in the outer equation (8.37) we note that the matching condition (8.39) across the junction becomes

$$\tau(\hat{\eta} = 1) = \frac{\tilde{a}_1}{a_2 f} \,. \tag{8.51}$$

This suggests that we should take

$$\tau \sim X^{-1}\hat{\tau}(\hat{\eta}) \tag{8.52}$$

in this small-X regime. In the entry region studied in Chapter 7 the y-scale increased linearly with x and so in the overlap region where $x \to \infty$ and $X \to 0+$ we expect that the outer region has velocity adjustments over a small region close to the junction. Hence we scale

$$\hat{\eta} = 1 - X\hat{\hat{\eta}} \,. \tag{8.53}$$

Then with this change of variable the governing equation (8.37) becomes

$$\tilde{a}_1 d_1 \hat{\tau}'' = -\hat{\tau} - (\hat{\hat{\eta}} + d_1)\hat{\tau}' \ , \tag{8.54}$$

an ordinary differential equation for $\hat{\tau}$, to leading order. By integrating (8.54) by parts with respect to $\hat{\hat{\eta}}$ we find

$$\tilde{a}_1 d_1 \hat{\tau}' = -(\hat{\hat{\eta}} + d_1)\hat{\tau} + d_4 \tag{8.55}$$

with an unknown constant d_4. But since we have assumed when X is small that the outer region is uniform far away from the junction we have thus assumed that $\hat{\tau} \to 0$ and $\hat{\tau}' \to 0$ as $\hat{\hat{\eta}} \to \infty$, so the constant $d_4 = 0$. The solution to (8.55) is then

$$\hat{\tau} = d_5 \exp\left(\frac{-(\hat{\hat{\eta}} + d_1)^2}{2\tilde{a}_1 d_1}\right) \ . \tag{8.56}$$

The junction condition (8.51) occurs where $\hat{\hat{\eta}} = 0$, which yields from (8.56):

$$d_5 = \frac{\tilde{a}_1}{a_2 d_1} \exp\left(\frac{d_1}{2\tilde{a}_1}\right) \ . \tag{8.57}$$

The condition (8.42) used in the numerical scheme to optimise f at each X-station comes from the requirement of an exact match of U_X across the junction. That is we require:

$$\left.\frac{\bar{a}_1 \tau_{\hat{\eta}}}{f-1}\right|_{\hat{\eta}=1} = \left.\frac{a_2 T_\eta}{f}\right|_{\eta=1} \ . \tag{8.58}$$

In the small-X regime this condition becomes

$$\left.\frac{\tilde{a}_1 d_1 \hat{\tau}'}{X}\right|_{\hat{\hat{\eta}}=0} = \left.\frac{a_2 T_0'}{d_1 X}\right|_{\eta=1} \ . \tag{8.59}$$

From (8.56) and (8.46) we can determine the values of $\hat{\tau}'(0)$ and $T_0'(1)$, which upon substitution into (8.59) yield

$$-d_1^2 d_5 \exp\left(\frac{-d_1}{2\tilde{a}_1}\right) = -\frac{d_1}{a_2}\left(\tilde{a}_1 + \frac{d_2 a_2^2}{d_1}\right) \ . \tag{8.60}$$

Substituting the value of d_5 from (8.57) gives

$$d_2 = 0 \implies D = 0 \implies d_3 = 2 \,, \tag{8.61}$$

the latter from equation (8.47). Finally, (8.50) now gives us

$$d_1 = 2(a_2 - \tilde{a}_1) \,. \tag{8.62}$$

All the constants are therefore determined.

In summary, the initial conditions at small values $\hat{X}$ of X are:

$$T = \left(1 - \frac{d_1}{2a_2}\eta\right)^2 \,; \tag{8.63a}$$

$$\tau = \frac{d_5}{\hat{X}} \exp\left(\frac{-\left(\frac{1-\hat{\eta}}{\hat{X}} + d_1\right)^2}{2\tilde{a}_1 d_1}\right) \,; \tag{8.63b}$$

$$f = d_1 \hat{X} \,; \tag{8.63c}$$

$$\hat{U}_{\mathcal{Q}} = a_2 \hat{X} \quad \text{(from (8.29)} \,; \tag{8.63d}$$

$$\text{where} \quad d_1 = 2(a_2 - \tilde{a}_1) \tag{8.63e}$$

$$\text{and} \quad d_5 = \frac{\tilde{a}_1}{a_2 d_1} \exp\left(\frac{d_1}{2\tilde{a}_1}\right) \,, \tag{8.63f}$$

where $\tilde{a}_1, a_2$ are already known.

Results

The numerical scheme outlined above was run over a variety of grids and grid-convergence of the results was demonstrated. A typical grid had 101 points in each layer (that is, in both the η-layer and the $\hat{\eta}$-layer), an X-step size of 0.01, and was tested to an accuracy of 10^{-10}. We determined for each grid a value of $\hat{X}$ from which to start the computation and for which the results were stable over small modifications to this value. In the case of the above grid the

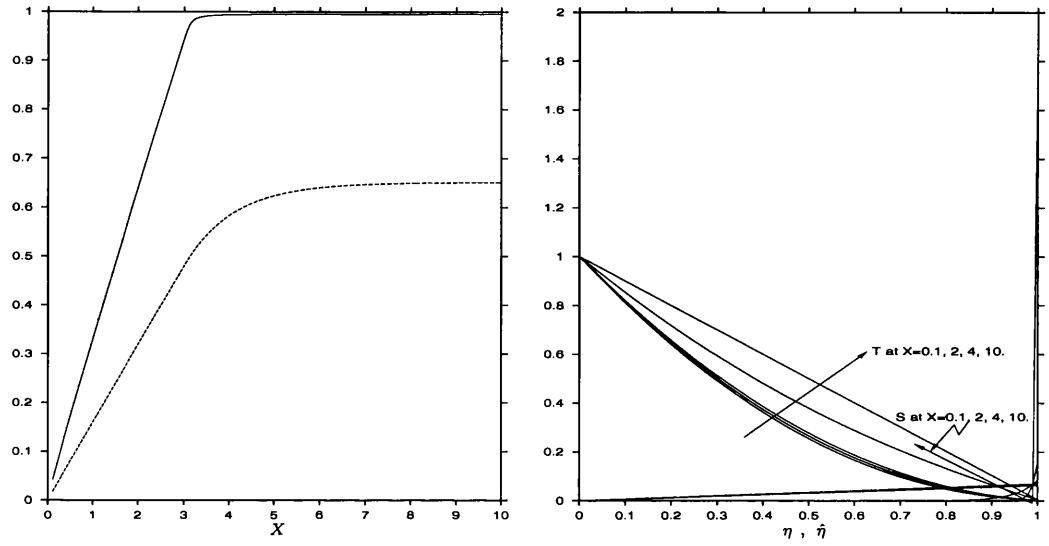

Figure 8.3: Left hand side: plot of f (solid) and $\hat{U}_{\mathcal{L}}$ against X. Right hand side: the development of T and S with X.

computation was started from $X = 0.1$. The results of this computation are shown in Figure 8.3.

The developments of f and $\hat{U}_{\mathcal{L}}$ are seen to be virtually linear until around $X = 3.5$, where a sudden bending occurs over a short distance and a far-downstream asymptote appears to be reached relatively quickly. In fact, the graph on the left hand side of Figure 8.4 shows that the linear growths which occur for $\mathcal{O}(1)$ values of X are very close to the small-X asymptotes of f and $\hat{U}_{\mathcal{L}}$ given in (8.63c) and (8.63d), respectively. The sudden bending away from the small-X asymptotes will be investigated analytically in §8.1.4. The graph on the right hand side of Figure 8.4 shows how the location of the bending is stable over a variety of grids. What is more, the value of $f(X = 10)$ was stable to three decimal places over all grids which showed convergence, and the value of $\hat{U}_{\mathcal{L}}(X = 10)$ agreed to two decimal places. These far-downstream

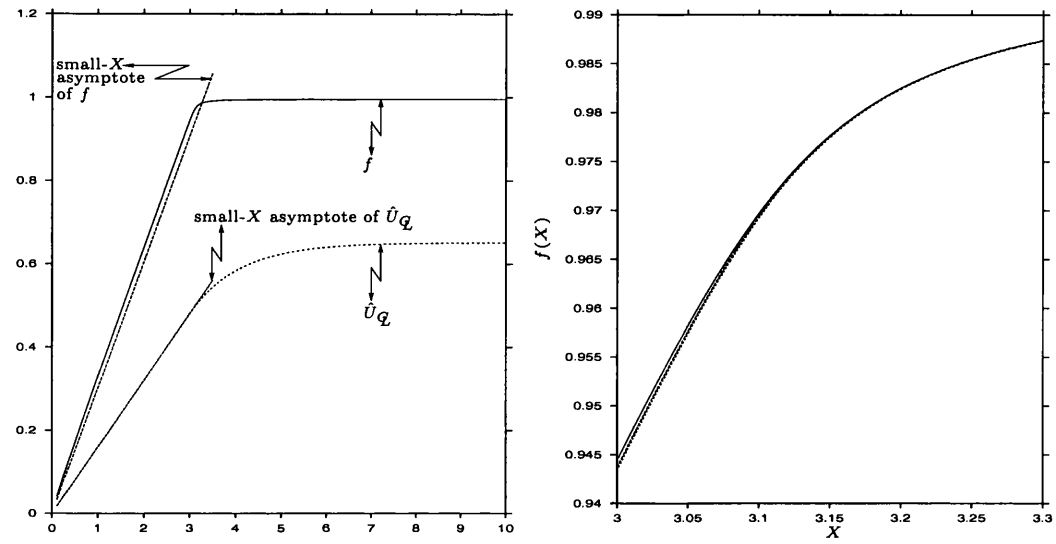

Figure 8.4: Left hand side: f, $\hat{U}_{\mathcal{L}}$, and their small-X asymptotes. Right hand side: closeup of the sudden bending of f, showing results over three grids with step $dX = 0.01, 0.001, 0.0001$ and suitable refinements of the η and $\hat{\eta}$ step sizes.

asymptotes are

$$f(10) = 0.995 \quad , \quad \hat{U}_{\mathcal{L}}(10) = 0.65 \; . \tag{8.64}$$

Large-X asymptotes

The apparent attainment of constant values of f and $\hat{U}_{\mathcal{L}}$, *i.e.* fully developed flow, for large values of X suggests examining the governing equations (8.26) in the limit $X \to \infty$. Returning to equation (8.31) we see that the inner part of (8.26) becomes simply

$$T_{yy} = 0 \tag{8.65}$$

if X-derivatives are negligible in the limit as $X \to \infty$, and thus

$$T = Ay + B \; , \tag{8.66}$$

with A, B being unknown constants. The conditions (8.34) and (8.35) yield $B = 1$ and $A = \frac{1}{f}\left(\left(\frac{\bar{a}_1}{fa_2}\right)^2 - 1\right)$, so that

$$T = \left(\left(\frac{\bar{a}_1}{fa_2}\right)^2 - 1\right)\frac{y}{f} + 1 \quad \text{as} \quad X \to \infty \,. \tag{8.67}$$

Examining equation (8.36) enables us to show that in the limit $X \to \infty$ the outer part of (8.26) becomes

$$\tau_{yy} = 0 \implies \tau = C(y-1) \,, \tag{8.68}$$

again provided that X-derivatives are negligible. The condition (8.39) then yields $C = \frac{\bar{a}_1}{a_2 f^2(f-1)}$, so that

$$\tau = \frac{\bar{a}_1(y-1)}{a_2 f^2(f-1)} \,. \tag{8.69}$$

Imposing next continuity of U_X across the junction $y = f$ requires

$$\bar{a}_1 \tau_y = a_2 T_y \quad \text{at } y = f, \tag{8.70}$$

which upon substitution of the expressions (8.67) and (8.69) yields the relation

$$a_2^2(f^3 - f^2) + \bar{a}_1^2 = 0 \,. \tag{8.71}$$

Recall that $\bar{a}_1 = a_1 \hat{U}_{\mathcal{L}}$ and so (8.71) only gives a value for f in the limit of large X when $\hat{U}_{\mathcal{L}}$ is already known in the limit. Therefore not only is $\hat{U}_{\mathcal{L}}$ an important parameter in the development of the flow in this case, but it is also an important net effect, since it influences the downstream asymptote. It would seem at this stage that in order to determine $\hat{U}_{\mathcal{L}}$ at a far-downstream position, a full computation in the development region leading up to the fully developed region would need to be done. This is certainly different from the laminar case where a knowledge of the pressure difference alone between the

start and the fully developed region provides the centre-line velocity. On the other hand, the linear growth in line with the small-X asymptote, coupled with the sudden bending and attainment of the large-X asymptote described above, point towards a useful predictive tool for $\hat{U}_{\mathcal{L}}$ and f which we shall describe further in the analytical work of §8.1.4.

Finally here, if we substitute the computed large-X values of $\hat{U}_{\mathcal{L}}(10)$ given in (8.64) into (8.71) we obtain a cubic equation for f:

$$0.16^2(f^3 - f^2) + (0.65 \times 0.0168)^2 = 0 \implies f = \begin{cases} 0.995\ , \\ 0.071\ , \\ -0.066\ . \end{cases} \tag{8.72}$$

Only the first of these alternatives is physically realistic, and it is in fact equal to the computed large-X value of f given in (8.64). That demonstrates a consistency between the current analysis and the numerical results.

8.1.3 Comparisons with experiments

In this section we compare the computed results shown in Figure 8.3 with experimentally determined values of f and $\hat{U}_{\mathcal{L}}$, as well as the prediction (8.25) with empirical data. The Reynolds numbers given in the experimental references were converted to their equivalent values for the choice of Reynolds number factors made in this chapter, and it is these equivalent values which are quoted below.

In Figure 8.5 we compare the prediction with the data of [51] for the two Reynolds numbers considered in that paper. In detail, the measurement taken at a given point in the duct in [51] is the non-dimensional pressure difference Δp between the pressure at that point and the exit pressure. The data in [51]

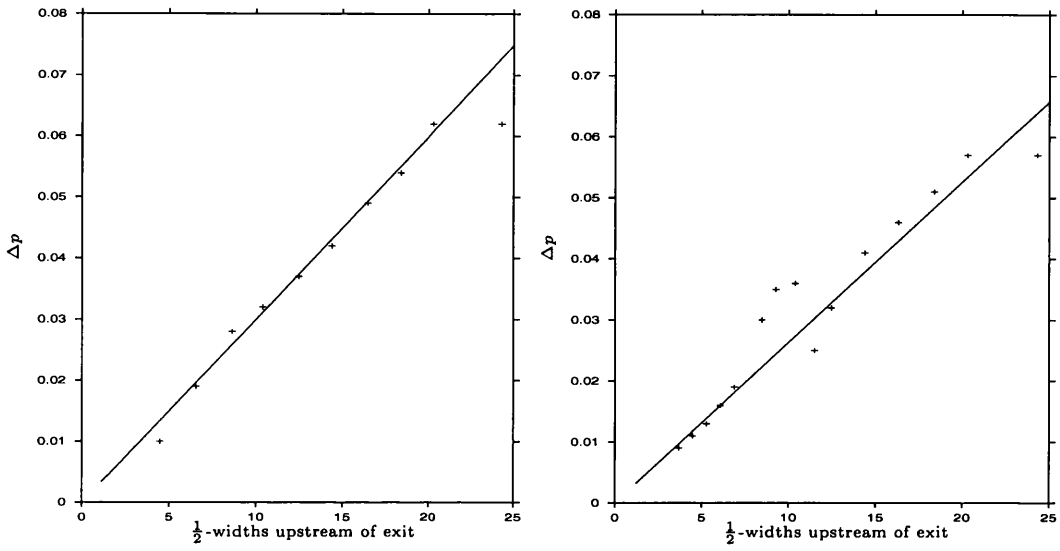

Figure 8.5: Left hand side: comparison between (8.25) (line) and [51] at $Re = 30,800$. Right hand side: comparison between (8.25) (line) and [51] at $Re = 61,600$. Δp is the pressure difference described in the text.

is plotted with the number of half-widths running from zero at the exit in an upstream direction. It is clear from Figure 8.5 that the prediction (8.25) gives values which agree very well indeed with the empirical data.

In Figure 8.6 we compare the total centre-line velocity u_Q derived from the numerical results with three data sets from: [59] (with measured $Re = 1.7 \times 10^5$); [20] (with measured $Re = 9 \times 10^4$); [56] (with measured $Re = 2.07 \times 10^4$).

While the numerical results in Figure 8.6 certainly capture the nature and location of the bending very well, the value of u_Q is correct only to within an order of magnitude. However, it should be recalled that we are only considering the first term in the perturbation expansion of u and that higher-order terms should correct the value. Indeed, a comparison of some numerical results with experimental data in [60, pp.32–33] showed that including just the first term in the expansion gave only qualitative agreement whereas including

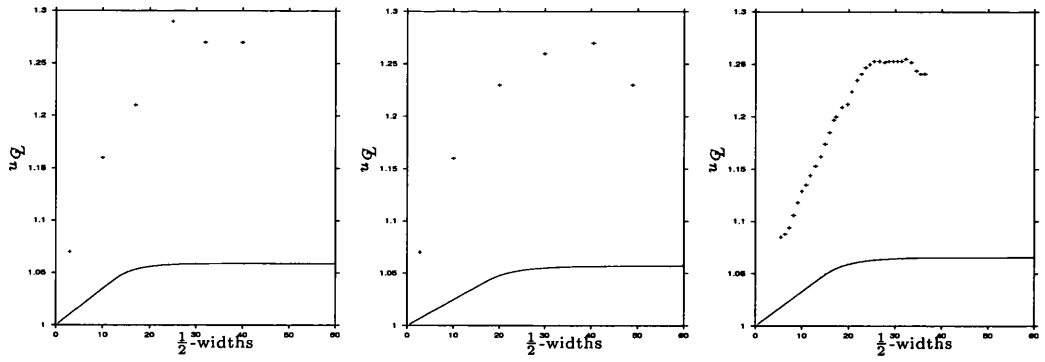

Figure 8.6: Left to right: comparisons between numerical results and [59], [20], [56].

several higher-order terms brought the numerical predictions very close to the empirical values. It is interesting to note in this context that the pressure predictions are very close indeed to the experimental data.

8.1.4 Small-$\bar{a}_1$ analysis

In this section we show or confirm that the sudden bending of f as it approaches the centre-line is smooth over a short length scale. To do so, we neglect the outer part of the TBL model for $y > y_J$, based on the assumption that the constant a_1, where $\bar{a}_1 = a_1 \hat{U}_Q$, which appears in (8.22) is sufficiently small (in fact it is 0.0168). This helpful approximation, which corresponds to a rational analysis for $\bar{a}_1$ tending to zero, has been previously used for example in [60], where it provided a check on derived results.

The *major* feature when $\bar{a}_1$ is small is that the two linear sections of f — the first when f increases in line with its small-X asymptote and the second when f is apparently constant — describe the majority of the solution, in agreement with the full computations presented above. See Figure 8.7.

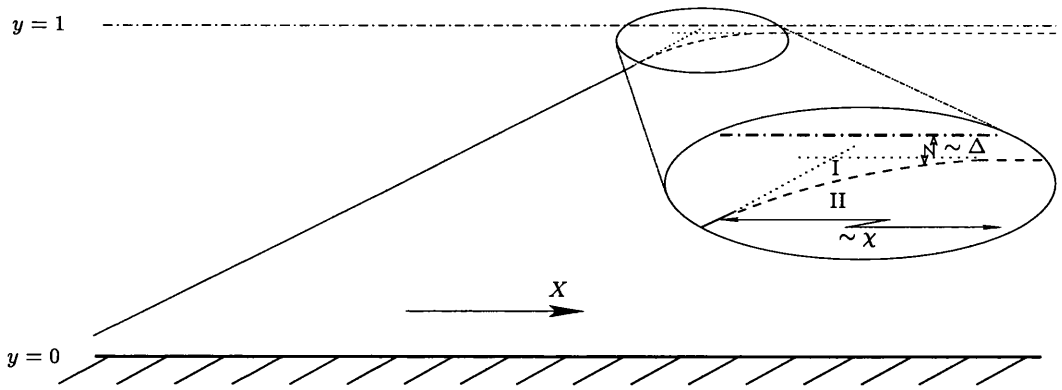

Figure 8.7: Length scales and regions of the small-$\bar{a}_1$ analysis.

New scales

We consider the small bending region shown in Figure 8.7 in which we will demonstrate that f bends smoothly. The scalings are:

$$X = X_0 + \chi\tilde{X} + \dots \; ; \tag{8.73a}$$

$$f = 1 - \Delta\tilde{f}(\tilde{X}) + \dots \; , \tag{8.73b}$$

where X_0 is constant. Furthermore, in order to neglect the outer part of the model we let

$$\bar{a}_1 = \delta\hat{U}_{\mathcal{L}} \tag{8.74}$$

for $\delta \ll 1$, and we note that $\hat{U}_{\mathcal{L}}$ is considered an $\mathcal{O}(1)$ constant here since $\hat{U}_{\mathcal{L}} = a_2 X_0 + \mathcal{O}(\chi)$.

The governing equations in the bending region follow from examining the leading order balances of (8.26). We will let τ^{I} denote τ in the outer part, or region I, of (8.26) and τ^{II} denote τ in the inner part, or region II.

Since $y \sim 1$ in region II, the length scales balance to give

$$\tau^{\mathrm{II}} \sim \chi^{-1} \; . \tag{8.75}$$

We can determine the order of magnitude of τ^{I} from the junction condition (8.39) which gives

$$\tau^{\mathrm{I}} \sim \delta \ . \tag{8.76}$$

Additionally, in the outer region we have $y = 1 - \Delta\tilde{y}$ and so the balance of length scales in the outer part of (8.26) yields the relation

$$\chi\delta \sim \Delta^2 \ . \tag{8.77}$$

Finally, we note that in the region of interest we must have

$$\frac{df}{dX} \sim 1 \tag{8.78}$$

in order to match with the incoming $\mathcal{O}(1)$ slope since $f = 2a_2X_0 + \mathcal{O}(\delta)$ there from (8.63c,e). This together with (8.77), gives:

$$\delta \sim \Delta \sim \chi \ , \tag{8.79}$$

which fixes the local scalings.

Governing equations near the junction

The work above suggests expanding τ^{I} as:

$$\tau^{\mathrm{I}} = \delta\tau^{(1)} + \dots \ , \tag{8.80}$$

so that when $\tilde{y} \sim 1$ a leading order examination of the outer part of (8.26) gives the diffusion equation

$$\tau^{(1)}_{\tilde{X}} = \hat{U}_{\mathcal{L}}\tau^{(1)}_{\tilde{y}\tilde{y}} \tag{8.81}$$

subject to the conditions:

$$\tau^{(1)} = 0 \qquad \text{at} \quad \tilde{y} = 0 \ ; \tag{8.82a}$$

$$\tau^{(1)} = \frac{\hat{U}_{\mathcal{L}}}{a_2} \quad \text{at} \quad \tilde{y} = \tilde{f}(\tilde{X}) \ . \tag{8.82b}$$

This linear problem can only be solved once an expression for the junction contribution $\tilde{f}(\tilde{X})$ is known, as discussed on page 265 below.

The scaling for τ^{II} comes from the necessity of matching τ across the junction, which suggests that

$$\tau^{\mathrm{II}} \sim \delta \tag{8.83}$$

close to the junction. On the other hand, there must also be an order unity variation of τ^{II} in order to match with the incoming flow. Therefore where y is of $\mathcal{O}(1)$ we must have

$$\tau^{\mathrm{II}} = \tau_0(y) + \delta\tau_1(\tilde{X}, y) + \dots \,, \tag{8.84}$$

with the profile $\tau_0(y)$ being known. This provides the following leading order balance of the inner part of (8.26),

$$\tau_{1\tilde{X}} = a_2(y^2\tau_0^2)_{yy} \tag{8.85}$$

when $y \sim 1$, subject to the conditions:

$$\tau_0(y) = 0 \qquad \text{at} \quad y = f \,; \tag{8.86a}$$

$$\tau_1 = \frac{\hat{U}_{\mathcal{Q}}}{a_2} \quad \text{at} \quad y = f \,. \tag{8.86b}$$

We observe that (8.86a) is consistent with neglecting the outer part of the model. Since the right hand side of (8.85) is a function of y only we can integrate directly to obtain

$$\tau_1 = a_2\tilde{X}\left((y\tau_0)^2\right)_{yy} + g_1(y) \tag{8.87}$$

for some function $g_1(y)$. The conditions (8.86a,b) yield $g_1(y) = \frac{\hat{U}_{\mathcal{Q}}}{a_2}$, thus giving:

$$\tau_1 = a_2\tilde{X}\left((y\tau_0)^2\right)_{yy} + \frac{\hat{U}_{\mathcal{Q}}}{a_2} \tag{8.88}$$

where y is of order unity.

Close to the junction, where $y = 1 - \Delta\tilde{y}$ once more, we therefore have

$$\tau^{\mathrm{II}} = \delta\tau^{(2)} + \dots \ , \tag{8.89}$$

and so the inner part of (8.26) becomes

$$\tau^{(2)}_{\tilde{X}} = a_2 \left(\tau^{(2)2}\right)_{\tilde{y}\tilde{y}} \ , \tag{8.90}$$

leading to a non-linear diffusion problem for $\tau^{(2)}$ which is discussed below on page 264. The local-bending problem of (8.90) and its boundary conditions has not been solved to date. Nevertheless it appears to allow matching upstream at large negative $\tilde{X}$ with the incident straight-f form holding ahead of the bending region, and its downstream properties are of interest as described below.

Large positive $\tilde{X}$

In the limit $\tilde{X} \to \infty$, in the downstream end of the bending region, we anticipate the emergence of an $\tilde{X}$-invariant state f_∞ for f. Equation (8.81) there yields

$$\tau^{(1)} = \lambda_1\tilde{y} + \lambda_2 \quad \text{as} \quad \tilde{X} \to \infty \ , \tag{8.91}$$

but $\lambda_2 = 0$ from (8.82a). Furthermore, conditon (8.82b) gives $\lambda_1 = \frac{\hat{U}_G}{a_2\tilde{f}_\infty}$ and so as $\tilde{X} \to \infty$ we know that

$$\tau^{\mathrm{I}} = \delta\frac{\hat{U}_G}{a_2\tilde{f}_\infty}\tilde{y} + \dots \ . \tag{8.92}$$

As in the discussion below starting on page 264, there may well be streamwise flow development even relatively far downstream of the bending region. However, if we suppose for now that in this downstream region there is no

streamwise flow development to influence the junction then, from considering (8.90) in the limit $\tilde{X} \to \infty$, we obtain:

$$\tau^{(2)} = (\mu_1 \tilde{y} + \mu_2)^{\frac{1}{2}} , \tag{8.93}$$

with μ_1, μ_2 unknown constants. Continuity of τ therefore requires

$$\left(\frac{\hat{U}_{\mathcal{Q}}}{a_2} \right)^2 = \mu_1 \tilde{f}_\infty + \mu_2 , \tag{8.94}$$

while continuity of $\hat{U}_X$ requires

$$\hat{U}_{\mathcal{Q}} \tau^{(1)}_{\tilde{y}} = a_2 (\tau^{(2)2})_{\tilde{y}} \quad \text{at} \quad \tilde{y} = \tilde{f}_\infty . \tag{8.95}$$

Therefore, with (8.91), (8.82b) and (8.93) we deduce that

$$\mu_1 = \frac{\hat{U}^2_{\mathcal{Q}}}{a_2^2 \tilde{f}_\infty} , \tag{8.96}$$

which substituted into (8.94) gives

$$\mu_2 = 0 . \tag{8.97}$$

In summary we have as $\tilde{X} \to \infty$:

$$\tau^{(1)} = \frac{\hat{U}_{\mathcal{Q}}}{a_2 \tilde{f}_\infty} \tilde{y} + \ldots ; \tag{8.98a}$$

$$\tau^{(2)} = \frac{\hat{U}_{\mathcal{Q}}}{a_2 \tilde{f}_\infty^{\frac{1}{2}}} \tilde{y}^{\frac{1}{2}} + \ldots . \tag{8.98b}$$

Hence at the junction $\tilde{y} = \tilde{f}_\infty$ we have equality of these two expressions. Since the predictions (8.98a,b) are obtained by considering only the *leading-order* correction term, we feel that the simplifying assumption of this section provides us with a useful indicative tool with $\hat{U}_{\mathcal{Q}}$ constant. We recall that this tool is predicated on the assumption on page 262 above of no streamwise flow development in the downstream end of the bending region.

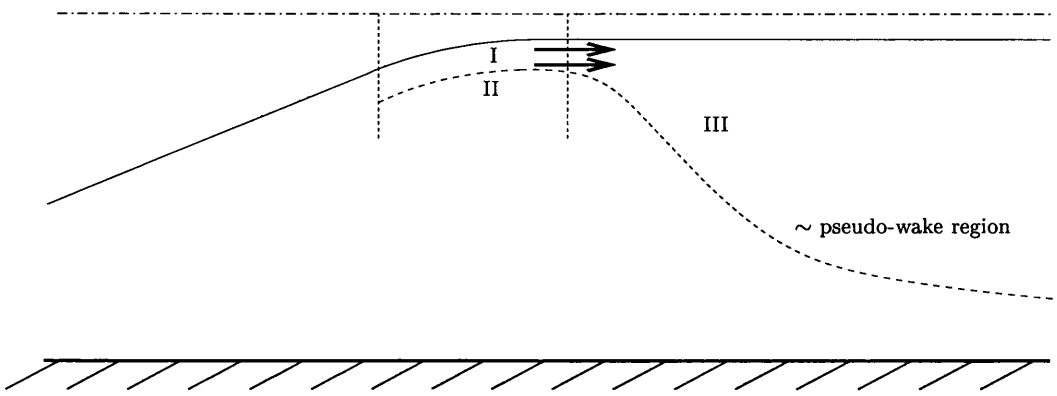

Figure 8.8: Regions of the flow field.

Discussion

Returning to the non-linear equation (8.90) we note that the condition on $\tau^{(2)}$ at the junction is

$$\tau^{(2)}(\tilde{y} = \tilde{f}) = \frac{\hat{U}_{\mathcal{L}}}{a_2} \ . \tag{8.99}$$

The condition on $\tau^{(2)}$ as $\tilde{y} \to \infty$ required to match with τ_1 in (8.84)–(8.88) raises some questions. If we first suppose that $\tau^{(2)} \sim c\tilde{y}$ in the limit $\tilde{y} \to \infty$, for some non-zero constant c, then in (8.84) we need to take

$$\tau^{\mathrm{II}} \sim f_1(y) + \delta f_2(\tilde{X}, y) \tag{8.100}$$

such that $f_1(y) \sim \delta c\tilde{y}$ as y approaches the junction. This suggests setting $f_1(y) = c(1-y)$ such that

$$\tau^{\mathrm{II}} \sim c(1-y) + \delta f_2(\tilde{X}, y) \ , \tag{8.101}$$

where the first term on the right hand side matches with τ_0 and the second with τ_1.

However, the incoming flow has $\tau = -\frac{1}{2a_2} + \frac{1}{y}$ from (7.51), which suggests that $T = (y\tau)^2 = \left(1 - \frac{y}{2a_2}\right)^2$. With the scale change, the implication that

$$T_0 \sim (1-y)^2 \tag{8.102}$$

near the junction seems to indicate that $c = 0$ in the above.

The above discussion indicates a term in $\tilde{y}^{\frac{1}{2}}$ becoming important, making the downstream region very much like the wake flow reported in [60]. The schematic configuration of the regions is represented in Figure 8.8. The pseudo-wake flow for large $\tilde{X}$ feels the inflow determined by solving the non-linear problem for $\tau^{(2)}$ and a continued development of the interface between regions I and III may invalidate the results for large $\tilde{X}$ obtained above. We note that as the thickness of the pseudo-wake region increases (as $\tilde{X}$), the region gradually feels the influence of the lower wall.

Finally, we observe that continuity of $\hat{U}_X$ across $y = f$ yields:

$$\bar{a}_1 \tau_y^{\mathrm{I}}\Big|_{y=f} = a_2 (y^2 \tau^{\mathrm{II}2})_y\Big|_{y=f} \tag{8.103}$$

$$\Longrightarrow \hat{U}_{\tilde{Q}} \tau_{\tilde{y}}^{(1)}\Big|_{\tilde{y}=\tilde{f}} = 2a_2 \tau^{(2)} \tau_{\tilde{y}}^{(2)}\Big|_{\tilde{y}=\tilde{f}}. \tag{8.104}$$

Once the non-linear problem involving (8.90) has been solved for $\tau^{(2)}$ we can use (8.104) to determine $\tilde{f}$ precisely and hence the linear problem for $\tau^{(1)}$ on page 260 above can be solved.

8.2 The quasi-straight axisymmetric three-dimensional duct

In this section we turn our attention to the merged flow in an axisymmetric three-dimensional duct. The configuration diagram is shown in Figure 8.9.

8.2.1 Governing equations

Since $\hat{u}_2$ is driven by $\hat{K}_2$ in the downstream far-field of the entry region, from equation (7.14), $\hat{u}_2$ remains zero in the quasi-straight case. Furthermore, sec-

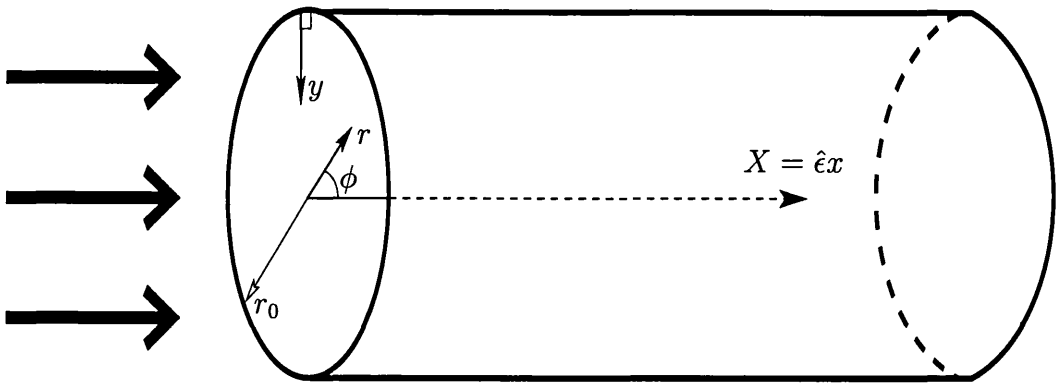

Figure 8.9: Coordinate configuration for the three-dimensional axisymmetric duct. Note that the boundary layer is not shown and that the duct is considerably longer than indicated here.

ondary flow-generating sharp corners are absent in the cross-section if we consider an axisymmetric duct, and so then we only need to solve for U in the X-direction and V in the wall-normal (radial) direction.

Full equations

The full dimensional general axisymmetric equations are given in [15, p.259] as:

$$\text{Continuity:} \qquad \frac{\partial}{\partial x_D}(r_D \bar{\rho}_D \bar{U}_D) + \frac{\partial}{\partial y_D}(r_D \overline{\rho V}_D) = 0; \tag{8.105a}$$

$$\text{Momentum:} \qquad \bar{\rho}_D \bar{U}_D \frac{\partial \bar{U}_D}{\partial x_D} + \overline{\rho V}_D \frac{\partial \bar{U}_D}{\partial y_D} = -\frac{\partial \bar{p}_D}{\partial x_D} + \frac{1}{r_D}\frac{\partial}{\partial y_D}\left(r_D\left(\bar{\mu}_D \frac{\partial \bar{U}_D}{\partial y_D} - \bar{\rho}_D \overline{u'v'}_D\right)\right), \tag{8.105b}$$

where r_D is a known function of y_D, bars indicate averaged quantities, and primes indicate fluctuating quantites, as in Chapter 6. Note that the slender layer approximation has been used here since $x_D \gg y_D$ far downstream in the merged region.

We model the turbulent stress term with the Cebeci-Smith model as previously, and re-iterate that the analysis holds in general for any two-tiered algebraic mixing-length model. The eddy-viscosity B_D in the axisymmetric case is given in [15, pp.255–256] as

$$B_D = \begin{cases} L_D^2 \frac{r_D}{r_{0D}} \left| \frac{\partial U_D}{\partial y_D} \right| \gamma_{\text{tr}} & , \ 0 \leqslant y \leqslant y_{JD} \ , \\ \alpha (U_{\mathcal{Q}})_D \delta_{1D} \gamma_{\text{tr}} & , \ y_{JD} \leqslant y \leqslant r_{0D} \ , \end{cases} \tag{8.106a}$$

where

$$L_D = 0.4 r_{0D} Ln \left(\frac{r_D}{r_{0D}} \right) \left[1 - exp \left(-\frac{r_{0D}}{A_D} Ln \left(\frac{r_D}{r_{0D}} \right) \right) \right] \ , \tag{8.106b}$$

$$\delta_{1D} = \int_0^{r_{0D}} \left(1 - \frac{U_D}{(U_{\mathcal{Q}})_D} \right) \left(1 - \frac{y_D}{r_{0D}} \right) dy_D \ . \tag{8.106c}$$

We take the intermittency factor γ_{tr} to be unity and $\alpha = a_1 = 0.0168$, as throughout this thesis.

Referring to Figure 8.9 we have $y_D = r_{0D} - r_D$. Furthermore, in keeping with §8.1, we non-dimensionalise the length scales on r_{0D} which we take to be constant. The mean density and mean molecular viscosity are also taken to be constant. As previously, we non-dimensionalise the velocities on the upstream uniform flow, the pressure is non-dimensionalised on twice the upstream dynamic pressure head, and in the following work we omit the bars since it is understood that mean quantities are considered. Finally, we take $Re \gg 1$ such that the laminar viscous stress terms vanish to leading order.

The non-dimensional governing equations are thus:

$$((1-y)U)_x + ((1-y)V)_y = 0 \ ; \tag{8.107a}$$

$$UU_x + VU_y = -p_x - \frac{BU_y}{(1-y)} + (BU_y)_y \ , \tag{8.107b}$$

where in the limit $Re \to \infty$ the non-dimensional eddy-viscosity is:

$$B = \begin{cases} a_2(1-y)Ln^2(1-y)U_y & , \ y < y_J \ ; \\ a_1\delta_1 & , \ y_J < y < 1 \ , \end{cases} \tag{8.108a}$$

and

$$a_1 = 0.0168 \ , \quad a_2 = 0.16 \ , \quad \delta_1 = \int_0^1 \left(1 - \frac{U}{U_{\mathcal{L}}}\right)(1-y)\ dy \ . \tag{8.108b}$$

We observe that the curvilinear coordinate system has introduced an extra factor $(1-y)$ in the continuity equation. Further, there are now two terms involving the eddy-viscosity B in the x-momentum equations, and the form of B in the inner region now contains a Ln term which was not there in the two-dimensional case.

Perturbed forms

For consistency with the work of Chapters 6 and 7 and with §8.1 we take the following velocity and pressure perturbations when $x = \hat{\epsilon}^{-1}X$ and $y \sim 1$:

$$U = 1 + \hat{\epsilon}\hat{U} + \dots \ ; \tag{8.109a}$$

$$V = \hat{\epsilon}^2\hat{V} + \dots \ ; \tag{8.109b}$$

$$p = 1 + \hat{\epsilon}p_1(X) + \hat{\epsilon}^2 p_2(X,y) + \dots \ . \tag{8.109c}$$

With these perturbations the quasi-displacement δ_1 becomes:

$$\delta_1 = \int_0^1 \left(1 - (1 + \hat{\epsilon}\hat{U} + \dots)(1 - \hat{\epsilon}\hat{U}_{\mathcal{L}} + \dots)\right)(1-y)\ dy \tag{8.110a}$$

$$= \hat{\epsilon}\hat{\delta}_1 + \dots \ , \tag{8.110b}$$

$$\text{where } \hat{\delta}_1 = \int_0^1 (\hat{U}_{\mathcal{L}} - \hat{U})(1-y)\ dy \ . \tag{8.110c}$$

Consequently, examining (8.107a,b) and (8.108a,b) to leading order gives:

$$\left((1-y)\hat{U}\right)_X + \left((1-y)\hat{V}\right)_y = 0\ ; \tag{8.111a}$$

$$\hat{U}_X = -p_{1X} + \frac{1}{(1-y)}\left((1-y)\hat{B}\hat{U}_y\right)_y\ , \tag{8.111b}$$

where

$$\hat{B} = \begin{cases} a_2(1-y)Ln^2(1-y)\hat{U}_y & ,\ y < y_J\ , \\ a_1\hat{\delta}_1 & ,\ y_J < y < 1\ . \end{cases} \tag{8.111c}$$

The boundary conditions as $y \to 0+$ are:

$$\hat{U} \sim 1 \cdot Ln(y) + \ldots \quad \text{and} \quad \hat{V} = 0\ . \tag{8.112}$$

Equation (8.111b) can be solved for $\hat{U}$ and then $\hat{V}$ can be found separately from (8.111a).

8.2.2 Analysis and comparisons with experiments

Integration of (8.111a) gives:

$$\frac{d}{dX}\int_0^1 \hat{U}(1-y)\ dy + \left[(1-y)\hat{V}\right]_0^1 = 0\ , \tag{8.113a}$$

$$\text{that is:} \quad \int_0^1 \hat{U}(1-y)\ dy = \text{constant for all } X. \tag{8.113b}$$

Since $\hat{U}$ is zero at $X \to 0+$ we have

$$\int_0^1 \hat{U}(1-y)\ dy \equiv 0 \text{ for all } X. \tag{8.114}$$

Then equation (8.110c) is

$$\hat{\delta}_1 = \int_0^1 \hat{U}_{\mathcal{L}}(1-y)\ dy - \int_0^1 \hat{U}(1-y)\ dy \tag{8.115}$$

where the second integral on the right hand side is zero by (8.114). Thus

$$\hat{\delta}_1 = \frac{1}{2}\hat{U}_{\mathcal{L}} \ . \tag{8.116}$$

We note that $\hat{\delta}_1$ in the two-dimensional duct is twice the centre-line velocity term $\hat{U}_{\mathcal{L}}$, whereas here it is $\frac{1}{2}\hat{U}_{\mathcal{L}}$, which is a considerable difference between the two-dimensional and three-dimensional axisymmetric cases.

We observe that for a function G defined in the duct the double integral over the cross section is:

$$\begin{aligned}\int_0^{2\pi}\int_0^1 G(x,r,\phi)r\ drd\phi &= \int_0^{2\pi}\int_1^0 G(x,(1-y),\phi)(1-y)\ (-dy)d\phi \\ &= \int_0^{2\pi}\int_0^1 \bar{G}(x,y,\phi)(1-y)\ dyd\phi \ .\end{aligned} \tag{8.117}$$

In the axisymmetric case considered here all the principal variables are functions of x and r only. Then integrating (8.111b) over the cross-section yields

$$\int_0^{2\pi}\int_0^1 \hat{U}_X(1-y)\ dyd\phi = -p_{1X}\int_0^{2\pi}\int_0^1 (1-y)\ dyd\phi + \int_0^{2\pi}\int_0^1 \left((1-y)\hat{B}\hat{U}_y\right)_y\ dyd\phi \tag{8.118}$$

which by (8.114) reduces to:

$$\frac{1}{2}\cdot p_{1X}\cdot 2\pi = 2\pi\cdot\left[(1-y)\hat{B}\hat{U}_y\right]_0^1 \ . \tag{8.119}$$

Since $\hat{U}_y = 0$ at the centre-line to preserve symmetry, and by using the wall boundary condition on $\hat{U}$ given in (8.112) together with the series expansion of $Ln(1-y)$, we obtain

$$p_{1X} = -2a_2 \ , \tag{8.120}$$

which predicts a pressure gradient twice as great as the two-dimensional case.

We may compare the prediction (8.120) with the experimental data of [52]. Measurements of the non-dimensional pressure difference Δp between the current X-station and the exit pressure are plotted in [52] for two Reynolds

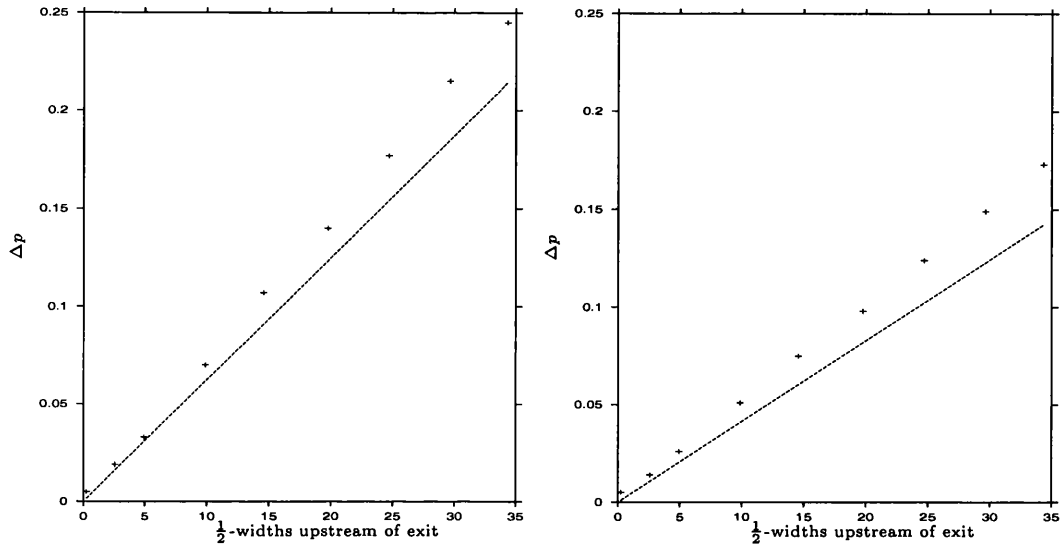

Figure 8.10: Left hand side: comparison between (8.120) (line) and [52] at $Re = 25,000$. Right hand side: comparison between (8.120) (line) and [52] at $Re = 250,000$. Δp is the pressure difference described in the text.

numbers corresponding to 2.5×10^4 and 2.5×10^5 as we have defined Re. We plot against distance in half-widths measured from zero at the exit and increasing upstream. The comparison is shown in Figure 8.10. We observe that the prediction (8.120) compares very well with the experimental values particularly near the exit of the duct where perhaps the flow is more fully developed.

8.2.3 Small-a_1 analysis

In this section we utilise the numerical smallness of a_1 in the outer part of the eddy-viscosity model as we did in §8.1.4. With this approximation we will show that the centre-line velocity increases linearly with X over an $\mathcal{O}(1)$ section in the X-direction, and that far downstream the junction position $y_J = f(X)$ is constant and lies very near the duct centre-line.

The governing equation now becomes

$$\hat{U}_X = a_2 \left(2 + \frac{1}{(1-y)} \left((1-y)^2 Ln^2 (1-y) \hat{U}_y^2 \right)_y \right) \tag{8.121}$$

for $y < y_J$, from (8.111b,c) and (8.120). The boundary condition as $y \to 0+$ is still as that in (8.112), but the requirement at the unknown $y = y_J$ is

$$\hat{U}_y = 0 \ , \tag{8.122}$$

due to the smallness of a_1. In order to make the governing equation appear more compact we let

$$F(X,y) = \frac{\hat{U}}{2a_2} - X \ , \tag{8.123a}$$

$$\text{and} \quad \sigma(X,y) = (1-y) Ln(1-y) \hat{U}_y \ , \tag{8.123b}$$

so that (8.121) becomes:

$$F_X = \frac{\sigma \sigma_y}{1-y} \ . \tag{8.124}$$

In addition we introduce the junction-fitted coordinate $\eta = \frac{y}{f}$ such that $\eta = 0$ at the wall and $\eta = 1$ at the junction. Equation (8.124) then becomes:

$$F_X = \frac{1}{f} \left(f' \eta F_\eta + \frac{\sigma \sigma_\eta}{1 - \eta f} \right) \ , \tag{8.125}$$

where $'$ denotes differentiation with respect to X. The boundary conditions on F are

$$F_\eta = 0 \quad \text{at} \quad \eta = 1 \ , \tag{8.126a}$$

$$\text{and} \quad F_\eta \sim \frac{1}{2a_2 \eta} \quad \text{as} \quad \eta \to 0+ \ . \tag{8.126b}$$

The first of these conditions requires that $F_\eta = 0$ and hence $\sigma = 0$ at $\eta = 1$. Then $F_X = 0$ at $\eta = 1$ and thus

$$\hat{U}(y = f) = 2a_2 X + c_1 \ . \tag{8.127}$$

There is no significant variation in $\hat{U}$ between $y = f$ and the centre-line $y = 1$ since we have neglected the outer part of the model, and so (8.127) gives the centre-line velocity as

$$\hat{U}_{\mathcal{L}} = 2a_2X + c_1 \tag{8.128}$$

for X of order unity. We note that this linear growth rate is twice that of the corresponding result for the two-dimensional case.

In order to determine next the far-downstream position f_∞ of the junction f we consider the limit $X \to \infty$ in (8.125). We first observe that we expect $F_X = -1$ in the limit $X \to \infty$ and so we consider

$$\frac{\sigma\sigma_\eta}{f_\infty(1 - \eta f_\infty)} = -1 \ . \tag{8.129}$$

Hence

$$\sigma = f_\infty^{\frac{1}{2}}(\eta^2 f_\infty - 2\eta + d_1)^{\frac{1}{2}} \tag{8.130}$$

for some constant d_1. Since $\sigma \to -1$ as $\eta \to 0+$ from (8.126b) we obtain $d_1 = f_\infty^{-1}$, and so

$$\sigma = (\eta^2 f_\infty^2 - 2\eta f_\infty + 1)^{\frac{1}{2}} \ . \tag{8.131}$$

Finally, we require $\sigma = 0$ at $\eta = 1$ from (8.126a) which implies $(f_\infty - 1)^2 = 0$, giving:

$$f_\infty = 1 \ . \tag{8.132}$$

The small-a_1 analysis has thus shown that, after linear growth in the centre-line velocity for X of order unity, a downstream state emerges where the centre-line velocity is constant and the junction position is constant and lies very near the centre-line. We recall that this is an approximation to its true position. We conclude that the three-dimensional axisymmetric case is therefore similar to the two-dimensional case in the above sense, and the flow development predicted here is shown in Figure 8.11.

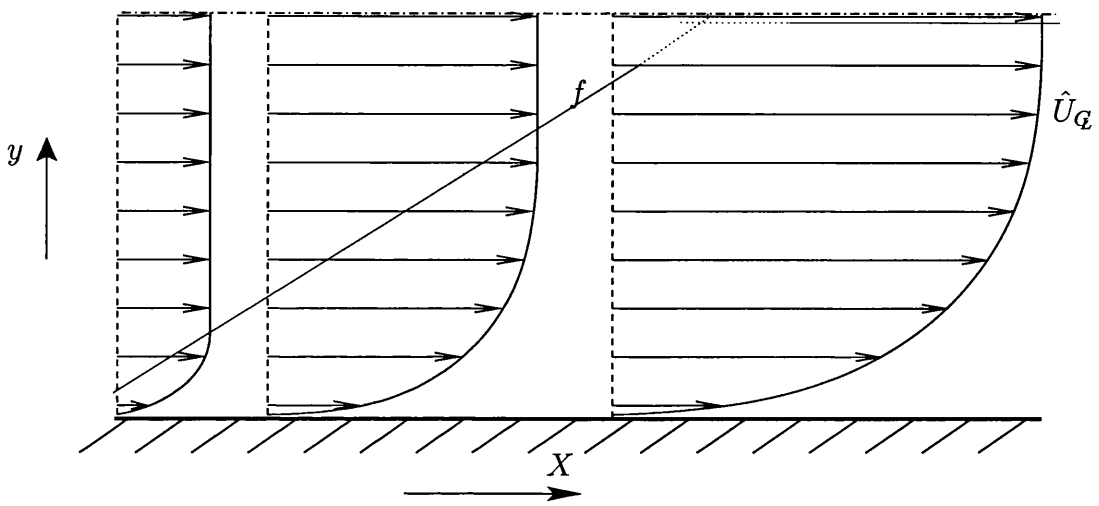

Figure 8.11: Predicted flow development from the small-$\bar{a}_1$ analysis if $\hat{U}_X = 0$ downstream. This is a two-dimensional representation of the three-dimensional axisymmetric flow.

8.3 Final discussion

A significant point is that the important parameter $\hat{U}_{\mathcal{L}}$ (centre-line velocity contribution) has "memory", in the sense that it is coupled with the total flow development and cannot simply be predicted even in fully developed motion from a knowledge of the pressure gradient in the duct. At first sight, the strong dependence of the flow on $\hat{U}_{\mathcal{L}}$ coupled with the memory of $\hat{U}_{\mathcal{L}}$ suggests that, in most flow situations, a substantial calculation needs to be performed in order to determine the far-downstream fully developed form. However, we have shown in this chapter that a potentially powerful predictive tool is suggested by the development of f (junction position) and $\hat{U}_{\mathcal{L}}$. This development firstly involves f and $\hat{U}_{\mathcal{L}}$ growing linearly, exactly in line with their entry-region asymptotes. Both curves then bend suddenly (where the junction position closely approaches the centre-line) and attain their far-downstream uniform

values within a very short streamwise distance. This behaviour was apparent from the numerical results and is consistent with an asymptotic study.

Also there is a further connection with the experimental work of [2]. We mentioned above that the pressure predictions are much closer to empirical values than are the centre-line velocity predictions. In [2], the pressure gradient was established within 15 diameters, whereas the centre-line velocity was not yet established after 40.

Part III

Conclusions

Chapter 9

Conclusions and further work

9.1 Summary

The effects of streamwise curvature on the flow through ducts was studied in two parts in this thesis. Part I concerned the influence of curvature on the core flow, while Part II studied the curvature effects on the growth and development of turbulent boundary layers in the duct.

In **Chapter 2**, as an extension to [77], the entry region of the bend was studied first. It was shown that the apparent pressure discontinuity at the start of the bend experienced by the flow on the full-bend length scale is smoothed across the onset of the bend over a short entry region length scale due to an upstream influence. A similar mechanism acts at the end of the bend. Then over the longer scale we solved the governing equations of the inviscid incompressible case. The closeness between the numerical results and the analytical predictions was described in line with [77]. Solutions were also obtained for novel initial conditions which highlighted the dependence of the far-downstream flow on the initial conditions. The far-downstream behaviour

is also dependent on the length of the bend and the relative strength of the incident swirl.

Chapter 3 provided a summary of relevant thermodynamics, including in §3.3 the equations necessary for the extension of the work in Chapter 2 to include compressibility. This led into **Chapter 4** whose main focus was on the compressible inviscid case in which the density varies. The integrals over cross-sections of the leading order variable parts of both the streamwise velocity and the density were found to be conserved through the length of the bend, but the density along streamlines is driven by vorticity. The vorticity grows linearly with θ. The far-downstream behaviours beyond a bend termination or when the bend is maintained indefinitely were also studied. In the first case, θ-invariant states emerge far downstream, whereas in the second case the variable components of the streamwise velocity and of the density attain θ-invariant states but the vorticity grows linearly with θ. Over a longer length scale this behaviour continues, suggesting the appearance downstream of a more strongly non-linear regime. Also, there exists a singularity in the vorticity close to the corners but not in the density.

Chapter 5 was principally on computations, first for the compressible inviscid case. We employed a fourth-order accurate compact differencing scheme with mid-point averaging in the marching (θ) direction. The numerics confirmed the predictions from Chapter 4. The θ-invariant states are clearly due to the mixing of the profiles apparent from the numerics due to the non-zero swirl. Once again, the non-zero initial swirl regime highlighted the importance of the initial conditions and showed the strength of the mixing effects of the swirl (which grew non-linearly through the bend here); a four-cell structure was mixed around to a two-cell structure.

Second, we addressed the fully non-linear compressible inviscid case. Bulk properties were derived as part of the numerical planning. The numerics were run over a wide range of initial conditions and parameter values. Vorticity grows linearly with θ but the streamwise velocity is not mixed, and pressure and density evolve very weakly. In the absence of curvature no evolution occurs if the initial swirl is zero. When the curvature is weak vorticity grows linearly with θ before connecting with a more curvature-driven region downstream. When the curvature is of order unity then just after the start of the curved section the streamwise velocity and the density are conserved, while vorticity evolves linearly with θ.

We examined the fully non-linear inviscid incompressible case, and we showed that the fully non-linear compressible inviscid case reduces to the fully non-linear incompressible inviscid case, in contrast to the weakly non-linear cases where density made a distinct difference. However, with a weakly varying cross-sectional area p_0 and ρ would in general be expected to vary.

The governing equations of Part I are summarised in **Appendix A**.

Part II concerned the growth and development of the turbulent boundary layer in the duct and the work therein holds in general for any two-tier mixing-length model of the eddy-viscosity. **Chapter 6** gave a general discussion and the governing equations for the inlet flow in a straight duct and the entry flow in a curved duct were derived.

In **Chapter 7** we showed that the velocities split into a core-flow influence and a fully turbulent part which in the streamwise direction behaves like that in a turbulent boundary layer over a flat plate. There is in general a non-zero cross-flow. We derived solutions for the fully turbulent streamwise and cross-flow velocities. The fully turbulent streamwise velocity has no dependence on

the coordinate which runs around the duct, but the fully turbulent cross-flow velocity in general does. A study of the fully turbulent cross-flow velocity showed that at this length scale it asymptotes to a constant value at the wall. There are three distinct downstream regimes in the curved duct depending on the relative magnitudes of the swirl in the core flow and the turbulent fluctuations: the quasi-straight merged turbulent boundary layer; the interaction regime; and the regime in which the turbulent boundary layer stays thin.

Chapter 8 studied the quasi-straight merged case. In the two-dimensional case the quasi-displacement is equal to the leading order variation in the streamwise centre-line velocity and the pressure grows in proportion to the distance downstream. Computational work showed linear growth in both the junction position and the centre-line velocity, followed by a sudden bending to the far-downstream asymptotes. An analysis based on neglecting the outer part of the turbulent boundary layer showed that the sudden bending is smoothed over a short length scale and possibly connects with a pseudo-wake flow downstream. Predictions and numerical results were compared with experiments.

Next, the quasi-straight three-dimensional axisymmetric case was considered with predictions for the linear growth of the quasi-displacement and pressure. An analysis based on neglecting the outer part of the turbulent boundary layer suggested that the junction position increaes linearly until close to the centre-line before suddenly becoming constant. Comparisons with empirical data were made. Connections with Fanno flow are discussed in **Appendix C**; the effects of the turbulent boundary layer described by a two-tier mixing-length model agree with Fanno flow effects in the duct.

Recommendations for industry have been collated in **Appendix D** with

reference to the main text of the thesis.

§§2.1 and 8.1.4 represent joint work with Professor FT Smith.

9.2 Further work

The points 1–4 below are suggestions for areas of related study. As such, a more detailed outline is given for them than for the remaining points which extend more directly from the work of this thesis.

1. An extension mentioned in [77] to the weakly non-linear cases is to study the **unsteady** effects by replacing the operator ∂_θ by the scaled operator $\partial_t + \partial_\theta$. In this way the reported results of those cases will remain the same in a forward-moving frame. Notably, the unsteady weakly non-linear compressible inviscid case cannot feature shocks. However, the leading-order variation in streamwise velocity in the fully non-linear compressible inviscid case admits the appearance of shocks in the flow. In this latter case the scaled operator ∂_t is added to $U\partial_\theta$ in the equations (A.6a–e), creating a largely numerical problem.

   In a straight duct the flow becomes quasi-one dimensional and numerical results would be compared with classical shock-tube properties (as found in any basic text book on compressible flow). Similarly, in the limit of large time the results should correspond to those of the fully non-linear case. We note that there may be an opportunity for analytical work in the regime when the curvature parameter Λ is small and a small perturbation is imposed upon a classical planar shock.

   The above work would be an important addition since empirical data appears to show the presence at least of compression waves in the mo-

tivating industrial problem [55]. Furthermore, the sudden pressure rise which is a characteristic of shock waves has previously been exploited in machines designed to sort rocks and minerals [4]. The unsteady three-dimensional development and propagation of an initially planar shock in a curved duct are not well understood and indeed we have been unable to find any previous work which attempts to address the problem in three dimensions. Much previous work concentrates on the effects on the propagation of the shock caused by changes in duct cross-sectional area. Such area changes may be smooth or sudden, large or small; for example, the work in [38] and more recently for two dimensional ducts in [44], in which it is shown that some expansion effects are genuinely two-dimensional and cannot be treated in a quasi-one dimensional formulation. Such work is also relevant to industry when ducts of different cross-sections are joined.

It is hoped that a study of the unsteady shock propagation would reveal the effects of curvature on the shock. In particular, a question of some importance to industry and related academic questions (see point 4) is whether an initially planar shock normal to both walls remains normal when passing through a bend, and indeed whether it remains planar at all. Should the shock become curved, for example, then the recent work of [57] and references therein may be of use. See also [19, pp.200ff].

The computation of flows with shocks is the subject of the review paper [58] which contains many useful references and comparisons between so-called "old-fashioned" methods and "more modern" ones. The numerical techniques employed in this thesis would be classified as "old-fashioned" in [58], and yet the paper concludes that such techniques can work as

effectively as the "more modern" ones. Extending the numerical techniques of the current thesis to the computation of unsteady flows with shocks is therefore a reasonable prospect.

Finally here we note that there are several questions related to the above proposed extension. For example, the effects of a finite-time opening of the diaphragm (frequently modelled as instantaneous) is treated analytically in one dimension in [92], and extended more recently to include disspative effects in [1]. Additionally, industrial environments are frequently dust-laden, and the shock-attenuating effects of dust in a duct is studied in [45] and references therein which may provide starting points for a similar analysis in curved ducts. We also note that much work on shocks in ducts appears to be motivated by the compression waves generated by high-speed trains entering tunnels, such as in [40] and references therein.

2. In unsteady compressible flows with **shocks** through straight ducts the growth of the turbulent boundary layer influences the shock propagation. This extension to point 1 above clearly ties in also with the turbulent boundary layer work of the current thesis, and in particular with the Fanno flow effects of Appendix C in which we mention that these effects tend to drive the Mach number towards unity. The influence of the turbulent boundary layer on shock propagation appears to have first come to the attention in the field of aerospace engineering, for example in [88] and references therein. The influence continues to be of interest and more recent relevant examples are [62] and cited references.

3. In addition to the unsteady effects described in point 1 above, a study

of the **pulsatile** nature of the motivating industrial problem would help to increase the physical relevance of the model. Such work may build on the large body of literature concerning the (viscous) pulsatile flow of blood through blood vessels, and also on [74] and references therein.

4. An issue of some significance to the motivating industrial application is the detail of the **expulsion of a shock** from the exit of the duct into the atmosphere. This addition builds naturally on the work in point 1 above. As the shock is expelled from the duct it sets in motion the external quiescent fluid and therefore the shape and velocity of the expelled shock can be expected to influence the initial conditions of the resultant external jet (whose details are being studied by Mr P.E. Westwood at UCL).

   A brief summary of previous work in the general area of shocks expelled from ducts into the atmosphere now follows. In [93], small shocks are imposed upon the main shock and the development of these "shock-shocks" is studied in a kind of perturbation theory for shock waves. We note in passing that it is this theory, developed also in [93] for flows on curved walls, which is expanded in the reference [1] cited above on page 283. Of particular relevance to this discussion is the diffraction of shocks around convex corners in two dimensions studied in [93]. A strong planar shock diffracting around a corner of small angle becomes downstream a planar shock moving in the same direction as the incident shock and attached via a shock section curved by a Prandtl-Meyer expansion fan to a wall-normal planar shock which propagates along the wall. Since there is a maximum angle (the Mach angle) through which a shock can turn, the curved shock section may be replaced by a curved compression wave as

the angle of the corner increases, as shown in [93, p.162]. This theory is generalised to shocks diffracting across convex edges in three dimensions in [94] and tested experimentally in [69]. It would be useful to examine the above topic in more detail and to study the theory for curved ducts, incorporating predictions from point 1 above.

A review of the above literature and references therein suggests that the shape of the duct exit is important in determining the downstream external behaviour of the flow. Currently, the motivating industrial set up features a 90° flanged exit, but a detailed study of the exit-shape effects may suggest changes to this design.

Of great importance to the modelling of the external dynamics is the behaviour of the flow as it suddenly exhausts into the atmosphere. In the incompressible cases, a potential flow spherical expansion is one possibility, while the formation of a jet of rapidly moving fluid surrounded by quiescent fluid is a second possibility. There is a fundamental difference between these two alternatives and careful examination of existing empirical studies would be required in order to create a physically realistic model. In the compressible case, it may be that as the high pressure region of fluid behind the shock emerges into the relatively low pressure atmosphere the flow expands producing an expansion fan and generates new wall shocks via a process similar to the original diaphragm-opening effect. If so, the details of [93, 94, 69] above should emerge. The work in [49, pp.8-34–8-37] may also be of assistance here.

Two expected outcomes of the above work would be a quantification of the axial decay in shock strength and an investigation of the possible interaction of wall shocks from adjacent ducts. Such predictions could

be compared with the empirical work of [70].

Finally, we note that the diffraction of shocks across sharp corners in two dimensions produces vorticity at the corners as described for example in [80]. An extension of such previous work to study the vorticity generated by a curvature-perturbed shock in three dimensions may also be of interest to industry.

5. Throughout this thesis the walls of the duct have been taken as perfectly insulating. In reality, sorting machines work in a variety of environments and temperatures ranging from sub-zero to in excess of 40°C. Although the present work is inviscid and non-heat conducting, a study of the effects of adiabatic **bulk heat addition** may be of interest to industry, as well as posing interesting academic questions. Another, related, feature of interest to the turbulent boundary layer study is the effect of wall roughness.

6. The numerical schemes described in §5.3 for solving the fully non-linear equations were sufficiently robust that we could make favourable comparisons with analytical work in an order unity region of the flow. However, it would be desirable to have numerical solutions extending to the end of the bend — and preferably beyond — in order to make the study more complete. It is possible that the use of other numerical techniques such as those mentioned on page 167 could **extend the validity of the numerical solutions**.

7. In the turbulent boundary layer work of Part II of the current thesis, the boundary layer was assumed to have undergone **transition to turbulence** at some unspecified point x_{tr} upstream of the region of study.

Knowledge of the location of x_{tr} and the cause of transition (is it, for example, a result of an upstream influence of the onset of the bend?) would be useful in making the treatment more general. The reference [23] and references therein may be of use here.

8. In Chapter 7 we reported the behaviour of the outer part of the turbulent boundary layer. A study of the **behaviour of the sublayer** when subjected to the streamwise curvature would be an important extension. For example, a more detailed analysis of the manner in which the external influences are felt by the inner layer would be a part of such an extension.

9. A study of the influence of **sharp corners** in the duct cross-section on the growth and development of the turbulent boundary layers in curved ducts could be of use to industry. Previous work referred to in Appendix B suggests that sharp corners are not desirable from the industrial viewpoint of maximising throughflow and minimising secondary flow (although we note in passing that the converse is desirable when designing heat exchangers, for example). A quantification of the secondary flow in turbulent boundary layers in the vicinity of sharp corners when streamwise curvature is also present would be both useful and interesting.

10. A complete study of the downstream **core-turbulent boundary layer interaction** region if the turbulent fluctuations and the core swirl are comparable, as discussed on page 209, would be useful. However, this case presents some apparently challenging modelling issues. The buoyancy analogy modification to the algebraic eddy-viscosity model may well provide sufficiently accurate solutions. It is to be hoped that the reported suppression of turbulence on the convex wall of a rectangular

duct and its enhancement on the concave wall (as discussed, for example, in [8, p.375]) would emerge from this analysis.

11. In the work of Part II only the leading order variations in the turbulent boundary layer velocities were studied. An investigation of the behaviour of the **higher order** components would at the very least be expected to make the pressure and centre-line velocity predictions of Chapter 8 correspond more closely with empirical data.

12. A study of the proposed **pseudo-wake** structure far downstream of the bending region in §8.1.4 of the two-dimensional merged case would be of interest.

13. It is important to devise a numerical scheme to solve the **three-dimensional axisymmetric merged** (or merging) case of §8.2 and then to extend the theory and numerics to general cross-sections. This would provide numerical solutions which could be tested against empirical data, and help to validate the predictions of the small-a_1 analysis.

14. A further important extension to Chapter 8 would be to include the effects of **curvature** more. An analytical approach for weak curvature would be to study a small perturbation to the derived quasi-straight solutions.

The above points contain our main recommendations for further research in the area.

Part IV

Appendices

Appendix A

Equations from Part I

A.1 Incompressible Inviscid case

$$V_y + W_z = 0 \ , \tag{A.1a}$$

$$U_\theta + VU_y + WU_z = -p_0'(\theta) \ , \tag{A.1b}$$

$$V_\theta + VV_y + WV_z = -p_{1y} \ , \tag{A.1c}$$

$$W_\theta + VW_y + WW_z - 2\Lambda U = -p_{1z} \ . \tag{A.1d}$$

A.2 Compressible Inviscid case

$$V_y + W_z = 0 \ , \tag{A.2a}$$

$$U_\theta + VU_y + WU_z = -p_1'(\theta) \ , \tag{A.2b}$$

$$V_\theta + VV_y + WV_z = -p_{2y} \ , \tag{A.2c}$$

$$W_\theta + VW_y + WW_z = -p_{2z} + \Lambda(2U + \hat{\rho}) \ , \tag{A.2d}$$

$$\frac{\gamma p_0}{\alpha}\left(\hat{\rho}_\theta + V\hat{\rho}_y + W\hat{\rho}_z\right) = p_1'(\theta) + \Lambda W\theta_1^2 \ . \tag{A.2e}$$

A.3 Incompressible Viscous case

$$\bar{U}_\theta + V_y + W_z = 0 \,, \tag{A.3a}$$

$$\bar{U}\bar{U}_\theta + V\bar{U}_y + W\bar{U}_z = -p_0'(\theta) + \frac{1}{Re_{re}}\nabla_{2D}^2\bar{U} \,, \tag{A.3b}$$

$$\bar{U}V_\theta + VV_y + WV_z = -p_{2y} + \frac{1}{Re_{re}}\nabla_{2D}^2 V \,, \tag{A.3c}$$

$$\bar{U}W_\theta + VW_y + WW_z - \bar{U}^2\alpha\theta_1^2 = -p_{2z} + \frac{1}{Re_{re}}\nabla_{2D}^2 W \,. \tag{A.3d}$$

A.4 Compressible Viscous case

$$(\bar{\rho}\bar{U})_\theta + (\bar{\rho}V)_y + (\bar{\rho}W)_z = 0 \,, \tag{A.4a}$$

$$\bar{\rho}(\bar{U}\bar{U}_\theta + V\bar{U}_y + W\bar{U}_z) = -p_0'(\theta) + \frac{1}{Re_{re}}\left[(\bar{\mu}\bar{U}_y)_y + (\bar{\mu}\bar{U}_z)_z\right] \,, \tag{A.4b}$$

$$\begin{aligned}\bar{\rho}(\bar{U}V_\theta + VV_y + WV_z) = -p_{2y} + \frac{1}{Re_{re}}\Big[&(\bar{\mu}\bar{U}_y)_\theta + (\bar{\mu}V_z + \bar{\mu}W_y)_z \\ &+\frac{2}{3}(2\bar{\mu}V_y - \bar{\mu}W_z - \bar{\mu}\bar{U}_\theta)_y\Big] \,,\end{aligned} \tag{A.4c}$$

$$\begin{aligned}\bar{\rho}(\bar{U}W_\theta + VW_y + WW_z - \bar{U}^2\alpha\theta_1^2) = -p_{2z} + \frac{1}{Re_{re}}\Big[&(\bar{\mu}\bar{U}_z)_\theta \\ &+(\bar{\mu}V_z + \bar{\mu}W_y)_y \\ &+\frac{2}{3}(2\bar{\mu}W_z - \bar{\mu}V_y - \bar{\mu}\bar{U}_\theta)_z\Big] \,,\end{aligned} \tag{A.4d}$$

$$\begin{aligned}\bar{\rho}\left(\bar{U}\bar{T}_\theta + V\bar{T}_y + W\bar{T}_z\right) = (\gamma-1)M_D^2\Big[&\bar{U}p_0'(\theta) \\ &+\frac{1}{Se_{re}}\left((\bar{\mu}\bar{T}_y)_y + (\bar{\mu}\bar{T}_z)_z\right) + \frac{\bar{\mu}}{Re_{re}}\left(\bar{U}_y^2 + \bar{U}_z^2\right)\Big] \,,\end{aligned} \tag{A.4e}$$

$$\bar{\mu} = c_H\bar{T} \,, \tag{A.4f}$$

$$\bar{\rho}\bar{T} = \gamma M_\infty^2 p_0 \,. \tag{A.4g}$$

A.5 Fully Non-Linear Incompressible Inviscid case

$$U_\theta + V_y + W_z = 0 \ , \tag{A.5a}$$

$$UU_\theta + VU_y + WU_z = -p_0'(\theta) \ , \tag{A.5b}$$

$$UV_\theta + VV_y + WV_z = -p_{2y} \ , \tag{A.5c}$$

$$UW_\theta + VW_y + WW_z - \Lambda U^2 \alpha \theta_1^2 = -p_{2z} \ . \tag{A.5d}$$

A.6 Fully Non-Linear Compressible Inviscid case

$$(\rho U)_\theta + \rho(V_y + W_z) = 0 \ , \tag{A.6a}$$

$$\rho(UU_\theta + VU_y + WU_z) = -p_0'(\theta) \ , \tag{A.6b}$$

$$\rho(UV_\theta + VV_y + WV_z) = -p_{2y} \ , \tag{A.6c}$$

$$\rho(UW_\theta + VW_y + WW_z - \Lambda U^2 \alpha \theta_1^2) = -p_{2z} \ , \tag{A.6d}$$

$$p_0 = \rho^\gamma \ . \tag{A.6e}$$

Appendix B

The turbulent boundary layer equations in detail

As noted in [54], the choice of curvilinear coordinates can be arbitrary, but the various measures of coordinate curvatures associated with them are not, and in fact reveal an "...intimate connection with the surface geometery ..." through the *geodesic curvatures* to be introduced below. Though the particular choice of curvilinear coordinates may greatly simplify the equations involved, the boundary conditions may in turn become overly complicated.

Orthogonality implies the length segment ds has

$$(ds)^2 = h_1^2(dx_1)^2 + h_2^2(dx_2)^2 + h_3^2(dx_3)^2 \ . \tag{B.1}$$

In general, the *length functions* h_i depend on x_i, but we will make the assumptions that the surface defined by the interior wall of the duct is regular and not excessively curved. These assumptions stipulate that the results hold only away from any corners. For some work on the secondary flows in turbulent ducts induced by corners see for example [33]. More generally, by assuming that the surface is not excessively curved we mean to say that the curvature of

the cross-sectional profile is small in comparison to the boundary layer thickness (which we shall see to be of $\mathcal{O}((Ln(Re))^{-1})$. In essence, this ensures that the walls act as if flat on a TBL length scale. In situations not to be considered in depth here, when this condition does not hold, then it is possible to modify the algebraic model . Accordingly, one approach is to model both transverse and streamline curvature with buoyancy terms, considered for example in [67, pp.602ff] and references accompanying the discussion on page 209. In such cases the turbulent oscillations in the transverse directions are damped due to centrifugal forces restricting inward motion, and a centripetal lift resisting outward motion ([67, pp.488–9]). Such curvature effects are reportedly stronger in laminar flows ([67, p.589]). As discussed in [54, p.288] and elsewhere, the assumption of small cross-sectional curvature leads to:

$$h_1 = h_1(x_1, x_2) \quad ; \quad h_2 = h_2(x_1, x_2) \quad ; \quad \bar{h}_3 \equiv 1 \ , \tag{B.2}$$

where $\bar{h}_3$ is the x_3 metric on the boundary layer length scale such that $\bar{h}_3 \equiv 1$ implies that we measure the actual distance normal to the wall.

Using standard general transformation formulae we can write the full continuity equation as:

$$\frac{1}{h_1 h_2 h_3}\left[\frac{\partial}{\partial x_1}(h_2 h_3 u_1) + \frac{\partial}{\partial x_2}(h_1 h_3 u_2) + \frac{\partial}{\partial x_3}(h_1 h_2 u_3)\right] = 0 \ . \tag{B.3}$$

Using either Christoffel symbols or vector geometry (see *e.g.* [54, p.60])), the components of the inertia term in the momentum equations,

$$(\boldsymbol{u} \cdot \boldsymbol{\nabla})\boldsymbol{u} = (\text{grad } \boldsymbol{u})\boldsymbol{u} \ , \tag{B.4}$$

in the curvilinear system can be derived. After applying the simplifications

(B.2) they are:

$$\text{grad } \boldsymbol{u} = \begin{pmatrix} \frac{1}{h_1}\frac{\partial u_1}{\partial x_1} - K_2 u_2 & \frac{1}{h_2}\frac{\partial u_1}{\partial x_2} + K_1 h_2 & \frac{\partial u_1}{\partial x_3} \\ \frac{1}{h_1}\frac{\partial u_2}{\partial x_1} + K_2 u_1 & \frac{1}{h_2}\frac{\partial u_2}{\partial x_2} - K_1 u_1 & \frac{\partial u_2}{\partial x_3} \\ \frac{1}{h_1}\frac{\partial u_3}{\partial x_1} & \frac{1}{h_2}\frac{\partial u_3}{\partial x_2} & \frac{\partial u_3}{\partial x_3} \end{pmatrix} , \tag{B.5a}$$

where we have introduced the curvature parameters

$$\begin{aligned} K_1 &= -\frac{1}{h_1 h_2}\frac{\partial h_2}{\partial x_1} \quad \text{(for } x_2 \text{ constant)}, \\ K_2 &= -\frac{1}{h_1 h_2}\frac{\partial h_1}{\partial x_2} \quad \text{(for } x_1 \text{ constant)}. \end{aligned} \tag{B.5b}$$

As in [5, pp284ff] K_1 and K_2 define (the negative values[1] of) the *geodesic curvatures* of x_2 and x_1, respectively. We also note the definition of the *Gaussian* (or *total*) curvature K, defined by:

$$K = \frac{1}{h_1 h_2}\left[\frac{\partial}{\partial x_1}(h_2 K_1) + \frac{\partial}{\partial x_2}(h_1 K_2)\right] , \tag{B.6}$$

which is the same everywhere on the surface. A *developable* surface is one for which $K = 0$, in which case $h_i \equiv 1$ for all i. The Gaussian curvature is related to the choice of coordinates and a good general discussion of the choice of coordinates is given in [54, pp292–3].

The viscous term in the momentum equations is $\mu \cdot \text{div}(\text{def } \boldsymbol{u})$, which (following [54]) we write as:

$$\begin{aligned} (\text{div } (\tau_{ij}))_i = &\frac{h_i}{\sqrt{g}} \sum_j \frac{\partial}{\partial x_j}\left(\frac{\tau_{ij}\sqrt{g}}{h_i h_j}\right) + \sum_j \frac{\partial h_i}{h_j \partial x_j}\frac{\tau_{ij} + \tau_{ji}}{h_i} \\ &- \sum_j \frac{\partial h_j}{h_i \partial x_i}\frac{\tau_{jj}}{h_j} , \end{aligned} \tag{B.7}$$

where $\sqrt{g} = h_1 h_2 h_3$.

[1] We say the negative values because they can be defined without the minus sign. However, the inclusion of the minus sign above is more in keeping with some modern-day uses, for example in [26].

Thus with the above assumptions and definitions in mind, we have the following:

$$\begin{aligned} x_1\text{-mtm:}\quad & \frac{u_1}{h_1}\frac{\partial u_1}{\partial x_1} + \frac{u_2}{h_2}\frac{\partial u_1}{\partial x_2} + u_3\frac{\partial u_1}{\partial x_3} - K_2 u_1 u_2 + K_1 u_2^2 = -\frac{1}{h_1}\frac{\partial p}{\partial x_1} \\ & + \frac{1}{h_1}\frac{\partial \tau_{11}}{\partial x_1} + \frac{1}{h_2}\frac{\partial \tau_{12}}{\partial x_2} + \frac{\partial \tau_{13}}{\partial x_3} \\ & - K_1(\tau_{11} - \tau_{22}) - K_2(\tau_{12} - \tau_{21}) \ ; \end{aligned} \tag{B.8a}$$

$$\begin{aligned} x_2\text{-mtm:}\quad & \frac{u_1}{h_1}\frac{\partial u_2}{\partial x_1} + \frac{u_2}{h_2}\frac{\partial u_2}{\partial x_2} + u_3\frac{\partial u_2}{\partial x_3} - K_1 u_1 u_2 + K_2 u_2^2 = -\frac{1}{h_2}\frac{\partial p}{\partial x_2} \\ & + \frac{1}{h_1}\frac{\partial \tau_{21}}{\partial x_1} + \frac{1}{h_2}\frac{\partial \tau_{22}}{\partial x_2} + \frac{\partial \tau_{23}}{\partial x_3} \\ & - K_1(\tau_{12} - \tau_{21}) - K_2(\tau_{22} - \tau_{11}) \ ; \end{aligned} \tag{B.8b}$$

$$\begin{aligned} x_3\text{-mtm:}\quad & \frac{u_1}{h_1}\frac{\partial u_3}{\partial x_1} + \frac{u_2}{h_2}\frac{\partial u_3}{\partial x_2} + u_3\frac{\partial u_3}{\partial x_3} = -\frac{\partial p}{\partial x_3} \\ & + \frac{1}{h_1}\frac{\partial \tau_{31}}{\partial x_1} + \frac{1}{h_2}\frac{\partial \tau_{32}}{\partial x_2} + \frac{\partial \tau_{33}}{\partial x_3} \\ & - K_1\tau_{31} - K_2\tau_{32} \ . \end{aligned} \tag{B.8c}$$

We note that

$$\tau_{ij} = \frac{\tau_{Lij}}{Re} + \tau_{Tij} \ , \tag{B.9}$$

and as a consequence of incompressibility this reduces (see *e.g.* [54, p.25]) to:

$$\tau_{ij} = \frac{1}{Re}(\text{grad } \boldsymbol{u})_{ij} + \tau_{Tij} \ . \tag{B.10}$$

enabling us to write the viscous terms directly from (B.5a,b).

Where δ represents the TBL thickness we have the following orders of magnitude in the TBL:

$$u_1, u_2, x_1, x_2, h_1, h_2 \sim 1 \quad ; \quad x_3 \sim \delta \quad ; \quad K_1, K_2 \sim 1 \quad ; \tag{B.11}$$

with continuity ensuring $u_3 \sim \delta$.

The continuity equation is therefore unchanged in the TBL. The left hand side of the x_1-momentum equation is of $\mathcal{O}(1)$ and since all stresses vanish at the

edges of the TBL, the pressure gradient felt there must be of $\mathcal{O}(1)$ also, so we shall retain the pressure gradient (in the x_1- and x_2-momentum directions) in the momentum equations. This is analagous to the approach explained in [15, p.67]. See also equation (B.14) below.

The Newton laminar stresses in the x_1-momentum equation are all of $\mathcal{O}(Re^{-1})$, with the exception of

$$\frac{\partial}{\partial x_3}\left(\frac{1}{Re}(\text{grad } \boldsymbol{u})_{13}\right) = \frac{1}{Re}\frac{\partial}{\partial x_3}\left(\frac{\partial u_1}{\partial x_3}\right) \sim Re^{-1}\delta^{-2} \ . \tag{B.12}$$

We choose $Re^{-1}\delta^{-2} \sim 1$ in order to retain this contribution, but since we take $Re \to \infty$ the other laminar stress terms do not appear at this level. A similar argument exists based on dimensional quantities, *c.f.* [15, pp.66ff].

Arguments to determine the contributions retained from the Reynolds stresses are considered in detail in [15, pp.69ff], and will not be repeated here. The analysis in [15] enables us to write the x_1- and x_2-momentum equations:

$$\frac{u_1}{h_1}\frac{\partial u_1}{\partial x_1} + \frac{u_2}{h_2}\frac{\partial u_1}{\partial x_2} + u_3\frac{\partial u_1}{\partial x_3} - K_2 u_1 u_2 + K_1 u_2^2 = -\frac{1}{h_1}\frac{\partial p}{\partial x_1} + \frac{1}{Re}\frac{\partial}{\partial x_3}\left(\frac{\partial u_1}{\partial x_3}\right) + \frac{\partial \tau_{T13}}{\partial x_3} \ ; \tag{B.13a}$$

$$\frac{u_1}{h_1}\frac{\partial u_2}{\partial x_1} + \frac{u_2}{h_2}\frac{\partial u_2}{\partial x_2} + u_3\frac{\partial u_2}{\partial x_3} - K_1 u_1 u_2 + K_2 u_2^2 = -\frac{1}{h_2}\frac{\partial p}{\partial x_2} + \frac{1}{Re}\frac{\partial}{\partial x_3}\left(\frac{\partial u_2}{\partial x_3}\right) + \frac{\partial \tau_{T23}}{\partial x_3} \ . \tag{B.13b}$$

The leading-order balance of the x_3-momentum equation yields

$$-\frac{\partial p}{\partial x_3} = 0 \ , \textit{i.e:} \quad p = p(x_1, x_2) \ , \tag{B.14}$$

and so we can determine p in terms of its edge values.

The boundary conditions are as follows:

$$\boldsymbol{u} = (u_1, u_2, u_3) \equiv \mathbf{0} \quad \text{at} \quad x_3 = 0 \quad \text{(no slip)} \; ; \tag{B.15a}$$

$$\text{non-wall shear stresses} = 0 \quad \text{at} \quad x_3 = 0 \quad \text{and at} \quad x_3 \geqslant x_{3e} \; ; \tag{B.15b}$$

$$\boldsymbol{u} = \boldsymbol{u}_w \quad \text{at} \quad x_3 = x_{3e} \; , \tag{B.15c}$$

where $\boldsymbol{u}_w$ is the core flow at the wall of the duct.

The next important step is to model the turbulent stress terms. Although such models arise from hypothetical considerations, the important constants involved are usually determined from experiments only, and the one we will choose is that proposed by Cebeci and Smith [15]. The decisions affecting this choice have been covered in §6.1, where also we remind the reader that a specific model is chosen to give us numerical answers, but that many of the results which follow hold in general for two-tier mixing-length algebraic eddy viscosity models.

Following [15] we set in the dimensional equations:

$$-\overline{\rho u_i' u_3'} = \rho B_i \frac{\partial u_i}{\partial x_3} \; . \tag{B.16}$$

We will furthermore make the assumption of isotropic eddy viscosity, setting $B_1 \equiv B_2 \equiv B$. Anisotropy can apparently be significant, though only when the ratio of the boundary layer thickness to the radius of curvature of the streamlines becomes large, as discussed in [64, pp.537–8] and [67, p.640].

In the original two-dimensional formulations, it was known that a TBL has a two-tiered structure. In the outer layer there is a balance between inertial and turbulent forces, whilst in the wall or inner layer, viscous and turbulent forces balance. As discussed, the detailed asymptotic structure of the layers has also been shown to hold in three-dimensional layers in [26] (earlier work by [15] shows consistency) and so we will safely make the assumption here.

Note that the outer layer is somewhat more important here as it determines the thickness of the boundary layer. In other applications, the inner layer can be the most important layer, for example in heat transfer — see *e.g.* [28]. The dimensional form of the eddy-viscosity is as follows:

$$B_D = \begin{cases} L_D^2 \left[\left(\frac{\partial u_{1D}}{\partial x_{3D}} \right)^2 + \left(\frac{\partial u_{2D}}{\partial x_{3D}} \right)^2 \right]^{\frac{1}{2}} & , \; x_{3D} < x_{3DJ} \; , \\ a u_{tD} \delta_{1D} & , \; x_{3De} > x_{3D} > x_{3DJ} \; , \end{cases} \tag{B.17}$$

where $a = 0.0168$ is an experimental constant, x_{3DJ} is the unknown junction between the inner and outer layers, and the so-called *displacement thickness* is

$$\delta_{1D} = \int_0^\infty 1 - \frac{(u_{1D}^2 + u_{2D}^2)^{\frac{1}{2}}}{u_{tD}} \, dx_{3D} \; , \tag{B.18a}$$

$$\text{where} \quad u_{tD} = (u_{1De}^2 + u_{2De}^2)^{\frac{1}{2}} \text{ is the total velocity .} \tag{B.18b}$$

In this instance, the external potential flow will impose small variations on $\boldsymbol{u}_\infty = U_{D\infty}(1,0,0)$ and so to leading order in that case, $u_t = 1$. In external flows, such as the flow past a swept infinite cylinder, the external potential flow is varied significantly away from the free-stream and so one needs to leave in terms of u_{1e} and u_{2e} (see *e.g.* [15, p.781]). It is the discrepancy at the edge which matters, and the edge values are very close to the ∞ values in the former case. Note also that we will non-dimensionalise the TBL velocities on $U_{D\infty}$ — the incident dimensional core flow velocity used to non-dimensionalise the core flow velocities — whereas in swept-cylinder flows in [15] u_e is used, and in an external small cross-flow case with stream-line coordinates in [15], u_s is used. The choice of $U_{D\infty}$ here is not the only consistent one. In [60] the equivalent of the dimensional total edge velocity u_{tD} is used, and this would lead to a simpler form of the outer part of the eddy viscosity, though importantly to the leading order which we exclusively consider herein, there would be no change

to either the equations or the results. Choosing to non-dimensionalise the TBL velocities on u_{tD} would not lead to much confusion if extended to the non-dimensionalising factor for the core flow, since upstream of the analytical region we are assuming slip, and thus $U_{D\infty} \sim u_{tD}$. The Reynolds number would also be of the same order of magnitude.

In a laminar boundary layer the adjustment to the external flow velocity occurs smoothly, and so a definition of an "edge" and a "thickness" δ is somewhat arbitrary, as discussed in [67, p.30], though a common definition is the distance from the wall by which the velocity has attained 99% of the external value. The situation with TBLs is different since the potential (irrotational) external flow is non- (or weakly-) fluctuating, whilst the flow in the TBL is rotational and fluctuating. This defines an "edge" to the TBL, but it is an edge with strong spatial and temporal fluctuations, or *intermittencies.* The *intermittency factor* given on [67, p.513] can be used to define another thickness δ_e giving the time-averaged position of the well-defined edge. In fact, $\delta_e = 0.78\delta$.

We will not consider intermittency in our models as it has a complicating effect without generating any new information here. Consequently, the displacement thickness we have defined above has the most physical significance, since it can be thought of as the distance by which the external potential flow field is displaced due to the viscosity near the wall. This does not remove all ambiguity, since displacement thicknesses can also be defined in different directions. The displacement thickness in three dimensions is even more ambiguous, as described in [26, p.53]. Further note that if we take the above definition of δ as the distance by which $u = 0.99u_\infty$ then $\delta \approx 3\delta_1$ [67, p.32] for a flat plate. The name of $u_t - (u_1^2 + u_2^2)^{\frac{1}{2}}$ is the *resultant velocity defecit.*

In the above expression, $a = 0.0168$ and is generally assumed to be an

experimentally-determined universal constant, but it has been shown (*e.g.* [14]) that for low Re (typically for $Re < 6000$) it varies as a function of *Coles' parameter*. This does not concern us here but see for example [15, §6.2.4] where the universality of this and other constants is discussed. Furthermore,

$$L_D = \kappa x_3 \left[1 - exp\left(\frac{-x_3}{A}\right)\right] , \tag{B.19a}$$

where $\kappa = 0.4$ is von Kármán's (dimensionless) constant, (B.19b)

and $A_D = A^+ \frac{\nu}{N} u_\tau^{-1}$ is *Van Driest's damping parameter*, (B.19c)

where $A^+ = 26$ is a dimensionless constant. (B.19d)

and $u_\tau = \left(\frac{\tau_w}{\rho}\right)^{\frac{1}{2}}$ is the *wall friction velocity*, (B.19e)

with $\frac{\tau_w}{\rho} = \nu \left[\left(\frac{\partial u_1}{\partial x_3}\right)_w^2 + \left(\frac{\partial u_2}{\partial x_3}\right)_w^2\right]^{\frac{1}{2}}$, (B.19f)

and $N = \left[\frac{p^+}{u_{3w}}\left[1 - exp(11.8u_{3w}^+)\right] + exp(11.8u_{3w}^+)\right]^{\frac{1}{2}}$, (B.19g)

where $u_{3w}^+ = \frac{u_{3w}}{u_\tau}$, $p^+ = \left(\frac{\nu u_t}{u_\tau^2}\right)\frac{du_t}{ds}$. (B.19h)

The symbol p^+ is the dimensionless pressure gradient parameter, and $u_{3w} = 0$ since there is no mass transfer through the walls, so $u_{3w}^+ = 0$ and $\frac{du_\infty}{ds} = 0$ so $p^+ = 0$ and $N = 1$.(Note that for compressible flows there exist expressions for A, see *e.g.* [15, p.217].) Thus

$$L_D = 0.4x_3 \left[1 - exp\left(-\frac{x_3}{A}\right)\right] , \tag{B.20a}$$

with $A_D = 26\nu^{\frac{1}{2}} \left[\left(\frac{\partial u_1}{\partial x_3}\right)_w^2 + \left(\frac{\partial u_2}{\partial x_3}\right)_w^2\right]^{-\frac{1}{4}}$. (B.20b)

We non-dimensionalise u_i on $U_{D\infty}$ as before; x_i on l_D. The non-varying parameters ν_D, μ_D, ρ_D are factored out. Thus the eddy viscosity in the inner

region takes the form:

$$B_D = U_{D\infty} l_D 0.16 x_3^2 \left[1 - exp\left(-\frac{Re^{\frac{1}{2}}}{26} x_3 \left[\left(\frac{\partial u_1}{\partial x_3} \right)_w^2 + \left(\frac{\partial u_2}{\partial x_3} \right)_w^2 \right]^{\frac{1}{4}} \right) \right]^2 \times \left[\left(\frac{\partial u_1}{\partial x_3} \right)^2 + \left(\frac{\partial u_2}{\partial x_3} \right)^2 \right]^{\frac{1}{2}} . \quad \text{(B.21)}$$

For the outer region,

$$B_D = U_{D\infty} l_D a u_t \delta_1 , \quad \text{(B.22a)}$$

$$\text{where} \quad \delta_1 = \int_0^\infty 1 - \frac{(u_1^2 + u_2^2)^{\frac{1}{2}}}{u_t} \, dx_3 . \quad \text{(B.22b)}$$

We clearly have therefore, $B_D = u_{D\infty} l_D B$ in both regions. A similar non-dimensionalising of the Reynolds stresses yields

$$\frac{\partial \pi_{i3D}}{\partial x_{3D}} = \frac{\rho_D U_{D\infty}^2}{l_D} \frac{\partial}{\partial x_3} \left(B \frac{\partial u_i}{\partial x_3} \right) . \quad \text{(B.23)}$$

We are now in a position to write down the TBL equations in full, retaining the curvature terms dictated by our chosen geometry, and employing the Cebeci-Smith model.

Appendix C

Fanno flow effects

Flow near the start of the long quasi-straight duct

This appendix is based on the note [75]. We consider the equation (8.111b) with the expression (8.111c) in the limit $X \to 0+$. In this region, the TBL is not fully merged and it matches with the $x \to \infty$ limit of the entry region analysis for small β in Chapter 7. Thus the TBL flow described by (8.111b) does not hold in a core region of the three-dimensional axisymmetric duct, and the outer part of the model in (8.111c) does not extend to the centre-line at $y = 1$. Consequently, (8.114) no longer holds.

We note that for the variable $\hat{U}(X, y)$, its mean value $\bar{U}(X)$ is defined as

$$\bar{U}(X) = \frac{\int_0^{2\pi}\int_0^1 \hat{U}(1-y)\, dyd\phi}{\int_0^{2\pi}\int_0^1 1\cdot(1-y)\, dyd\phi} = \frac{\int_0^{2\pi}\int_0^1 \hat{U}(1-y)\, dyd\phi}{\pi} . \tag{C.1}$$

Thus an integration of (8.111b) yields

$$\pi(\bar{U} + p_1)_X = 2\pi \left[(1-y)\hat{B}\hat{U}_y\right]_0^1 . \tag{C.2}$$

By the above discussion, $\hat{B} = 0$ at $y = 1$ and so:

$$(\bar{U} + p_1)_X = 2a_2 \left[-(1-y)^2 Ln^2(1-y)\hat{U}_y^2\right]\Big|_{y\to 0+} , \tag{C.3}$$

from (8.111c). The behaviour of $\hat{U}$ as $y \to 0+$ is given by (8.112), which gives us

$$\bar{U}_X + p_{1X} = -2a_2 \ . \tag{C.4}$$

On the other hand, we note from [49, p.8-24] that quasi-one dimensional Fanno flow in a circular duct has

$$\rho_D u_D u_{Dx_D} + p_{Dx_D} = -\frac{2f_D u_D^2}{D_D} \ , \tag{C.5}$$

where the subscript $_D$ represents dimensional quantities, f_D is the wall friction factor, and D_D is the dimensional diameter of the circular duct. (The general expression for D_D in other cross-sections is given on [49, p.8-24]). In the incompressible case that we study here, we take $f_D = \rho_D \cdot f$ and thus Fanno flow is governed by

$$uu_x + p_x = -\frac{2fu^2}{D} \ . \tag{C.6}$$

Furthermore, we recall from Chapter 8 that the following hold:

$$x = \hat{\epsilon}^{-1} X \ ; \tag{C.7a}$$

$$u = 1 + \hat{\epsilon}\hat{U}(X, y) + \dots \ ; \tag{C.7b}$$

$$p = 1 + \hat{\epsilon} p_1(X) + \dots \ , \tag{C.7c}$$

where $\hat{\epsilon} = (Ln(Re))^{-1}$. Thus (C.6) becomes

$$\hat{U}_X + p_{1X} = -\frac{2f}{\hat{\epsilon}^2 \pi} \ , \tag{C.8}$$

to leading order.

A typical mean friction factor is $f = 0.005$ as quoted on [49, p.8-27]. For (C.4) and (C.8) to agree here thus requires

$$f = 0.16\pi \, (Ln(Re))^{-2} \ , \tag{C.9}$$

corresponding to a Reynolds number of approximately $Re \approx 2.26 \times 10^4$, which is certainly within the range of Re considered in this analysis.

Discussion

We note that the above analysis holds in general for any two-tier mixing-length model. The analysis described above is interesting in its own right since it shows that the wall frictional effects in a duct can be modelled by the mean influences of the growth of the TBL described by a two-tier mixing-length model.

In a nod towards future work here we mention that the compressible theory of Fanno flow yields connections between the Mach number M and the wall frictional effects. It can be shown (see *e.g.* [49]) that Fanno flow effects drive the Mach number towards unity, which could have interesting ramifications for the design of industrial ducts conveying high-Reynolds number flows.

Appendix D

Engineering guidelines

This appendix has been organised under headings of the principal factors which influence the flow development in the three-dimensional curved duct.

Influence of input streamwise velocity

- *Shear*:— Vertical variations in the input streamwise velocity drives the swirl (2.34b, 4.25, 5.23c and the discussion which begins on page 88) and should therefore be minimised by smoothing the walls upstream, weakening upstream bends, and minimising variations associated with the opening of the valve. For example, equations (2.41, 4.41) show that halving the input shear halves the growth rate of the integrated swirl. Swirl is to be avoided since it misdirects the output jet.

- *Streamwise velocity is conserved*:— In all cases the streamwise velocity is conserved in magnitude and is simply mixed around by the swirl (pages 54, 88, 163 and §5.2.3), suggesting that the useful (*i.e.* streamwise) energy of the flow behind the shock is largely conserved. (We recall that this thesis studies the flow following the shock in the motivating

industrial system and therefore cannot account for the large pressure and streamwise velocity drops.)

- *Turbulent effects*:— The size of the input streamwise velocity determines the Reynolds number Re (defined again below). In turn, this influences the size of the parameter β defined on page 194 as follows:

$$\beta = \epsilon Ln(Re) = \epsilon Ln\left(\frac{U_{D\infty} h_D}{\nu_D}\right) , \tag{D.1}$$

where ν_D is the *kinematic viscosity.* The factors in (D.1) can each be adjusted since: ϵ is the level of input swirl; $U_{D\infty}$ is the size of the input streamwise velocity; h_D is the typical duct width; and ν_D is the kinematic viscosity which depends for example on the fluid used. As explained on page 210, the turbulent effects can be minimised over a full-bend length scale by making β large; current empirical data for the motivating industrial system suggest that β is of order unity. β can be made larger by increasing $\epsilon, U_{D\infty}, h_D$ and/or decreasing ν_D.

Increasing ϵ requires increasing the level of swirl which has detrimental effects as discussed under the next heading. *Increasing* h_D would entail greater quantities of gas per diaphragm-opening and may reduce the accuracy of the ejectors since they would have larger blast "footprints". ν_D *can be reduced* in several ways. Temperature reductions would work, but large changes are needed to make a significant difference . Increasing the pressure of the gas supply would presumably lead to higher pressures and densities in the flow behind the shock due to the ensuing higher shock speeds, and the increase in density would decrease ν_D, as required. Different gases have different ν_D. At atmospheric pressure and room temperature, air has $\nu_D = 1.5 \times 10^{-5}\mathrm{m}^2\mathrm{s}^{-1}$ while carbon dioxide has

$\nu_D = 8.03 \times 10^{-6}\mathrm{m}^2\mathrm{s}^{-1}$ which is lower. Increasing the chamber pressure would also *increase* $U_{D\infty}$ which is desirable here.

Put simply, increasing the chamber pressure could reduce the effects of turbulence, as could supplying the ejectors with gases with lower kinematic viscosities than air.

Large pressure drops can occur due to turbulent boundary layer thicknesses (blocking effect) as in Chapter 8. These will be affected also by curvature if β is of $\mathcal{O}(1)$.

Influence of input swirl

- *Mixing*:— Swirl evolves throughout the bend, but in every case the greater the input swirl the stronger the swirl is by the end of the bend. The swirl mixes around the streamwise velocity which we suppose can have a positive effect with regard to the ideal nearly-uniform exit profile; if the flow enters the bend with a highly non-uniform profile then it can be mixed to a more uniform profile by the end of the bend. However, due to the turn-over distance described on page 115, current typical bend lengths used in practice are not always sufficient to mix profiles to a nearly uniform state. Increasing the bend length is not recommended due to the relationship between bend length and swirl strength described under the subsequent heading.

- *Density*:— The input swirl drives the density evolution in the weakly non-linear analysis via the action of equation (4.38b). However, the double integral of the density remains constant in the bend, from equation (4.49), suggesting an anti-symmetric development of the density profile. Zero input swirl leads to density variations typically of the order of

$0.02 \times \epsilon$, *i.e.* around 0.25% of the input density, from Figure 5.3, and only slightly larger for the non-zero input swirl, as shown in Figure 5.16.

- *Pressure conservation*:— In the weakly non-linear incompressible inviscid and compressible inviscid analyses, the pressure term p_1 is conserved (equations (2.36) and (4.37)) in ducts of constant cross-section. This suggests that the pressure variations are proportional to ϵ^2 at most, *i.e.* around 1% of the main flow. In general, a double integral of (2.34a) or (4.10b) gives p_1 by the flow rate, while p_2 can be found from

$$\nabla^2_{2D} p_2 = 2(\Lambda U_Z + V_y W_z - V_z W_y) \tag{D.2}$$

in the incompressible case, and by a double integral of (4.10d), with reference to (4.49), in the compressible case. Both are influenced by the input swirl since they are driven by the evolving swirl in the bend. The fully non-linear cases had conservation of the leading order parts of the density and pressure (as discussed in §5.4.7) and so the variations are of the order of ϵ or around 10% at most.

- *Non-linearity*:— We repeat that the non-linear nature of the equations means that input flow configurations cannot be correlated directly or easily with output configurations; each input must be considered on a case-by-case basis. However, bulk general predictions can be made, as above.

Influence of bend length

- *Swirl*:— In all cases the swirl grows throughout the bend and thus reducing the bend length will reduce the output swirl. For longer bends the swirl over a cross-section is proportional to the bend length (by 4.58)

and so halving the bend length will halve the output integral of the swirl. The effect of exit swirl on the interaction of adjacent external jets is being considered by Mr PE Westwood at UCL, but generally swirl is to be avoided since it misdirects the output jet.

- *Density*:— In the weakly non-linear compressible invisicid analysis, the density variation evolves following a particle in the bend but is maintained for each particle beyond the bend termination. Shorter bend lengths therefore lead to smaller density variations in general. In this context, we mention that since vertical variations in density also drive the swirl through the bend (from equation (4.25)), input variations should be minimised through measures such as those under the topic "*Shear*" on page 306 above.

Influence of bend severity

- *Less severe*:— Although we have assumed the same duct curvature throughout, the factor α, defined by (2.28) in the weakly non-linear cases and (4.13) in the fully non-linear cases, effectively measures bend severity. As discussed in [77, §6], a weaker bend corresponds to smaller α and this can be shown to increase the strength of the swirl response since the bend length increases accordingly. Similar conclusions hold in the weakly non-linear compressible inviscid regime with additionally a stronger response of the density via equation (4.38b). The appearance of the factor α in the equations of the fully non-linear cases suggests that the response to curvature may be weaker here but grows stronger over a longer bend length.

- *More severe*:— Larger values of α suggest responses over shorter dis-

tances, with the swirling motion secondary but growing rapidly in amplitude and leading to a downstream fully non-linear region.

Influence of duct cross-sectional profile

- *Corners and swirl*:— Large values of the swirl appear close to sharp corners in the duct cross-section, as in §4.4.3. The recommendation is to smooth the corners, as shown in [77].

- *Corners and turbulence* :— Sharp corners also lead to complications with respect to the turbulent boundary layer development of Part II. Again, sharp corners are to be avoided.

- *Connecting ducts*:— Though not considered herein, joining together end to end ducts of different cross-sectional shape, or the same shape but different area, can have detrimental effects on the flow development, as referred to in the discussions in Chapter 9. The suggestion is to smooth such joins.

Bibliography

[1] J.D. Au, M. Torrilhon & W. Weiss. The shock tube study in extended thermodynamics. *Physics of Fluids*, 13(8):2423–2432, 2001.

[2] A.R. Barbin, & J.B. Jones. Turbulent flow in the inlet region of a smooth pipe. *Journal of Basic Engineering*, 85:29–34, March 1963.

[3] B. Basara & S. Jakirlic. Flow in curved pipes. *International Journal for Numerical Methods in Fluids*, 42:89–116, 2003.

[4] Sarah Bee of Sortex, Ltd. Personal communication, May 2002.

[5] Robert J.T. Bell. *Coordinate Geometry of Three Dimensions.* MacMillan & Co, Ltd., 1937.

[6] Robert P. Benedict. *Fundamentals of Pipe Flow.* John Wiley & Sons, 1980.

[7] S.A. Berger, L. Talbot & L.-S. Yao. Flow in curved pipes. *Annual Review of Fluid Mechanics*, 15:461–512, 1983.

[8] Peter S. Bernard & James M. Wallace. *Turbulent Flow.* John Wiley & Sons, 2002.

[9] H. Bippes. Basic experiments on transition in three-dimensional boundary layers dominated by crossflow instability. *Progress in Aerospace Sciences*, 35:363–412, 1999.

[10] N.D. Blackaby. *On viscous, inviscid and centrifugal instability mechanisms in compressible boundary layers, including nonlinear vortex/wave interaction and the effects of large Mach number on transition.* PhD thesis, University of London, 1991.

[11] P. Bradshaw. The analogy between streamline curvature and buoyancy in turbulent shear flow. *Journal of Fluid Mechanics*, 36(1):177–191, 1969.

[12] L.A. Catalano. A new reconstruction scheme for the computation of inviscid compressible flows on 3D unstructured grids. *International Journal for Numerical Methods in Fluids*, 40:273–279, 2002.

[13] Tuncer Cebeci. Wall curvature and transition effects in turbulent boundary layers. *AIAA Journal*, 9(9):1868–1870, 1971.

[14] Tuncer Cebeci. Calculation of unsteady two-dimensional laminar and turbulent boundary layers with fluctuations in external velocity. *Proceedings of the Royal Society of London A*, 355:225–238, 1977.

[15] Tuncer Cebeci & A.M.O. Smith. *Analysis of Turbulent Boundary Layers.* Academic Press, 1974.

[16] Tuncer Cebeci & Douglas E. Abbott. Boundary layers on a rotating disc. *AIAA Journal*, 13(6):829–832, 1975.

[17] Tuncer Cebeci & Peter Bradshaw. *Momentum Transfer in Boundary Layers.* McGraw-Hill, 1977.

[18] Tuncer Cebeci, K.C. Chang, C. Li & J.H. Whitelaw. Turbulence models for wall boundary layers. *AIAA Journal*, 24(3):359–360, 1986.

[19] C.J. Chapman. *High Speed Flow.* Cambridge University Press, 2000.

[20] Raviprakash Chinni, Vireshwar Sahai & Sastri Munukutla. Computational study of developing turbulent pipe flow. In Chwang, Lee & Leung, editor, *Hydrodynamics.* Balkema, 1996.

[21] Chuen-Yen Chow. *An Introduction to Computational Fluid Dynamics.* Wiley, 1979.

[22] Ernst Becker (Trans. E.L. Chu). *Gas Dynamics.* Academic Press, 1968.

[23] D.A.R. Davis & F.T. Smith. On subsonic, supersonic and hypersonic inflectional-wave/vortex interaction. *Journal of Engineering Mathematics*, 30:611–45, 1996.

[24] P.J. Davis & P. Rabinowitz. *Numerical Integration.* Blaisdell Publishing Co., 1967.

[25] W.R. Dean. The streamline motion of fluid in a curved pipe. *Philosophical Magazine*, 30:673–93, 1928.

[26] A.T. Degani, F.T. Smith & J.D.A. Walker. The structure of a three-dimensional turbulent boundary layer. *Journal of Fluid Mechanics*, 250:43–68, 1993.

[27] John W. Dettman. *Applied Complex Variables.* Dover, 1984.

[28] P.A. Durbin. A Reynolds stress model for near-wall turbulence. *Journal of Fluid Mechanics*, 249:465–498, 1993.

[29] J.G.M. Eggels, F. Unger, M.H. Weiss, J. Westerweel, R.J. Adrian, R. Friedrich & F.T.M Nieuwstadt. Fully developed turbulent pipe flow: a comparison between direct numerical simulation and experiment. *Journal of Fluid Mechanics*, 268:175–209, 1994.

[30] L.B. Ellis & P.N. Joubert. Turbulent shear flow in a curved duct. *Journal of Fluid Mechanics*, 62(1):65–84, 1974.

[31] J. Eustice. Experiments of streamline motion in curved pipes. *Proceedings of the Royal Society of London A*, 85:119–131, 1911.

[32] G. Gauthier, P. Gondret & M. Rabaud. Centrifugal instabilities in a curved duct of small aspect ratio. *Physics of Fluids*, 13(10):2831–2834, 2001.

[33] F.B. Gessner & J.B. Jones. On some aspects of fully-developed turbulent flow in rectangular channels. *Journal of Fluid Mechanics*, 23(4):689–713, 1965.

[34] J.H. Grindley & A.H. Gibson. On the frictional resistance to the flow of air through a pipe. *Proceedings of the Royal Society of London A*, 80:114–139, 1908.

[35] Newman A. Hall. *Thermodynamics of Fluid Flow.* Longmans, 1957.

[36] P. Hall & F.T. Smith. The nonlinear interaction of Tollmien-Schlichting waves and Taylor-Goertler vortices in curved channel flows. *Proceedings of the Royal Society of London A*, 417:255–282, June 1988.

[37] P. Hall & M. Malik. The growth of Goertler vortices in compressible boundary layers. *Journal of Engineering Mathematics*, 23:239–51, 1989.

[38] Seymour C. Himmel. Application of the method of coordinate perturbation to unsteady duct flow. Technical report, NACA Technical Memorandum 1439, 1958.

[39] John Hinch. Personal communication, 23rd June 2003.

[40] M.S. Howe, M. Iida, T. Fukuda & T. Maeda. Theoretical and experimental investigation of the compression wave generated by a train entering a tunnel with a flared portal. *Journal of Fluid Mechanics*, 425:111–132, 2000.

[41] G.D. Huffman & P. Bradshaw. A note on von Karmàn's constant in low Reynolds number turbulent flow. *Journal of Fluid Mechanics*, 53(1):45–60, 1972.

[42] I.A. Hunt & P.N. Joubert. Effects of small streamline curvature on turbulent duct flow. *Journal of Fluid Mechanics*, 91(4):633–659, 1979.

[43] K.S. Hwang, G.X. Cui, Z.S. Zhang & B.C. Feng. Quantitative visualisation of the near-wall structures in a turbulent pipe flow by image correlation velocimetry. *Experiments in Fluids*, 32:447–452, 2002.

[44] O. Igra, L. Wang & J. Falcovitz. Non-stationary compressible flow in ducts with varying cross-section. *Proceedings of the Institution of Mechanical Engineers*, 212(G):225–243, 1998.

[45] O. Igra, X. Wu, G.Q. Hu & J. Falcovitz. Shock wave propagation into a dust-gas suspension inside a double-bend conduit. *Journal of Fluids Engineering*, 124:483–491, 2002.

[46] H. Ito. Friction factors for turbulent flow in curved pipes. *Journal of Basic Engineering*, 81D:123–134, 1959.

[47] H.Ito. Pressure losses in smooth pipe bends. *Journal of Basic Engineering*, 82D:131–143, 1960.

[48] Ahmad Farid Khorrami. *Hypersonic Aerodynamics on Flat plates and Thin Airfoils.* PhD thesis, Oxford University, 1991.

[49] Doyle D. Knight. Inviscid compressible flow. In Richard W. Johnson, editor, *The Handbook of Fluid Dynamics.* CRC Press, 1998.

[50] Y. Kohama. Three-dimensional boundary layer transition on a concave-convex curved wall. In R. Narashima H.W. Liepmann, editor, *Turbulence Managment and Relaminarisation*, Proceedings of the IUTAM Symposium Bangalore, India, 1987. Springer-Verlag, 1988.

[51] John Laufer. Investigation of turbulent flow in a two-dimensional channel. Technical report, NACA Report 1053, 1949.

[52] John Laufer. The structure of turbulence in fully developed pipe flow. Technical report, NACA Report 1174, 1952.

[53] H.W. Liepmann & A. Roshko. *Elements of Gasdynamics.* Wiley, 1957.

[54] A. Mager. Three-dimensional laminar boundary layers. In F.K. Moore, editor, *Theory of Laminar Flows*, volume IV of *High Speed Aerodynamics and Jet Propulsion.* OUP, 1964.

[55] Adric Marsh of Sortex, Ltd. Personal communication, May 2003.

[56] A. Melling & J.H. Whitelaw. Turbulent flow in a rectangular duct. *Journal of Fluid Mechanics*, 78(2):289–315, 1976.

[57] A. Monica & Phoolan Prasad. Propagation of a curved weak shock. *Journal of Fluid Mechanics*, 434:119–151, 2001.

[58] Gino Moretti. Computation of flows with shocks. *Annual Review of Fluid Mechanics*, 19:313–337, 1987.

[59] Shin-ichi Nakao. Turbulent flow in square ducts after an expansion. *AIAA Journal*, 24(6):979–982, June 1986.

[60] A. Neish & F.T. Smith. The turbulent boundary layer and wake of an aligned flat plate. *Journal of Engineering Mathematics*, 22:15–42, 1988.

[61] Erdal Oktay, İ Sinan Akmandor and Ahmet Ş Üçer. A numerical solution of 3D inviscid rotational flow in turbines and ducts. *International Journal for Numerical Methods in Fluids*, 26:907–926, 1998.

[62] Deepak Om, & Morris E. Childs. Multiple transonic shock-wave/turbulent boundary-layer interaction in a circular duct. *AIAA Journal*, 23(10):1506–1511, 1985.

[63] Michael E. O'Neill & Frank Chorlton. *Viscous and Compressible Fluid Dynamics.* Ellis Horwood, 1989.

[64] Jean Piquet. *Turbulent Flows.* Springer-Verlag, 1999.

[65] Patrick J. Roache. *Computational Fluid Dynamics.* Hermosa, 1982.

[66] P.J. Roache. Quantification of uncertainty in computational fluid dynamics. *Annual Review of Fluid Mechanics*, 29:123–60, 1997.

[67] H. Schlichting & K. Gersten. *Boundary Layer Theory.* Springer-Verlag, 8th edition, 2000.

[68] Walter R. Schwarz & Peter Bradshaw. Turbulence structural changes for a three-dimensional turbulent boundary layer in a 30° bend. *Journal of Fluid Mechanics*, 272:183–209, 1994.

[69] B.W. Skews. The shape of a diffracting shock wave. *Journal of Fluid Mechanics*, 29(2):297–304, 1967.

[70] S.A. Sloan & M.A. Nettleton. A model for the decay of a wall shock in a large abrupt area change. *Journal of Fluid Mechanics*, 88(2):259–272, 1978.

[71] F.T.Smith. Fluid flow into a curved pipe. *Proceedings of the Royal Society of London A*, 351:71–87, 1976.

[72] F.T. Smith. Steady and unsteady boundary-layer separation. *Annual Review of Fluid Mechanics*, 18:197–220, 1986.

[73] F.T. Smith. A reversed-flow singularity in interacting boundary layers. *Proceedings of the Royal Society of London A*, 420:21–52, 1988.

[74] F.T. Smith. Air flow pulsing through an ejector duct, a report to Sortex Ltd. Technical report, Department of Mathematics, University College London, 1999.

[75] F.T. Smith. Personal communication, 28th February 2000.

[76] F.T. Smith & M.A. Jones. One-to-few and one-to-many branching tube flows. *Journal of Fluid Mechanics*, 423:1–31, 2000.

[77] F.T. Smith & L. Li. Swirl flow effects in a duct bending through a substantial angle. *Journal of Engineering Mathematics*, 43:315–346, 2002.

[78] K. Stewartson. *The Theory of Laminar Boundary Layers in Compressible Fluids.* OUP, 1964.

[79] B.S. Stratford. The prediction of separation of the turbulent boundary layer. *Journal of Fluid Mechanics*, 5:1–16, 1958.

[80] M. Sun & K. Takayama. Vorticity production in shock diffraction. *Journal of Fluid Mechanics*, 478:237–256, 2003.

[81] V.V. Sychev. On turbulent boundary layer separation. In F.T. Smith & S.N. Brown, editor, *Boundary Layer Separation*, Proceedings of the IUTAM Symposium 1986. Springer-Verlag, 1987.

[82] L. Talbot and S.J. Wong. A note on boundary-layer collision in a curved pipe. *Journal of Fluid Mechanics*, 1982.

[83] A.B. Tayler. *Notes on Compressible Flow.* OUP, 1965.

[84] G.I. Taylor. The criterion for turbulence in curved pipes. *Proceedings of the Royal Society of London A*, 124:243–249, 1929.

[85] S. Thangam & N. Hur. Laminar secondary flows in curved rectangular ducts. *Journal of Fluid Mechanics*, 217:421–440, 1990.

[86] James L. Thomas, Boris Diskin, Achi Brandt. Textbook multigrid efficiency for fluid simulations. *Annual Review of Fluid Mechanics*, 35:317–40, 2003.

[87] J. Thomson. On the origin of windings of rivers in alluvial plains with remarks on the flow of water round bends in pipes. *Proceedings of the Royal Society of London A*, 25:5–8, 1876.

[88] Robert L. Trimpi & Nathaniel B. Cohen. A nonlinear theory for predicting the effects of unsteady laminar, turbulent, or transitional boundary layers on the attenuation of shock waves in a shock-tube with experimental comparison. Technical report, NACA Technical Note 4347, 1958.

[89] M. Van Dyke. *Album of Fluid Motion.* Parabolic Press, 1982.

[90] J.D.A. Walker, M.C. Ece & M.J. Werle. An embedded function approach for turbulent flow prediction. *AIAA Journal*, 29:1810–1818, 1991.

[91] A.J. Ward-Smith. *Internal Fluid Flow.* Clarendon Press, Oxford, 1980.

[92] Donald R. White. Influence of diaphragm opening time on shock-tube flows. *Journal of Fluid Mechanics*, 4(6):585–599, 1958.

[93] G.B. Whitham. A new approach to problems of shock dynamics Part I. Two-dimensional problems. *Journal of Fluid Mechanics*, 2(2):145–171, 1957.

[94] G.B. Whitham. A new approach to problems of shock dynamics Part II. Three-dimensional problems. *Journal of Fluid Mechanics*, 5(3):369–386, 1959.

[95] D.C. Wilcox & T.L. Chambers. Streamline curvature effects on turbulent boundary layers. *AIAA Journal*, 15(4):574–580, 1977.

[96] Tianglang Yang & Liqiu Wang. Solution structure and stability of viscous flow in curved square ducts. *Journal of Fluids Engineering*, 123:863–868, 2001.

[97] J. Zhang & B. Lakshminarayana. Computation and turbulence modeling for three-dimensional boundary layers including turbomachinery flows. *AIAA Journal*, pages 1861–1869, November 1990.